

MOVPE Growth and Characterisation of
ZnO Properties for Optoelectronic Applications

Dissertation

Zur Erlangung des akademischen Grades

doctor rerum naturalium
(Dr. rer. nat.)

genehmigt durch die Fakultät für Naturwissenschaften
der Otto-von-Guericke-Universität Magdeburg

von Dipl. Phys. Nikolay Oleynik

geboren am 25.04.1979 in Kirovskij, Gebiet Taldy-Kurgan, Kasachstan

Gutachter: Prof. Dr. Alois Krost

Univ. Magdeburg/FNW/Institut für Experimentelle Physik

Prof. Dr. Andreas Waag

Techn. Univ. Braunschweig/Institut für Halbleitertechnik

eingereicht am: 06.09.2006

verteidigt am: 07.03.2007

Abstract

Eine neue Methode der metallorganischen Gasphasenepitaxie (MOVPE) für das Wachstum und die Dotierung von hochwertigem ZnO Schichten wurde in dieser Arbeit entwickelt. ZnO ist ein potenzielles optoelektronisches Material für effektive Lichterzeugung im grünen bis ultravioletten Spektralbereich.

Optoelektronische Anwendungen von ZnO erfordern Verunreinigungs-freie monokristalline Schichten mit glatter Oberfläche und niedriger Kristallgitter-Defektkonzentration. Am Anfang dieser Arbeit gab es nur wenige Berichte über MOVPE Wachstum von polykristallinem ZnO. Die meist sehr geringe Qualität dieser ZnO Schichten wurde den für epitaktisches Wachstum meist ungeeigneten Substraten und den Gasphasen-Vorreaktionen zwischen dem Zn- und den O-Vorläufern zugeschrieben. Um die ZnO Qualität zu kontrollieren, wurden einige O-Vorläufer für das Wachstum auf GaN/Si(111) oder GaN/Saphir Substraten mit unterschiedlichen Reaktortemperaturen und -drücken geprüft. ZnO Schichten mit XRD Halbwertsbreiten der (0002) Rockingkurven von 180" und schmaler Kathodolumineszenz von 1.3 meV der dominierenden Emission I_8 wurden mit einem zweistufigen Verfahren synthetisiert. Diese Prozedur beginnt bei niedriger Temperatur mit einer mit tertiär-Butanol gewachsenen ZnO Schicht, und einer nachfolgend gewachsenen Hochtemperaturschicht mit N_2O als O-Vorläufer.

Die p-Typ Dotierung des normalerweise als n-Typ Halbleiter vorliegendem ZnO gestaltet sich als sehr schwierig. Diese Dotierungs-Asymmetrie ist problematisch für ZnO-basierte Bauelemente. Seit 1992 haben einige Publikationen über die Herstellung von p-Typ ZnO berichtet, diese Ergebnisse sind aber immer noch, mangels fehlender Reproduzierbarkeit, fraglich. Intrinsische Defekte, Nichtstöchiometrie und Wasserstoff sind Quellen der n-Typ Leitfähigkeit von ZnO. Zusammen mit einer niedrigen Löslichkeit der möglichen p-Typ Dotanden und der tiefen Position der Störstellenniveaus erklären diese Faktoren teils die Schwierigkeit einer p-Typ Dotierung in ZnO. Jedoch gibt es keinen vollständig beschriebenen Mechanismus der Asymmetrie von ZnO Dotierung.

In dieser Arbeit wurden NH_3 , unsymmetrisches Dimethylhydrazin (UDMHy), Diisobutylamin und NO als Stickstoff-Vorläufer für die p Typ Dotierung von ZnO untersucht. Einige NH_3 und UDMHy-dotierte Proben haben eine Verringerung der Elektronkonzentration nach dem Tempern gezeigt, aber keine zuverlässige p-Typ Leitfähigkeit. NO als Vorläufer führt zur sehr glatten Schichten mit einer starken Verringerung der Wachstumsrate, jedoch beeinflusst er nicht die optischen und elektrischen Eigenschaften des ZnO. Diisobutylamin verschlechtert die Eigenschaften von ZnO, ein Stickstoff-Einbau wurde nicht beobachtet. Eine braune Farbe der Proben wird beobachtet, wenn man NH_3 oder UDMHy verwendet hat. Aus der starken Verringerung der Ladungskonzentration gegenüber der Hintergrunddotierung und dem Verhalten der DAP Lumineszenz wurde gezeigt, dass der Stickstoff als ein Akzeptor in ZnO mit UDMHy erfolgreich eingeführt werden kann.

Abstract

In this work a new Metalorganic Vapor Phase Epitaxy (MOVPE) method was developed for the growth and doping of high-quality ZnO films. ZnO is a unique optoelectronic material for the effective light generation in the green to the UV spectral range.

Optoelectronic applications of ZnO require impurity-free monocrystalline films with smooth surfaces and low concentration of the defects in the crystal lattice. At the beginning of this work only few reports on MOVPE growth of polycrystalline ZnO existed. The low quality of ZnO is attributed to the lack of an epitaxially matched substrate, and gas-phase prereactions between the Zn- and O-precursors. To achieve control over the ZnO quality, several O-precursors were tested for the growth on GaN/Si(111) or GaN/Sapphire substrates at different reactor temperatures and pressures. ZnO layers with XRD rocking curve FWHMs of the (0002) reflection of 180'' and narrow cathodoluminescence of 1.3 meV of the dominant I₈ emission were synthesized using a two-step growth procedure. In this procedure, ZnO is homoepitaxially grown at high temperature using N₂O as O-precursor on a low temperature grown ZnO buffer layer using tertiary-butanol as O-precursor.

p-Type doping of ZnO, which usually exhibits n-type behaviour, is very difficult. This doping asymmetry represents an issue for ZnO-based devices. Beginning from 1992, a growing number of reports have been claiming a fabrication of p-type ZnO, but, due to the missing reproducibility, they are still questionable. Native defects, non-stoichiometry, and hydrogen are sources of n-type conductivity of ZnO. Together with a low solubility of the potential p-type dopants and deep position of impurity levels, these factors partly explain p-type doping difficulties in ZnO. However, there is no fully described mechanism of the ZnO doping asymmetry yet.

In this work, NH₃, unsymmetrical dimethylhydrazine (UDMHy), diisobutylamine, and NO nitrogen precursors were studied for p-type doping of ZnO. Some NH₃- and UDMHy-doped samples have shown a reduction in the electron concentration after post-growth rapid thermal annealing, but no reliable p-type conductivity was observed. The use of the NO precursor results in very smooth layers with a strong drop in growth rate. However, it does not influence the optical and electrical properties of the ZnO. Diisobutylamine deteriorates the properties of ZnO and does not lead to nitrogen incorporation. A brownish color of the samples is observed when using NH₃ or UDMHy. From the strong reduction in the carrier concentration about one order of magnitude lower than the background doping concentration, and the behavior of the DAP luminescence, it is concluded that nitrogen as an acceptor can be successfully introduced in ZnO using UDMHy.

Parts of this work were already published:

E. Mueller, D. Livinov, D. Gerthsen, C. Kirchner, A. Waag, N. Oleynik, A. Dadgar, and A. Krost, NATO Science Series, II: Mathematics, Physics and Chemistry, **194** (Zinc Oxide), 99-111 (2005).

A. Krtschil, A. Dadgar, N. Oleynik, J. Bläsing, A. Diez, and A. Krost, Applied Physics Letters **87**, 262105 (2005).

A. Dadgar, A. Krtschil, F. Bertram, S. Giemsch, T. Hempel, P. Veit, A. Diez, N. Oleynik, R. Clos, J. Christen, and A. Krost, Superlattices and Microstructures **38**, 245 (2005).

A. Dadgar, N. Oleynik, J. Bläsing, S. Deiter, D. Forster, F. Bertram, A. Diez, M. Seip, A. Greiling, J. Christen, and A. Krost, Journal of Crystal Growth **272**, 800 (2004).

F. Bertram, D. Forster, J. Christen, N. Oleynik, A. Dadgar and A. Krost, Journal of Crystal Growth **272**, 785 (2004).

F. Bertram, D. Forster, J. Christen, N. Oleynik, A. Dadgar, and A. Krost, Appl. Phys. Lett. **85**, 1976 (2004).

A. Krost, J. Christen, N. Oleynik, A. Dadgar, S. Deiter, J. Bläsing, A. Krtschil, D. Forster, F. Bertram, and A. Diez, Appl. Phys. Lett. **85**, 1496 (2004).

S. Deiter, H. Witek, N. Oleynik, J. Bläsing, A. Dadgar, and A. Krost, Zeitschrift für Kristallographie **219**, 187 (2004).

A. Dadgar, N. Oleynik, D. Forster, S. Deiter, H. Witek, J. Bläsing, F. Bertram, A. Krtschil, A. Diez, J. Christen, and A. Krost, J. Cryst. Growth **267**, 140 (2004).

N. Oleynik, A. Dadgar, J. Bläsing, M. Adam, A. Krtschil, D. Forster, F. Bertram, A. Diez, M. Seip, A. Greiling, J. Christen, and A. Krost, Jpn. J. Appl. Phys. **42**, 7474 (2003).

N. Oleynik, M. Adam, A. Krtschil, J. Bläsing, A. Dadgar, F. Bertram, D. Forster, A. Diez, A. Greiling, M. Seip, J. Christen, and A. Krost, Journal of Crystal Growth **248**, 14 (2003).

N. Oleynik, A. Dadgar, J. Christen, J. Bläsing, M. Adam, T. Riemann, A. Diez, A. Greiling, M. Seip, and A. Krost, phys. stat. sol. (a) **192**, 189 (2002).

Table of contents

| | |
|---|----|
| 1. Introduction..... | 1 |
| 2. ZnO properties..... | 3 |
| 2.1. Structural and crystalline properties..... | 3 |
| 2.2. Polar surfaces and etching..... | 4 |
| 2.3. Optical properties..... | 4 |
| 2.4. n- and p-type conductivity | 6 |
| 2.5. Nitrogen doping..... | 7 |
| 3. Characterization techniques..... | 11 |
| 3.1. Surface morphology..... | 11 |
| 3.2. Capacitance-voltage measurements..... | 11 |
| 3.3. Cathodoluminescence..... | 12 |
| 3.4. X-ray diffraction..... | 13 |
| 3.4.1. $\tilde{\omega}$ and θ - 2θ scans around the [0001] direction..... | 14 |
| 3.4.2. XTS θ - 2θ scans around the $[10\bar{1}0]$ direction..... | 15 |
| 3.4.3. GID ω -scans around the $[10\bar{1}0]$ direction..... | 15 |
| 3.4.4. Reciprocal space mapping..... | 16 |
| 3.5. Transmission Electron Microscopy | 17 |
| 4. MOVPE system and rapid thermal annealing..... | 19 |
| 4.1. Metal organic vapor phase epitaxy of ZnO..... | 19 |
| 4.1.1. Substrate choice | 21 |
| 4.1.2. Carrier gases..... | 23 |
| 4.2. <i>In-situ</i> measurement..... | 24 |
| 4.3. Doping methods..... | 24 |
| 4.4. Rapid thermal annealing..... | 25 |
| 5. Growth of undoped ZnO..... | 27 |
| 5.1. O-precursors..... | 27 |
| 5.1.1. Iso-propanol..... | 28 |

| | |
|---|-----|
| 5.1.2. Acetone..... | 35 |
| 5.1.3. Diethyl-ether..... | 37 |
| 5.1.4. Tertiary-butanol..... | 37 |
| 5.1.4.1. Growth parameter variation..... | 37 |
| 5.1.4.2. <i>In-situ</i> annealing and Ostwald ripening..... | 44 |
| 5.1.5. N ₂ O..... | 53 |
| 5.2. Two-step growth..... | 57 |
| 5.2.1. Buffer thickness and growth temperature..... | 57 |
| 5.2.2. Buffer layer annealing..... | 67 |
| 5.2.3. DMZn flow variation..... | 75 |
| 5.3. Three-step growth..... | 79 |
| 6. Nitrogen doping | 83 |
| 6.1. NO..... | 83 |
| 6.2. Diisobutylamine..... | 87 |
| 6.3. Ammonia..... | 91 |
| 6.3.1. Two-step growth..... | 91 |
| 6.3.2. Two-step growth with reduced DMZn flow | 105 |
| 6.4. UDMHy..... | 109 |
| 6.4.1. Two-step growth..... | 109 |
| 6.4.2. Three-step growth | 115 |
| 7. Summary..... | 119 |
| 8. Appendix..... | 121 |
| 8.1. Zn- and O-precursors..... | 121 |
| 8.1.1. Dimethylzinc..... | 121 |
| 8.1.2. Iso-propanol | 121 |
| 8.1.3. Diethylether | 122 |
| 8.1.4. Acetone | 122 |
| 8.1.5. Tertiary-butanol..... | 124 |
| 8.1.6. N ₂ O..... | 125 |
| 8.2. N- and P-precursors..... | 126 |
| 8.2.1. Nitric Oxide | 126 |
| 8.2.2. Diisobutylamine | 127 |

| | |
|--------------------------------|-----|
| 8.2.3. Ammonia | 127 |
| 8.2.4. Dimethylhydrazine | 128 |
| 8.2.5. Phosphine..... | 128 |
| 9. References..... | 129 |
| 10. Acknowledgements..... | 141 |

1. Introduction

Semiconductor industry is continuously bringing new inventions into our everyday life. For example, the mass-producible and high-quality blue-ultraviolet GaN-based light emitting diodes and lasers are used in blue-ray DVDs, displays, and traffic signals.

Zinc oxide ($E_g=3.37$ eV at room temperature) is unique optoelectronic material for the effective light generation in the green to the UV spectrum range. Its high exciton binding energy of 60 meV [Hum73] allows excitonic optically pumped lasing at room temperature [Kli78, Bag97, Yu97, Bag98]. Higher exciton binding energy of 90 - 100 meV is achievable by fabrication of ZnO-related superlattices [Sun00, Chi03]. The possibility of band-gap tuning from 3 eV to 4.5 eV in small lattice mismatched $Mg_xZn_{1-x}O$ and $Zn_xCd_{1-x}O$ alloys was demonstrated [Oht98, Mak01, Tak03, Ron04], and high-quality quantum wells were obtained. Additionally, ZnO is a polaritonic medium for microcavity polariton lasers [Kav02, Zam02].

ZnO is naturally n-type semiconductor, which can hardly be doped to become a p-type. This doping asymmetry represents an issue for optoelectronic applications of ZnO. Native defects, the non-stoichiometry, and hydrogen are the sources of n-type conductivity of ZnO [Man65, Ave67, Kob96, Suk82, Wal00, Par02, The02, The03]. Low solubility of the dopants [Ave67, Par02], and deep position of the impurity levels [Wal00, Par02] represent the main difficulties for achieving p-type material. Beginning from 1992 [But92] until now [Per05, Lim05], a growing number of reports have been claiming the growth of p-type ZnO by pulsed laser deposition, sputtering, metalorganic vapor phase epitaxy, and molecular beam epitaxy. However, no growth technique is proven to achieve reliable, reproducible high-quality p-type ZnO.

Metal Organic Vapor Epitaxy* (MOVPE) method [Man68] offers the reproducible growth of high-quality, pure films with homogeneous properties over a large substrate area. MOVPE is an effective means for the growth and doping of ZnO because it is proper for the growth of other wide-band gap compound semiconductors which have asymmetrical doping issue (GaN, ZnSe).

At the beginning of this work only few reports on MOVPE growth ZnO existed [Sav64, Rya68, Ker70, Shi78, Gha80, Lau80, Shi81, Rot81]. These films, however, were used for applications like transparent conduction oxides or waveguides. The surface of the films was so rough that the film must be lapped and polished [Cha75]. Most of the films had low crystalline quality due to the lack of suitable substrate for epitaxy. Additionally, gas-phase prereac-

* From Greek „epi“ - on and „taxis“ – ordering; the process of growing single-crystal layers of semiconductor materials onto the surface of a single crystal substrate.

tions severely degraded the quality of ZnO layers due to the lack of the appropriate O-precursor.

The main goals of this work were to find a suitable substrate for epitaxy, develop growth procedures of ZnO with suited O-precursors, to investigate the properties of ZnO, and to dope it in order to achieve p-type conductivity.

The structure of the thesis is as follows. Chapter 2 describes the structural, optical, and electrical properties of ZnO. Chapter 3 gives an overlook of the characterization techniques employed for the characterization of the ZnO films. Chapter 4 deals with some issues of MOVPE growth, doping, and post-growth rapid thermal annealing of ZnO. Chapters 5 and 6 describe and discuss the results of investigation of the properties of MOVPE grown ZnO. Chapter 7 summarizes the results of this work.

2. Properties of ZnO

2.1. Structural and Crystalline Properties

As it was mentioned in the introduction, ZnO films did not fit the requirements for optoelectronic applications until the 1981.* One of the ZnO epitaxy issues is the lack of the lattice-matched substrate with a similar crystalline structure.

Crystal lattice of ZnO was investigated already in 1930s and in 1950s [Bun35, Bra35, Hel50, Rym52, Cim57, Gra54]. ZnO has a wurtzite structure** which represents a hexagonal closed-packed lattice (Fig. 2.1, left). The coordinate system of the unit cell consists of 4 vectors, with \vec{a}_1 , \vec{a}_2 and \vec{a}_3 lying in the same plane, and \vec{a}_4 perpendicular to them (Fig. 2.1, right).

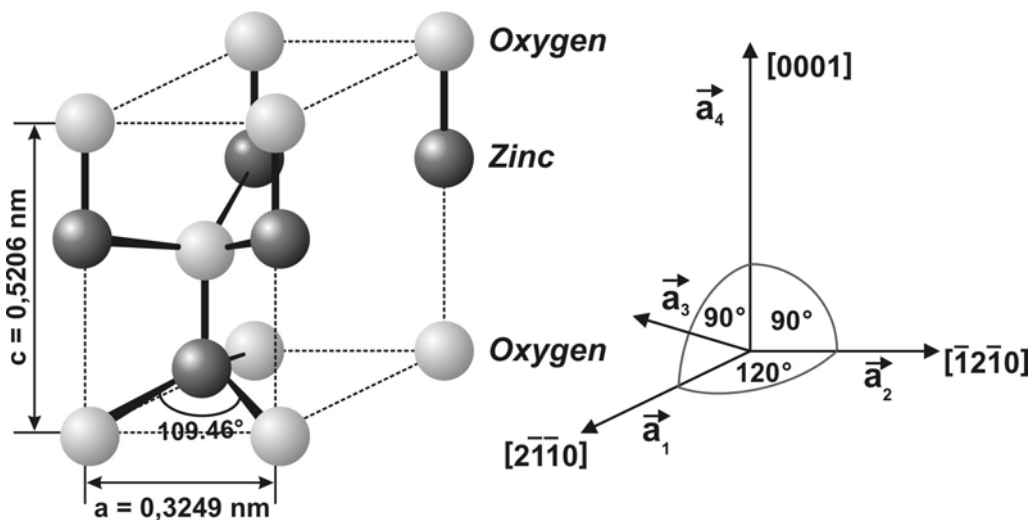


Fig. 2.1. ZnO unit cell (picture after [Rie01]).

Besides the lattice matching, the choice of the substrate for the epitaxy of ZnO includes some additional considerations, which are discussed in Chapter 4.1.1.

Another issue of ZnO epitaxy is the significant scattering of the measured ZnO lattice parameters reported in different researches. For example, the reported \vec{a} lattice parameter values vary from 0.32475 to 0.32501 nm, and the c lattice parameter values - from 0.52042 to 0.52075 nm [Özg05]. On the one side, this scattering directly refers to the use of different mismatched substrates and the growth processes. On the other side, it is attributed to the fundamental property of the ZnO, the deviation from stoichiometry [Kal81]. Non-stoichiometry

* In 1980s – 1990s ZnO was not studied extensively. Nowadays the interest to this topic is on the rise again.

** The word ‘wurtzite’ originates from the French chemist, Ch. A. Wurtz (1817-1884). According to the review of Özgüer *et al.*, the zinblende structure of ZnO is achievable by growth on cubic substrates, and the rocksalt structure - at high pressures [Özg05]. ZnO discussed in this work was not synthesized under those conditions.

of ZnO strongly influences its optical and electrical properties. In particular, it is one of the reasons for the doping asymmetry of ZnO (Chapter 2.4).

2.2. Polar Surfaces and Etching

From the crystalline structure of ZnO, it is evident that it has different polar surfaces along the *c*-axis, Zn-polarity and O-polarity, Fig. 2.1. Similar to GaN, which has the same crystalline structure, the ZnO polarity influences its physical and chemical properties. Still, there are some open questions. For example, the polarity of GaN influences its impurity doping efficiency [Li00], yet there is a controversy which polarity is better for *p*-type doping of ZnO [Hon02].*

The polarity of ZnO was studied by means of X-ray diffraction and chemical etching already in 1960s [Col62, Mar62]. At the present time, it is usually determined by the chemical etching in different acid solutions. The etching rate of O-polar sample is much higher than that of the Zn-polar one [Col62]. The etching of ZnO is well established, as demonstrated in a number of studies beginning from 1990s [Vel90, Zhu04, Wan05]**. Taking into account that the control over ZnO polarity is recently proclaimed [Hon02, Kat04], this opens prospect for the industrial microprocessing of the ZnO-based devices.

2.3. Optical Properties

According to Kaldis *et al.*, ZnO is noted as a material with high luminescence intensity from the beginning of 20th century [Kal81]. For example, ZnO powders served as a material for short decay time cathodoluminescence screens in 1940s [Rie41]***. Nowadays, in high quality ZnO crystals at helium temperature very narrow excitonic recombination lines (40 μ eV) are resolved (Tab. 2.1) [Mey03, Mey05]. Additionally, the excitonic luminescence is detected at room temperature because of exciton binding energy of 60 meV [Hum73]. This energy is higher than in GaN (21-25 meV), which also makes ZnO exceptionally attractive for optoelectronics. The luminescence spectrum of ZnO consists of three groups of peaks which are situated in the ultra-violet and visible region of the electromagnetic spectrum (360 nm to 750 nm). Beside others, it includes band-to-band, free-to-bound transitions,

* More on the properties of ZnO films with the different polar surfaces can be found e. g. in the review of Ozgur *et al.* [Özg05].

** See the review of Pearton *et al.* [Pea04].

*** Reference from [Kal81].

| Line | Wavelength (nm) | Energy (eV) | Literature source | Chemical identity [Mey05] |
|-----------------|-----------------|-------------|-------------------|---------------------------|
| A _L | 367.12 | 3.3772 | [Lan82b] | |
| A _T | 367.26 | 3.3759 | [Lan82b] | |
| A _F | 367.38 | 3.3748 | [Lan82b] | |
| I ₀ | 367.63 | 3.3725 | [Rey65] | |
| I ₁ | 367.71 | 3.3718 | [Rey65] | |
| I _{1a} | 368.13 | 3.3679 | [Rey65] | |
| I ₂ | 368.19 | 3.3674 | [Rey65] | |
| I ₃ | 368.29 | 3.3665 | [Rey65] | |
| I _{3a} | 368.34 | 3.3660 | [Rey65] | |
| I ₄ | 368.34 | 3.3660 | [Rey65] | H |
| I ₅ | 368.86 | 3.3614 | [Rey65] | |
| I ₆ | 368.92 | 3.3608 | [Rey65] | Al |
| I _{6a} | 368.96 | 3.3604 | [Rey65] | Al |
| I ₇ | 369.01 | 3.3600 | [Rey65] | |
| I ₈ | 369.03 | 3.3598 | [Rey65] | Ga |
| I _{8a} | 369.08 | 3.3593 | [Lan82] | Ga |
| I ₉ | 369.37 | 3.3567 | [Lan82] | In |
| I ₁₀ | 369.76 | 3.3531 | [Lan82] | |
| I ₁₁ | 370.28 | 3.3484 | [Lan82] | |

Tab. 2.1. Recombinations lines of excitonic luminescence in ZnO. A_L and A_T are the longitudinal and transversal free A-exciton states.

and donor-acceptor pair (DAP) recombinations.* For example, a blue-green emission centered around 500 nm originates from a Zn vacancy and an interstitial Zn [Jin00], O vacancy [Byl78, Rie52, Kro54, Pro95] and interstitial O [Ege96, Hah65, Liu92], and DAP recombination [Gar02]. An orange-red emission at 1.9 eV assigned to Li and Na impurities [Mey05]. Excitonic luminescence is reviewed in more details elsewhere [Rey65, Loo76, Pre88, Lan99, Mey04, Mey05].

* A detailed description of those recombination processes in semiconductors in general can be found elsewhere [Kli95, Rei98]. Defect luminescence in ZnO is also described in the review of Özgür *et al.* [Özg05].

Spatial Distribution and Localization of the Luminescence

As it has been shown in the work of Meyer *et. al*, there is a strong spatial localization of excitonic luminescence which is caused by the structural defects in ZnO [Mey03]. Spatially and spectrally resolved cathodoluminescence measurements which were used in this work allowed examining the properties of the ZnO films (Chapter 3.3). The detection of the luminescence from donor- and acceptor-bonded excitons gives information about distribution of the defects and recombination centers in ZnO. Thus the correlation between the surface morphology and optical properties, and information about stress inside the ZnO layer can be determined.

2.4. n- and p-type Conductivity

Undoped ZnO exhibits n-type conductivity^{*}, and resists being doped p-type. This technological issue pulls up the use of ZnO for optoelectronics. What is more, the fundamental explanations of natural n-type conductivity and asymmetrical doping of ZnO are still disputable.

In literature, the n-type conductivity of ZnO is attributed to native defects, non-stoichiometry, and hydrogen^{**}. Sukkar *et al.* has shown that non-stoichiometric ZnO has natural excess of Zn or deficiency of oxygen [Suk82]. However, it is unknown whether the donor is a zinc interstitial (Zn_i) or an oxygen vacancy (O_v) [Kal81]. On the one side, Thomas discussed zinc interstitials as the cause of high conductivity of zinc pretreated samples [Tho56]. Sukkar and Kohen supported this with the ionic diffusion and size considerations [Suk82, Koh00]. Opposite to those arguments, oxygen vacancies were claimed responsible for n-type conductivity of ZnO on the basis of the calculation of reaction rates, diffusion experiments, electrical conductivity and Hall-effect measurements [Kal81, Bag97]. Apart from this discussion, interstitial atomic hydrogen is theoretically predicted to introduce a shallow donor state with ionization energy of about 0.05 eV in ZnO [Wal00, Wal01, Wal02, Tho03, Oha02].

* ZnO is feasibly doped n-type with group-III elements such as In, Al, Ga, B [Tho59, Min85, Nin97, Hir98], Si [Min85], and F [Hu91].

** Hydrogen in ZnO was investigated already in the 1950s [Mol54, Lan57, Tho56, Tho59]. Mollwo has found that heating ZnO in hydrogen increases its conductivity and changes its luminescent properties [Mol54]. It is remarkable that the first study of the hydrogen influence on the semiconductor properties was investigated in the case of ZnO, according to van de Walle [Wal00]. Nowadays, hydrogen in ZnO attracts attention because it passivates the green luminescence [Str03], influences the catalytic activity and adsorption of gases [Mey03], and affects the polar surfaces of ZnO differently [Los05].

Those theoretical conclusions are experimentally supported by the electron paramagnetic resonance measurements of bulk single-crystals [Hof02, Pol03, Ip03]. Van de Walle *et al.* and Kohan *et al.* have theoretically demonstrated that native defects are not responsible for the high-concentration of shallow donors [Koh00]. What is more, Van de Walle *et al.* proposes that unintentionally incorporated hydrogen is the primal factor responsible for the n-type conductivity in ZnO [Wal00].

One of the reasons for the conductivity control difficulty is a low solubility of acceptor atoms. According to some theoretical studies, the maximal achievable concentration of the acceptors is lower than the lowest of the donors [Ave67, Par02]. In addition, bringing the acceptor atom in the other site or in the interstitial position converts it into donor atom [Man65, Ave67, Par02]. However, Look *et al.* have experimentally demonstrated that N can be doped to a level of more than 10^{19} cm^{-3} [Loo02]. n-type ZnO films with lower donor concentrations were reported, see the review of Oezguer *et al.* for some examples [Ozg05]. It is not enough, however, to simply bring a large amount of acceptor atoms in the ZnO film to achieve the p-type semiconductor. According to theory, the doping with shallow acceptors generates the compensating donor defects, such as vacancies or interstitials [Man65, Ave67, Par02]. Besides, acceptors can couple with defects to form electrically inactive complexes [Man65, Ave67, Par02]. Thus, the appropriate doping process should be developed.

2.5. Nitrogen Doping

p-type ZnO can be hypothetically achieved by doping with either group-I or group-V elements. Doping with group-I elements is possibly more effective than doping with group-V elements because of more shallow acceptors [Yam99, Par02]. Several reports on ZnO doping with Li, Na, and K [Sch70, Sch68, Val91], Cu [Kan91], Ag [Ka91] exist. On the other side, it was observed that doping with group-I elements increases donor concentration instead. This is attributed to tendency of group-I dopants to occupy the interstitial sites, partly due to their small atomic radii, Tab. 2.2. Additionally, doping with Na and K induces lattice strain due to the change of the bond length, which leads to the formation of the vacancies which compensate the dopants [Par02]. The Group-V elements have low solubility in ZnO due to the mismatch in ionic radii for P, As, and Sb as compared to O, Tab. 2.2. Several papers on p-type ZnO doping by P, As, and Sb were published [Kim03, Ryu03, Heo03, Heo04, Lim04, Loo04, Lim05, Vai05, Che05], however the results were not reproducible or questionable [Loo01,

| Atom | Valence | Radius (Å) |
|-----------|-----------|--------------|
| Zn | +2 | 0.60 |
| Li | +1 | 0.59 |
| Ag | +1 | 1.00 |
| Ga | +3 | 0.47 |
| Al | +3 | 0.39 |
| In | +3 | 0.62 |
| O | -2 | 1.38 |
| N | -3 | 1.46 |
| P | -3 | 2.12 |
| As | -3 | 2.22 |
| F | -1 | 1.31 |

Tab. 2.2. Valence and ionic radii of the chemical elements.

Loo04]. Phosphor doping was attempted in this work, but only polycrystalline ZnO was obtained (Chapter 8.2.5).

From the theory, nitrogen is the most promising element for *p*-type ZnO [Par02]. As it is already mentioned, nitrogen can be brought into ZnO to the concentrations of more than 10^{19} cm^{-3} [Loo02]. In the other experiments electron paramagnetic resonance measurements have demonstrated that N substitutes O in the ZnO lattice [Car01, Gar02, Gar03]. There are some reports on *p*-type ZnO, achieved with following precursors and growth methods: NH_3 (CVD, MOCVD) [Min97, Hua02, Yyan03, Xli03, Wan03b, Rom03], N_2O [Jos99], NO [Xu04], N_2 (MBE) [Loo02], monomethyl-hydrazine (MOMBE) [Ash02], pulsed laser deposition (PLD) [Jos99, Jos99, Tab02, Guo02], and sputtering [Hua03, Lu03, Wan03b, Sin03]. Unfortunately, these experiments are still irreproducible. One of the explanations for the difficulties with nitrogen doping is the formation of the double N complex, which promotes the formation of the compensating defects [Yan01]. Besides, this topic together with the specific aspects of native defects energetics is thoroughly discussed elsewhere [Koh00, Oba01, Zha01, Lee01, Par02, Wan03, Bar05].

Apart from direct doping, there are some promising exotic methods for ZnO. For example, the use of Ga (or Al or In) and N ions simultaneously (so-called codoping method) was proposed from the solid theoretical considerations [Yam99, Yam00, Yam02, Mat03]. Supporting those predictions, experimental works on codoped *p*-type ZnO were published [Jos01, Nak01, Ash02, Mat03, Ye04, Ye05, Yua05]. Unfortunately, those experiments were not reproducible (Lee *et al.* attributes this to a potential problem that isolated Ga atoms will compensate the N–Ga–N acceptors [Lee01]). Besides codoping with Ga, the simultaneous incorporation of hydrogen and nitrogen into ZnO is a promising method too [Wal01, Zun03]. For *p*-type GaN [Neu95, Nak96], for example, hydrogen increases the acceptor solubility and

suppresses the native defect compensation effects [Wal01, Xli05]. However, it is unknown if that works for ZnO. According to the theoretical work, it depends on the energetics of N–H complexes (hydrogen must be removed during the post-growth anneal) [Wal01, Xli05].

3. Characterization Techniques

In order to investigate ZnO properties, X-ray diffraction, cathodoluminescence, photoluminescence, capacitance-voltage, Nomarski, scanning electron, transmission electron and atomic force microscopy measurements were performed.

3.1. Surface Morphology

Optoelectronic applications of ZnO require smooth, defect-free surface. Particles, stains, scratches, cracks, pits and hillocks in the epitaxial film deteriorate the performance of the optoelectronic device. For the study of the surface morphology of ZnO films, standard Nomarski, scanning electron, and atomic force microscopy were used.

Differential interference contrast microscopy (Nomarski microscopy)* improves optical film visibility and brings more detail to the image in comparison to the convenient optical microscope. A description of the Nomarski microscopy technique can be found in the review of Davidson *et al.* [Dav99].

Atomic force microscopy (AFM)** gives 3D information about the topology of the surface (hillocks and holes can not be always distinguished in Nomarski and scanning electron microscopies). AFM technique is not bound by conventional restrictions such as diffraction caused by the relatively large wavelength of light. The limit is imposed by the geometrical size of the stylus probe [Bin86].

Scanning electron microscopy (SEM)*** uses electrons for imaging. The advantages of SEM over light microscopy include much higher magnification, and greater depth of field (~100 times that of light microscopy). A detailed description of the SEM technique can be found elsewhere [Rei98].

3.2. Capacitance-Voltage Measurements

The carrier concentration and type of conductivity should be reliably measured in the quest for p-type conducting ZnO. Some reports, claiming p-type ZnO (see the references in Chapter 2.6), have questionable Hall effect measurements, and thus can never be reproduced.

* was established by G. Nomarski in 1950s.

** was constructed by G. B. Binning, C. F. Quate and Ch. Gerber in 1986, [Bin86].

*** was invented by M. Knott and E. Ruska in 1930.

Capacitance-voltage measurements^{*} were used for the study of the electrical properties of ZnO in this work. The underlying GaN buffer layer and the substrate influence the electrical measurement of ZnO layer. For example, if the underlying GaN layer has a higher carrier concentration than ZnO layer, then the electrical measurement results in the measurement of GaN layer. This issue can be eliminated either by growing of the thicker ZnO layer or by doping of GaN layers with Iron^{**}.

The convenient Hall-effect measurements were not performed in this work. According to Look *et al.*, Hall effect measurement is complicated by small Hall voltages measured in p-type ZnO due to the lower than 1 cm²/Vs hole mobility [Loo04]. Taking into account that it is difficult to fabricate high-quality ohmic contacts to ZnO [Tuz01, Son03, She03, Ip04, Lim05, Kim05], a sample can appear p-type conducting material because of contact noise during one of the multiple Van der Pauw measurements [Loo04].

The type of conductivity and the impurity distribution were determined using the Schottky model [Sch38] by measuring the capacitance C per unit area as a function of voltage using the equation [Sze91]:

$$N_D = \frac{2}{q\epsilon_s} \left[\frac{1}{-d(1/C^2)/dV} \right]$$

Equivalent circuit of the capacitance bridge represents either a condenser with the capacity C_p with a parallel resistor R_p or a condenser with the capacity C_s and a serial resistor R_s. The parallel resistivity describes the possible leak currents and serial resistivity gives the conductive properties of ZnO. In the ideal case R_s is small and R_p is very large. At two differently large areas mercury gets into contact with a sample surface by evacuating the area between the mercury and the sample surface. The smaller contact usually behaves as a Schottky contact and the larger one is Ohmic.

3.3. Cathodoluminescence Measurements

The information on spatial and spectral distribution of the luminescence is achieved from the cathodoluminescence measurements.^{***}

A standard experimental setup intended to investigate microcathodoluminescence of

* This method is described in [Dad99].

** The doping of n-type GaN with Iron decreases its carrier concentration.

*** See also Chapter 2.3, "Spatial Distribution and Localization of the Luminescence".

ZnO samples includes a SEM (JEOL 6400), a system which collects light radiation and brakes it out a microscope column (collector system), a system for spectral analysis of radiation (monochromator), and a system which monitors CL radiation (see a more detailed description of the method in [Chr91]). The collector system consists of an elliptical focusing mirror and lenses. Using the detector system (MCP Si-reticon for the wavelength range of 180-920 nm; and InGaAs-reticon for the wavelength range of 800 – 1750 nm) a broad range of the ZnO spectrum from near band edge luminescence to the deep levels can be investigated. Cryostat cooled by liquid He in the temperature range of 5 K - 300 K allows to perform CL measurements at low temperatures. In the CL measurements performed in this work an accelerating voltage of 5 KeV was used.

The experimental data obtained are visualized as the composition of two lateral coordinates (x,y) along the surface or cross section of the ZnO film and correlate to local intensities and wavelengths. The information can then be extracted from this data: local spectrum $I(x,y,\lambda)$, integrated spectrum $I(\lambda)$, monochromatic intensity maps $I(x,y,\lambda_1)$, panchromatic intensity maps $I(x,y,[\lambda_1-\lambda_2])$, and wavelength images (CLWI) $\lambda(x,y)$.

3.4. X-ray Diffraction*

Several X-ray diffraction methods** were used for the determination of the crystalline quality, type of lattice, lattice parameters, and crystal orientation of ZnO. ω -scans in (0002) geometry were performed in order to determine the tilting of the ZnO columns, and in $(10\bar{1}0)$ geometry in order to determine the twisting of the ZnO columns.*** The *c*- and *a*-lattice parameters were determined from the θ - 2θ scans of (0002) and $(10\bar{1}0)$ ZnO reflections, respectively. The variation of the lattice parameters in the layer was assessed from the full width at half maximum of the X-ray diffraction peaks obtained in these measurements.

* X-ray diffraction was discovered in 1912; x-rays were discovered in 1895 by the German physicist Wilhelm Conrad Röntgen.

** More on characterization of epitaxial semiconductor layers can be found in the book “High-resolution X-ray Diffraction”, A. Krost *et al.*, [Kro96].

*** In order to achieve a first idea about the quality of the epitaxial film rocking-curve measurement is usually performed. It is a ω -scan performed with a wide open detector. No rocking curves were measured in this work, because the 2θ peak position of ZnO and GaN are lying so close to each other that they are not distinguishable.

3.4.1. ω - and θ - 2θ Scans around the [0001] Direction

An URD 6 diffractometer (Seifert/FPM Freiburger Präzisionsmechanik) was used for the determination of the c -lattice parameter and the tilting of ZnO columns. A schematic depiction of ω - and θ - 2θ scans is shown in Fig. 3.1. A copper X-ray source generates a divergent non-monochromatic x-ray beam with a spatial size of $0.04 \times 8 \text{ mm}^2$. A Ge(111) crystal and slits are used to achieve an almost parallel monochromatic beam. After the X-rays are diffracted on the sample, they go through the third slit to a scintillation detector.

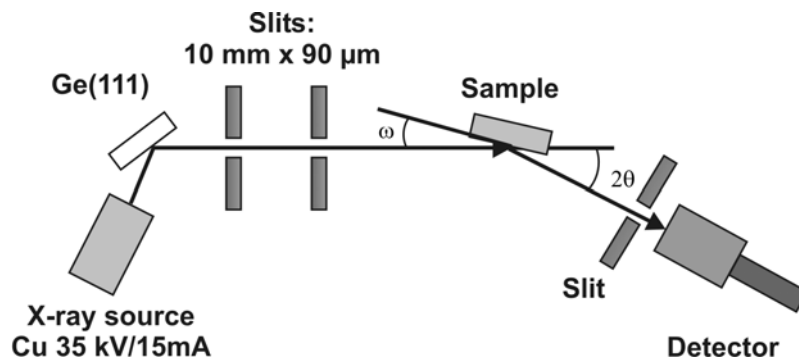


Fig. 3.1. Schematic view of URD 6 diffractometer.

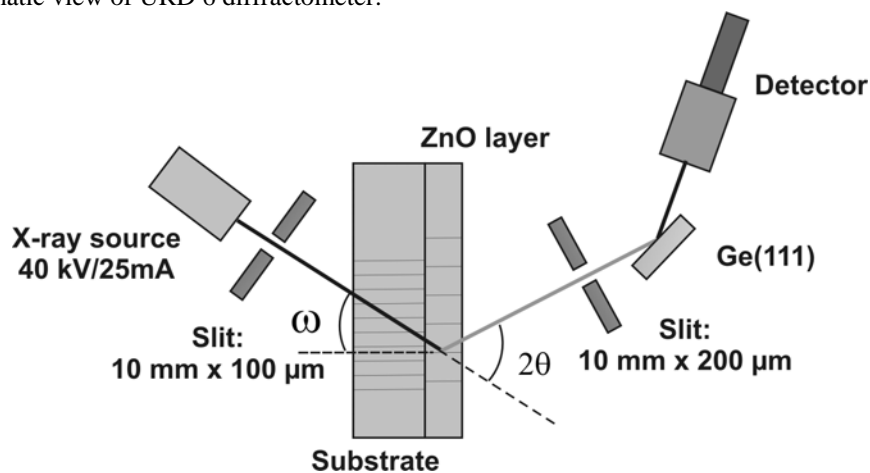


Fig. 3.2. Schematic view of the D5000 diffractometer.

3.4.2. XTS θ - 2θ Scans around the $[10\bar{1}0]$ Direction

X-ray transmission scattering (XTS) θ - 2θ scans around the $(10\bar{1}0)$ reflection were performed in order to determine the a -lattice parameter of the ZnO films. A D5000 (Bruker AXS) diffractometer was used for these measurements (Fig. 3.2). The spatial size of the X-ray beam is $0.1 \times 12 \text{ mm}^2$. The slit and the monocrystalline Ge (220) monochromator on the secondary part of the device are suppressing the $K\alpha_2$ -radiation. 2:1-scans were performed in transmission geometry, i.e. the sample is situated perpendicular to the direction of the incoming X-ray

beam, which is passing through the sample to be detected on the other side of the layers. In such a geometry, the lattice planes $(10\bar{1}0)$ lying perpendicular to the surface of the sample were investigated.

3.4.3. GID ω -scans around the $[10\bar{1}0]$ and $[30\bar{3}0]$ Directions

Fig. 3.3 depicts the photo of the experimental setup (Seifert/FPM) used for GID measurements. X-rays are emitted from a standing head-on-down source. The X-ray beam is parallelized in order to achieve a low axial divergence by the collimator which consists of parallel highly absorbing metal plates. The especially designed sample holder and the goniometer allow to vary the incidence angle of X-ray and thus to change the penetration depth of X-rays into the ZnO film. GID technique is used for the determination of the twist of ZnO columns. Those measurements were performed in $(10\bar{1}0)$ geometry. Besides that, in order to determine the Scherrer size and inhomogeneous distortions in the ZnO, additional measurements were performed in $(10\bar{1}0)$ and $(30\bar{3}0)$ geometries.

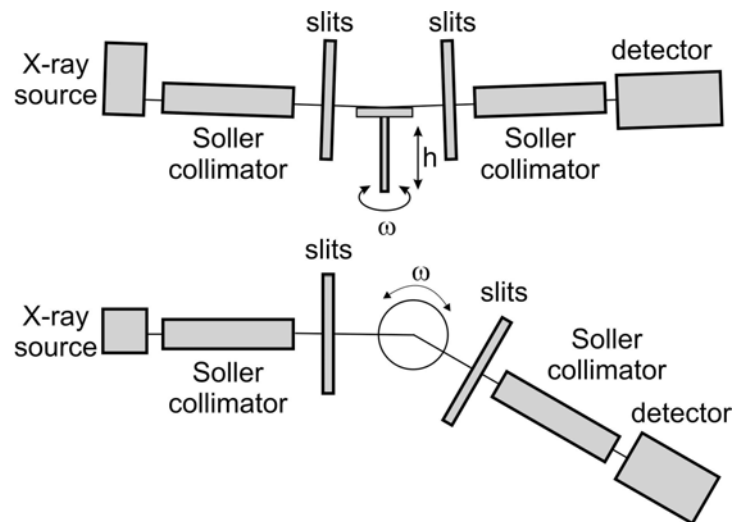


Fig. 3.3. Schematic overview of the GID experimental setup.

3.4.4. Reciprocal Space Mapping

For reciprocal space mapping in the symmetrical (0002) and asymmetrical $(20\bar{2}4)$ geometries the diffractometer XRD 3003 HR (Seifert/FPM) was used, (Fig. 3.4). On the primary site of the device the X-ray source, a multilayer parabolic mirror (Bragg mirror) and a monochromator are mounted in order to achieve highly collimated monochromatic X-ray beam. The monochromator represents four Ge (220) monocrystals. The secondary optics consists of

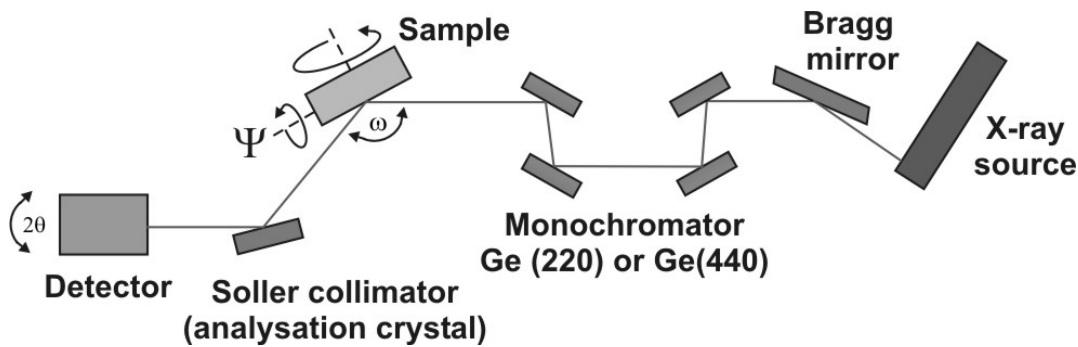


Fig. 3.4. Schematic view of the XRD 3003 HR diffractometer.

the Ge (220) analyzer monocrystal for the angle resolution and the detector. This analyzer crystal is especially useful for symmetrical reciprocal space mappings because the c -lattice parameter of ZnO and the underlying GaN layer are very close to each other; thus higher resolution is needed.

For the asymmetrical reciprocal space mapping the Soller collimator was used because the intensity of the reflections in this geometry was too low for using the Ge analyzer, while the resolution of peaks from ZnO and GaN in such a geometry is sufficient for the measurement.

3.5. Transmission Electron Microscopy

Transmission electron microscopy (TEM) measurements were performed in the group of Prof. Gerthsen (University of Karlsruhe) to study the distribution of edge, mixed and screw dislocations in ZnO epilayers grown by two-step growth method (Chapter 6.2.2). Dislocations and stacking faults severely reduce the efficiency of optically active material when present with the densities higher than 10^8 cm^{-2} [Loo05].* Such high densities are not rare in devices based on ZnO.** For example, vertical threading dislocations have concentration of 10^{10} cm^{-2} in epi-ZnO/Al₂O₃, which drops the carrier mobility to less than $100 \text{ cm}^2 (\text{Vs})^{-1}$ [Loo05]. The influence of dislocations on the electrical transport in epilayers was investigated earlier in 1980s, as pointed out by Mueller *et al.*, [Mue05] (see the references within).

According to Mueller *et al.*, only few TEM studies on the defect structure in ZnO were

* This issue existed for example, in GaN epitaxy. Nowadays, it is solved [Dad03a].

** Taking into account the presence of native point defects, which also act as scattering centers, no wonder that the reported mobilities even in single-crystalline epitaxial ZnO are poor in comparison to those of bulk ZnO, see the review of Oezguer for examples [Ozg05].

published [Nar98, Hon00, Vig01]; although several studies appeared recently [Nak98, Lim01, Wal04, Bar04], the number of TEM studies of ZnO is still low when related to the number of reports on ZnO topic in general.

200 keV Philips CM 200 FEG/ST microscope which is equipped with a field emission gun was used for TEM measurements [Mue05]. Dislocation Burgers vectors \mathbf{b} were analyzed on the basis of the $\mathbf{bg} = 0$ extinction criterion using different imaging vectors \mathbf{g} . The weak-beam technique was applied to improve the resolution [Wil96]. Cross-section samples along the $\langle 11\bar{2}0 \rangle$ - and $\langle 1\bar{1}00 \rangle$ -zone axes were prepared applying the technique described by Strecker *et al.* using 3.5 keV Xe^+ ions for the final ion milling to minimize radiation damage with an ion current of 1 mA and an incidence angle of 14 degrees [Str93]. More on transmission electron microscopy technique in general can be found elsewhere [Wil96].

4. MOVPE System and Rapid Thermal Annealing

The early reports on ZnO growth utilized growth techniques such as magnetron sputtering [Hac94, Gar98] and chemical vapor deposition [Tik80, Kas81, Sri95]; however, the films were mainly polycrystalline. Subsequently, higher-quality ZnO was grown using molecular-beam epitaxy (MBE) [Che98, Fon99], pulsed-laser deposition (PLD) [Vis98], and hydride or halide vapour-phase epitaxy (HVPE) [Kas83, Tak99]. Among those growth methods, MOVPE is the most promising method for optoelectronic applications, because it offers large-scale production of high-quality films with homogeneous properties.

4.1. Metal Organic Vapor Phase Epitaxy of ZnO

MOVPE after its invention in 1969 [Man69] is nowadays a wide-spread and well developed semiconductor growth technique. It is based on chemical reactions which employ various gaseous, liquid and solid precursors*. Fig. 4.1 shows the MOVPE AIXTRON 200/4 RF-S system used for the growth of ZnO and GaN films in this work.

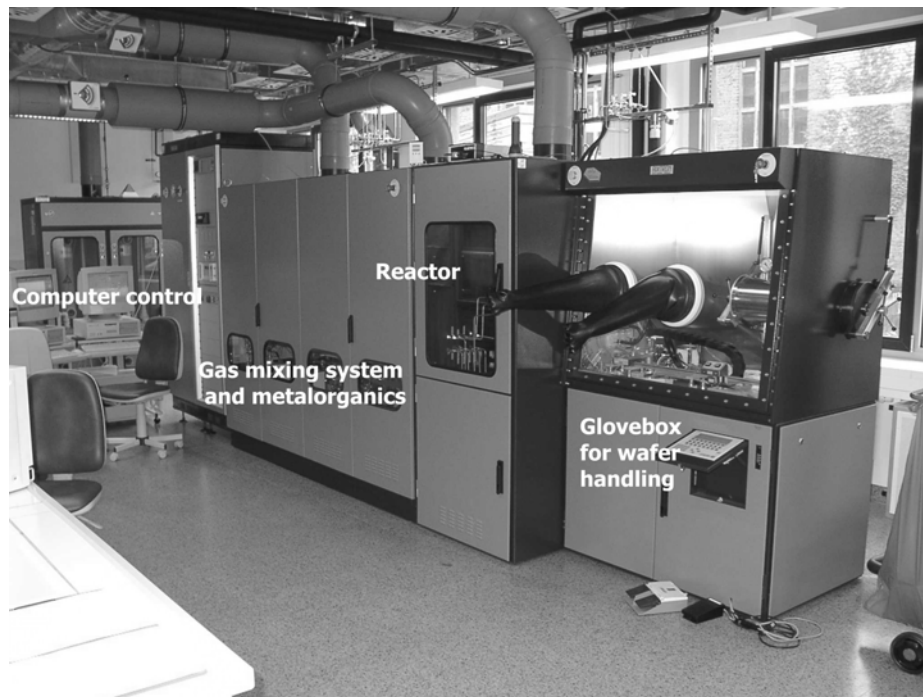


Fig. 4.1. AIXTRON 200/4 RF-S reactor system.

Fig. 4.2 shows a schematic overview of the MOVPE system. Firstly, the gas mixing system controls the gas flow using pressure regulators, mass flow controllers (MFCs), and pneumatic valves to achieve a laminar flow. A carrier gas is used to transport the reactants to the substrate and to carry away the byproducts of the reaction. All these flows are directed

* Some chemical properties of precursors used in this work are discussed in Chapter 8.

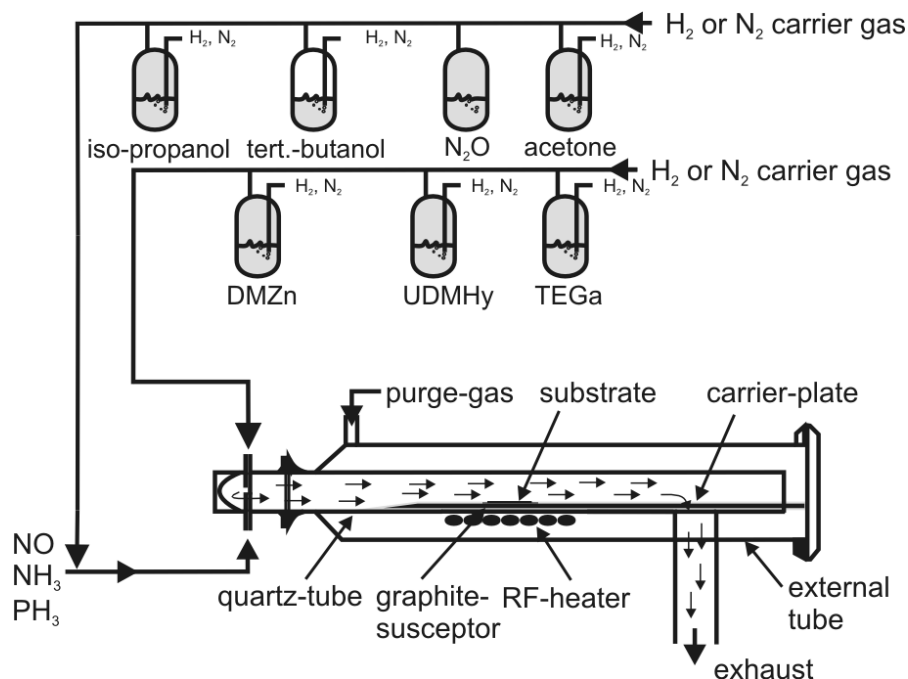


Fig. 4.2. Schematic view of the MOVPE.

into either the reactor or a vent line. The Zn- and O-precursors have a separated injection system to minimize pre-reactions in the gas lines. The metalorganic sources are placed in temperature-controlled baths. Secondly, a vacuum pump and a pressure controller with a throttle valve are used to control the reactor pressure. The substrate and the susceptor are significantly hotter than any other part of the reactor. The substrates are placed on a susceptor, which is made of SiC-coated graphite and heated by radio frequency (RF) induction. This material is compatible with the reactants and does not contaminate the system. Finally, the toxic exhaust gases are removed by using a wet chemical scrubber.

4.1.1. Substrate Choice

In order to reduce the strains, crack and dislocation density* in epitaxial ZnO film, the substrate with the similar crystallographic symmetry, smallest lattice mismatch** and in-plane linear expansion coefficients should be chosen. Besides, no chemical reaction (corrosion, for example) on the substrate surface should occur, because it serves as a perturbation factor for epitaxy. For ZnO, no ideally suited epitaxial substrate exists. This is why the growth mechanisms of ZnO are complicated by the initial nucleation layer and structural defects [Lor00, Kim97, Che00]. A number of studies have been conducted on GaN [it has no perfect substrate for epitaxy too], and significant progress has been made [Rou99, Hey99]. However, no sys-

* More on the properties and X-ray characterization of epitaxial films can be found in [Kro96].

** Lattice mismatch is determined from: $f_0 = \frac{a_{ZnO} - a_{substrate}}{a_{substrate}}$.

tematic research on the ZnO growth mechanism has been reported yet [Che01]. There are several possible substrates as candidates for ZnO growth:

- a) ZnO by itself;
- b) Si;
- c) sapphire;
- d) epitaxial GaN on Sapphire or on Si;
- e) buffer layers.

Table 3.1 summarizes the different properties of those substrates.*

a) ZnO itself is the most appropriate substrate for ZnO growth, but ZnO substrates are still expensive (~200 € for 1 cm²) and not available in appropriate quality. Bulk ZnO crystals are mainly grown by hydrothermal [Shi99, Sek00, Sak01], vapor phase [Shi71, Nte99, Alb91, Mat99], and melt growth methods [Sus99]. The quality and the properties of those bulk samples differs significantly. For example, Kohl *et al.* have shown that the Zn atoms start to evaporate from the Zn-face ZnO at temperatures as low as 380 °C, while on the O surface that

Table 4.1. The properties of prospective substrate materials for MOVPE of ZnO.

| Material | a lattice parameter, Å | c lattice parameter, Å | Thermal conductivity, W/cm×K | Lattice mismatch Δ(%) | In-plane thermal linear expansion coefficient, 10 ⁻⁶ K |
|---------------------------------------|------------------------|------------------------|------------------------------|-----------------------|---|
| ZnO | 3.249 [Lan82] | 5.206 [Lan82] | 0.54 [Sla72] | - | 5.61 [Vis98] |
| GaN | 3.189 [Lan82] | 5.185 [Lan82] | 1.3 [Mar69] | 1.8 | 5.59 [Mar69] |
| Si(111) | 5.43 [Les95] | -- | 1-1.5 [Lan82] | 15,3 | 2.59 |
| Al ₂ O ₃ (0001) | 4.758 [Les95] | 12.991 | 0.5 | 18 ^{*)} | 7.5 |

*) Similar to AlN, InN, and GaN, [0001]-oriented ZnO grows on [0001]-oriented Al₂O₃ with the in-plane epitaxial relationship ZnO[10 $\bar{1}$ 0] || Al₂O₃ [11 $\bar{2}$ 0] [Vis97]. The *c*-plane of ZnO rotates by 30° in the *c*-plane of the Al₂O₃, which leads to alignment of ½ (30 $\bar{3}$ 0) planes of Al₂O₃ with (2 $\bar{1}$ 10) of *a*-planes of ZnO [Nar02,Ozg05].

* Some heteroepitaxy experiments were also reported on SiC [Joh92], GaAs [Shi94, Hwa03], CaF₂ [Ko03], and ScAlMgO₄ [Oht99] substrates. However, the quality of these ZnO films is lower, as compared to that of ZnO films grown on a) - e) substrates.

takes place above 600 °C [Koh74]. More recently, other groups [Sak00, Sak01, Kat03] have shown that ZnO substrates with different polarity require different pre-growth surface preparation. Several attempts were performed on „epi-ready“ commercially available substrates in this work, but were not successful. However, the use of other bulk ZnO substrates can be very practical.

b) The direct growth of high-quality ZnO on Si is difficult because of silicon dioxide formation (the formation enthalpy of SiO₂ (910.7 kJ/mol) is larger than of ZnO (350.4 kJ/mol)) [Lad80]. This amorphous layer degrades the crystalline quality of the overgrown film. For example, no ZnO growth on Si was found experimentally when N₂O was used as an oxidation source.*

c) Many studies on the growth of ZnO films have used c-plane [Fon99], a-plane [Fon01] and r-plane [Hag99] sapphire as substrates because oxygen sublattice of sapphire has the hexagonal symmetry of ZnO. Additionally, high quality, low cost Al₂O₃ wafers are commercially available [Pea04]. Because of those advantages, ZnO films grown on the sapphire substrates are often used for non-optoelectronic applications. For example, according to Pearson *et al.*, most MBE layers since 1996 have been grown on sapphire (Al₂O₃) [Pea04]. On the other side, the heteroepitaxy of ZnO on sapphire is problematic for optoelectronic applications. Even after a 30° in-plane rotation to reduce the lattice mismatch (from 32% to 15%)** , ZnO films usually display large mosaicity, high dislocation density (>10¹⁰ cm⁻²) and low mobilities (less than 100 cm²V⁻¹s⁻¹ at room temperature) as compared to bulk single crystals (Hall mobility of 200 cm²V⁻¹s⁻¹) [Cro74, Fon99, Oht99, Che00, Hon00, Loo05]. Several attempts to grow ZnO directly on sapphire were made in this work. Simultaneous switching of both Zn- and O-precursors, growth using Zn nucleation layer or oxygen pretreatment of sapphire substrate at different temperatures resulted in polycrystalline or no film at all.

d) GaN has the wurtzite structure with close to ZnO lattice matching (Tab. 4.1). Additionally, cheap, high-quality, smooth epitaxial GaN layers are available [Dad03]. To the beginning of this work, there have been only few reports on the growth of ZnO on GaN [Lei91, Joh96, Hey96, Vis98, Nar98, Hon00]. MOVPE-grown GaN layers on Si (111) or on sapphire [Dad00], were used as templates for ZnO growth in this work. The templates were chemically cleaned with acetone, iso-propanol, H₂SO₄ and rinsed in deionized water before loading into the reactor.

* The use of N₂O oxygen precursor for MOVPE growth of ZnO requires high temperatures, see chapter 5.1.6.

** ZnO: *a*=0.3249 nm and *c* =0.5206 nm; Al₂O₃: *a*=0.4758 nm and *c*=1.299 nm.

e) The use of buffer layer can significantly improve the quality of ZnO layers. When the influence of the substrate orientation and buffer layers on the main ZnO layer are considered, buffer “homoepitaxy” of ZnO is the most efficient method for achievement of high-quality layers [Ko00, Che01, Kat03]. Low temperature grown ZnO buffer layers on GaN/Sapphire or on GaN/Si(111) were used in two-step ZnO growth in this work (Chapter 6.2).

4.1.2. Carrier Gases

Hydrogen and nitrogen were used in this work as carrier gases. Firstly, nitrogen is commercially cheaper and safer than hydrogen (4 % of hydrogen in air is ignitable). Nitrogen and hydrogen molecules have different masses. The precursor molecules decompose better when heavy nitrogen is used instead of hydrogen [Har96]. Therefore, the gas-phase pre-reactions between Zn- and O-precursors* can be reduced by using hydrogen.

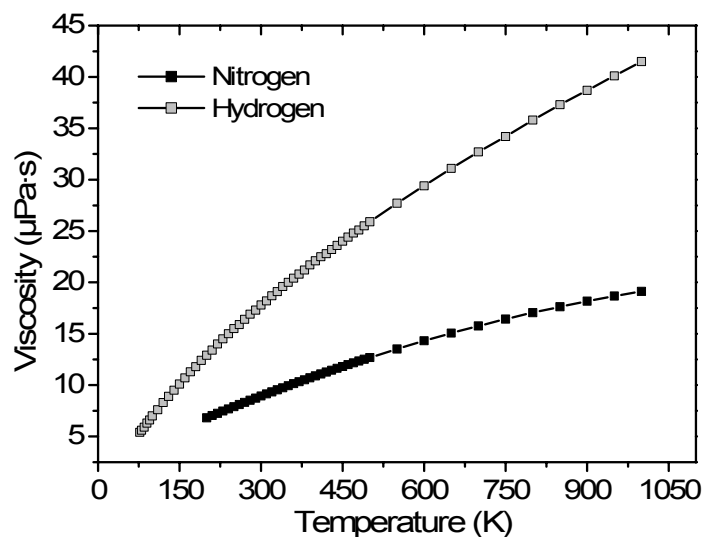


Fig. 4.3. Viscosities of hydrogen and nitrogen vs. temperature [Lem01].

Secondly, these gases have different influence on the growth process depending on the growth conditions. The difference between the viscosities of hydrogen and nitrogen is increasing with an increasing of the temperature (Fig. 4.3). The heat transport is higher when hydrogen is used [Lem01]. Nitrogen is quite inert with respect to ZnO even at high temperatures. With hydrogen not only the chemisorption and physisorption was observed, but also the corrosion of the solid ZnO to form H₂O and metallic Zn at the temperatures 600 – 900 °C [Gru57, Kal81]. Thus, when ZnO is grown at high temperatures, the use of nitrogen is prefer

* See Chapter 5.1. Generally, the pre-reaction issues can be overcome by the use of other precursors and the variation of the process parameters, for example substrate temperature, reactor flow and pressure.

able. Thirdly, hydrogen in ZnO influences the ZnO luminescent properties and increases electrical conductivity of ZnO.** However, as it has been shown in the studies of Mollwo, Thomas and Lander, solubility of hydrogen at the temperature range below 450 °C is small and the diffusion times are long independent on the hydrogen pressures [Mol54, Tho56, Lan57]. This is why the use of hydrogen as a carrier gas at low growth temperatures (<450 °C) does not influence the donor concentration in ZnO film.

4.2. *In-situ* Measurement

An *in-situ* tool for assessing the ZnO growth rate and thickness in this work was reflectometry measurement (Fig. 4.4). It measures the reflected light intensity from a thin film. The phase relationship of the reflections from the top and bottom of ZnO layer is determined by the difference in optical path lengths of the two reflections. The reflectance of a thin film will vary periodically with inverse wavelength. During epitaxy, when the thickness of ZnO is varying, the reflectance of the film is also oscillating. The amplitude and periodicity of the reflectance of a growing film is determined by the film's thickness and the optical constants. More on the topic of *in-situ* characterization of thin films growth can be found elsewhere [Flo01, Flo02, Kro05].

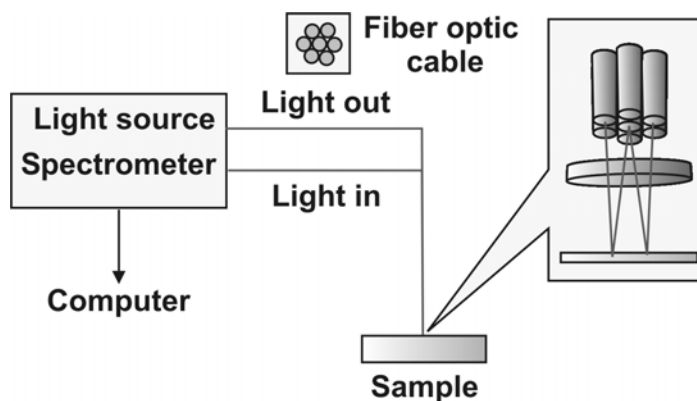


Fig. 4.4. Schematic view of *in-situ* reflectometry measurement.

4.3. Doping Methods

As it has been discussed in Chapter 2.5, nitrogen is a good candidate for a shallow *p*-type dopant in ZnO, although it is not very soluble. Several methods have been used for ZnO doping: ion implantation [Sch85, Kob96, Lin04], diffusion [Rom03], and *in-situ* doping during growth (references in Chapters 2.3-2.5). In the work of Meyer *et al.* the photoluminescence measurements of the samples doped by these methods have provided strong evidence

** See Chapters 2.4 and 2.5.

that nitrogen on an oxygen site is the acceptor [Mey05]. However, according to Pearton *et al.*, the convenient implantation can not be directly used for the ZnO, since ZnO “has more than one sublattice and compensating defects, such as antisites, or complexes of vacancies and interstitials that can dominate the electrical behavior of the implanted region” [Pea04, Lin04]. Thus, the process of impurity doping by ion implantation in ZnO still needs development [Pea04]. On the other side, *in-situ* doping during MOVPE growth has been shown to be a very effective method for other compound semiconductors, such as GaN. This is why doping experiments in this work were performed by direct switching of the dopant precursor into MOVPE reactor. Some chemical properties of precursors used for doping of ZnO are discussed in more detail in Chapter 8.

4.4. Rapid Thermal Annealing

As it has been discussed in Chapter 2.5, the simultaneous incorporation of hydrogen when ZnO is doped with nitrogen may actually be beneficial for achieving p-type doping [Wal01] by removing hydrogen during post-growth rapid thermal annealing. According to review of Pearton *et al.*, hydrogen can be removed from ZnO at temperatures significantly lower than for GaN [Pea04]. Additionally, Pearton *et al.* conclude from the work of Wraback *et al.*, that slow diffusing H₂ molecules or larger clusters do not form in ZnO during the anneal [Wra99, Pea04], supporting this with the observations of an implant-damaged trap-controlled release of H from the ZnO lattice for temperatures lower than 500 °C [Ip03].

Since ZnO is typically non-stoichiometric with a lack of oxygen, high-temperature treatment may result in an excess of oxygen from the ZnO layer [Kal82]. For example, the ZnO film preferentially loses oxygen at annealing temperatures as low as 500 °C when the annealing ambient is nitrogen [Pea04], and reduction of the ZnO films occurs at 600 °C when the annealing ambient is hydrogen [Gru57, Kal81]. This is why annealing has been performed in oxygen ambient in this work.

A photo of the rapid thermal annealer is shown in Fig. 4.5. The samples are located on a SiC-coated graphite susceptor which is mounted inside a quartz glass reactor. High temperatures are achieved by light irradiation from halogen lamps symmetrically arranged around the glass tube. It is possible to achieve wafer temperature ramp rates in excess of 100 °C / sec. In order to increase the effectiveness of the annealer, and to avoid the useless dissipation of heat, mirrors are introduced around the lamps. The whole system is fitted up with a cooling system and controlled by a computer. Oxygen flow of about 0.2 l/min at atmospheric pressure was

achieved by the combination of oxygen source and the vacuum pump mounted on the different sides of the rapid thermal annealer. Annealing temperature was varied from 2 min to 10 min, and the temperature from 700 °C to 1000 °C.

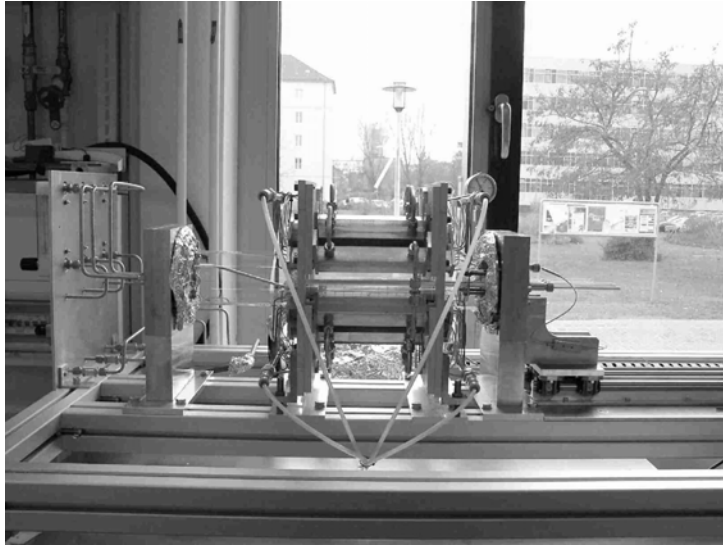


Fig. 4.5. Rapid thermal annealer.

5. Growth of Undoped ZnO

For the fabrication of high-quality p-type ZnO, firstly the epitaxy of undoped ZnO should be established. This included the experimental testing of the precursors for ZnO growth (Chapter 5.1), and the development of the growth methods (Chapters 5.2 and 5.3). Secondly, the doping study followed (Chapter 6).

5.1. O-precursors

There are about 300 organometallic volatile Zinc compounds [Dic94]. The common metalorganic Zn precursor used for ZnO growth is DEZn [Ker70, Gha80, Lau80, Shi81, Rot81, Oda85, Shi88, Shi90, Wen91, Hu92, Yos93, Kim94, Li97, San98, Lia98, Hah98, Wra99, Gor99, Ash00, Liu00, Par01, Oga01, Lia01, Wan01, Gru02, Sal02, Shi02, Oga02, Wan02, Oga03, Kir03, Li03, Du03]. Because of premature homogeneous reactions of DEZn with some oxidants in the gas phase, which limit the process, DMZn [Smi83, Sol83, Wri84, Bet88, Mar89] is more suitable Zn-precursor. Zinc acetylacetonate $Zn(C_5H_7O_2)_2$ is a precursor both for Zn and O [Rya68, Kor69, Oga90], which makes it very simple in use, but the VI-II ratio is fixed if no other O precursor is introduced in the reactor.

ZnO was grown by MOVPE using diethylzinc [Ker70] or dimethylzinc [Smi83] in the presence of oxygen [Sav64, Rya68, Ker70, Gha80, Rot81, Smi83, Shi88, Tab95, Kob96, Li97, Lia98, Wra99, Liu00, Par01, Lia01, Wan01, Wan02, Wan02, Du03, Wal02] or water [Gha80, Rot81, Shi88, Mar89, Li97, Kau88, Oga90, Wen91, Yos93, Min94, Sat94, Kob96, San98, Shi02]. However, it resulted in gas phase pre-reactions leading to the formation of particles in the gas phase and cold zone of the reactor, and poor film morphology. Less reactive oxygen sources, like CO_2 [Lau80, Shi81, Mar89, Hag00, Sek00, Li03], tetrahydrofuran, and furan [Kau89] were studied. These precursors are not appropriate because they slowed ZnO growth rates.

Organic oxides, like alcohols (iso-propanol [Gru02a, Gru02, Kir03], tertiary-butanol [Oda85, Hah98, Sal02, Kir03]), ethers (diethylether) and ketons (acetone) are less reactive in comparison to oxygen and water (Chapter 8). The use of tBuOH instead of O_2 or H_2O has been proposed by Oda *et al.* [Oda85]. The works of Kaufmann *et al.* and Hahn *et al.* also support the idea that tBuOH is a promising candidate for using in ZnO MOVPE [Kau88, Hah98].

The oxynitrides (like N_2O [Lau80, Shi81, Mar89, Hag00, Sek00, Li03, Sol83, Shi88, Shi90, Oga01, Oga02a], NO [Li03], NO_2 [Sol83, Shi88, Shi90, Oga01, Oga02b]) are also attractive for the use as oxygen precursor for the epitaxy of ZnO. In contrast to organics, those

compounds offer the absence of methyl groups, which allows the elimination of an unintended carbon incorporation into ZnO during epitaxy. Additionally, the stability of those precursors requires higher growth temperatures ($> 500\text{ }^{\circ}\text{C}$) which can have a positive effect on the ZnO crystallinity and surface morphology (Chapter 8). Besides, they contain nitrogen which can be incorporated into the film and act as an acceptor, which can lead to the the formation of p-type ZnO.

Taking into account those considerations, iso-propanol, tertiary-butanol, acetone, diethylether, laughing gas, N_2O , and nitric oxide, NO were used for ZnO growth in this work. DMZn was used as Zn-precursor.

5.1.1. Iso-propanol

The substrate temperature was varied in the range of $400 - 500\text{ }^{\circ}\text{C}$, the VI-II ratio - between 7 and 80, and the reactor pressure between 300 and 500 mbar.

Best layers could be obtained in the temperature range from $400\text{ }^{\circ}\text{C} - 475\text{ }^{\circ}\text{C}$ at reactor pressures of 300 - 500 mbar, and a VI-II ratio of ~ 45 . In AFM measurements a relatively large root mean square (rms) roughness of 70 nm and 25 nm is determined on a $30 \times 30\text{ }\mu\text{m}^2$ and a $3 \times 3\text{ }\mu\text{m}^2$ area, respectively, for a $\sim 1\text{ }\mu\text{m}$ thick ZnO layer (Fig. 5.1). Hexagonal pyramids or pyramidal terminated hexagonal prisms having an average diameter of $\sim 6.5\text{ }\mu\text{m}$ are observed.

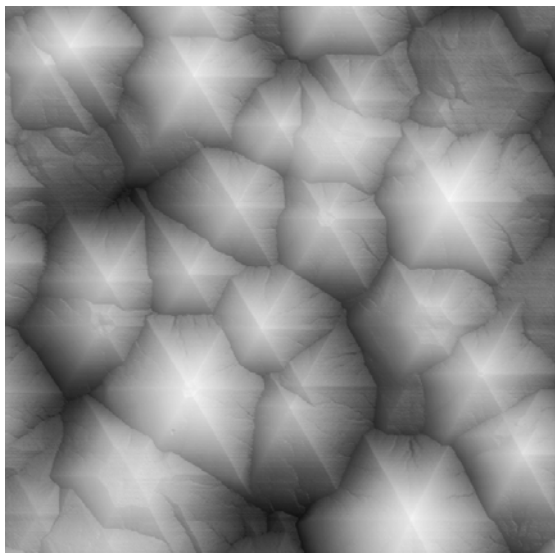


Fig. 5.1. AFM image of a $30 \times 30\text{ }\mu\text{m}^2$ region of a $\sim 1\text{ }\mu\text{m}$ thick ZnO layer on GaN. The max height is 426 nm. The hexagons are twisted by $\pm 1.2^{\circ}$.

The surface of these hexagons exhibits clearly visible edges, separating triangular facets with an inclining angle below 5° . With decreasing VI-II ratio the size of the hexagons decreases and the top facet roughens. A twist is clearly visible by the different orientation of the edges on the top facets and is estimated from the $30 \times 30\text{ }\mu\text{m}^2$ AFM image (Fig. 5.1) to $\pm 1.2^{\circ}$.

The dependence of the growth rate on the DMZn-flow indicates that pre-reactions significantly reduce the DMZn efficiency for low Zn-flows (Fig. 5.2). In addition, particles likely generated by gas phase pre-reactions lead to the formation of defects.

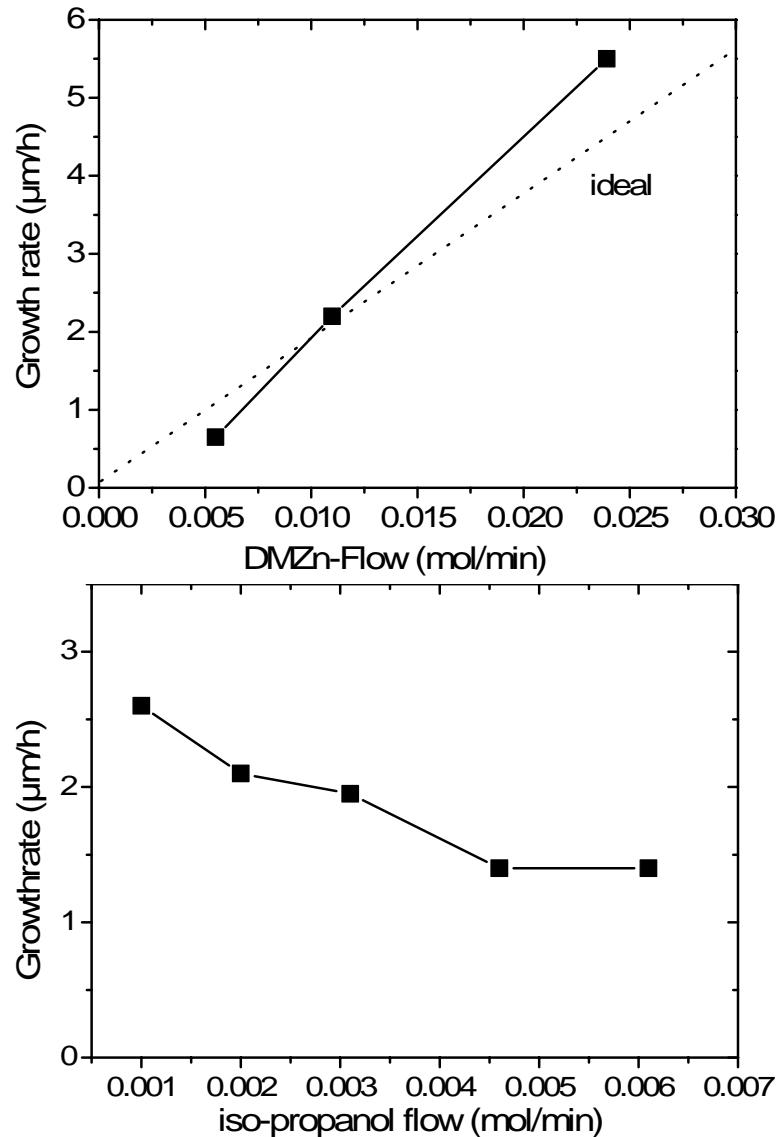


Fig. 5.2. Growth rate of ZnO versus flow of the precursors. Pre-reactions lead to a reduced DMZn efficiency. However, an unambiguous correlation of particle generation to the growth conditions was not possible. Besides gas phase pre-reactions, deposits on the reactor tube may be an alternative possible source of the particles. The particles are usually correlated to a polycrystalline deposit in the center of a flat circular growth defect (Fig. 5.3, right). Although Iso-propanol offers lower reactivity with DMZn than water and oxygen, still the particle generation limits the growth process. When cleaved, the samples show a smooth edge at the ZnO/GaN boundary and no indication of layer separation for layers $\sim 1 \mu\text{m}$ or a nano-crystalline columnar ZnO growth (Fig. 5.3). In X-ray diffraction Θ - 2Θ measurements the ZnO (0002) reflection splits up into two peaks (Fig. 5.4). This is shown in reciprocal space maps around the symmetric (0002) reflections in Fig. 5.5. The splitting indicates a relaxation of the ZnO towards the GaN

layer as indicated by the two ZnO peaks in the (0002) map. Additionally, this sample was etched and Θ - 2Θ measurement of the ZnO (0002) reflection has been made (Fig. 5.4).

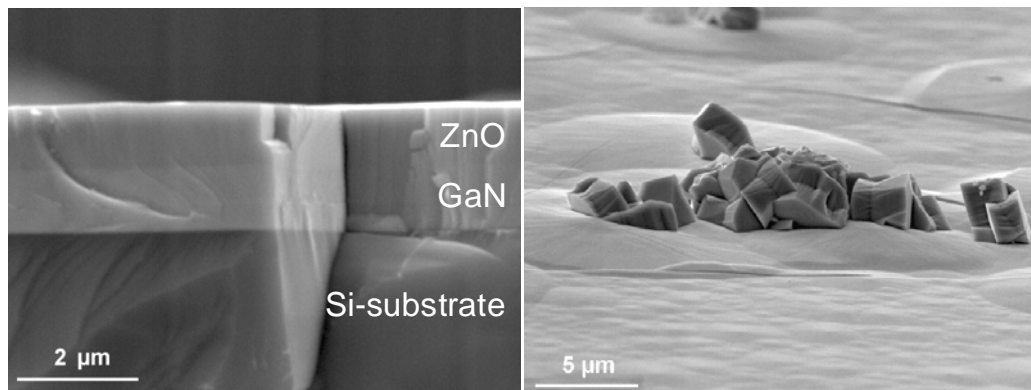


Fig. 5.3. SEM images of a $\sim 1 \mu\text{m}$ thick ZnO layer on a $\sim 1 \mu\text{m}$ thick GaN layer on Si(111). In cross section of a cleaved sample (left) no layer separation is observable. Particles (right) lead to defects and a rough surface.

The unetched sample shows compressive and nearly relaxed ZnO components while only the relaxed component remains for the etched sample, i.e. the compressive part of the ZnO sample is at the top surface. As it has been described in Chapter 2, the etching rate of O-polar sample is much higher than that of the Zn-polar one. The growth orientation is found to be

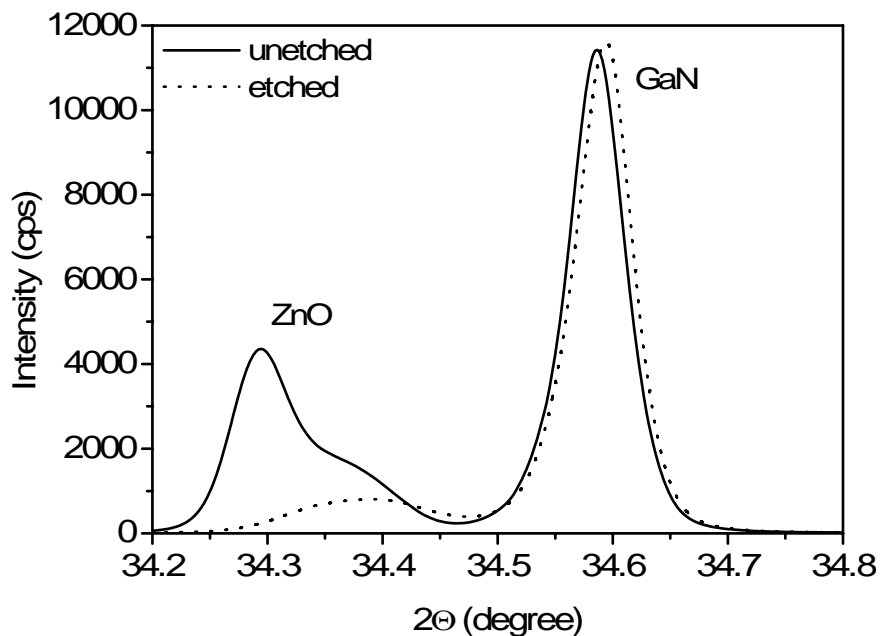


Fig. 5.4. Θ - 2Θ measurements of the ZnO (0002) reflection of an etched and unetched ZnO sample.

Zn-face by etching with H_3PO_4 during 2 seconds (Fig. 5.3). In addition to strain relaxation, in x-ray reciprocal space maps the GaN(0002) reflection of the $2.4 \mu\text{m}$ thick ZnO/GaN/Si(111) sample is found to be considerably broadened (Fig. 5.5). This indicates a strong chemical reaction at the ZnO/GaN interface during MOVPE growth, also found for the strained part of

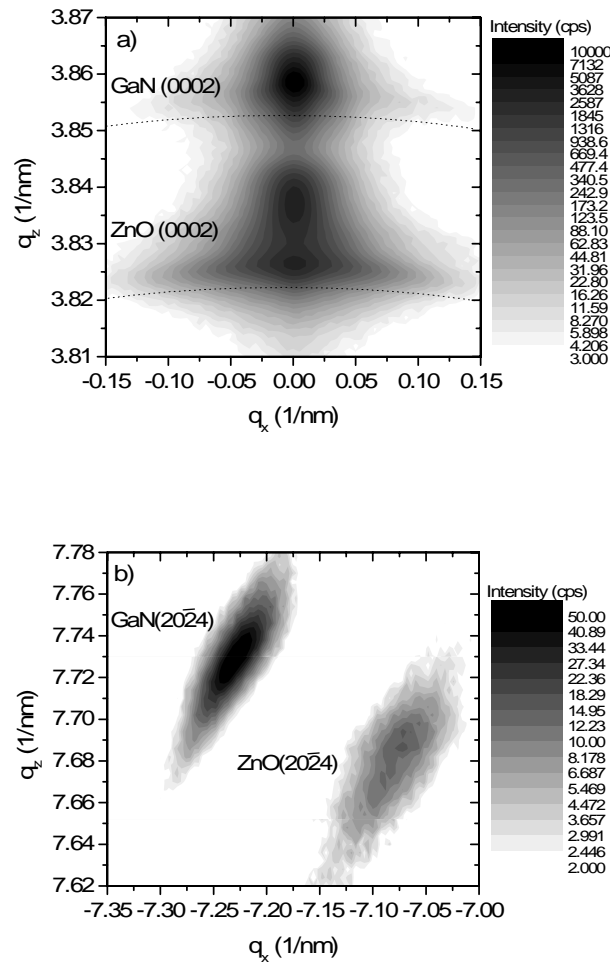


Fig. 5.5. X-ray reciprocal space maps around the GaN(0002) a), and GaN($20\bar{2}4$) b), reflections of a $2.4\ \mu\text{m}$ thick ZnO layer on GaN/Si(111). The broadening around the GaN and ZnO peaks in the map of the (0002) reflection (dotted lines) indicates a distorted region between the two layers. VI-II ratio = 7.5, growth rate = $5.5\ \mu\text{m/h}$, thickness = $1.4\ \mu\text{m}$, reactor pressure = 500 mbar, temperature = $400\ ^\circ\text{C}$.

the ZnO sample, which shows a similar broadening. This is indicative for a strong tilting of the individual ZnO columns in the ZnO/GaN interface region. The thickness of this distorted region can be estimated to 100 nm. Such a relaxation is also observed for the $1\ \mu\text{m}$ thick ZnO sample in CL cross-section measurements (Fig. 5.5).

The thickness of this distorted region can be estimated to 100 nm. Such a relaxation is also observed for the $1\ \mu\text{m}$ thick ZnO sample in CL cross-section measurements (Fig. 5.6). The monotonic increase in intensity and the energy shift of 4.7 meV towards the luminescence peak energy of fully relaxed ZnO can be correlated to a relaxation of tensile strain accompanied by a gradient of the internal piezoelectric fields. A similar field-induced blue shift was reported within the first $4\ \mu\text{m}$ growth of thick CVD ZnO epi-layers [Rie02]. In surface

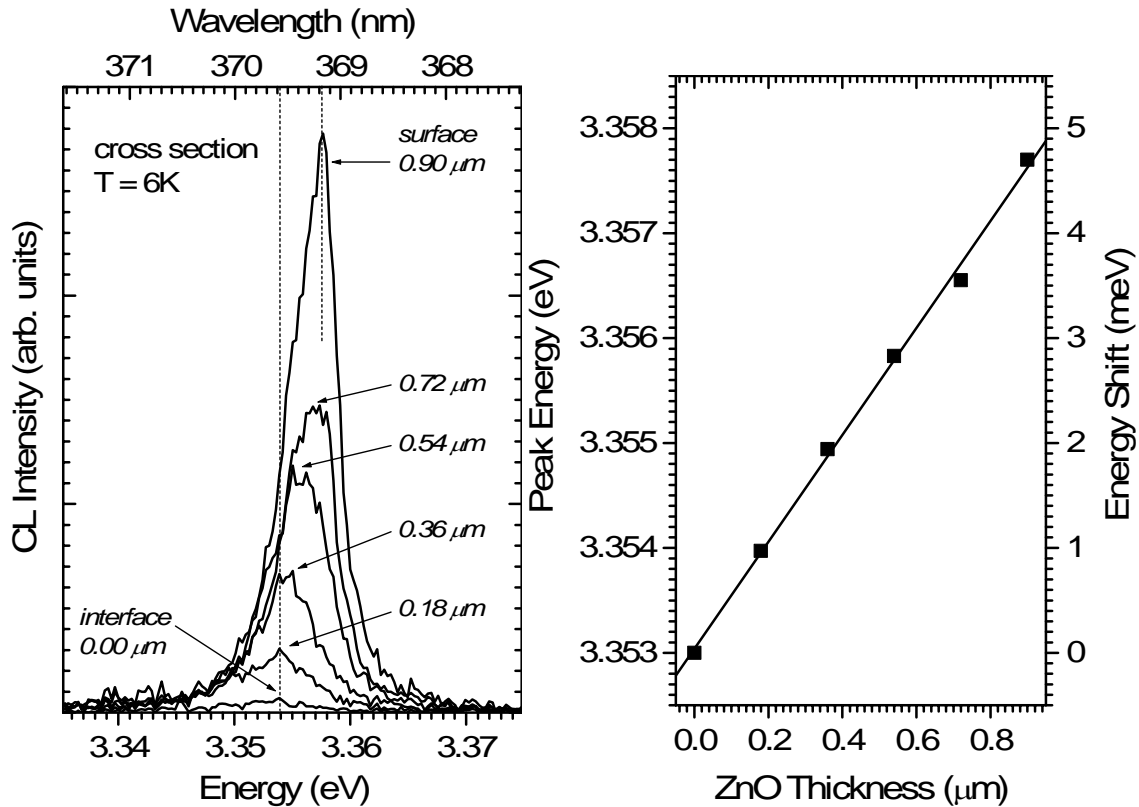


Fig. 5.6. CL spectra from top to the ZnO/GaN interface of a 1 μm thick ZnO layer on GaN/Si. An energy shift of about 5 meV together with a monotonic increase in intensity is observed indicating the relaxation of strain and internal fields.

plan view CL measurements the 1 μm thick sample emits narrow luminescence centered around 369.7 nm (Figs. 5.6, 5.7). The near band-edge luminescence is dominated by a narrow (A^0, X) emission. A weak DAP luminescence and almost no luminescence in the green to yellow region was observed (see inset in Fig. 5.7). From the energetic position of the (A^0, X) luminescence a tensile stress of 0.1 GPa is determined for the ZnO surface, which results from the combination of compressive stress induced by the GaN layer and tensile thermal stress due to the smaller expansion coefficient of Si. Results from spatially and spectrally resolved CL microscopy are depicted in (Fig. 5.7) and show a homogenous dominance of the acceptor bound exciton. Although only a small lateral variation of the peak wavelength occurs (a mean value of $\langle E(A^0, X) \rangle = 3.3526$ eV and a standard deviation of $\sigma_E = 0.65$ meV is derived for the whole depicted area of $27 \mu\text{m} \times 18 \mu\text{m}$) it strongly correlates with the morphology of the hexagons at the surface. The scanning electron microscopy image of the surface is depicted in the upper left of Fig. 5.7.

The integral intensity image (Fig. 5.8, lower row, left) show strongest luminescence from the edges and the top of the hexagons, which partly results from the different light out-coupling efficiencies due to the pyramidal geometry. Thus the spectrally resolved data are

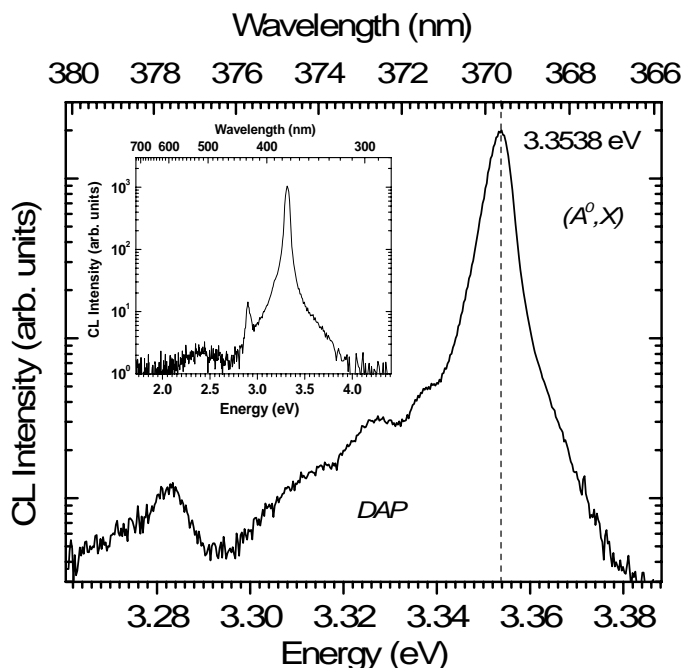


Fig. 5.7. CL spectrum of the near bandgap luminescence detected from the ZnO surface at 5 K. The position of the (A^0, X) emission corresponds to a tensile stress of ~ 0.1 GPa. The inset shows a spectral overview.

much more conclusive. The sets of monochromatic CL images at the bottom row of Fig. 5.8 clearly evidences the strain relaxation along the surface pyramid: The highest CL emission energies ($\lambda < 396.4$ nm; bottom left) are solely emitted from the tips of the pyramids, where strain relaxation is maximum, while the strongest red-shifted emission ($\lambda > 370.4$ nm; bottom right) corresponds to the base region where the original tensile strain of the ZnO layer surface is maintained. All pyramid side facets show CL emission at $\lambda = 369.70$ nm, regardless of their geometrical orientation indicating their partial strain relaxation (bottom right). The local spot mode CL spectra recorded at the top, the facets, and the base of one pyramid respectively (Fig. 5.8, upper right) clearly confirms this interpretation.

On the one side, ZnO growth using iso-propanol results in good surface morphology and intense cathodoluminescence of the films. On the other side, it also results in the prereactions which narrow the growth processing of the films. Although iso-propanol is less volatile than water and oxygen in reactions with DMZn, still it is not satisfactory enough for ZnO growth.

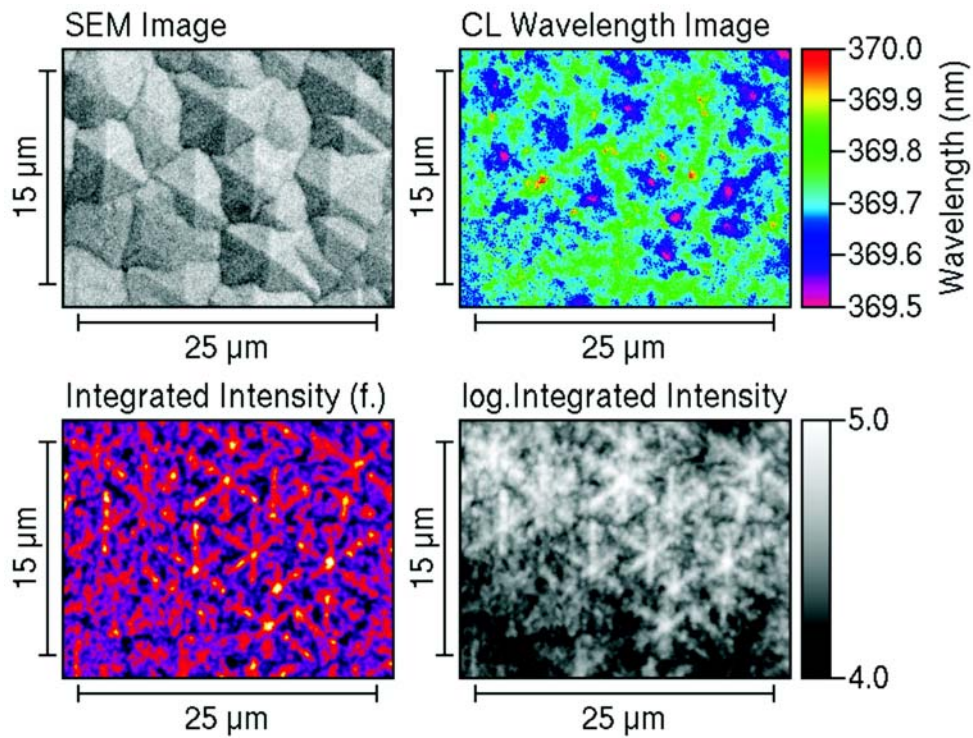


Fig. 5.8. Plan view cathodoluminescence images of a 1 μm thick ZnO sample on a GaN template. The SEM image clearly shows the hexagonal structure of the ZnO layer. The monochromatic CL images show a strong correlation with the surface morphology: a progressive strain relaxation as visualized by a spectral blue shift is clearly observed from the pyramid's bases to their tops.

5.1.2. Acetone

The growth conditions in experiments with acetone were similar to those with iso-propanol. The temperature was varied from 350 °C to 550 °C, and reactor pressure was 500 mbar. N₂ was used as a carrier gas. However, the properties of ZnO films grown with acetone drastically differ from those grown with iso-propanol.

The surface of ZnO films grown using acetone is rough. The layers represent sets of horizontal worm-like filaments which have nearly the same size (Fig. 5.9).

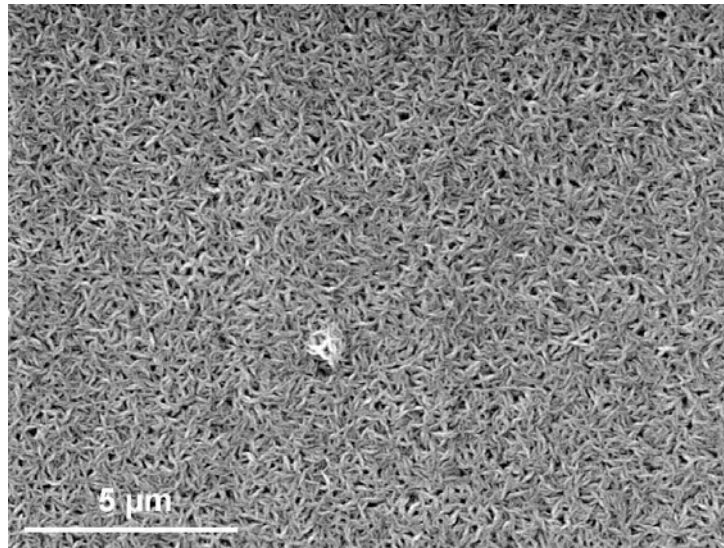


Fig. 5.9. SEM image of a ~1 μm thick ZnO layer grown using acetone on a ~1 μm thick GaN layer on Si(111).

In experiments with iso-propanol, ZnO preferably crystallizes in the [0001] direction.* In contrast to that, ZnO grown using acetone shows (0001) and/or (10 $\bar{1}$ 1) and/or (10 $\bar{1}$ 0) growth orientations, as evaluated from XRD measurements (Fig. 5.10). What is more, growth temperature influences the growth orientation of the ZnO films grown with acetone. ZnO grown at 350 °C has (10 $\bar{1}$ 1) orientation. An increase of the growth temperatures leads to the appearance of (10 $\bar{1}$ 1) and (10 $\bar{1}$ 0) modes. When the the growth temperature is increased to 500 °C, the (0002) growth orientation additionally emerges (Fig. 5.10, bottom). Overall, the crystalline quality of acetone-grown ZnO is poor compared to that of iso-propanol grown ZnO. Despite that, some growth conditions engineering can lead to reproducible growth of ZnO with different orientations. The nonpolar (10 $\bar{1}$ 0) surface for example is of particular interest from the viewpoint of surface chemistry, because the surface is terminated with the same number of O and Zn atoms [Duk77, Duk78]. However, those applications are beside the scope of this work.

* This is also general trend for ZnO, [Kal81].

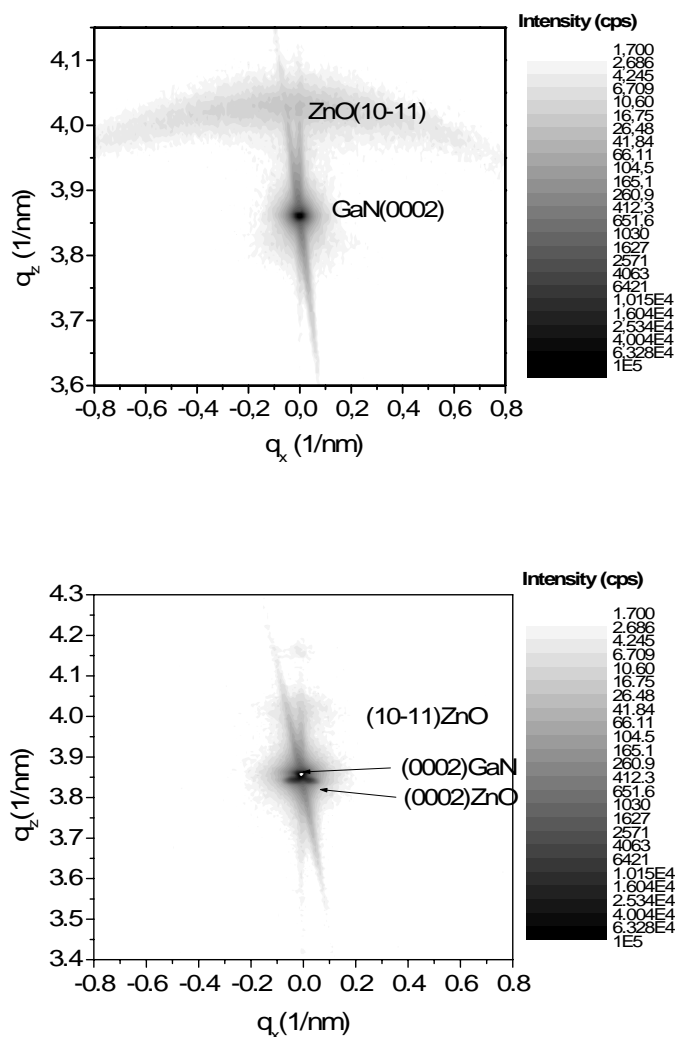


Fig. 5.10. X-ray reciprocal space mapping of ZnO film grown at 350 °C (top) and 500 °C (bottom).

Although no pre-reactions in the reactor and particles on the ZnO surface were observed in experiments with acetone, a strong deposition of carbon around the substrate in the reactor took place. Thus, unintentional doping of ZnO with carbon can be expected. Probably due to this doping the acetone-grown films did not show ZnO correlated luminescence in cathodoluminescence experiments. However, oxygen precursor should not unintentionally dope ZnO film with carbon. Additionally, reactor contamination with carbon leads to the poor growth results after several growth runs. Those factors point against the use of acetone for ZnO growth.

5.1.3. Diethyl-ether

Similarly to the experiments with acetone and iso-propanol, ZnO growth with diethyl-ether was performed at temperatures from 300 °C to 550 °C, and reactor pressures from 100 to 500 mbar. N₂ was used as a carrier gas.

In contrast to acetone- and iso-propanol grown ZnO, the diethyl-ether grown films contain some pyramidal 3D deposits (Fig. 5.11). No ZnO reflection in XRD measurements with position sensitive detector was found. Similarly to growth with acetone, a deposition of carbon is observed around the substrate in the MOVPE reactor. Thus, the use of diethyl-ether as O-precursor for ZnO growth is inappropriate.

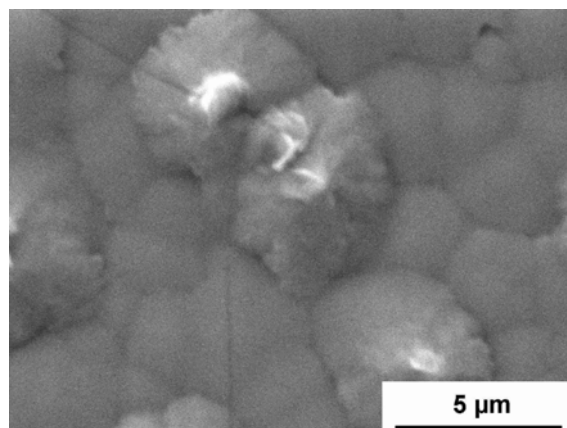


Fig. 5.11. SEM image of ZnO layer grown with diethyl-ether.

5.1.4. Tertiary-butanol

5.1.4.1. Growth Parameter Variation

First experiments with tertiary-butanol have demonstrated good quality of ZnO films. This is why growth conditions were varied in broader range than in experiments with iso-propanol, acetone, and diethyl-ether. Epitaxial growth has been performed for 30 minutes using H₂ carrier gas. To optimize the process parameters, the growth temperature, reactor pressure and tBuOH flows were varied in the ranges of 325-500 °C, 100-300 mbar, and 69-138 mmol/min, respectively. The ZnO growth rate was not significantly changed in all experiments and was in the range of 1-1.4 μm/h. In contrast to previously discussed experiments with O-precursors, no particle deposition, reactor pre-reactions and carbon deposition were observed. The most interesting results observed when DMZn and tBuOH flows were 2.5 mmol/min and 103 mmol/min, respectively, and the reactor pressure - 200 mbar.

The surface morphology of ZnO is dependent on the growth temperature. Up to 400 °C ZnO grows in 3D mode with vertical columns having heights from 20 to 100 nm, root-mean square (rms) surface roughness from 7 to 23 nm (Figs. 5.12, 5.13). The transition from 3D to

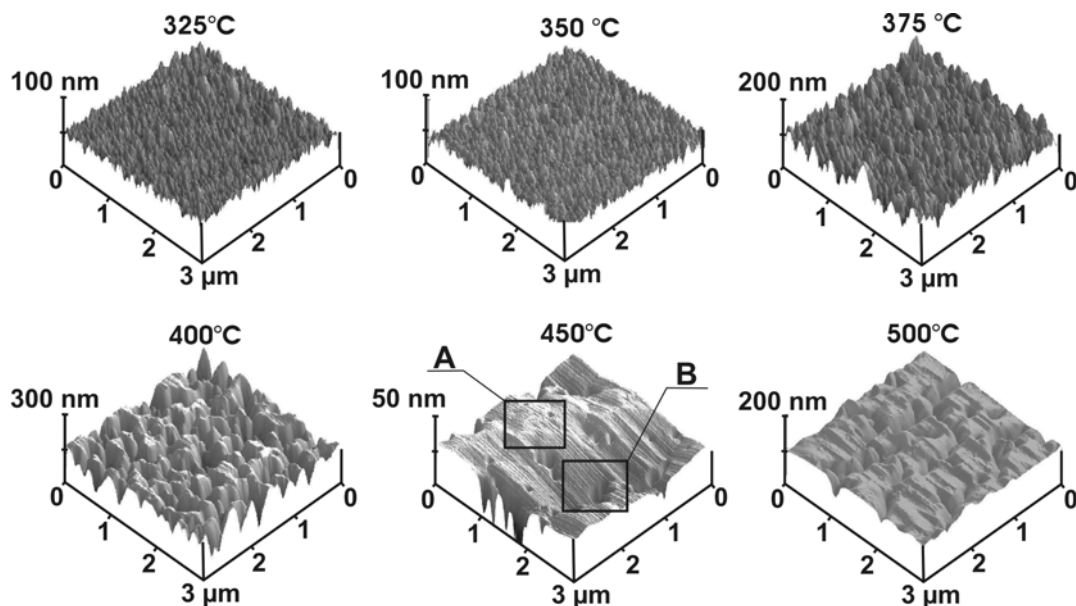


Fig. 5.12. AFM images of $\sim 0.5 \mu\text{m}$ thick ZnO layers grown at different temperatures. A and B rectangles ($800 \times 800 \text{ nm}^2$) plotted on the surface of ZnO grown at 450°C indicate flat and rough regions of the surface, respectively. RMS roughnesses are 7 nm (a), 9.3 nm (b), 0.89 nm ((b), region A), 11.7 nm ((b), region B), and 10.4 nm (c).

2D growth occurs between 400°C and 450°C , which is accompanied by a strong drop of the AFM rms roughness from 22.3 nm to 9.3 nm (Fig. 5.13). ZnO synthesized at 450°C and 500°C grows in a 2D growth mode (Fig. 5.12). The growth temperature influences the surface defect concentrations too (Figs 5.12 and 5.14). For example, ZnO grown at 450°C shows the smallest amounts of holes and cracks (Fig. 5.14). This sample is also the smoothest one,

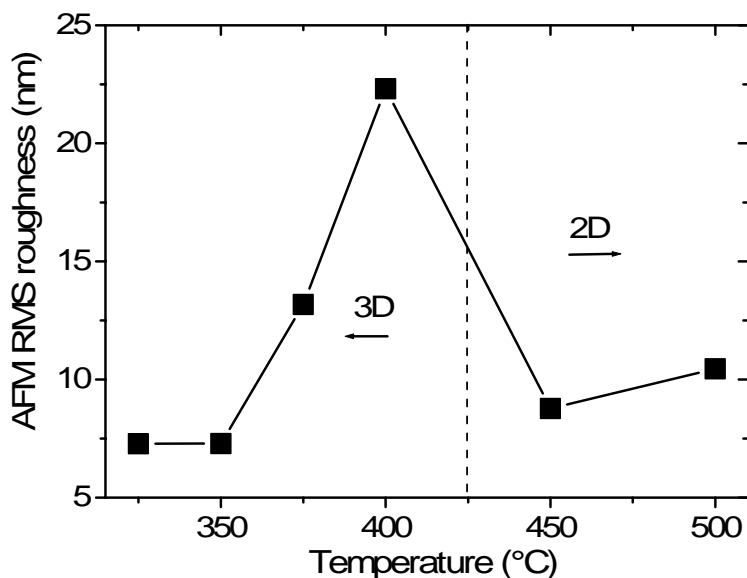


Fig. 5.13. AFM RMS roughness of ZnO versus growth temperature ($50 \times 50 \mu\text{m}^2$ scan). The dashed line indicates the boarder between 2D and 3D growth mode.

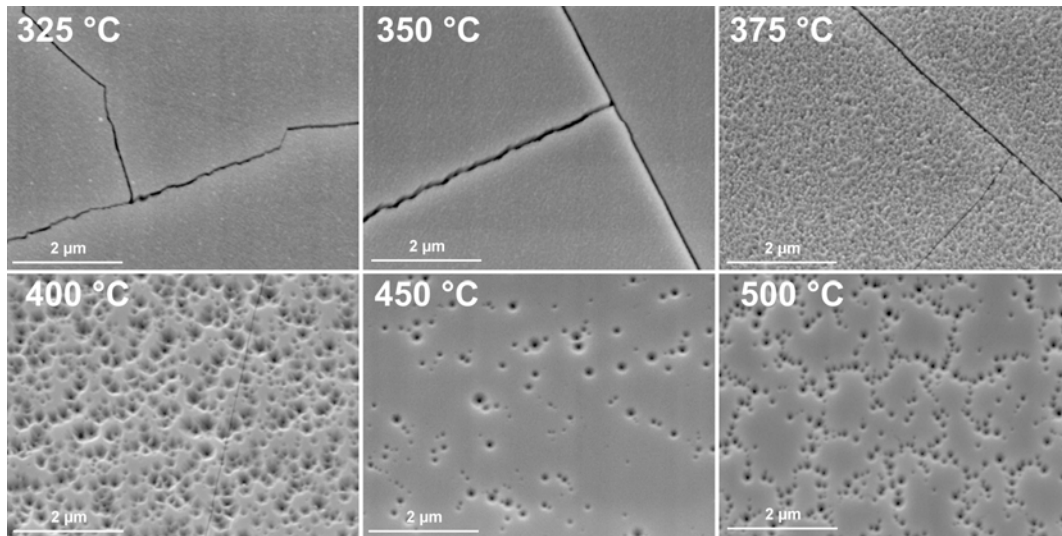


Fig. 5.14. SEM images of ZnO layers grown at different temperatures using tBuOH.

with the depth of the holes is at least 60-170 nm, as estimated from AFM. The holes might originate at dislocations in the GaN template or at the coalescence boundary of ZnO domains. Such holes were not observed in the surface of ZnO grown with i-PrOH. Additionally, the surface of i-PrOH grown samples was not influenced by the growth temperature, and was rougher due to hexagonal pyramids (AFM RMS roughness is 70 nm, $3 \times 3 \mu\text{m}^2$ area). Thus, the different growth mechanisms dominate the growth of iPrOH- and tBuOH-grown ZnO. The growth of ZnO using tBuOH allows optimisation of the ZnO surface properties.

From XRD measurements, ZnO is tensily stressed and has [0001] orientation. Similar to the surface morphology, the crystalline quality, strain state and lattice constants are influenced by the growth temperature. Additionally, coalescence growth, which leads to the holes in tBuOH-grown ZnO layers, has a certain influence on the strain in ZnO.

With increasing growth temperature from 325 °C to 450 °C the values of the in-plane lattice parameter a systematically decrease while those of the lattice parameter c systematically increase (Fig. 5.15). With increasing growth temperature both parameters are approaching the bulk values corresponding to a decrease in tensile stress. However, from a comparison of the thermal in-plane linear thermal expansion coefficients of ZnO ($5.61 \times 10^{-6} \text{ K}^{-1}$) [Vis98] and Si ($2.59 \times 10^{-6} \text{ K}^{-1}$) [Lan01] it can be expected that for ZnO grown at higher temperatures tensile stress increases. The experimentally observed decrease in tensile stress can be attributed to the growth of larger-sized ZnO crystallites in accordance with the observations of the surface morphology which indicates smaller-sized crystallites at lower

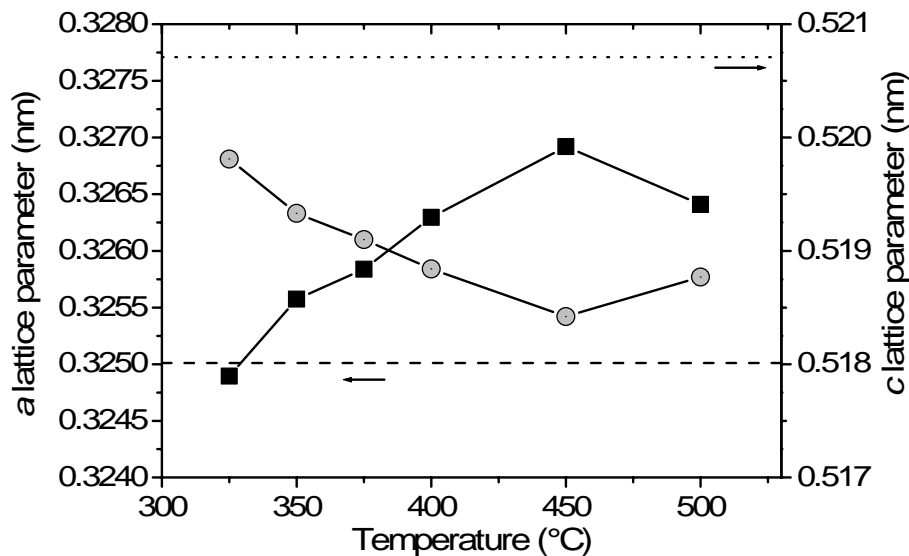


Fig. 5.15. ZnO lattice parameters c (■) and a (○) versus growth temperature. Dashed lines denote the literature values for relaxed ZnO [Lan01].

growth temperatures. A similar effect has been observed for the growth of GaN on silicon [Dad003]. In general, tensile stress originates in the 3D-growth mode when the gap between adjacent islands reaches a critical size which allows the islands to coalesce whereby their surface energy is reduced with the increase of elastic energy. Thus the amount of tensile stress depends on the number of islands [Hof76].

FWHMs of ZnO XRD ω -scans in (0002) geometry are varying from 720'' to 1620'' when the growth temperature is decreasing from 450 °C to 325 °C, Fig. 5.16. At 500 °C we observe an increase of the FWHM value to 860''. From Fig. 5.16, the sample grown at 450 °C demonstrates the best crystalline quality, which also correlates with the surface morphology

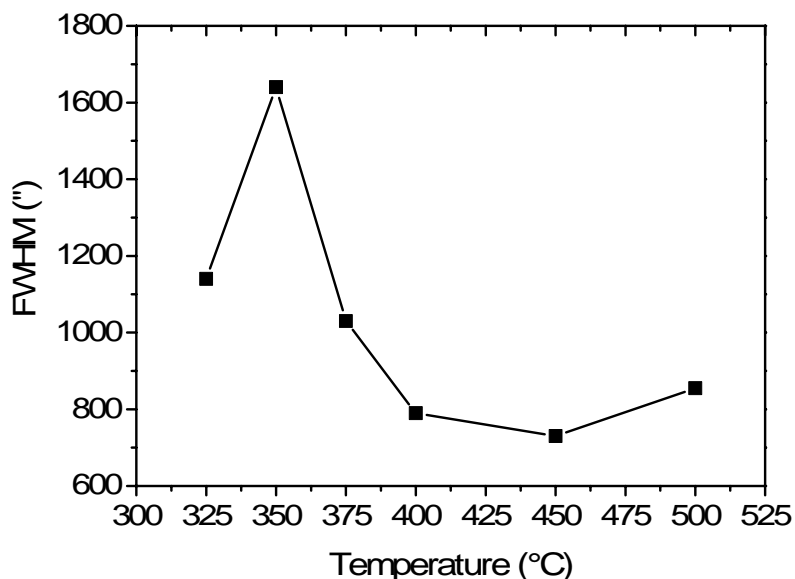


Fig. 5.16. FWHM of X-ray diffraction ω -scans around ZnO (0002) reflection versus growth temperature.

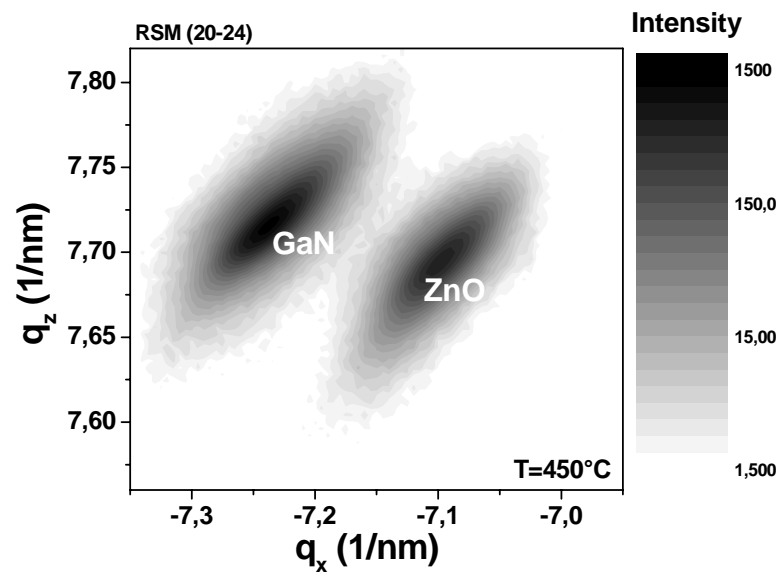


Fig. 5.17. X-ray reciprocal space maps around the asymmetrical $(20\bar{2}4)$ Bragg reflection of $\sim 0.5 \mu\text{m}$ thick ZnO layer grown at 450°C on a $\sim 1 \mu\text{m}$ thick GaN layer. observations. Fig. 5.17 shows XRD reciprocal space map (RSM) of this sample around the asymmetrical $(20\bar{2}4)$ Bragg reflection. Compared to the RSMs obtained from other samples (which are not shown here), this one shows the narrowest and highest intensity XRD peaks. ZnO grown at 450°C is partially relaxed. For comparison, for the best monocrystalline ZnO grown with *i*-PrOH the FWHM was $1590''$. This indicates an improvement of the crystalline quality when *t*BuOH is used as O-precursor instead of *i*PrOH.

Cathodoluminescence

Compared to *i*PrOH-, *t*BuOH-grown ZnO demonstrate better optical quality. Similarly to structural and surface morphology properties, the growth temperature strongly influences the optical properties of *t*BuOH-grown ZnO.

Cathodoluminescence spectra (Fig. 5.18) measured on the ZnO surface at 5 K for the layers grown in the temperature range of $325\text{--}500^\circ\text{C}$ exhibit intensive (A^0, X) exciton (assignment I_8 in [Gut88]). The presence of (A^0, X) -LO phonon peaks for samples grown at 450 and 500°C indicates a high crystalline quality for those layers, which also correlates with the results of the surface morphology and XRD measurements. The spectral resolution of the CL measurements shown in Fig. 5.18 is about 0.09 nm . As it was mentioned in Chapter 2, the CL spectrum of ZnO shows a lot of recombination lines, which are situated near to each other around 3.35 eV [Pre88]. This is why it is not possible to make a conclusion which recombination line dominates the CL spectra shown in Fig. 5.18. In Fig. 5.19 a blue shift of

the luminescence is observable with increasing growth temperature up to 450 °C and then is decreasing when increasing the growth temperature to 500 °C. The FWHM of the

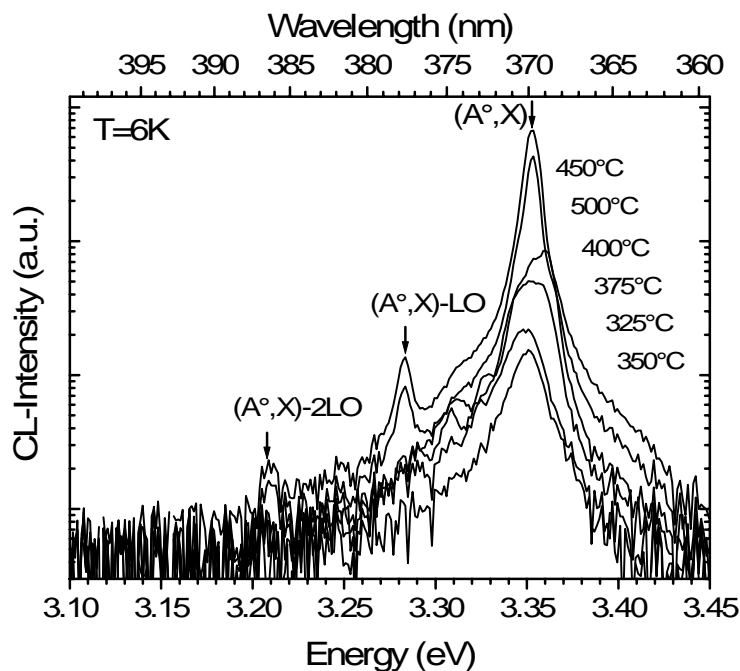


Fig. 5.18. Integrated CL spectrum measured from the surface of ZnO at 6 K. Sample grown at 450°C shows the highest CL intensity.

luminescence peaks for the material grown at different temperatures is in the range of 7 to 25 meV and decreases with increasing growth temperature up to 450 °C and then increases again, Fig. 5.18. The 450 °C-sample has the highest luminescence intensity from the surface at the (A^0_1, X) position, 369.7 nm (3.35 eV) and at the (A^0, X) -LO position 377.6 nm (3.28 eV), Fig. 5.19 a), b), and c).

In conclusion to this subchapter, different growth mechanisms govern the MOVPE of ZnO with *i*-PrOH and *t*BuOH. The use of *t*BuOH offers a pre-reaction free flexible manipulation of the ZnO properties by variation its growth temperature. From a comparison of the surface morphology, structural and optical qualities, ZnO layers grown at 450°C using *t*BuOH show the best properties overall.

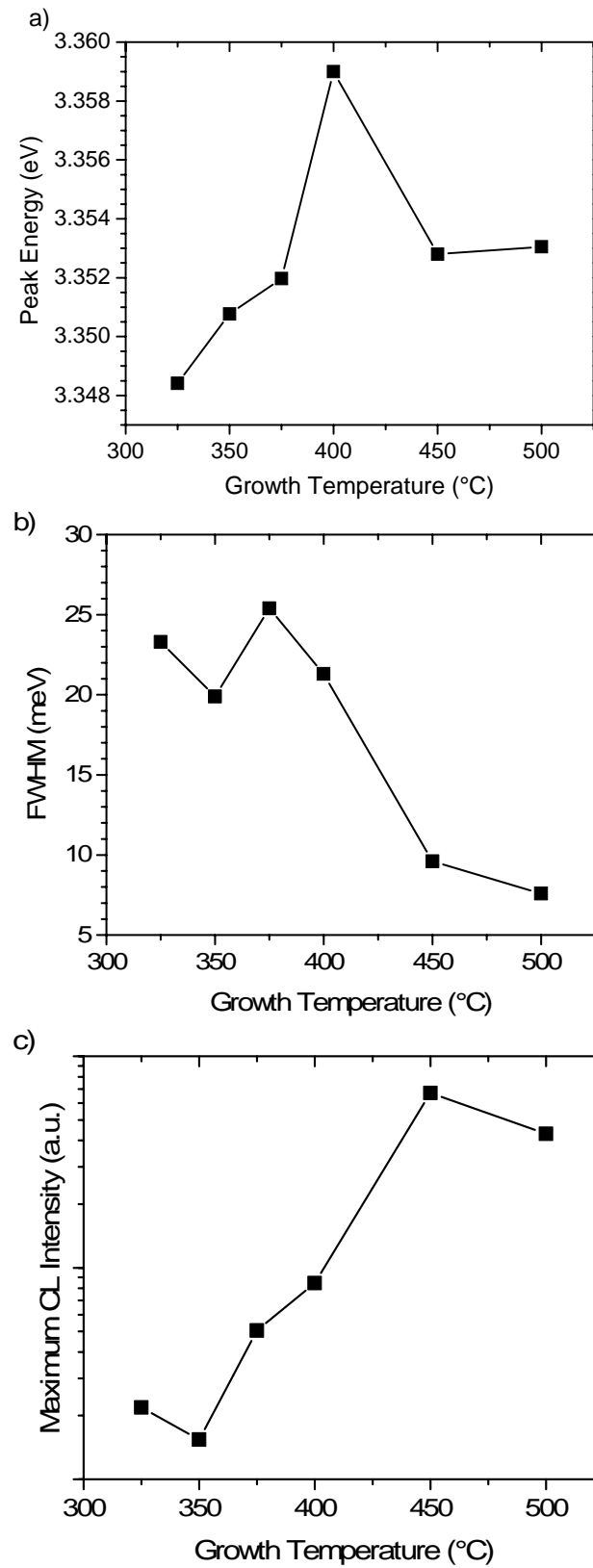


Fig. 5.19. a) CL maximum intensity peak position; b) FWHM and c) maximum CL intensity versus growth temperature of ZnO.

5.1.4.2. *In-situ* Annealing and Ostwald Ripening

tBuOH can be the best candidate for low-temperature ZnO growth without pre-reactions due to the formation of the stable adducts in the reactor. According to Oda *et al.*, stable adducts can be transported intact to the substrate and decomposed at the growing surface [Oda85].* The experimental results discussed in the previous subchapter have shown that the use of tBuOH results in good quality ZnO. In order to further improve the properties of ZnO grown with this precursor, *in-situ* annealing of ZnO was studied.

After completion of ZnO growth at 450 °C, the carrier gas was switched to N₂** , and N₂O was additionally switched on. Then the substrate temperature was ramped up to 900 °C during 3.5 min, followed by an annealing step for times varying from 0 to 8 min. The N₂O use is particularly suitable here due to the potential loss of oxygen from ZnO during the high-temperature processing (Chapter 4.4).

In-situ Observations

When growing the ZnO layer a decrease in the reflected intensity is observed in reflectivity measurements (Fig. 5.20). During the heat-up procedure the intensity of the reflected signal is slowly decreasing, and after the moment when the temperature reaches 820 °C it starts to increase. When the ZnO layer is annealed at 900 °C, the reflectivity signal increases and saturates, indicating surface smoothing.

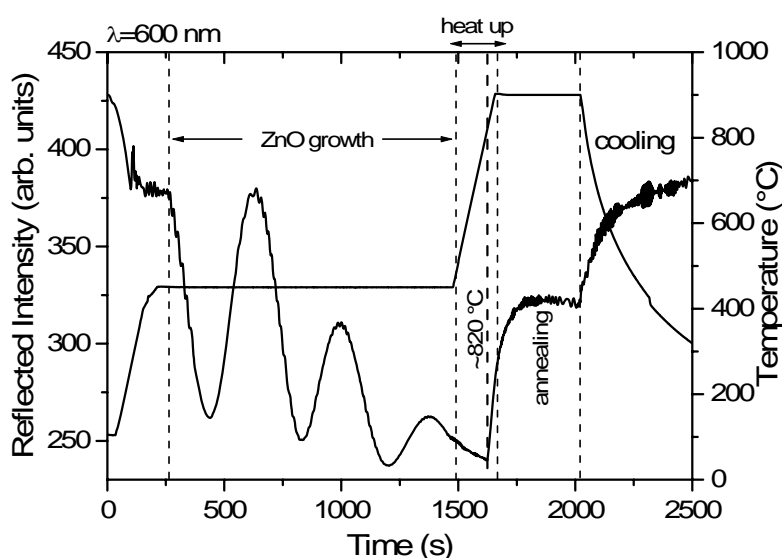


Fig. 5.20. *In-situ* reflectometry measurement of ZnO growth and *in-situ* annealing processes.

* See Chapter 8 for more discussion on this.

** High-temperature processing of ZnO should be performed without hydrogen, Chapter 4.1.2.

Surface Morphology

The change of the surface morphology is strongly pronounced in SEM images, Fig. 5.21. The as-grown layer contains a large amount of holes. After 0.5 min of annealing the holes start to disappear. A further increase of the annealing time results in the complete disappearance of the holes, but some irregularity in the form of hills occurs up to 2 min of annealing. Further annealing for 4-8 min results in a significantly smoothed surface, Fig. 5.21. In order to get better insight about the evolution of the surface morphology during annealing, AFM measurement were performed. Fig. 5.23 depicts AFM images ($3 \times 3 \mu\text{m}^2$ scan area, z-scale 0 - 250 nm) of the ZnO layers. The surface of the as-grown ZnO layer consists of three-dimensional (3D) pyramids with a mean diameter of about 400 nm and a RMS surface roughness of 33.4 nm (Fig. 5.24). During the first minute of thermal annealing the smaller ZnO pyramids disappear while the larger ones increase in size (Figs. 5.21, 5.22).

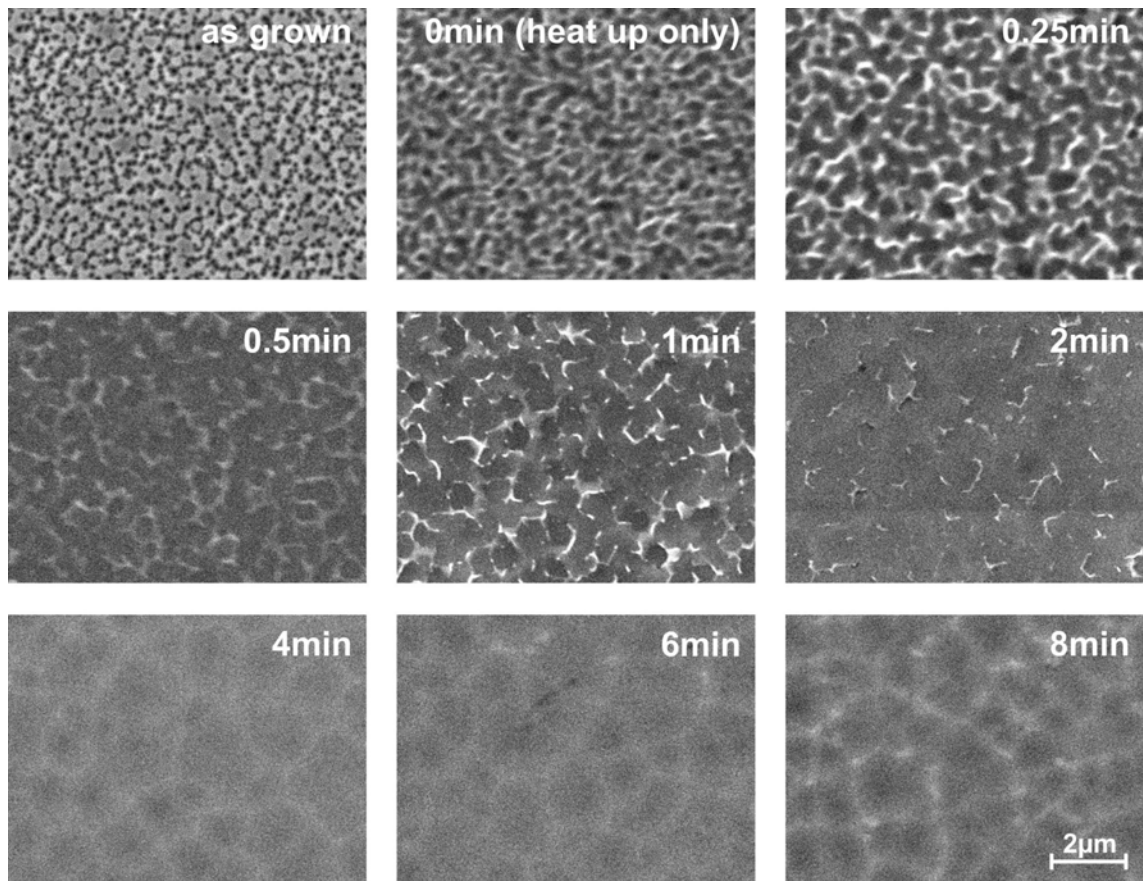


Fig. 5.21. SEM images of as-grown and annealed ZnO samples.

The RMS surface roughness decreases with increasing annealing time up to 0.25 min and subsequently increases again with increasing annealing time up to 1 min (Fig. 5.23). A maximum pyramid height of 150 nm is reached after 1 min of annealing with a RMS surface roughness of 42.3 nm as measured from AFM linescans.

These observations indicate that during the first 0.25 min the molecules dissolve from small unstable ZnO clusters, diffuse along the layer surface and are eventually attracted by the larger more stable pyramids. The 3D pyramid morphology sustains up 1 - 2 min of annealing time. A further increase of the annealing time then leads to an abrupt transition to a nearly two-dimensional (2D) surface morphology. Large, flat domains having an average diameter of about 1.6 μm (Fig. 5.21) and mirror like surfaces of RMS roughnesses below 10 nm (Fig. 5.22) evolve. A minor increase of the RMS surface roughness up to 16.2 nm (Fig. 5.23) was observed only for the longest annealing time of 8 min. In addition, the average domain size as counted from large-area AFM (not shown here) and SEM pictures (Fig. 5.23) monotonically increases with annealing time from 0.4 to 1.8 μm . The only exception is the sample annealed for 8 min.

XRD Measurements

XRD measurements show that the as-grown and annealed layers consist of [0001]-oriented, almost strain-free ZnO crystallites with lattice parameters close to the published literature values (Fig. 5.22). The spatial coherence length, i.e., the average crystallite size, as

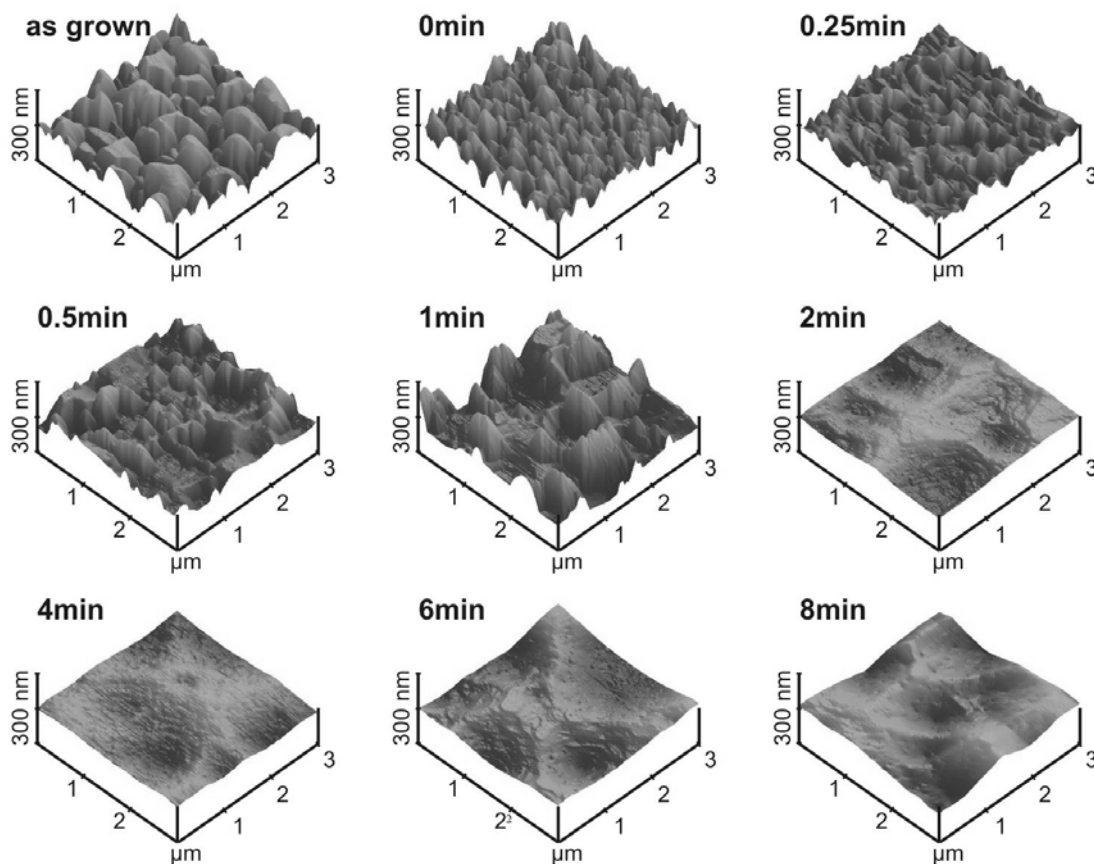


Fig. 5.22. AFM images of as-grown and annealed ZnO samples.

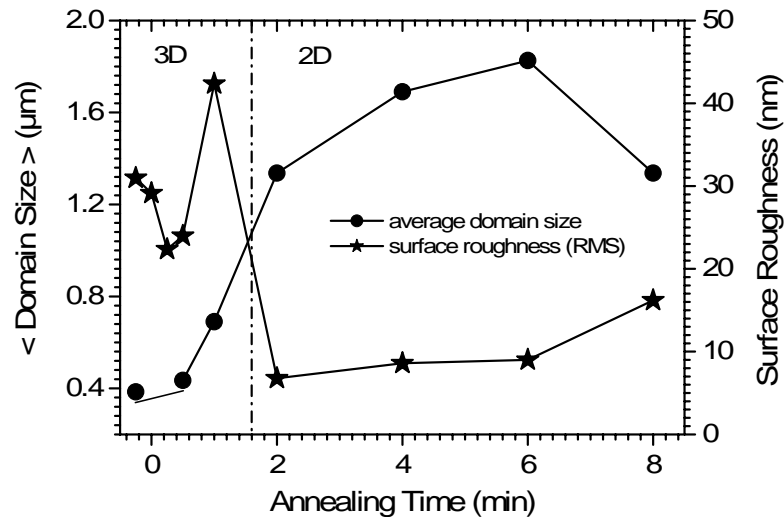


Fig. 5.23. Evolution of domain size (from SEM) and surface roughness.

well as the average inhomogeneous distortion along the a -axis were determined by ω - 2θ measurements around the $(10\bar{1}0)$ and $(30\bar{3}0)$ reflections (Fig. 5.24).

The average crystallite size follows the same trend during thermal annealing as the surface morphology. First, in the 3D phase, a strong drop in size from 140 nm to 80 nm is observed. After the transition to the 2D phase a recovery is achieved yielding cluster sizes of up to 160 nm. Simultaneously, the average inhomogeneous distortion of the ZnO crystallites rapidly drops in the 3D phase from about 0.19 % to below 0.09 % and remains at this low value in the 2D phase. The morphological evolution of ZnO during the first minutes of thermal annealing suggests that the cluster coarsening process is governed by Ostwald ripening [Ost00]. In general, Ostwald ripening occurs in the final stage of a first-order phase transition for the condensation of a metastable phase. The first stage is nucleation and the second stage is cluster growth depleting the metastable phase and causing stable clusters to grow regardless of their size. In the final stage, the larger clusters grow at the expense of smaller ones.

The thermodynamic driving force for such ripening is based on the Gibbs-Thomson equation, which relates the ratio of interfacial energy to thermal energy. Smaller clusters are thermodynamically less stable and eventually rapidly vanish, transferring their mass to the surface and on to larger clusters [Ost00]. With increasing time the cluster size distribution should evolve to a monodisperse distribution, ultimately consisting of a single large cluster [Lif61]. The phase transition and its influence on the optical quality of ZnO is also visible in the optical properties.

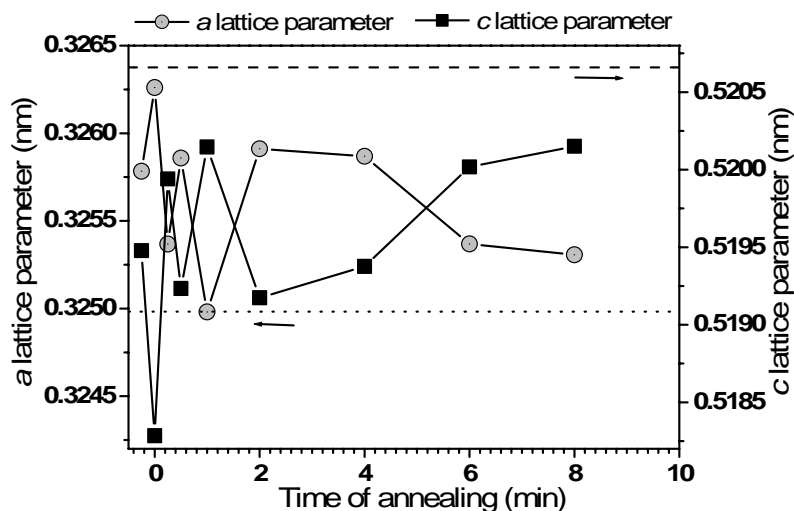


Fig. 5.24. *c* (black squares) and *a* (white circles) lattice parameters of ZnO annealed at 900 °C for different times. Horizontal dashed and dotted lines denote the literature values of ZnO *a*- and *c*-lattice parameters, respectively [Lan99].

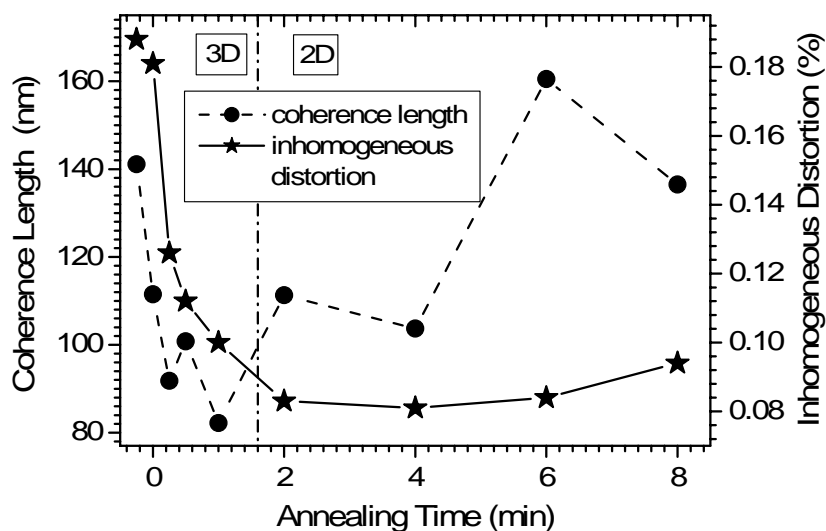


Fig. 5.25. Improvement of coherence length and inhomogeneous distortion obtained from XRD with annealing time.

Cathodoluminescence

Integral CL spectra obtained at room temperature from the annealed samples are shown in Fig. 5.26 for comparison. Annealing of ZnO leads to a decrease of the defect band luminescence intensity (near band edge luminescence decreases also but slower than defect band luminescence intensity), which indicates an improvement in the optical quality of ZnO upon annealing Fig. 5.27 shows low temperature integrated spectrums of ZnO. The integral spectrum of the as-grown sample shows well-resolved emission lines of bound excitons

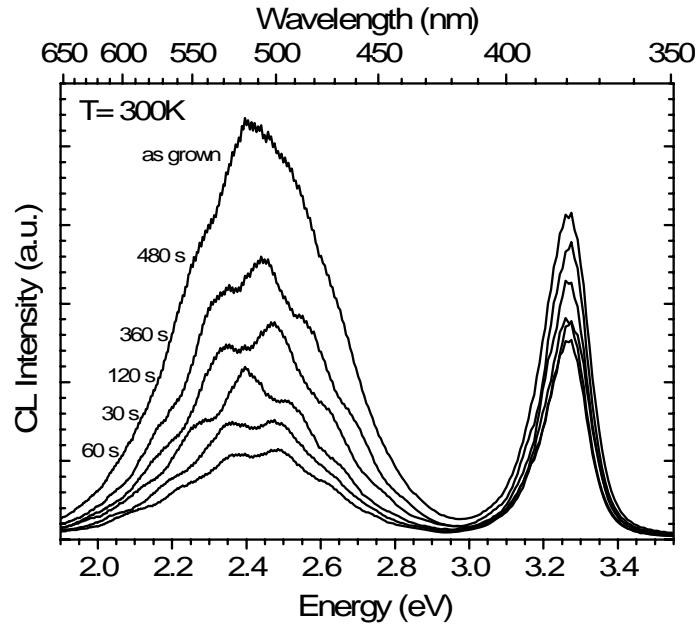


Fig. 5.26. Room-temperature cathodoluminescence measurements of ZnO annealed for different times.

(assignment according to reference [Gut88]) proving the high crystalline quality of the ZnO nanopryramids at the surface of this sample.

As a result of the phase transition a dramatic improvement in the lateral homogeneity is achieved. In Fig. 5.28 the corresponding CL wavelength images (CLWI), i.e., the spatial

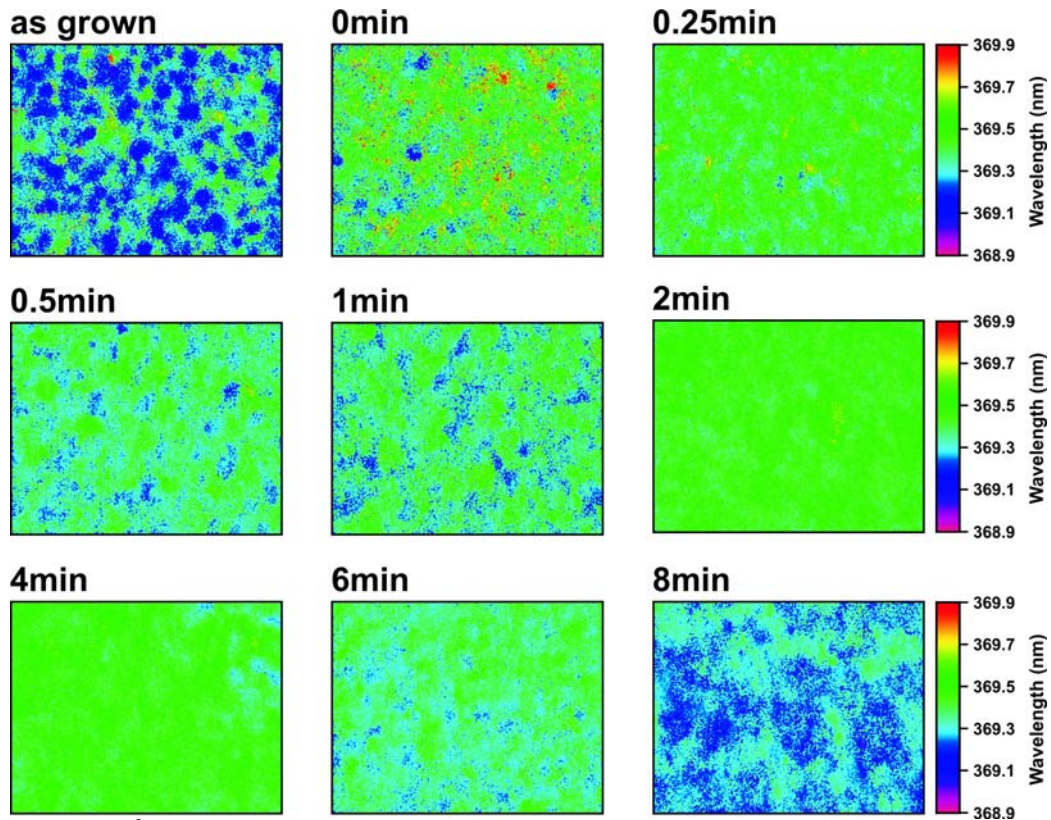


Fig. 5.28. $5 \times 9 \mu\text{m}^2$ CLWI images of ZnO annealed from 0 to 8 min.

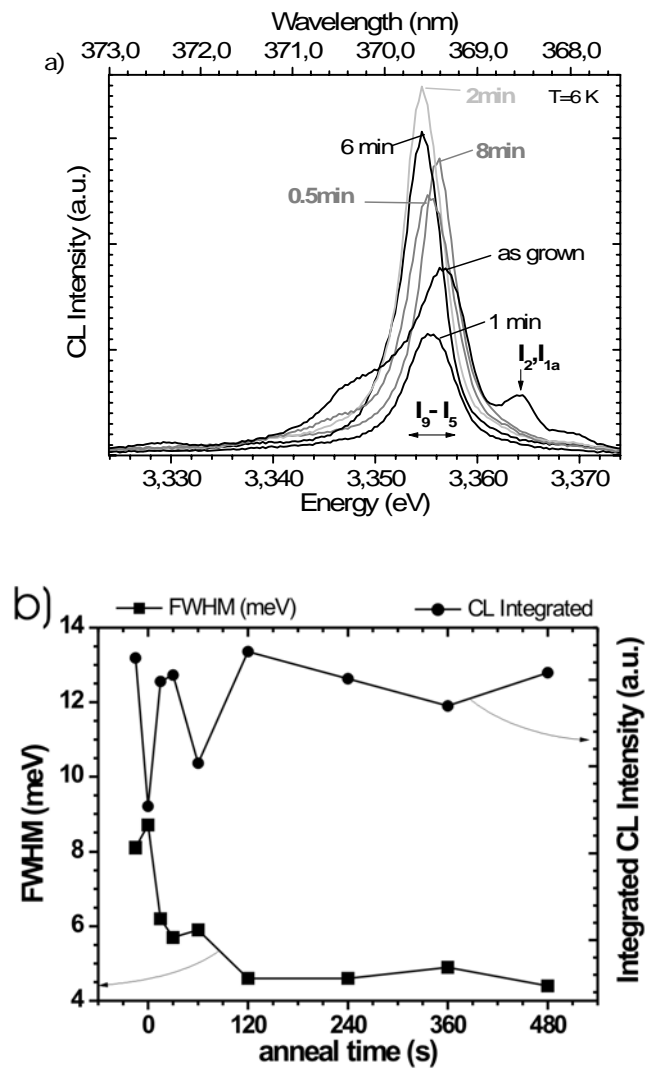


Fig. 5.27. Near band edge cathodoluminescence measurements of ZnO at 6 K, a). FWHM and integrated intensity for the samples annealed form different time, b).

distribution of the peak emission wavelength is depicted. While strong local fluctuations on a submicrometer scale are observed for the as-grown sample, the annealed samples show an almost perfect lateral homogeneity.

This is quantitatively analyzed by computing the histograms of the CLWI, i.e., the frequency of a specific wavelength within the area investigated. The result is summarized for the whole set of samples in Fig. 5.29 where the integral luminescence intensity, i.e., the quantum efficiency and the standard deviation of the histograms is plotted as a function of annealing time. The morphological phase transition directly correlates with a discontinuity of the optical properties. Upon annealing a strong reduction of the lateral fluctuation $\sigma_E < 0.6$ meV is achieved. The origin of the observed transition from a 3D to a 2D surface morphology

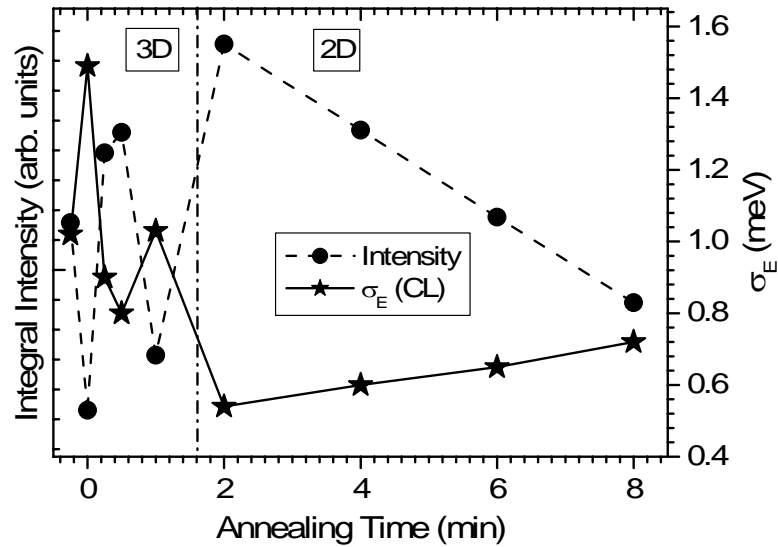


Fig. 5.29. Integral CL intensity and energy standard deviation of the CLWI histograms for all samples as a function of annealing time.

might be initiated by the complete desorption of all organic restmolecules stemming from the butanol-precursor allowing an unhindered surface diffusion for all ZnO molecules. In conclusion, growth of ZnO using tertiary-butanol together with an *in-situ* annealing procedure results in smooth films with good optical and structural qualities. Compared to ZnO layers, grown using iso-propanol, acetone, or diethyl-ether, tertiary butanol is the best O-precursor for the growth of ZnO at low-temperatures.

5.1.5. N₂O

N₂O is attractive O-precursor for growth of ZnO. Due to its higher binding energy, it is less volatile in reactions with DMZn in comparison to water, oxygen or alcohols. Its stability requires higher growth temperatures, which broadens the process parameter range for ZnO growth overall. To establish the growth parameters, the growth temperature was varied from 500 to 1000 °C, the reactor pressure from 100 to 500 mbar, and the VI-II ratio from 203 to 1625.

As expected, no surface particles and gas-phase pre-reactions were observed in experiments with N₂O. Stable reflected light intensity oscillations were observed in *in-situ* reflectometry measurement. Growth rates were not influenced by the growth parameters (0.8

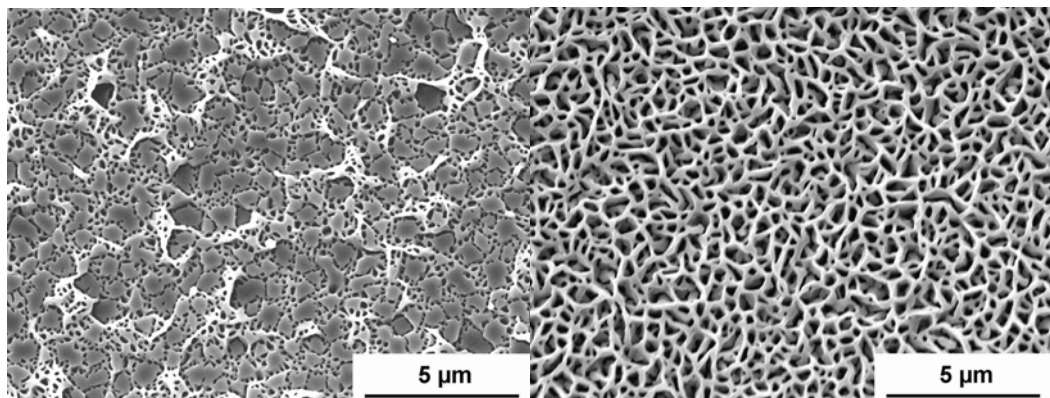


Fig. 5.30. SEM images of ZnO grown on GaN/Sapphire (left) and on GaN/Si (right).

– 1.2 μm/h). The surface of the ZnO films consists of a spongy structure with fluctuating density in lateral direction (Fig. 5.30). The growth parameter variation did not lead to the full surface coalescence. However, domain structure and partial coalescence is observable when growing on GaN/Sapphire substrate. Etching experiments (Fig. 5.31) together with cross sectional SEM (not shown here) indicate that the film is spongy beginning from the GaN/ZnO interface. The film density and homogeneity in the vertical direction is higher than

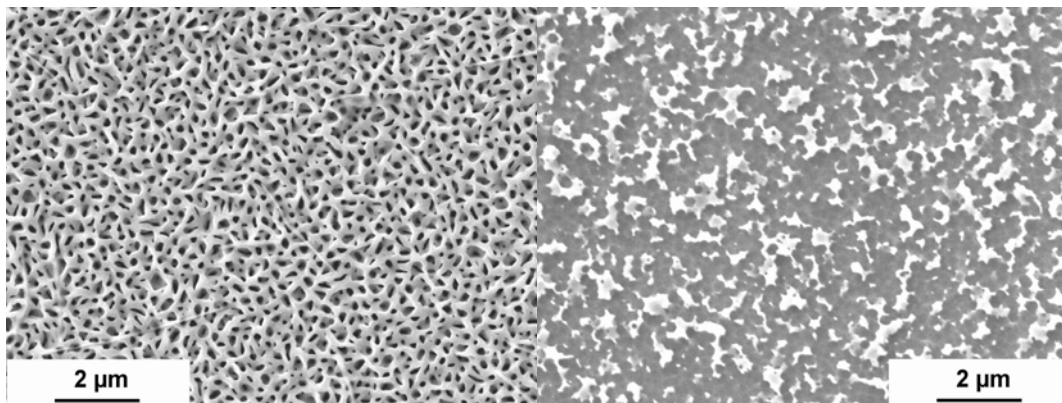


Fig. 5.31. SEM images of ZnO sample as-grown (left), and etched for 2 sec in H₃PO₄ (right).

in the lateral one. Those observations indicate that after the initial nucleation, the lateral overgrowth of ZnO is depressed, while the film is extensively growing in the vertical direction. The detailed study of the growth mechanisms is behind the scope of this work.

Despite its low density, ZnO grown with N_2O demonstrates high crystalline quality. For example, the films grown at $800\text{ }^\circ\text{C}$ at 200 mbar and a VI-II ratio about 1080 have ω -scans FWHM of $590''$ at $2\Theta=34,395^\circ$. Fig. 5.32 shows reciprocal space maps obtained in asymmetrical $(20\bar{2}4)$ and symmetrical (0002) XRD reflections of this sample. The growth orientation of ZnO films is (0001) . Comparing the positions of ZnO and GaN in the top picture, one finds that ZnO grows relaxed on GaN (Fig. 5.32, above). Considering both

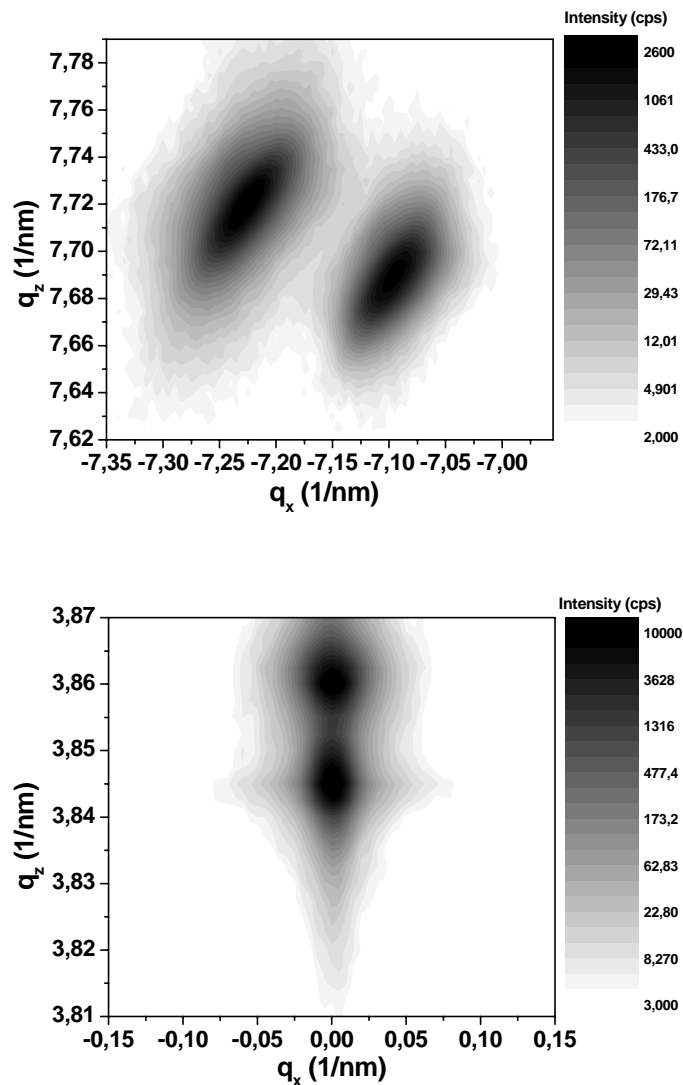


Fig. 5.32. Symmetrical (0002) , top, and asymmetrical $(20\bar{2}4)$, bottom, X-ray diffraction reciprocal space mapping of the ZnO. VI- II ratio = 1080, growth rate = $0.9\text{ }\mu\text{m/h}$, thickness = $0.9\text{ }\mu\text{m}$, reactor pressure = 200 mbar, temperature = $800\text{ }^\circ\text{C}$.

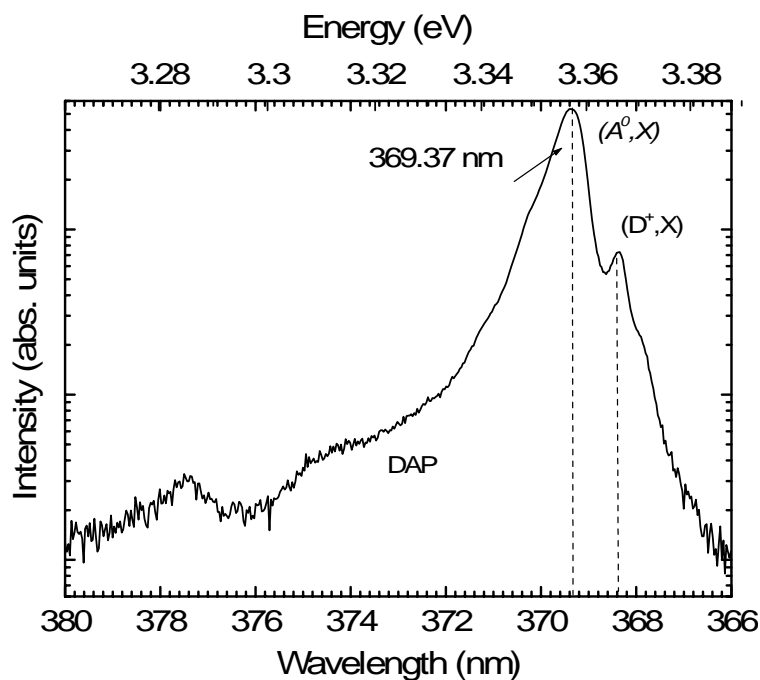


Fig. 5.33. CL spectrum of the near bandgap luminescence detected at 4.5K from the surface of ZnO grown on GaN/Si.

symmetrical and asymmetrical RSM depicted in Fig. 5.32, the mosaicity and tilting of ZnO columns is low. In XRD measurements ZnO grown with N₂O has a better crystalline quality compared to that of films grown with tBuOH and iPrOH. Thus, improvement of the lateral growth of the N₂O-grown ZnO will lead to the smooth films with exceptionally good crystalline properties.

ZnO grown with N₂O emits highly intense luminescence. It is centered around 3.353 eV (Fig. 5.33). The highest intensity of the near band-edge luminescence is situated around the (A⁰,X) peak emission. Spatially and spectrally resolved CL microscopy images of N₂O grown ZnO are shown in Fig. 5.34. The peak emission wavelength strongly correlates with the morphology of the surface. On the integral intensity image for ZnO the strongest luminescence stems from the conches of the net-like surface (Fig. 5.34, bottom row). All pyramid side facets show CL emission at $\lambda = 369.70$ nm.

In conclusion, the use of N₂O offers prereaction-free high-temperature growth of ZnO with the growth rates around 1 $\mu\text{m}/\text{h}$. The optical and crystalline quality of ZnO layers grown with N₂O is superior to those of ZnO grown with tertiary-butanol. However, in contrast to very smooth, homogeneous surface of *in-situ* annealed tBuOH-grown ZnO layers, N₂O-grown layers demonstrate rough spungy surface. The properties of the low-temperature tBuOH-grown ZnO make it very attractive for the buffering of subsequent high-temperature ZnO

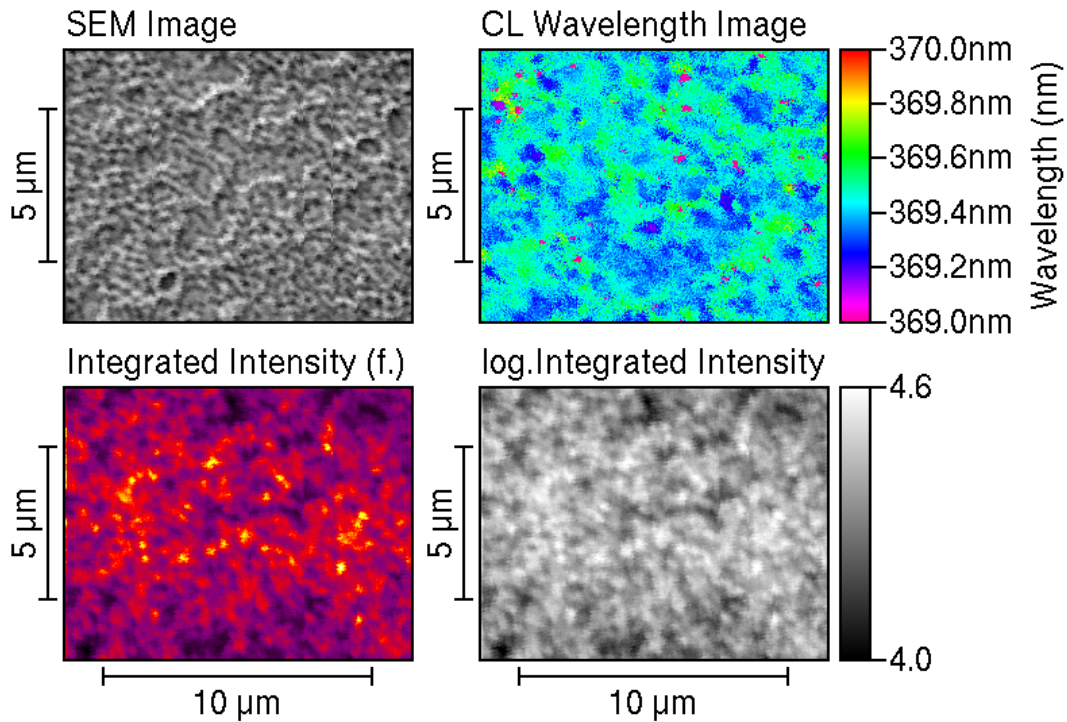


Fig. 5.34. Cathodoluminescence measurements of ZnO grown with N₂O. The maps were taken at 4.5 K.

layer grown with N₂O. Considering the absence of the ideally suited substrate for ZnO, the use of buffer layer can significantly improve the quality of ZnO layers (Chapter 4.1.1). Thus, two-step growth method emerges.

5.2. Two-step Growth

Minimisation of the intrinsic defects in epitaxial ZnO films has been one of the main issues in its optoelectronic applications (Chapter 1). From Chapter 5.1, tertiary-butanol and N_2O are the most promising O-precursors for the growth of high-quality ZnO. MOVPE growth using those precursors involves different process parameters and allows a flexible manipulation of ZnO properties. Therefore, the combination of the growth procedures offers promising advantages. For example, the bufferring of high-temperature grown ZnO with the low temperature layer partly eliminates the absence of the suitable substrate, which lowers stresses and the concentration of the detrimental defects and dislocations (Chapter 4.4). Additionally, it decreases Ga diffusion from the GaN substrate [Mey03]*.

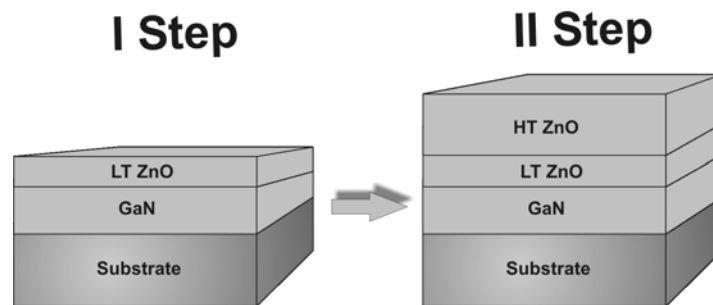


Fig. 5.35. Two-layer ZnO stack in two-step growth.

5.2.1. Buffer Thickness and Growth Temperature

The low-temperature (LT) ZnO buffer thickness and the second step (HT) growth temperature influence the two-step growth process. For example, they influence the thermal- and

| $T_{\text{growth}}, ^\circ\text{C}$ | 850 | 900 | 950 |
|-------------------------------------|-----|-----|-----|
| Buffer thickness, μm | | | |
| 0.22 | | * | |
| 0.44 | * | * | * |
| 0.66 | | * | |
| 0.88 | | * | |

Tab. 5.1. Variation of the growth conditions for the optimization of the two-step growth procedure.

lattice-mismatch induced stress in the layer stack. Additionally, LT-ZnO thickness may control the surface defect- and dislocation density on the HT ZnO interface.* The HT-ZnO

* Ga acts as a donor in ZnO.

* The dislocation density along the growth direction can be decreased by the dislocation annihilation.

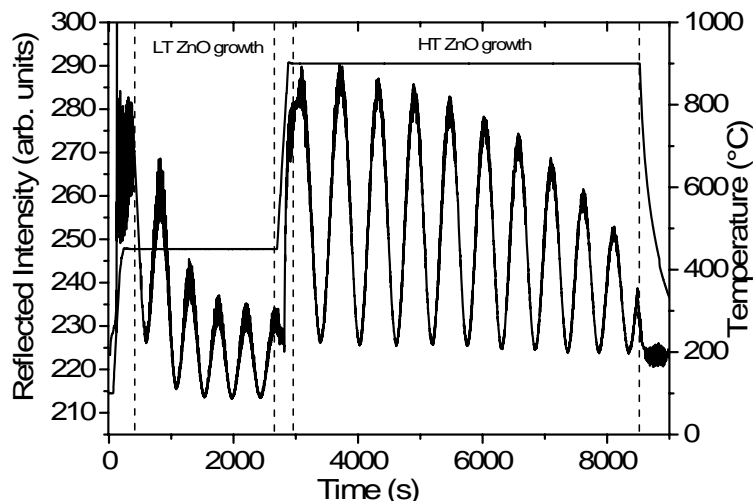


Fig. 5.36. *In-situ* reflectometry measurement of two-step growth.

growth temperature affects the growth mechanisms, which in turn determine the ZnO quality. To study the influence of LT-ZnO thickness and HT growth temperature on ZnO properties, these parameters were varied as shown in Tab. 5.1.**

Two-step growth itself proceeds as follows. After the growth of LT-ZnO, the 3.5 min temperature ramp followed (Fig. 5.35). Subsequently, HT-ZnO was grown with DMZn, N₂O, and t-BuOH flow rates of 2.5, 89.2 and 11.4 mmol/min, respectively.

From *in-situ* reflectometry measurements, the HT-ZnO growth rate is not affected by the growth conditions, and was about 0.8 μm/h. As the LT- and HT-growth proceed, the reflected intensity is decreasing, which indicates a slight ZnO surface roughening (Fig. 5.36). The intermediate temperature ramp leads to remarkable increase of the reflectivity signal, which indicates the sample surface smoothing (Fig. 5.36). The evolution of LT ZnO properties during the temperature ramp is discussed in the Chapter 5.2.2.

Firstly, the surface of two-step grown ZnO is smooth in comparison to N₂O-grown spongy ZnO. However, some holes and rough surface regions present (Fig 5.37). The average hole density (Tab. 5.2) and AFM RMS roughness (7 - 29 nm) do not correlate with the growth parameter variation. The smoothest sample is grown on 0.88 μm - thick LT ZnO at 900 °C. The best *in-situ* annealed LT ZnO have comparable roughness, Fig. 5.23.

** ZnO grown at 1000 °C shows a poor morphology and will not be discussed further.

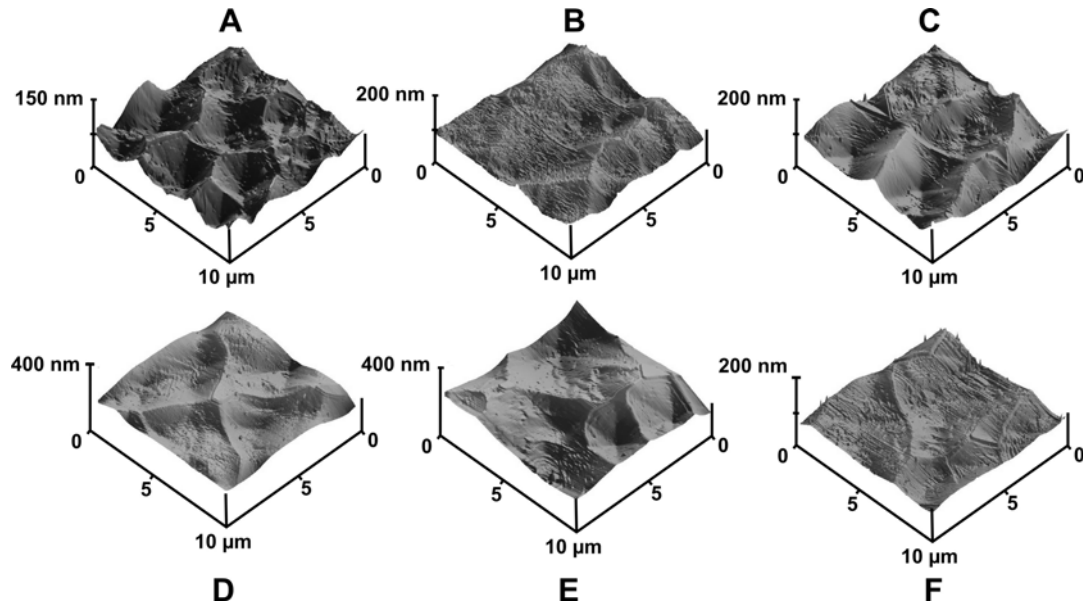


Fig. 5.37. AFM images of ZnO layers. A: 1.84 μm -thick ZnO layer grown at 850 $^{\circ}\text{C}$, B: 1.84 μm -thick ZnO layer grown at 900 $^{\circ}\text{C}$, C: 1.84 μm -thick ZnO layer grown at 950 $^{\circ}\text{C}$. D: 1.62 μm -thick ZnO layer grown at 900 $^{\circ}\text{C}$, E: 2.06 μm -thick ZnO layer grown at 900 $^{\circ}\text{C}$, F: 2.28 μm -thick ZnO layer grown at 900 $^{\circ}\text{C}$.

Secondly, XRD measurements demonstrate a significant improvement of the crystalline quality of HT ZnO after growth in the LT ZnO in comparison to the best single-grown HT ZnO, Table 5.1.* The (0002) ω -scan peak of the latter one has FWHM around 590'' (Chapter 5.1.5).

| $T_{\text{growth}}, ^{\circ}\text{C}$ | 850 | 900 | 950 |
|---------------------------------------|-------------------|-------------------|-------------------|
| Buffer thickness, μm | | | |
| 0.22 | | 1.4×10^5 | |
| 0.44 | 4.7×10^4 | 2.8×10^5 | 4.8×10^4 |
| 0.66 | | 2.3×10^4 | |
| 0.88 | | 1.9×10^5 | |

Tab. 5.2. Concentration of the holes in the surface of two-step grown ZnO (cm^{-2}), as calculated from 4.8×10^4 μm^2 area SEM scans.

* The ZnO domain tilting around the c -axis and twisting around the a -axis can be obtained from the FWHM of Θ - 2Θ -scans around the (0002) and (10 $\bar{1}$ 0) Bragg reflections, respectively. The inhomogeneity in the stress distribution, fluctuations of the lattice parameters and finite size effects along (0002) or (10 $\bar{1}$ 0) reflections can be obtained from FWHM of the ω -scans.

The growth orientation of two-step grown ZnO is [0001]. From the Table 5.3, the samples with the best structural quality are grown at 950 °C and 900 °C on the 0.44 μm – and 0.88 μm - thick LT ZnO, respectively. For the thicker one the total ZnO thickness adds up to 2.28 μm , and some cracks were observed in SEM. The cracking is caused by the stress relaxation, which is accumulating as the film grows thicker. Thus, although the growth on the thicker buffer offers good crystalline quality, it is limited by the cracking. For a more detailed evaluation reciprocal space maps of the best crack-free sample are plotted in Fig. 5.40. The ZnO grows fully relaxed on the GaN/sapphire template as visualized by the asymmetric $(20\bar{2}4)$ map (Fig. 5.38). The broadening of the XRD peaks is caused by the mosaicity of the layers. From the symmetric (0002) map, ZnO is of even higher crystalline quality than the underlying GaN (Fig. 5.38).

Table 5.3. FWHMs of different XRD measurements of ZnO versus growth temperature of the HT ZnO layer and the thickness of the LT ZnO.

| Growth temp. of the main ZnO layer (°C) | Thickness of ZnO buffer layer (μm) | FWHM (0002) ω -Scans (") | FWHM (0002) 2:1-Scans (") | FWHM $(10\bar{1}0)$ 2:1-Scans XTS (") | FWHM $(10\bar{1}0)$ ω -Scans GID (") | a-lattice parameter (nm) | c-lattice parameter (nm) |
|---|---|---------------------------------|---------------------------|---------------------------------------|---|--------------------------|--------------------------|
| 850 | 0.44 | 229 | 103 | 116 | 569 | 0,32525 | 0,52023 |
| 900 | 0.44 | 222 | 113 | 122 | 621 | 0,3253 | 0,52017 |
| 950 | 0.44 | 172 | 78 | 100 | 277 | 0,32552 | 0,5199 |
| 900 | 0.22 | 205 | 101 | 132 | 620 | 0,32538 | 0,519 |
| 900 | 0.66 | 218 | 109 | 159 | 650 | 0,32542 | 0,5203 |
| 900 | 0.88 | 164 | 74 | 103 | 336 | 0,32538 | 0,5199 |
| 950 | 0.88 | 186 | 88 | 113 | - | - | 0,5202 |

Thirdly, two-step grown ZnO layers emit highly intensive cathodoluminescence, which directly correlates with the ZnO structural properties. What is more, the bright CL emission characterized by a variety of sharp excitonic lines is observed for all samples. The spectra overall are dominated by an intense I_8 exciton emission and further bound exciton transitions, e.g., I_1 and I_0 , as well as the free exciton, and LO phonon replica are well resolved.

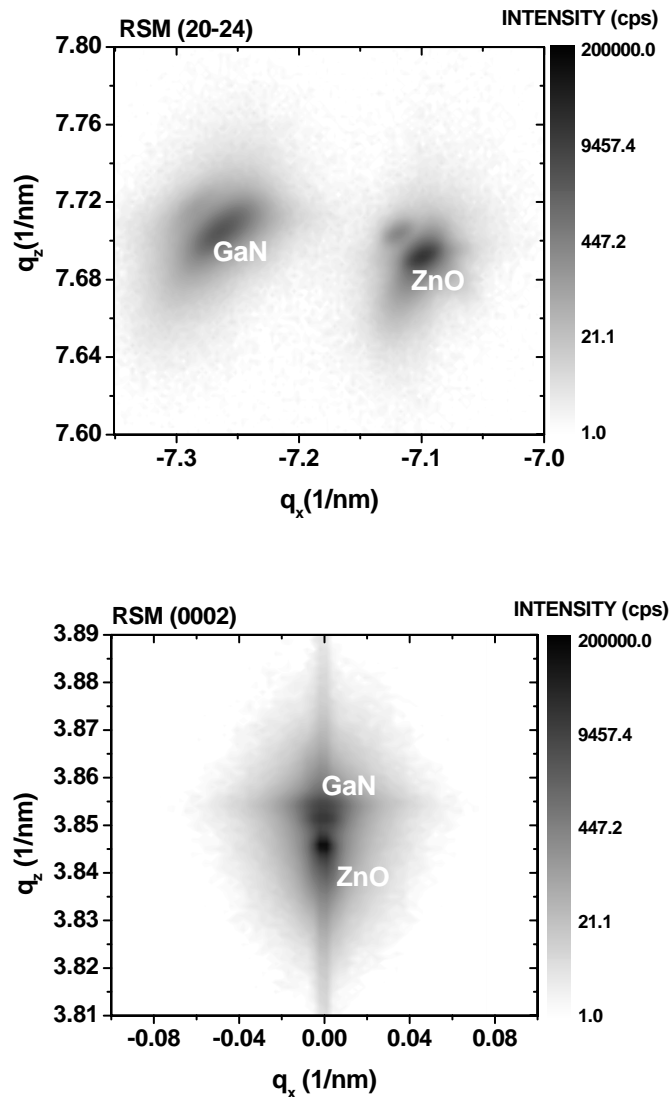


Fig. 5.38. X-ray diffraction reciprocal space maps around the asymmetrical $(20\bar{2}4)$, top, and symmetrical (0002) , bottom, Bragg reflection from 2.28 μm -thick ZnO grown on 1.5 μm thick GaN/ Al_2O_3 at 900 $^\circ\text{C}$.

Analogous to the crystalline, the optical properties of two-step grown ZnO are governed by LT ZnO thickness and HT ZnO growth temperature variation. For example, HT ZnO growth temperature influences the intensity of the luminescence (Fig. 5.39). The sample grown at 950 $^\circ\text{C}$ emits the brightest luminescence. The position of all CL peaks is not influenced by the growth temperature. In contrast, the line width strongly correlates with the growth temperature and systematically decreases from 3.2 meV (850 $^\circ\text{C}$) to 1.5 meV (950 $^\circ\text{C}$).

The FWHM of the luminescence peaks monotonically decreases from 2.6 to 1.5 meV with increasing LT ZnO thickness for a growth temperature of 900 $^\circ\text{C}$ (Fig. 5.40). For the layers grown at 950 $^\circ\text{C}$ on 0.44 - and 0.88 μm - thick LT ZnO, the same low values are obtained.

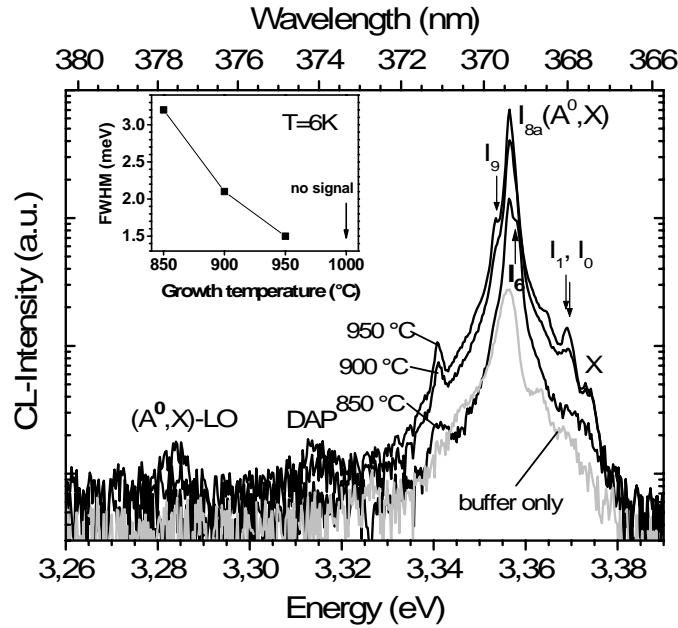


Fig. 5.39. Integral cathodoluminescence spectra taken at 5 K from the surface of ZnO grown at 850 °C, 900 °C, and 950 °C. The inset shows the FWHM of the dominant bound exciton line as a function of growth temperature.

From those observations, the highest quantum efficiency, narrowest emission lines, and highest lateral homogeneity are obtained for the two samples grown at 900 °C and 950 °C on 0.88 μm - and 0.44 μm - thick LT ZnO in perfect agreement with the X-ray data (Table 5.3).

The properties of the crack-free sample grown at 900 °C on 0.44 μm - thick will be discussed here for more detailed study (Fig. 5.41). In cross section CL scan, the weak and broad GaN emission (FWHM = 10 meV) is slightly red shifted at $\lambda = 357.4 \text{ nm}$ (3.468 eV) compared to the relaxed GaN evidencing small tensile stress.* The LT ZnO luminescence is governed by a weak and unstructured broad luminescence band (FWHM = 11 meV) indicating a high defect density and strong impurity incorporation. Starting at around 369.2 nm (3.357 eV) at the LT-ZnO/GaN interface, a strong red shift accompanied by a further broadening of the ZnO luminescence occurs with advancing growth. This red shift reaches its maximum (6 meV) at the LT/HT ZnO homointerface. The red shift of the ZnO emission may be explained by strong local impurity incorporation and/or local internal electrical fields (Franz-Keldysh effect) in the vicinity of the homointerface. A complete relaxation of this red shift is achieved within the first micrometer of the HT-ZnO layer accompanied by a dramatic line narrowing. The final sharp excitonic line I_8 (FWHM < 2 meV) can be clearly observed up to the sample surface

* Without the ZnO on top, the GaN would be compressively strained on sapphire.

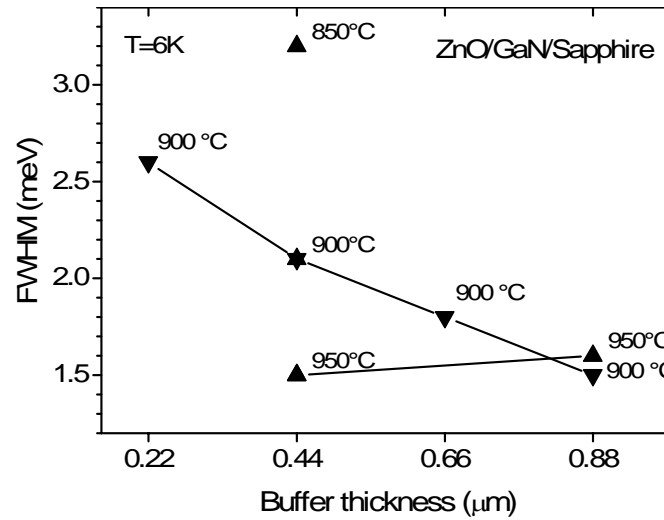


Fig. 5.40. Line width of ZnO emission lines as a function of low-temperature buffer layer thickness and growth temperature. The line width decreases with increasing growth temperature and with increasing layer thickness of the ZnO buffer.

(at $2.7 \mu\text{m}$) at $\lambda = 369.1 \text{ nm}$ (3.358 eV) and no further energy shift is observed. However, at the HT ZnO surface, an abrupt minor red shift by 0.2 nm (i.e. 2 meV) occurs.

This indicates a residual minor tensile strain of the ZnO layers, as the sample cross section is partially relaxed with respect to the layer's surface. The bound exciton line I_8 is related to Ga incorporation [Mey04], which could be incorporated from the under laying GaN template.

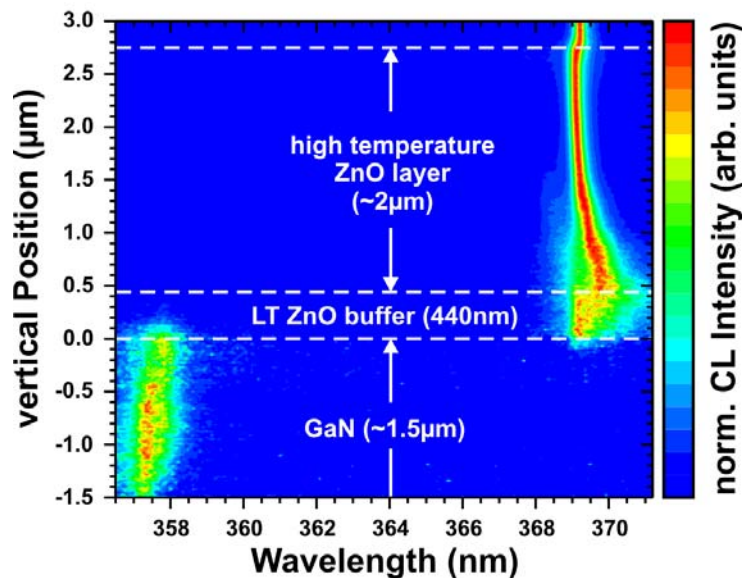


Fig. 5.41. Cross-sectional normalized CL spectrum linescan in growth direction (c-axis) directly visualizing the layer sequence of the two-step grown ZnO sample. The sample consists of a GaN layer on sapphire followed by a $0.44 \mu\text{m}$ thick low temperature ZnO buffer (LT ZnO) and the final $2.3 \mu\text{m}$ thick HT-ZnO layer.

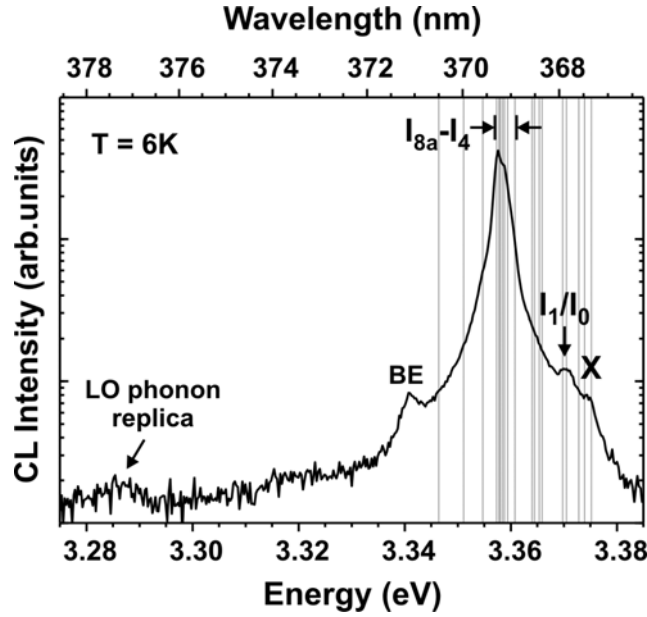


Fig. 5.42. Integral CL spectrum: the position of the free excitons X (around 3.377 eV), and donor bound excitons (D^0, X), i.e. $I_1 - I_{11}$ (3.372 – 3.348 eV) are marked by vertical lines (corrected by 2 meV red shift). An additional bound exciton (BE) as well as the LO phonon replica of I_8 are visible as well.

A spatially averaged CL spectrum recorded from this sample is plotted in Fig. 5.42 again. The averaged spectrum is dominated by the impurity bound exciton I_8 ($\lambda = 369.3$ nm, i.e. $E = 3.356$ eV, $\text{FWHM} < 3$ meV), in perfect agreement with the cross sectional CL data from the upper portion of the HT ZnO, depicted in Fig. 5.42. The free exciton X_A (3.374 eV), the bound excitons I_0, I_1 (3.370 eV), a bound exciton line labeled with BE at 3.341 eV (identified as structural defect [Mey04]) as well as the LO phonon replica from I_8 ($E = E(I_8) - 72$ meV) are visible (Fig. 5.42). All lines are 2 meV red shifted with respect to their fully relaxed position from Presser *et al.* [Pre88], evidencing the residual small tensile strain of the ZnO in perfect agreement with the cross sectional data above.

A scanning electron microscope (SEM) image is depicted in Fig. 5.43a. A clear correlation between the bound exciton complexes and the surface morphology is evident and directly imaged by CL microscopy. A CL wavelength image (CLWI) of I_8 , i.e., a mapping of the local wavelength peak position of I_8 is color coded in Fig. 5.43b. The local peak wavelength of I_8 changes with the position in the CL wavelength image (see Fig. 5.43b) and the wavelength contrast reproduces the shape of the hexagonal domains at the surface. The cathodoluminescence from the edges, which represent morphological boundaries, are blue shifted with respect to the center of domains ($\Delta E_{\text{max}} = 0.6$ meV). The single hexagonal columns coalesce at

the edges to a closed film during growth. Because of small disorientations of the columns (known from XRD) compressive stress is locally accumulated and leads to a weak blue shift

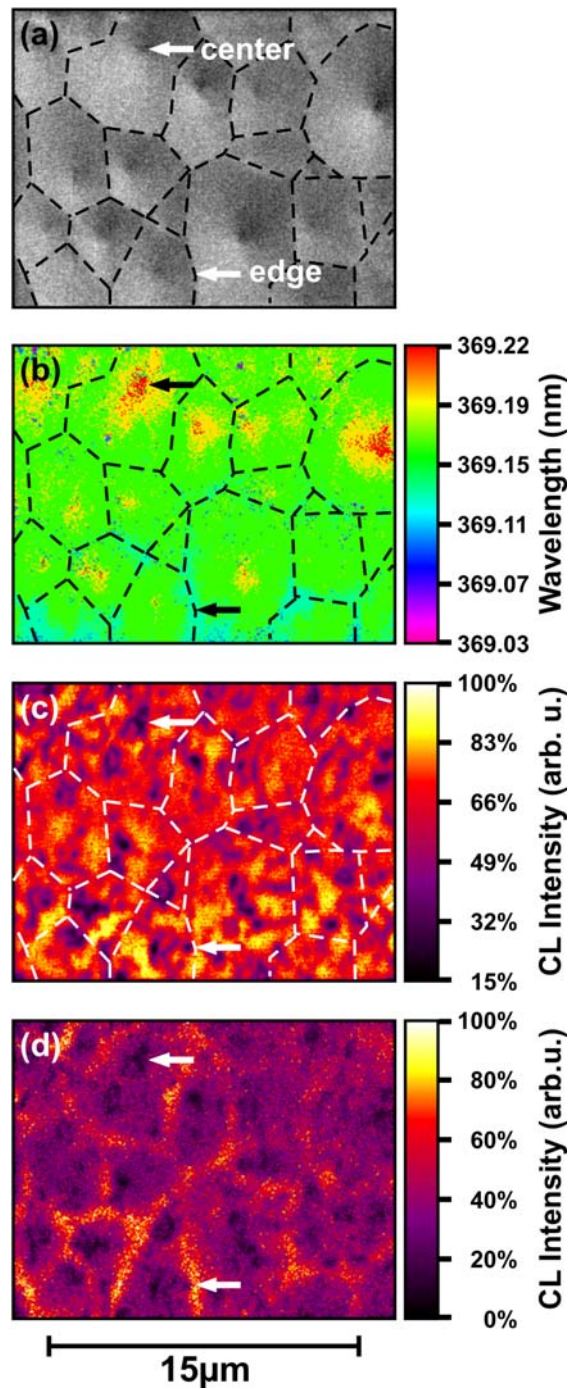


Fig. 5.43. Correlation of morphology and optical properties: (a) SEM plan view image, (b) mapping of the local peak wavelength of I_8 , and monochromatic images of the spectral region of I_8 (c) and I_0/I_1 (d).

of luminescence at the edges. In contrast, a significant red shift of I_8 is observed when reaching the pit at the very center of each domain. Nevertheless, the monochromatic intensity image of I_8 (Fig. 5.43c) visualizing the local quantum efficiency for I_8 is very homogeneous and barely correlates with the morphology. Exclusively at the very center of the domains, a drop

in the I_8 intensity by roughly one order of magnitude (note that the linear intensity scale of Fig. 5.43c ranges from 100% down to 15%) occurs. Here we find a gathering of nonradiative recombination centers, which are most likely caused by screw dislocations or bundles of them running in *c*-direction in the center of the hexagonal columns. In complete contrast, the monochromatic image of I_0/I_1 (Fig. 5.43d) is strongly modulated and perfectly correlates with the domain network. Significant I_0/I_1 luminescence is only observed at the domain boundaries. Local CL spectra recorded there show a pronounced I_0/I_1 emission, whereas inside of the domains no intensity is found in this spectral region. The luminescence of the bound excitons I_0/I_1 originates exclusively from domain borders directly evidencing a preferential accumulation of the impurities and/or defects responsible for I_0/I_1 at the domain boundaries.

In conclusion, the combination of LT ZnO growth using *t*BuOH with HT ZnO growth using N_2O has improved the surface morphology, crystalline and optical properties of ZnO in comparison to the best single-grown LT or HT ZnO. Very smooth layers with low surface defect concentration, narrow FWHM of intense XRD and CL peaks were synthesized. The best ZnO layers have remarkably higher crystalline quality than the underlying GaN. The LT ZnO thickness and HT ZnO growth temperature variation influences its crystalline and optical properties, which are in agreement with each other.

The use of different O-precursors, carrier gases and the temperature processing steps in one growth run broadens the space for further improvement of ZnO properties. Firstly, as it is discussed in Chapter 5.1.4, the *in-situ* annealing of LT ZnO is accompanied by the surface smoothing processes and improved its optical properties. To study this effect in LT-HT ZnO layer stack, the influence of intermediate *in-situ* annealing on the properties of two-step ZnO is discussed in the Chapter 5.2.2. Secondly, VI-II ratio in MOVPE of compound semiconductors has strong effect on the surface, optical, electrical, and structural qualities of the growing film. The study the influence of VI-II ratio on the properties of two-step grown ZnO is discussed in Chapter 5.2.3.

5.2.2 *In-situ* Annealing

On the one side, two-step growth offers flexible growth processing of ZnO. As a result of its implementation, the quality of ZnO layers is improved (Chapter 5.2.1). On the other side, the study of single LT-ZnO layer annealing has brought interesting results (Chapter 5.1.4). In particular, Ostwald ripening is observed, which leads to best LT-grown ZnO quality after the 4-min annealing. To further study and improve the two-step grown ZnO properties, an intermediate *in-situ* annealing of the LT ZnO is performed. To monitor the impact of the LT ZnO annealing, several non-annealed reference samples with different LT ZnO thicknesses (0.22 - 0.88 μm) were grown in those experiments (Tab. 5.4).

| T_{growth} , °C | Non-annealed 900 | Annealed 900 |
|---------------------------------|------------------|--------------|
| Buffer thickness, μm | | |
| 0.22 | * | * |
| 0.44 | * | * |
| 0.88 | * | * |

Tab. 5.4. Variation of the two-step growth conditions with and without *in-situ* annealing.

Direct information on the effect of the LT ZnO buffer layer annealing on the surface morphology of ZnO layer is achieved from SEM measurements, Fig. 5.44. The surface of the reference sample has larger inverted hexagonal pyramids in comparison to the annealed one. This has no influence on the surface roughness, however. AFM measurements reveal that both samples have rms surface roughness of ~ 2.5 nm. Thus, *in-situ* annealing of LT ZnO has no significant influence on the surface morphology of two-step grown ZnO.

The crystalline properties of the ZnO films are not strongly influenced by annealing and LT ZnO thickness variation too. This can be assessed from FWHM, and *a*- and *c*-lattice parameters plotted in Figs. 5.45 - 5.46, respectively.

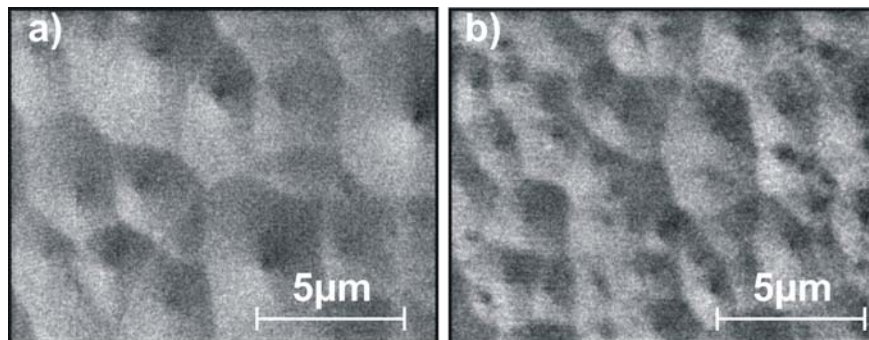


Fig. 5.44. SEM images of two ZnO layers with a) not annealed, and b) annealed LT ZnO buffer layer. The thickness of the LT ZnO buffer layer in both cases is 0.22 μm .

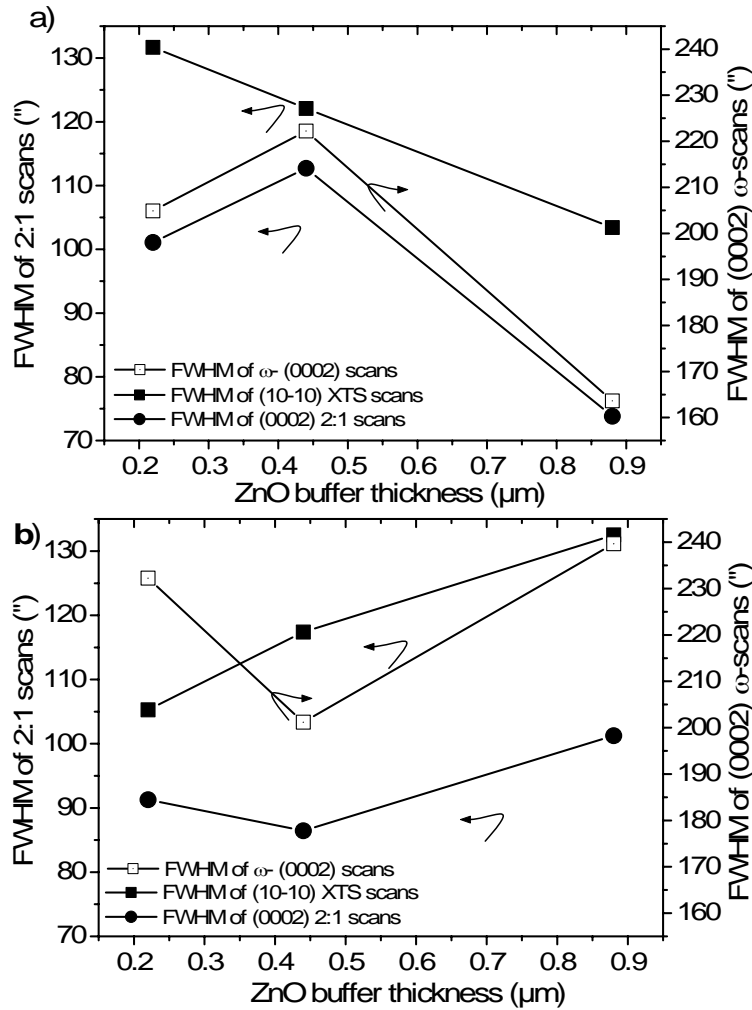


Fig. 5.45. FWHM of 2:1- and ω -scans of XRD measurements in the different geometries of the a) non-annealed, and b) annealed ZnO versus LT ZnO thickness.

Probably due to the small difference between those values (a - and c -lattice parameters are changing in the range $\pm 2 \times 10^{-4}$ nm, for example) there is no direct correlation observable between them. FWHM values for annealed and non-annealed layers show opposite behavior with a LT ZnO thickness increase. Similar effect is observed for a -lattice parameters of annealed and non-annealed layers, Fig. 5.46. Both annealed and non-annealed samples are tensile stressed.

In contrast to those observations, *in-situ* annealing has a pronounced effect on the luminescence properties of two-step grown ZnO. Firstly, cross section is discussed (Fig. 5.47). An annealing of the LT buffer layer changes the properties of the underlying GaN layer. High-intensity narrow GaN luminescence peaks observed around 359 nm from the non-annealed sample (Fig. 5.47, left), are dimmed and broadened after annealing (Fig. 5.47, right).

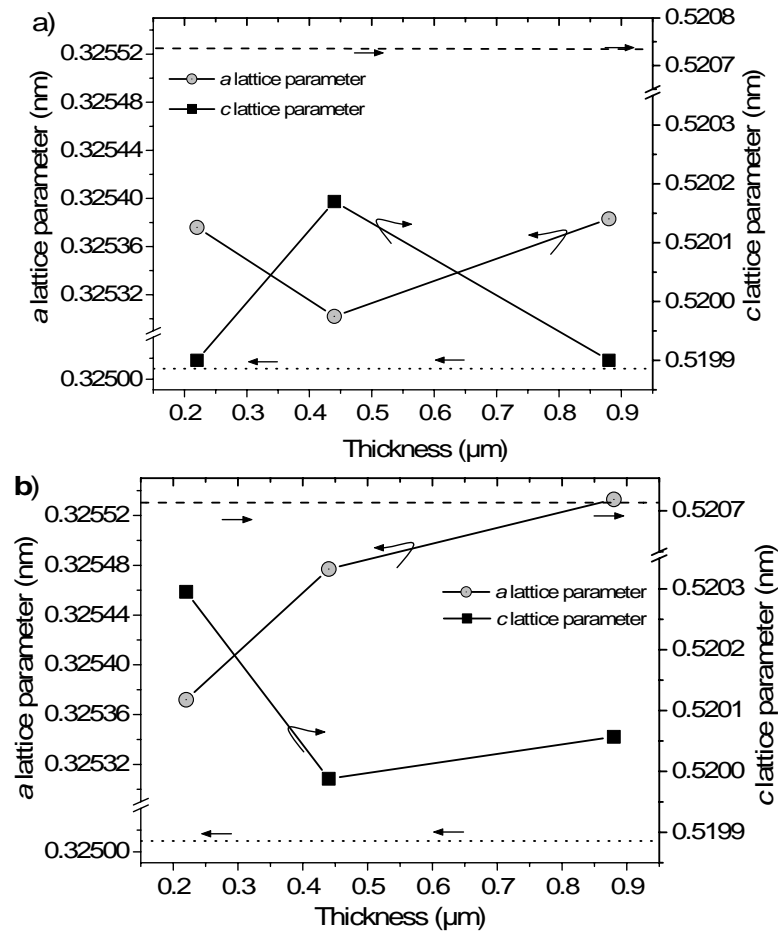


Fig. 5.46. Lattice parameters of the a) non-annealed, and b) annealed ZnO versus LT ZnO thickness. Dashed and dotted lines show relaxed values of ZnO lattice parameters [Lan99].

The degradation of GaN optical properties can be caused by the thermally activated diffusion of Zn into GaN layer.* In contrast to that, the optical quality of the annealed LT ZnO buffer layer prevails that of non-annealed, Fig. 5.47. The luminescence intensity of the LT annealed buffer layer is about one order of magnitude higher compared to that of the non-annealed layer, which is in agreement with the results in Chapter 5.1.4. Further on, LT ZnO annealing leads to an abrupt transition between the LT and HT layers, which is not the case for the non-annealed one (Fig. 5.48). As the HT growth proceeds, the luminescence line width narrows in annealed sample, while it broadens for not annealed one (Fig. 5.48). CLWI surface scans confirm this observation (Fig. 5.49). Besides, in contrast to annealed sample, the correlation of the lateral luminescence intensity distribution with SEM surface morphology is observed for the sample grown without *in-situ* annealing (Fig. 5.49). For the annealed sample, the lateral distribution of the luminescence is homogeneous, although pyramidal domains persist after annealing (only their lateral dimension is slightly changed, Fig. 5.47).

* Zinc has high diffusion coefficient in GaN.

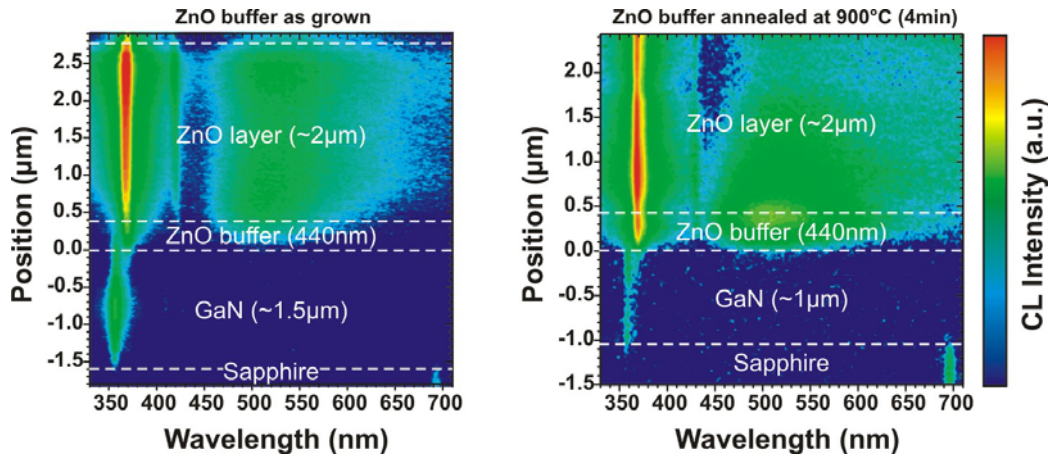


Fig. 5.47. Cross section CLWI image of two-step grown ZnO layer without LT ZnO annealing (left), and two-step grown ZnO layer with LT ZnO annealing (right).

On the one side, this can be explained by the defect delocalization. In other words, LT ZnO annealing leads to optical homogeneity of ZnO surface. On the other side, defects can still be localized but not emit light anymore.

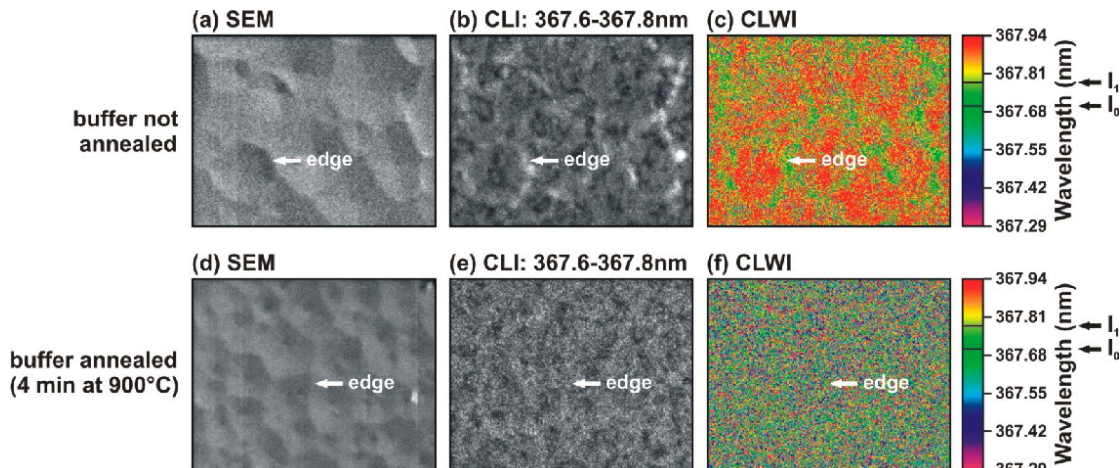


Fig. 5.48. (a), (d) SEM images; (b), (d) CL intensity images; (c), (f) CL wavelength intensity images of two ZnO layers with non annealed (above) and annealed (below) LT ZnO layer.

These speculations can be proved by plotting the integrated CL spectrum measured from the surface of the samples at 5 K (Fig. 5.50). The quantum efficiency of the luminescence emitted from the surface of the annealed samples is one order of magnitude smaller than that of the non annealed sample. It demonstrates that together with lateral homogeneity of luminescence lateral distribution, annealing it lowers overall intensity. Thus, annealing does not redistribute the surface defects, but rather optically deactivate them.

TEM measurements of the annealed sample, performed and analyzed in the group of Prof. Gerthsen, reveal a reduction of the threading dislocation density in two step grown ZnO layer (Fig. 5.51).

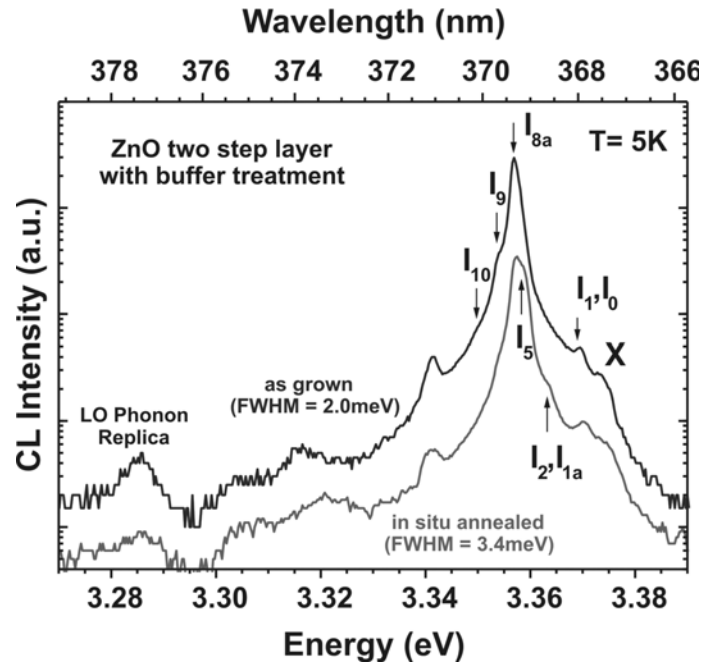


Fig. 5.49. Integrated CL spectra from the surface of ZnO layers grown with and without *in-situ* annealing of the LT ZnO layer.

The threading dislocation density reduction decreases due to their annihilation at the ZnO/GaN interface. The dislocation lines in the ZnO deviate frequently from the [0001] direction indicating a low degree of mosaicity, which is supported by the homogeneous contrast of the ZnO layer, and correlates with FWHM values of XRD measurements. According to Mueller *et al.*, the extinction of the dislocation contrast in Fig. 5.51 shows that

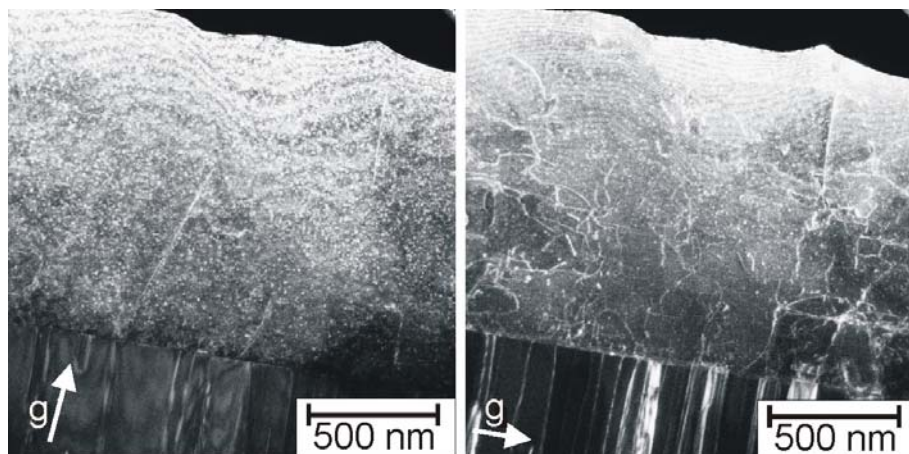


Fig. 5.50. Cross-section weak-beam images of the same area of a MOPVE-grown ZnO layer on $\text{Al}_2\text{O}_3(0001)$ with a thick GaN buffer layer taken with (a) $g = \{0002\}$ and (b) $g = (11\bar{2}0)$ taken under $g, 3g$ conditions. TEM images after [Mue04].

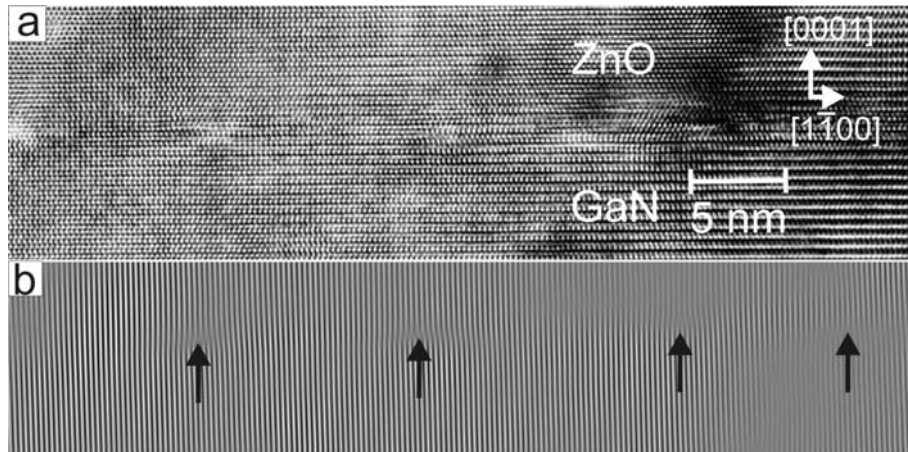


Fig. 5.51. (a) HRTEM image of the interface between the GaN buffer layer and ZnO along the $\langle 11\bar{2}0 \rangle$ -zone axis and (b) Fourier-filtered image showing only $\{1\bar{1}00\}$ lattice fringes. The arrows indicate $\{1\bar{1}00\}$ fringes inserted from the substrate side. TEM image is taken from [Mue04].

the majority of the dislocations is characterized by Burgers vectors of the type $\mathbf{b}_a = 1/3\langle 11\bar{2}0 \rangle$ [Mue04]. The line directions of threading dislocations extend typically along the $[0001]$ growth direction yielding a high fraction of edge dislocations. The domination of threading dislocations with \mathbf{b}_a can be understood by analyzing the misfit dislocations in a $\langle 11\bar{2}0 \rangle$ zone-axis high-resolution TEM (HRTEM) image of the GaN-ZnO interface (Fig. 5.55(a)). According to Mueller *et al.*, the $\{1\bar{1}00\}$ Fourier-filtered image Fig. 5.51 (b) shows that the misfit dislocations are characterized by one $\{1\bar{1}00\}$ plane inserted from below as expected due to the larger lattice parameter of the ZnO [Mue04]. Fig. 5.52 shows schematically the misfit dislocation orientation and possible Burgers vectors (grey vectors), as achieved by Mueller *et al.*, [Mue04]. The electron-beam direction and dislocation lines are aligned parallel to the $[11\bar{2}0]$ direction. 60° or 120° misfit dislocations are characterized by $\mathbf{b}_a = 1/3[\bar{1}2\bar{1}0]$ and $1/3[\bar{2}110]$. The edge component $\mathbf{b}_e = 1/2[1\bar{1}00]$ is compatible with an inserted $(1\bar{1}00)$ plane as observed in Fig. 5.51 (b). Mueller *et al.* assumes, that three set of misfit dislocations along the three $\langle 11\bar{2}0 \rangle$ directions are present in the (0001) interface plane. The misfit dislocations with \mathbf{b}_a are generated to relax the lattice-parameter mismatch. Dislocations with \mathbf{b}_a are most efficient because they are characterized by the longest Burgers vector edge component in the (0001) interface plane among all possible dislocation Burgers vectors. In addition, the strain energy of dislocations is $\sim \mathbf{b}_2$ which favors the formation of dislocations with the shortest overall Burgers vector \mathbf{b}_a . Since dislocations cannot end inside a perfect crystal and the Burgers vector is conserved along the dislocation line, the threading segments

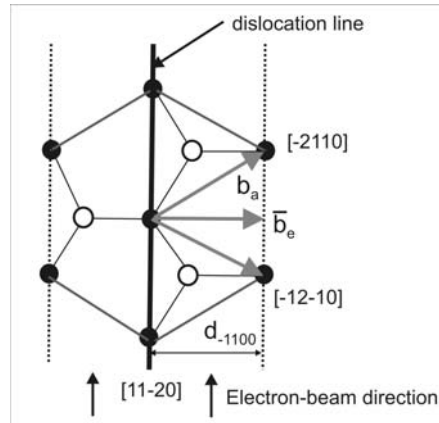


Fig. 5.52. Schematic representation of the orientation of a misfit dislocation (bold black line) and possible Burgers vectors (grey vectors) in the (0001) interface plane. Picture and model after [Mue04].

of misfit dislocations are also characterized by \mathbf{b}_a as observed in Fig. 5.51.

In conclusion, *in-situ* annealing of LT ZnO layer in two-step grown ZnO does not lead to a drastic changes of the surface morphology and crystalline properties. However, it changes the optical properties of all layers in GaN\LT ZnO\HT ZnO stack. In particular, annealing lowers the luminescence intensity from the ZnO surface. TEM studies of annealed ZnO revealed its high structural quality, which correlates with the results of X-ray diffraction and cathodoluminescence measurements. High morphological, structural and optical quality of ZnO layers grown using two-step growth with *in-situ* annealing has opened prospect for doping experiments which described and discussed in Chapters 6.3.1 (doping using ammonia).

5.2.3. DMZn Flow Variation

VI-II ratio variation influences the surface, optical, electrical, and structural qualities [Ko02, Kat03, Set04].* In this work, a decrease of VI-II ratio in experiments with i-PrOH lead to the decrease of the hexagon size on the ZnO surface and the roughening of the top facets (Chapter 5.1.1). To study the influence of VI-II ratio on the properties of two-step grown ZnO, DMZn flows and some other growth parameters were varied as shown in Tab. 5.5.

The use of small amounts of DMZn typically leads to stable oscillations of reflected light intensity and a low growth rate, Fig. 5.53, a). An increase of DMZn flow leads to a lowering of the overall reflected intensity as growth proceeds, which can indicate the roughening of the surface on the latest stages of growth, Fig. 5.53, b). ZnO grown with 2.2 - 3.3 mmol/min at 900 °C - 1000 °C is peeled off after ~20 min of HT growth, as observed in *in-situ* reflectometry measurement. The growth rate is proportional to the DMZn flow, which indicates O-rich condition, Fig. 5.54. Supporting those observations, Nomarski microscopy has shown that higher DMZn flows result in rougher surfaces and higher amounts of surface

| DMZn, mmol/min T _{growth} , °C | 0.55 | 1.1 | 2.2 | 3.3 |
|--|------|-----|-------|-----|
| 850 | * | | + | |
| 900 | * | * | # * + | * |
| 1000 | | | + | |

Tab. 5.5. The variation of DMZn flow, LT ZnO thickness, and HT growth temperature. +: 0.22 μm-thick ZnO buffer, *: 0.44 μm-thick ZnO buffer, ±: 0.66 μm-thick ZnO buffer, #: 0.88 μm-thick ZnO buffer. Gray signs indicate peeled off ZnO layer. The total reactor and N₂O flows were constant.

defects such as inverted hexagonal holes and pits (Fig. 5.55). Hole-free areas of the smoothest sample show extremely low AFM roughness of about 0.5 nm, Fig. 5.58. No inversion of the hexagonal holes and inverted pyramids into hillocks and pyramids was observed via AFM measurements. From those observations, high VI-II ratio leads to more stable growth of smooth ZnO. This effect was also observed when II/VI ratio was varied (from O-rich, stoichiometric, and to Zn-rich flow conditions) in experiments with ZnO growth using plasma-assisted molecular beam epitaxy [Ko02]. The smallest RMS roughness reported in the work of Ko *et al.* is 0.8 nm [Ko02].

* This effect was observed for compound semiconductors in general. For example, it has been reported that the Ga/N ratio influences the surface morphology and optical properties of GaN films [Tar97] and the dislocation generation [Hey00].

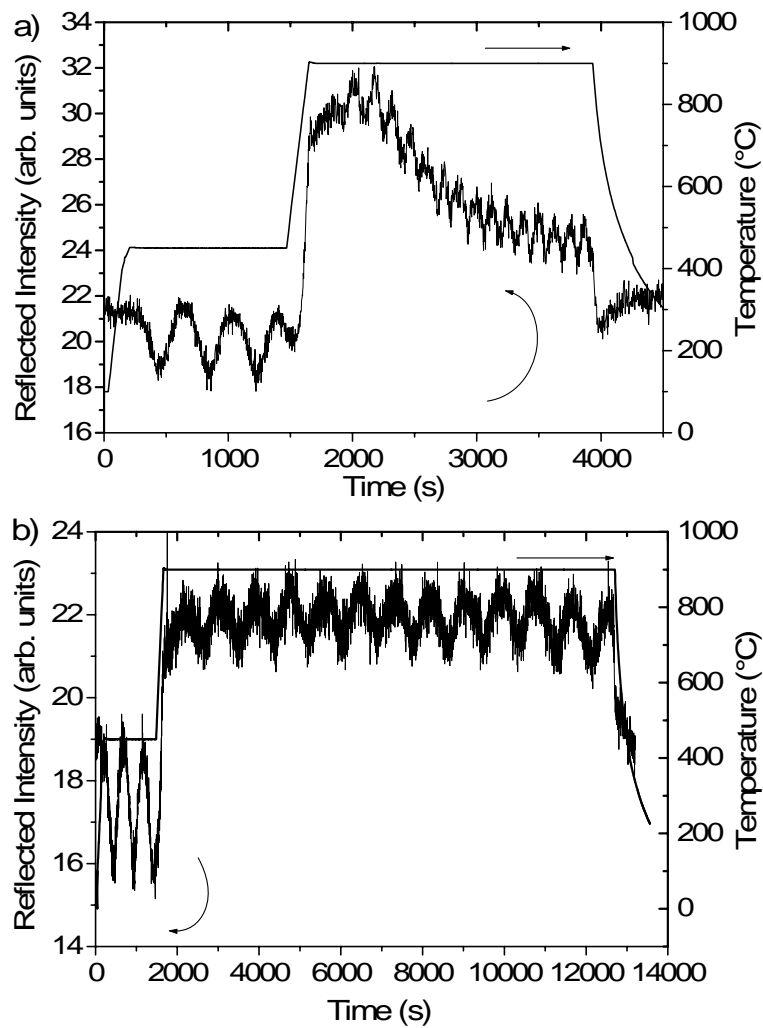


Fig. 5.53. *In-situ* reflectometry measurements of ZnO growth. DMZn flow: a) 3.3 mmol/min, b) 0.55 mol/min. HT-step growth temperature is 850 °C.

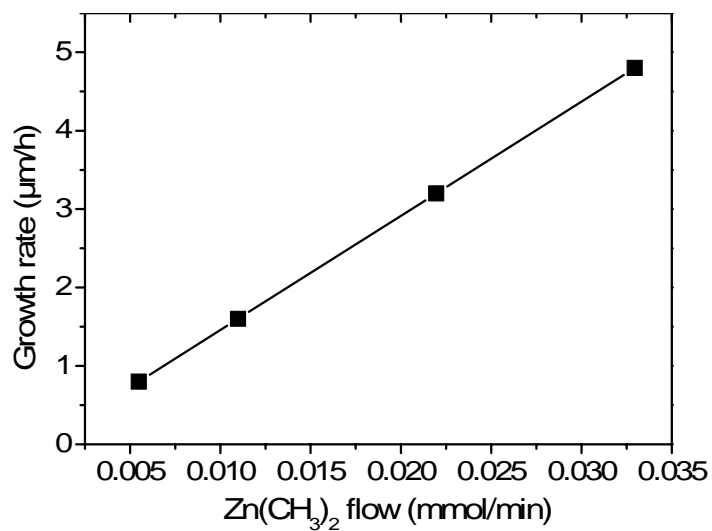


Fig. 5.54. ZnO growth rate versus DMZn flow determined from in-situ reflectometry measurement.

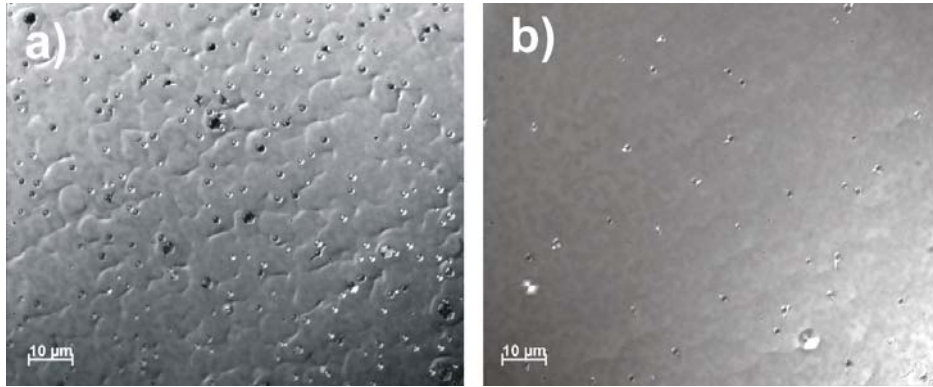


Fig. 5.55. Nomarski microscope images of ZnO samples grown with different amounts of DMZn.

DMZn flow: a) 3.3 mmol/min, b) 0.55 mmol/min.

XRD measurements reveal no direct correlation with the growth conditions (Figs. 5.57 - 5.58). FWHM values of 2:1-scans are small, and vary in relatively narrow range, from $\sim 90''$ to $\sim 130''$. The variation of the both lattice parameters from sample to sample is about 10^{-4} Å.

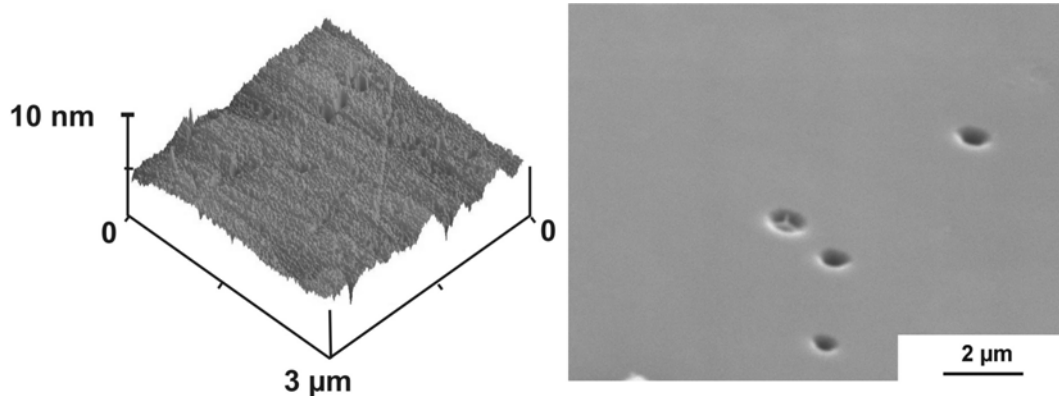


Fig. 5.56. AFM (left) and SEM (right) images of ZnO layer grown at 850 °C with 0.55 mmol/min of DMZn.

Low-temperature (4.5 K) photoluminescence from the surface of this sample is shown on Fig. 5.59. Near band edge spectral region exhibits manifold excitonic features with a narrow width of dominant high-intensity I_8 excitonic emission of 1.3 meV. The sample shows a two electron satellite (TES) recombination line, green luminescence (not shown here) and DAP band. The DAP band is strongly pronounced with well resolved LO phonon replicas.

In conclusion, high VI-II ratio leads to a stable growth of smooth ZnO with high-intensity narrow-peak excitonic emission of photoluminescence. High morphological, structural and optical quality of ZnO layers grown using two-step growth procedure with 0.55 mmol/min and 1.1 mmol/min flow of DMZn using *in-situ* annealing of low-temperature ZnO buffer layer has opened prospect for doping experiments which described and discussed in Chapters 6.1 (NO doping) and 6.4.1 (UDMH_y doping).

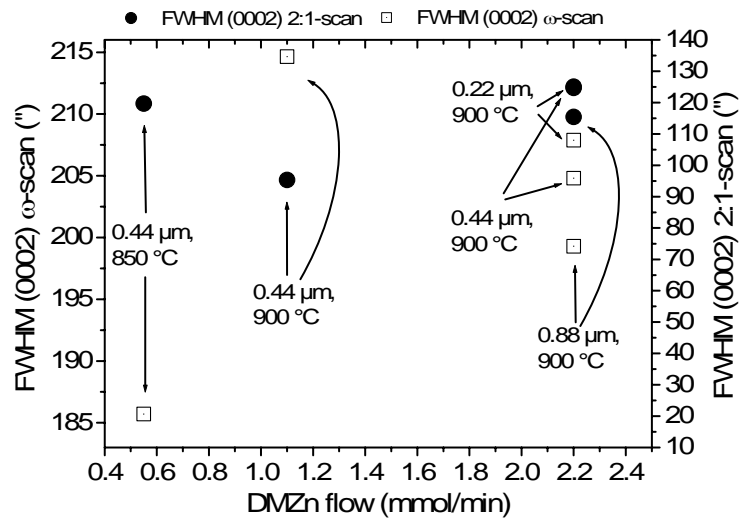


Fig. 5.57. FWHM of XRD 2:1- and ω -scans of ZnO (0002) reflection versus DMZn flow.

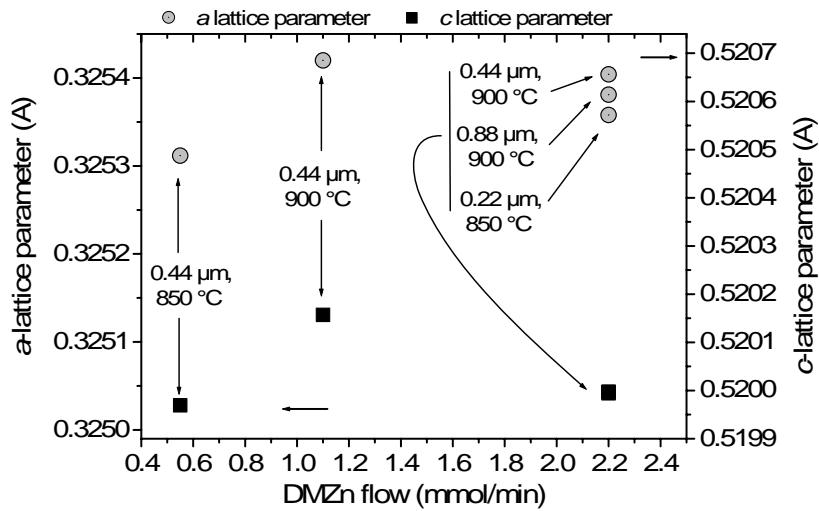


Fig. 5.58. *a*- and *c*-lattice parameters obtained from XRD measurements of two-step ZnO layers grown at different temperatures and with different LT ZnO layer thicknesses versus DMZn flows.

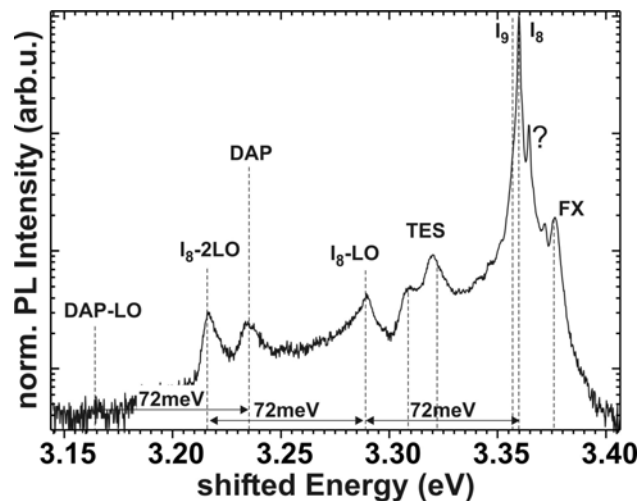


Fig. 5.59. Photoluminescence spectrum of ZnO layer grown at 850 °C with 0.55 mmol/min of DMZn.

5.3. Three-step Growth

The two-step ZnO growth offers advantages for further improvement of ZnO properties due to the use of different O-precursors, carrier gases and the temperature processing steps in one growth run. On the one side, the combination of this method with *in-situ* annealing of LT ZnO buffer layer and the reduction of DMZn flow results in high-quality HT ZnO (Chapters 5.2.2 and 5.2.3). On the other side, the use of NO precursor on the HT growth step results in even smoother ZnO layers with high optical and crystalline quality (Chapter 6.1). Therefore, a sequent arrangement of these processing steps can further improve the quality of ZnO films.

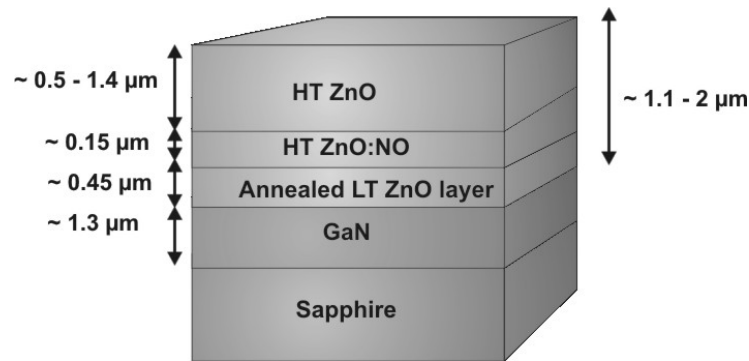


Fig. 5.60. Three-layer ZnO stack in three-step growth. The second step begins with a growth of a seed HT ZnO layer using N_2O and DMZn (5 min). Subsequently, the ZnO layer is grown (30 min), using a mixture of NO, N_2O and DMZn precursors. The flow rate of NO was 1.1 mmol/min. Then follows the third HT step without NO precursor. In the second and third step, DMZn flow is 0.55 mmol/min.

The growth time was proportionally increased to achieve the same to the described in Chapter 5.2.2.

In three-step growth, NO is switched on into the reactor after the growth and *in-situ* annealing of LT ZnO layer (Fig. 5.60). Subsequently, the third step followed at growth temperatures of 850 or 900 °C using N_2O and DMZn.

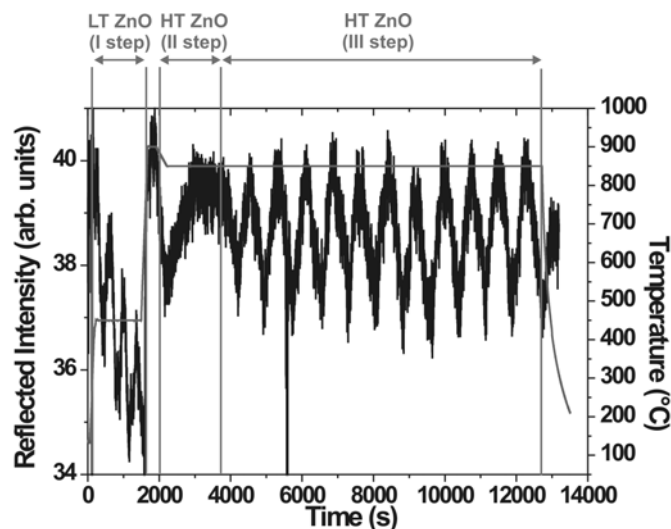


Fig. 5.61. *In-situ* reflectometry measurements of three-step growth.

NO-grown ZnO film has very small thickness, only a quarter of the reflected intensity oscillation was observed after 30 min of growth (Fig. 5.61). The growth rate, determined from *in-situ* reflectometry measurements, was 0.4 $\mu\text{m}/\text{hour}$. Due to the switching off the NO precursor, the growth rate on the third step is 1.5 $\mu\text{m}/\text{h}$ higher than on the second. Very stable oscillations were observed during the third step of growth without NO precursor (Fig. 5.61).

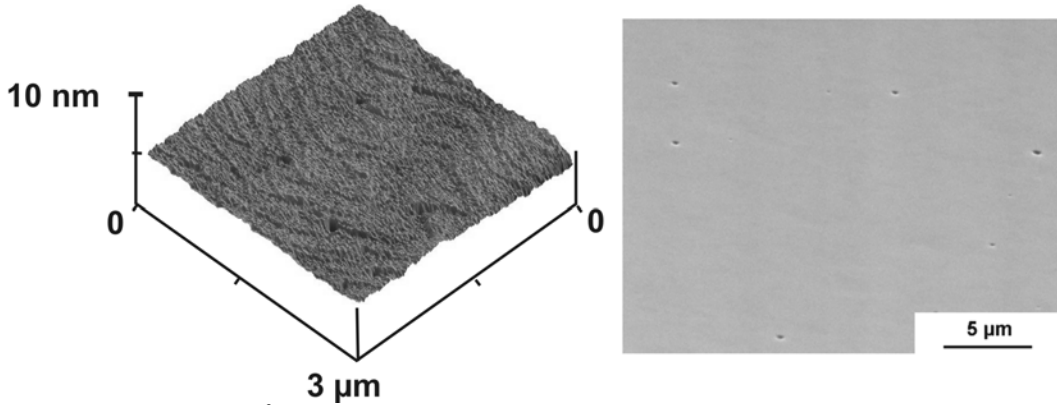


Fig. 5.62. AFM $3 \times 3 \mu\text{m}^2$ (left) and SEM (right) images of three-step grown ZnO.

Fig. 5.62 depicts the surface of three-step grown ZnO layer. The AFM rms roughness of this sample is 0.2 nm. Few inverted pits and holes on the surface of the layer are observable in SEM image (Fig. 5.62). These samples are smoother (AFM roughness 0.2 nm) and contain smaller amount of holes as compared to the samples grown under similar growth conditions but without addition of NO into MOVPE reactor (AFM roughness 0.5 nm, chapter 5.2.3).

High-resolution $(10\bar{1}0)$ and (0002) θ - 2θ scans, and (0002) ω -scans were employed in order to obtain information on the crystalline properties of the films. Lattice parameters of the films have not shown large difference upon increase the growth temperature from 850 to 900

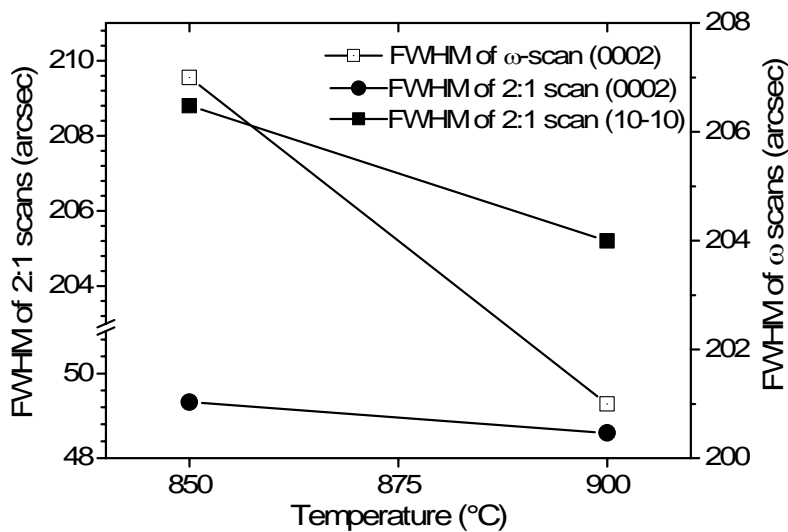


Fig. 5.63. FWHM values obtained from XRD θ - 2θ scans in $(10\bar{1}0)$ and (0002) geometries (left axis) and ω -scans in (0002) geometry (right axis) versus growth temperature.

°C (a lattice parameter - 0.3257 nm, and c -lattice parameter – 0.52014 nm). Similar situation is observed for the FWHM values (Fig. 5.63). For comparison, ZnO samples, two-step grown under similar conditions have slightly smaller lattice parameters (a lattice parameter - 0.32531 nm, and c -lattice parameter – 0.51997 nm). FWHM values are slightly higher compared to the FWHM of the ZnO layers grown using two-step growth method without addition of NO into MOVPE reactor (Chapter 5.2.3). Thus, in comparison to two-step grown ZnO, three-step growth improves the surface morphology of ZnO films with a slight degradation of its crystalline properties.

NO precursor contains a single nitrogen atom and can serve as a nitrogen precursor for ZnO doping (Chapter 6.1). To study the influence of NO on the electrical properties of three-step grown ZnO, RTA in combination with capacitance-voltage measurements were performed (Fig. 5.64). The carrier concentration of the not annealed ZnO layers grown at 850 °C and 900 °C has a value of around 10^{17} cm⁻³. For comparison, the carrier concentration of annealed and non-annealed two-step ZnO grown with and without NO, is lower by one order of magnitude. In contrast to that, RTA at 850 °C of three-step grown ZnO results in a decrease of the carrier concentration to 10^{16} cm⁻³. RTA at 900 °C leads to an increase of carrier concentration of 850 °C – grown ZnO to 10^{18} cm⁻³ (Fig. 5.64), and destroys the 900 °C – grown layer. RTA at 1000 °C destroys both 850 - and 900 °C – grown ZnO.

Since “NO-doping” of ZnO did not contribute to the carrier concentration of the undoped two-step grown film (Fig. 6.6, Chapter 6.1), and “NO-doped” layer in three-step grown ZnO is thin (~0.2 μm, Fig. 5.61), the observed variation of the carrier concentration after RTA

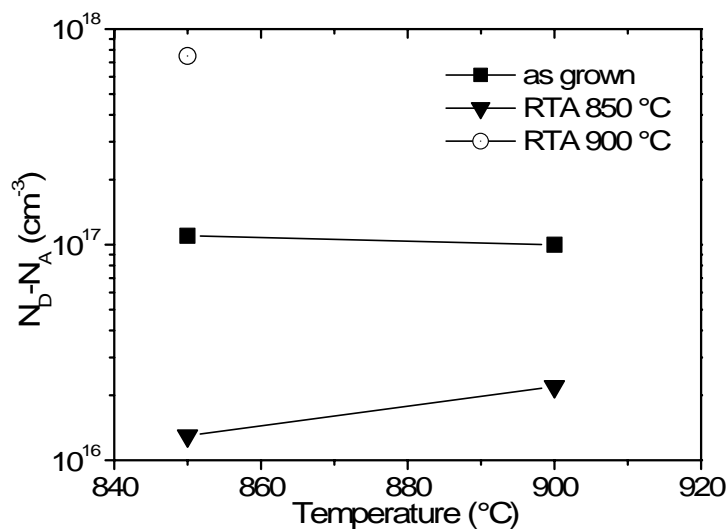


Fig. 5.64. Carrier concentration of as-grown and annealed undoped three-step grown ZnO layers versus growth temperature.

of three-step grown ZnO can not be attributed to nitrogen doping. Probably, interface between first and third step induced structural defects in ZnO film, which are responsible for this effect. This conclusion is supported by XRD measurements (three-step grown ZnO shows slightly higher FWHM values of diffraction peaks in comparison to two-step one as discussed above), and explains mechanical instability of three-step grown ZnO at elevated RTA temperatures.

In conclusion, three step growth results in a very smooth ZnO films with satisfactory crystalline properties. However, the interface between the first and third layer induces some structural defects which result in ZnO sensitivity to RTA processing. Still, this growth method can be employed for ZnO doping. Three-step growth is used for doping experiments with Diisobutylamine (Chapter 6.2), and UDMHy doping (Chapter 6.4.2).

6. Nitrogen Doping

In order to achieve p-type ZnO, a reproducible nitrogen doping process should be developed (Chapters 2.4 – 2.5). Two- and three-step growth methods offer a feasible variation of the growth parameters and provide high-quality of undoped ZnO (Chapter 5). Those methods were implemented for ZnO doping with different nitrogen precursors in this work.

6.1. NO

Nitrous monoxide is attractive nitrogen precursor for ZnO doping (Chapter 8.2.3). Yan *et al.* have theoretically predicted that p-type ZnO with high hole concentration and mobility can be achieved if NO molecules arrive intact at the ZnO growing surface [Yan01]. Li *et al.* have fabricated p-type nitrogen-doped ZnO by MOVPE on Corning 1737 glass substrates using diethylzinc, O₂, and/or NO gases as precursors [Li03]. ZnO films with high 10²¹ cm⁻³ N impurity level, however, had low hole concentration (10¹¹ cm⁻³), and authors called the ZnO films insulators. Joseph *et al.* have reported p-type ZnO, which, however, had unrealistically high mobility and carrier concentration [Jos99].

Several growth experiments with NO were performed in this work. Firstly, the N₂O source was switched off during HT growth and the growth temperature was varied from 400 °C to 900 °C. Then these experiments were repeated, but without LT ZnO growth. However, only a very small (lower than 0.1 μm/h) growth rate was observed. In contrast to that, Li *et al.* have observed considerable growth rate for LT ZnO growth (200 - 500 °C) using NO and DEZn. Anyway, their ZnO films were polycrystalline with FWHM of (0002) 2:1 scan more than 1300 arcsec. Secondly, the two-step growth* was employed. NO flows during HT ZnO growth were varied from 0 to ~3.35 mmol/min, while keeping the overall reactor flow constant. The HT growth temperature was 850 °C.

In-situ measurements show stable oscillations of the reflected intensity versus time (Fig. 6.1). The overall reflected intensity of undoped ZnO is slightly lowering after 7000 sec of growth, which indicates slight surface roughening as the growth proceeds (Fig. 6.1).

* Process parameters were as described in Chapter 5.2.3, on the GaN:Fe sapphire substrate. Under the given experimental conditions, the reactor contains a gas mixture of NO, N₂, N₂O, and DMZn products. Because the energy for breaking NO molecules, 6.6 eV, is 2.2 eV higher than that for N₂O molecules (4.4 eV) [Dat99], the dissociation of NO in gas phase can generally be neglected, and one can assume that NO molecules arrive intact at the ZnO growing surface. A calculation of the branching ratios can give the concentration distribution of NO, N₂, N₂O in the reactor. However, that is beyond the scope of this work. More on the decomposition of oxynitrides can be found elsewhere [Ste99].

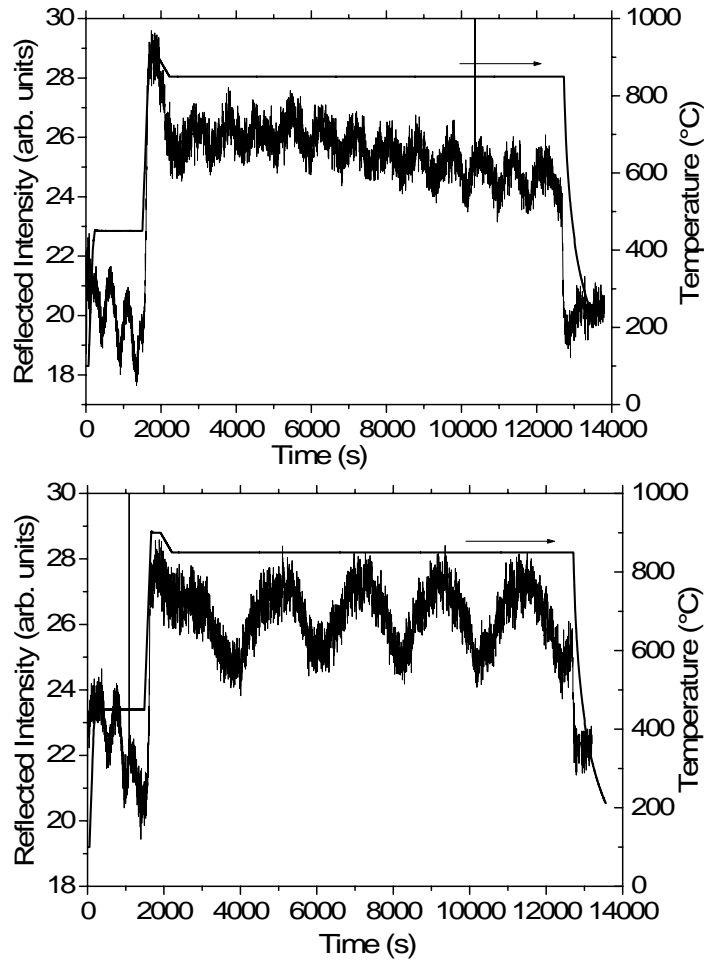


Fig. 6.1. *In-situ* reflectivity measurement of the undoped 1.85 μm -thick ZnO growth (top), and 1 μm -thick ZnO doping with 3.3 mmol/min NO (bottom).

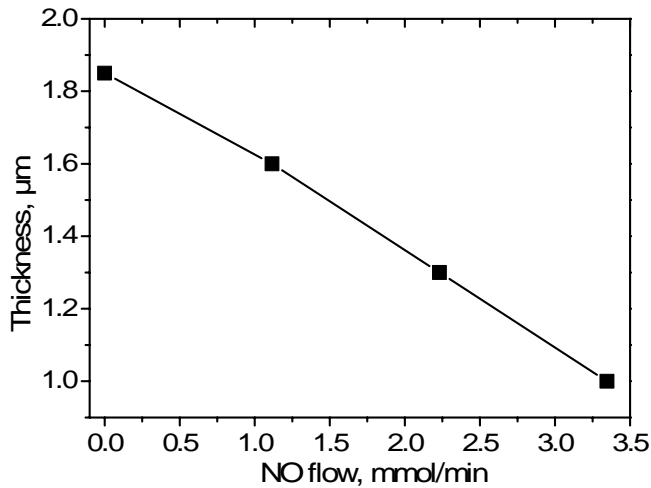


Fig. 6.2. ZnO growth rate determined from in-situ reflectometry measurement versus NO flow. An increase of NO flow leads to a proportional decrease of the growth rate.

A proportional lowering of the growth rate of ZnO with increasing of NO flow is observed (Fig. 6.2). Similar effect is observed in the work of Li *et al.* [Li03]. The high chemical activity of the NO radical is possibly responsible for the lowering of the ZnO growth rate (due to the etching reaction or to the removal of DMZn pyrolysis products from the ZnO-gasphase

interface region).

SEM and AFM measurements reveal a smooth and homogeneous surface of NO-doped ZnO with 0.5 nm RMS roughness (Fig. 6.3). NO-doped ZnO is smoother than undoped one, mostly due to the lower amount of holes and craters. Because of lower concentration of surface holes, SEM micrograph had to be taken under low scanning angle (Fig. 6.3),

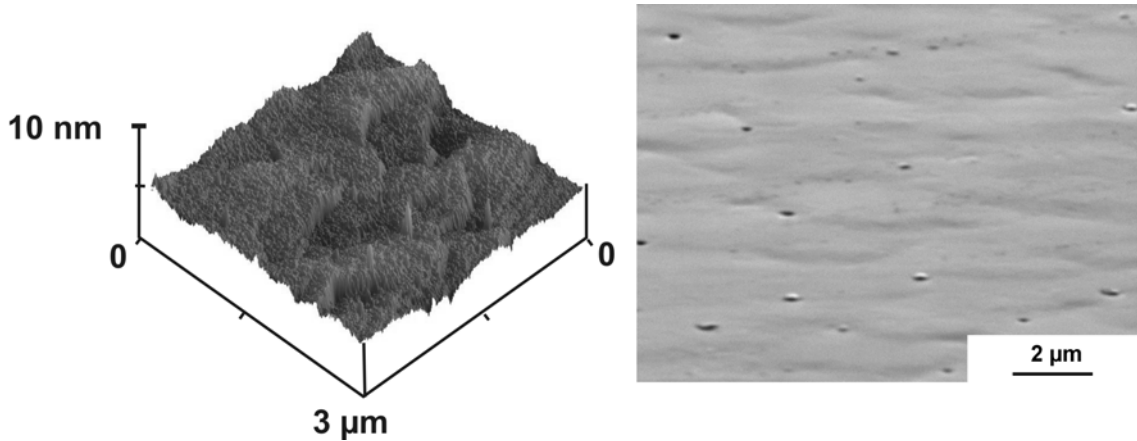


Fig. 6.3. AFM (left) and SEM (right) images of NO-doped ZnO. otherwise no defects on ZnO surface is observable.

XRD measurements have shown that NO-doped ZnO is single crystalline with (0001) plane parallel to the substrate surface. The lattice parameters of NO-doped ZnO are about the same as those of undoped one (c -lattice parameter: 0.52008 nm, a -lattice parameter: 0.32545 nm, Fig. 6.4). This can be expected since NO gas fraction is relatively small in comparison to that of N_2O , and can not influence the stress distribution in the film stack. Fig. 6.5 depicts the FWHM values achieved from the XRD measurements performed in the different geometries.

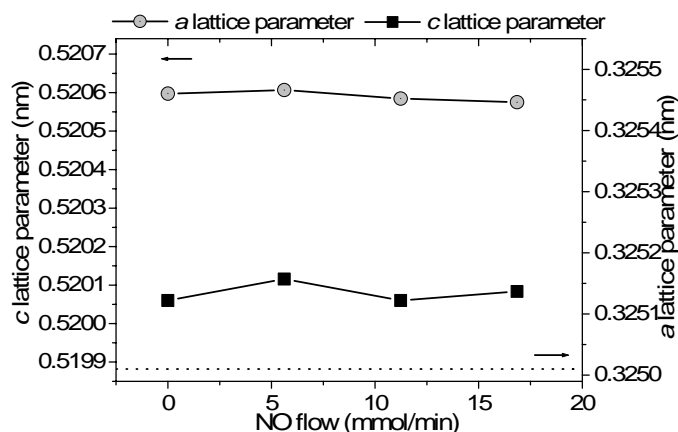


Fig. 6.4. c - and a -lattice parameters of ZnO films doped with NO. Dashed and dotted lines indicate relaxed ZnO lattice parameters [Lan01].

No correlation between the XRD peak width and the growth conditions is observed. FWHM values are at least 10 times smaller than those reported in the work of Li *et al.* [Li03].

CV measurements of non-annealed and annealed samples show that n-type films have nearly the same carrier concentration (Fig. 6.6). The low temperature PL luminescence intensity and the spectral features of the NO- and non-doped reference sample are about the

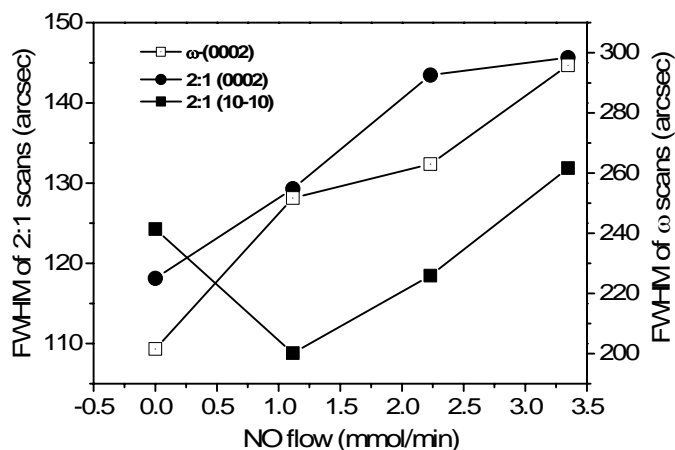


Fig. 6.5. FWHM values of XRD 2:1 scans in (0002) and $(10\bar{1}0)$ geometries (left axis) and ω -scans around (0002) peak (right axis) of ZnO versus NO flow.

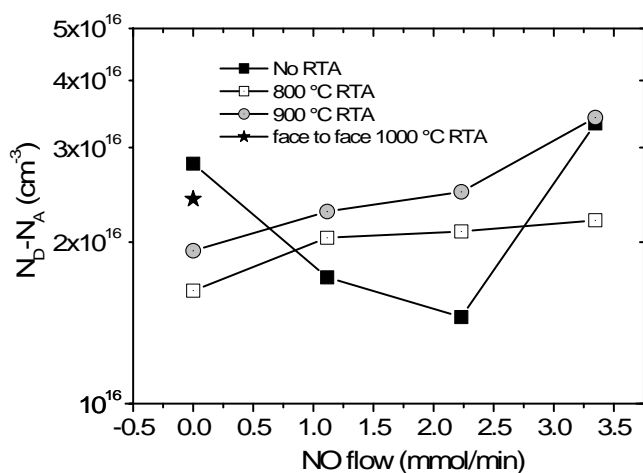


Fig. 6.6. Carrier concentration of ZnO films versus NO flow and annealed at different temperatures. same. The discussion of the spectral features of undoped ZnO reference sample are given in Chapter 6.2.3.

In conclusion, no reproducible and reliable experimental results on the achievement of p-type conductivity using NO precursor reported until now. From the results of X-ray diffraction, electrical and photoluminescence measurements it can be concluded that no nitrogen incorporation is achieved with the use of NO. However, the use of NO resulted in smooth ZnO films with high crystalline and optical quality. This is beneficial for the the use of NO precursor for three-step growth, Chapter 5.3.

6.2. Diisobutylamine

Diisobutylamine (Diis), with central single N atom surrendered by two -CH₂CH(CH₃)₂CH₃ groups (Chapter 8.2.4), is promising nitrogen precursor for ZnO doping. During HT growth its bulky organic tails are splitting, making N atom available for incorporation in ZnO lattice. Until now, there is no ZnO doping using Diis as a nitrogen precursor reported. In three-step growth, the Diis flow was varied from 0 to 1 mmol/min and the growth temperature from 850 to 900 °C on the third growth step (Tab. 6.1).

| Diis, mmol/min T _{growth} , °C | 0 | 0.14 | 0.27 | 0.55 | 0.87 | 1 |
|---|---|------|------|------|------|---|
| 850 | * | * | * | * | * | * |
| 900 | * | | | * | * | |

Tab. 6.1. Variation of Diis flow and growth temperature in three-step doping of ZnO.

The surface of the undoped reference ZnO layers is smooth with 0.2 nm AFM RMS roughness (Fig. 6.7 a)). In contrast to NO-doped ZnO, the Diis-doped ZnO has the rougher surface than the undoped one (Fig. 6.7 b). This can be caused by the presence of the CH₃-containing products from Diis decomposition. From SEM measurements, micrometer-sized hexagonal inverted pits in the surface have a higher density compared to the UDMHy-doped layers.

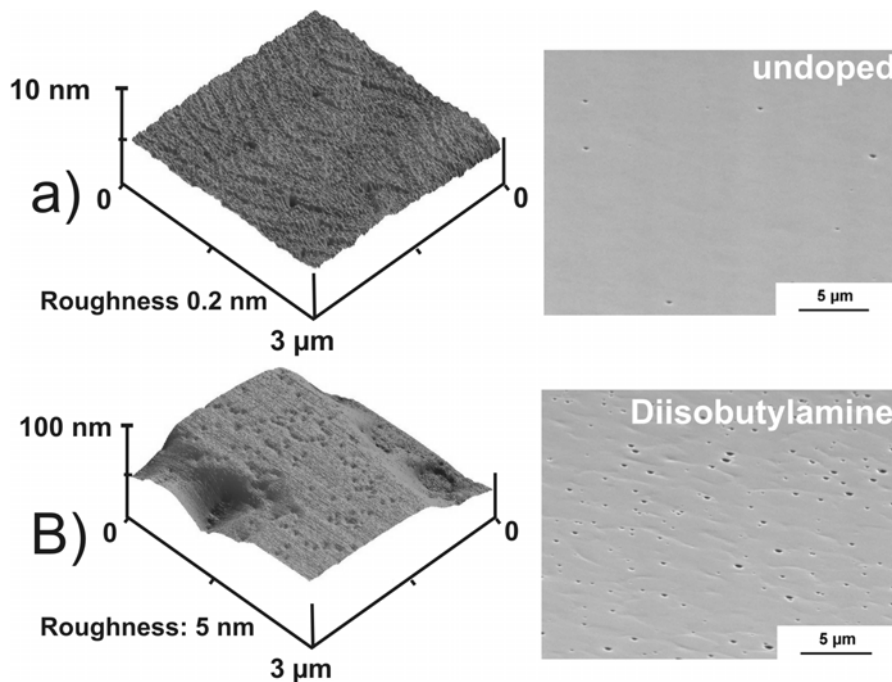


Fig. 6.7. AFM (left) and SEM (right) images of a) undoped, b) doped ZnO layers. An addition of diisobutylamine leads to the roughening of ZnO surface.

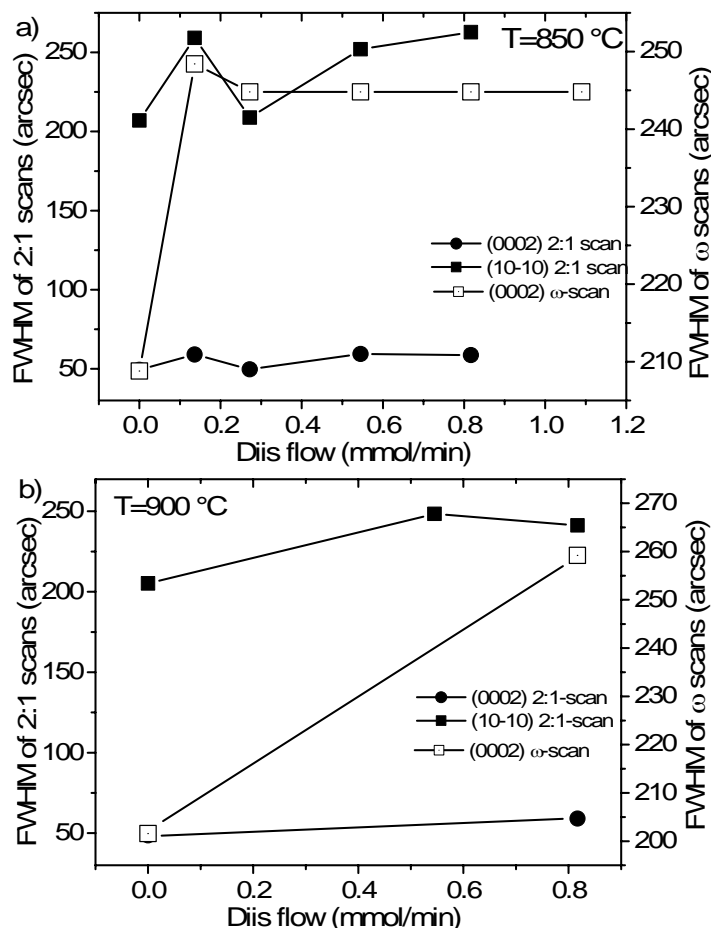


Fig. 6.8. FWHM obtained from X-ray diffraction measurements of diisobutylamine-doped (Diis) ZnO films. Growth temperatures are 850 °C a), and 900 °C b).

Fig. 6.8 depicts the FWHM of the X-ray diffraction peaks obtained from Diis-doped ZnO layers. An increase of Diis flow does not influence the FWHM of 2:1 measurements performed in (0002) geometry, Fig. 6.8. Those values are nearly the same to those of undoped ZnO films grown by three steps. FWHM of ω -scans in (0002) geometry increases drastically with doping, and remains constant with the further increase of Diis flow, Fig. 6.11. No correlation between FWHM of 2:1-scans performed in $(10\bar{1}0)$ geometry and Diis flow is observed, although FWHMs changing significantly, Fig 6.8. Lattice parameters measured for non-annealed ZnO films remain nearly the same with an increase of Diis flow, Fig. 6.9. Thus, doping using Diis leads to the degradation of the surface and crystalline properties of ZnO, but does not influence its strain state.

No reliable indication of a p-type conductivity was observed in electrical measurements. Fig. 6.10 compares the carrier concentration of ZnO films doped with different amounts of Diis. For low concentrations of Diis doping, no reduction in the carrier concentration was observed after annealing at 850 °C in comparison to the as-grown non annealed samples (Fig. 6.10, a)).

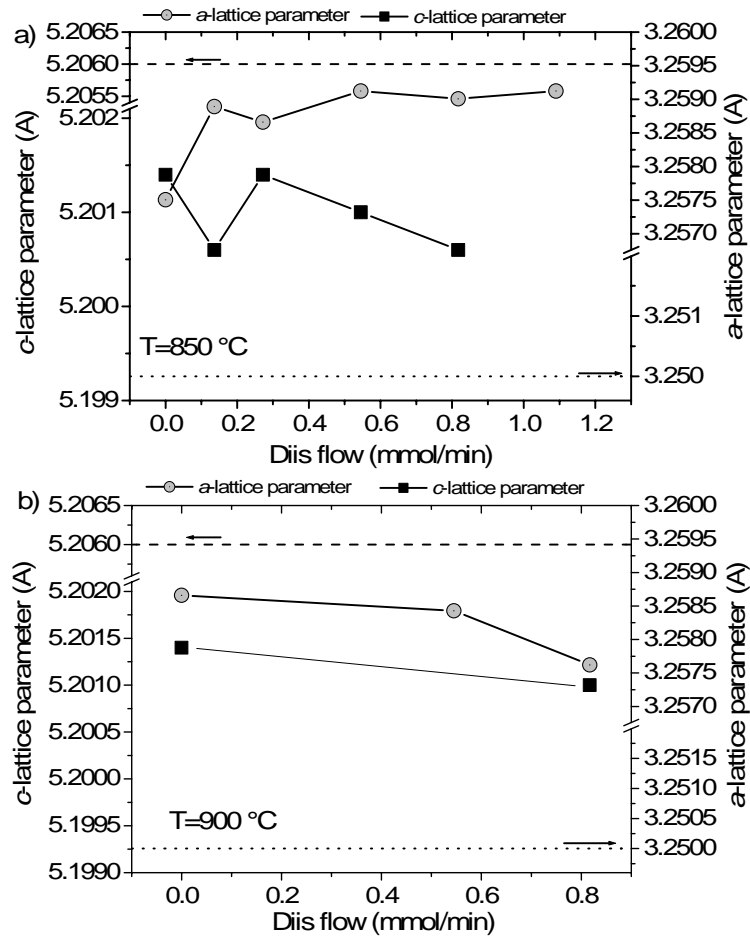


Fig. 6.9. *a*- and *c*- lattice parameters of ZnO obtained from X-ray diffraction measurements. Growth temperatures are 850 °C a), and 900 °C b). Horizontal dashed and dotted lines indicate the relaxed ZnO lattice parameters.

ZnO film doped with 0.55 mmol/min of Diis at 900 °C shows slight increase of carrier concentration after annealing at 850 °C (Fig. 6.10, b)). The ZnO film doped with 0.87 mmol/min of Diis at 900 °C could not be reliably measured after growth. However, after RTA the sample has shown carrier concentration which is similar to the sample doped with 0.55 mmol/min after 850 °C (Fig. 6.10, b)). Doping with 1.2 mmol/min of Diis at 850 °C leads to the small decrease of carrier concentration and does not correlate with an increase of annealing temperature from 850 °C to 950 °C (Fig. 6.10, a)). RTA of ZnO grown at 900 °C resulted in peeling of some films. Since only small drop of the carrier concentration in n-type ZnO films doped using Diis is observed, no luminescence measurements were performed.

In conclusion, nitrogen doping of ZnO using Diisobutylamine leads to the degradation of its surface morphology and its crystalline quality without influence on the strain in ZnO film stack. Post-growth RTA processing of diis-doped ZnO films represents an issue because of peeling effects. Additionally, low vapour pressure of Diis does not allow the flexible variation of MOVPE growth conditions.

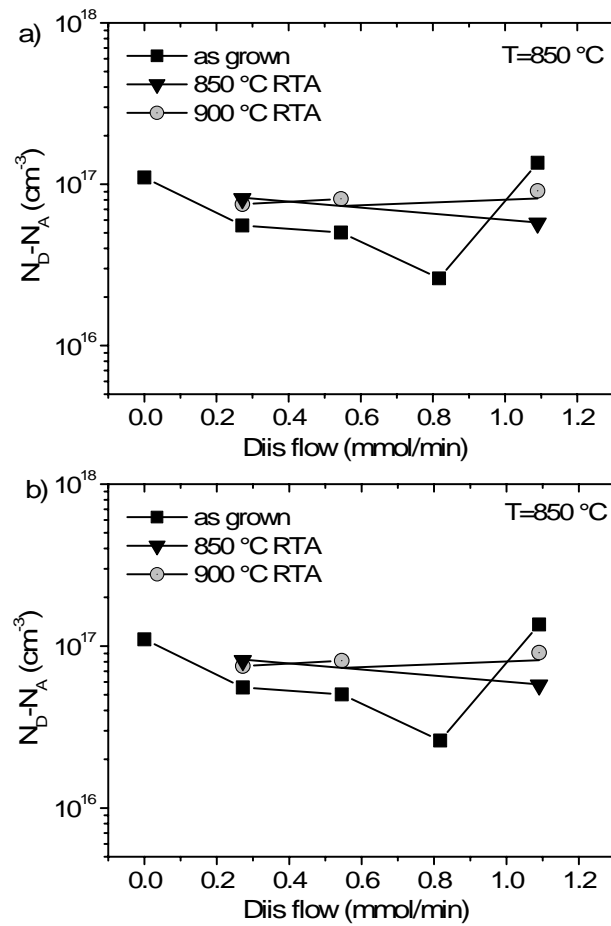


Fig. 6.10. Carrier concentration obtained from capacitance-voltage measurements of ZnO layers doped using Diisobutylamine. Growth temperature: a) 850°C , and b) 900°C .

A reduction in the carrier concentration with increasing annealing temperature was observed for some doped samples; however this reduction is smaller compared to some UD-MHy- or ammonia-doped ZnO films (Chapters 6.3 and 6.4). This is why the use of this precursor for p-type doping of ZnO is inappropriate.

6.3. Ammonia

Ammonia, the common nitrogen precursor for high-temperature GaN growth using MOVPE, has been the most “popular” nitrogen precursor for ZnO doping. Several groups claimed the achievement of p-type ZnO films by using NH_3 ; however, the results were non-reproducible or controversial (Chapters 2.3 – 2.5) [Min97, Hua02, Ash02, Ye03, Yyan03, Xli03, Wan03c, Wan03b, Rom03]. For nitrogen doping using ammonia, two-step growth method was used in this work.

6.3.1. Two-step Growth

Growth Conditions

In two-step growth experiments, nitrogen doping was achieved by switching on the ammonia in the reactor on the HT step.* For the control of the ZnO quality and the nitrogen incorporation, the temperature and ammonia flow were varied as shown in Tab. 6.2. Upper limits of these growth parameters were directly achieved from the experiments. An increase of ammonia flow and the temperature beyond these values lead to a severe film degradation.

Surface Morphology

As observed in *in-situ* reflectometry measurements, the ZnO growth rate is independent of the temperature and ammonia flow. A decrease of the overall reflected intensity was observed after 40 – 50 min of ZnO growth, indicating surface roughening. This was supported by SEM and AFM measurements, which have additionally shown that the surface roughens mainly by the generation of the holes (Fig. 6.11, a)-b)). The hole density does not systematically depend on the growth conditions. For example, the hole density is increasing from $0.5 \times 10^6 \text{ cm}^{-2}$ to $8.5 \times 10^6 \text{ cm}^{-2}$ with an increase of temperature from 800 °C to 1000 °C (ammonia flow 0.89 mmol/min). However, it is nearly the same (around 10^6 cm^{-2}) with an increase of ammonia flows from 0.2 to 0.7 mmol/min (for all growth temperatures). The surface degradation of ZnO upon doping with using ammonia can be attributed to several factors. At elevated temperatures ammonia radicals are highly active, which can cause chemical etching reactions. Besides, ammonia molecule contains three hydrogen atoms, which can lead to a reduction of ZnO by hydrogen. Although a number of publications appeared on the ZnO doping using ammonia (see Chapters 2.3 – 2.5 for some examples), no detailed study on this topic is reported.

* MOVPE-grown GaN layers doped with Iron were used as a substrate (Chapter 3.2).

| NH ₃ Flow mmol/min Temperature | 0 | 0.22 | 0.44 | 0.67 | 0.89 | 1.6 | 3.2 |
|---|---|------|------|------|------|-----|-----|
| 750 | | | | | X | | |
| 800 | X | X | X | X | X | | |
| 850 | | | | | X | X | X |
| 900 | X | | X | | X | X | |
| 950 | | | | | X | | |
| 975 | | | | | X | | |
| 1000 | X | | | | X | | |
| 1050 | | | | | X | | |

Tab. 6.2. Doping parameter variation in experiments with two-step growth of ZnO. The background in the table cells indicates the color of the sample achieved from CCD camera in the optical microscope. Increase of ammonia flow at low growth temperatures leads to a brownish color of the ZnO films.

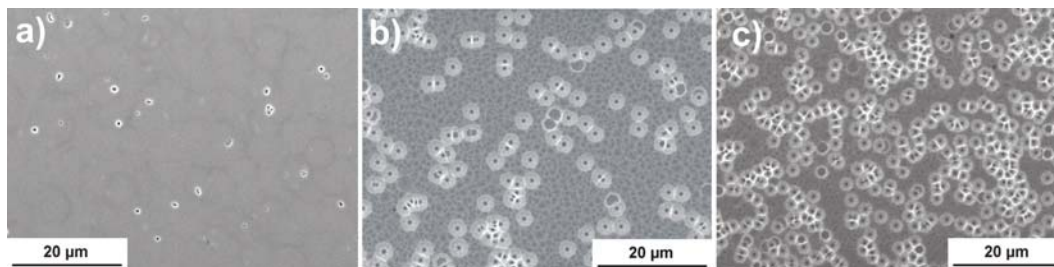


Fig. 6.11. SEM images of ZnO doped using ammonia. Growth temperature: 850 °C. Ammonia flows: a): 0.89 mmol/min, b): 1.6 mmol/min, c): 3.2 mmol/min.



Fig. 6.12. The colors of the ZnO films grown with increasing amount of ammonia (from left to the right). Growth temperature: 850 °C. Ammonia flows: a): 0.9 mmol/min, b): 1.6 mmol/min, c): 3.2 mmol/min.

Coloring of the ZnO Films

Besides the surface roughening, a brownish color of some samples was observed. The coloring was especially rich in the samples grown with high NH₃ flow and at low growth temperature (Tab. 6.2, Fig. 6.12).

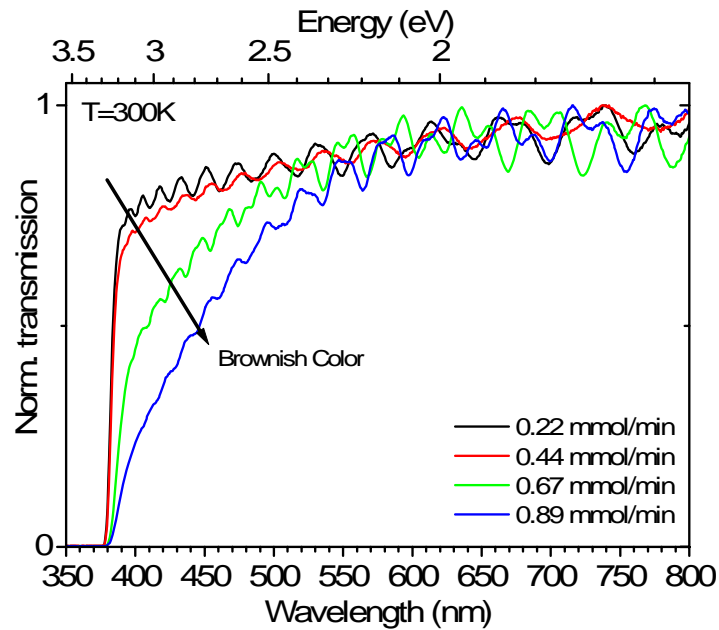


Fig. 6.13. Room temperature optical absorption measurements of the ZnO films grown at 800 °C with different amounts of ammonia. Optical data from the sapphire and GaN are subtracted.

Post-growth rapid thermal annealing at 800 °C and higher bleached the samples. The transparency of the substrate has allowed studying this coloring by optical absorption measurements (Fig. 6.13). Light absorption around 380 nm was observed in the room-temperature measurements. This absorption edge is defined by the ZnO band gap width, and the absorption centers. Lower-energy signal intensity (ZnO is transparent here) is mainly defined by the light scattering on the surface defects (Fig. 6.13). Thus, the coloring of ZnO samples is caused by the light absorption in blue and green spectral region. Such effects were reported in some publications on ZnO. Lander has observed the “beautiful amber coloring” of bulk ZnO samples after hydrogen ions bombardment [Lan57]. Minegishi *et al.* reported the ZnO coloring after the addition of ammonia into MOCVD reactor. [Min97]. The color becomes darker as the growth temperature increases from 650 °C to 800 °C regardless on Zn addition [Min97]. In the experiments of Garses *et al.*, coloring of the ZnO single crystals was observed after annealing between 600 °C and 900 °C in air or nitrogen [Gar01]. They have investigated this coloring by the absorption measurements with unpolarized light propagating along the ZnO *c* axis [Gar01]. From those measurements, Garses *et al.* suggest that “this coloring may represent transitions from singly ionized nitrogen acceptors to shallow donors and the conduction band or from singly ionized nitrogen acceptors to “deep” levels, such as transition-metal impurities or intrinsic defects” [Gar01].

Raman Measurements

In Raman measurements of samples grown at 800 °C only a highly doped sample (0.9 mmol/min) shows a drastic change in the Raman spectra which can be attributed to NH₃ doping (Figs. 6.14-6.15). Besides a significant broadening (8.3 cm⁻¹) of the E₂ ZnO Raman line (typically ~6 cm⁻¹) the line at 275 cm⁻¹ attributed to N is much more pronounced in this sample [Kas02]. Annealing of the samples has only a small impact on the Raman spectra of low N-doped ZnO, Fig. 6.15. The sample with NH₃ = 0.2 mmol/min shows only negligible changes. In the case of high NH₃ flows (0.9 mmol/min) a change and narrowing of the lines is observed. The E₂ ZnO line narrows from 8.3 to 6.3 cm⁻¹ and the line at 275 cm⁻¹ is strongly reduced in intensity; this sample is only slightly brown compared to other samples grown with lower ammonia flows and higher temperatures. Those observations confirm that nitrogen incorporated into ZnO as a result of using ammonia for doping and correlates with the results of the optical absorption measurements.

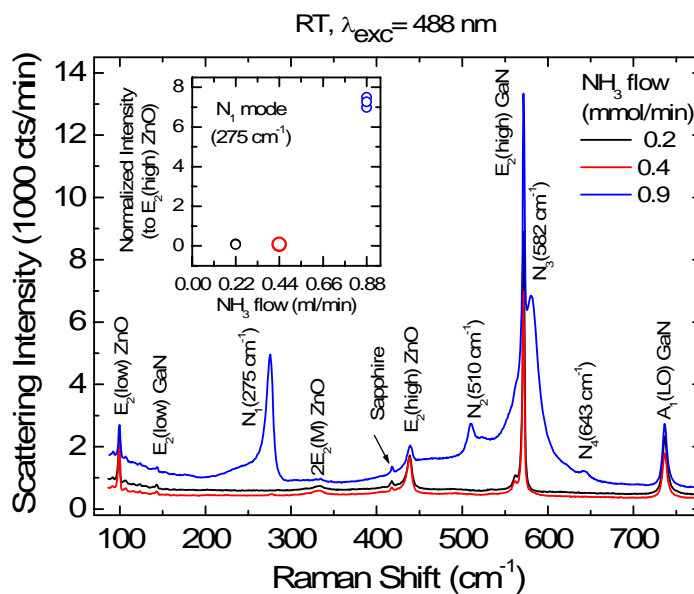


Fig. 6.14. Raman spectra of not annealed ZnO samples doped using different amounts of NH₃. T_{growth} = 800 °C.

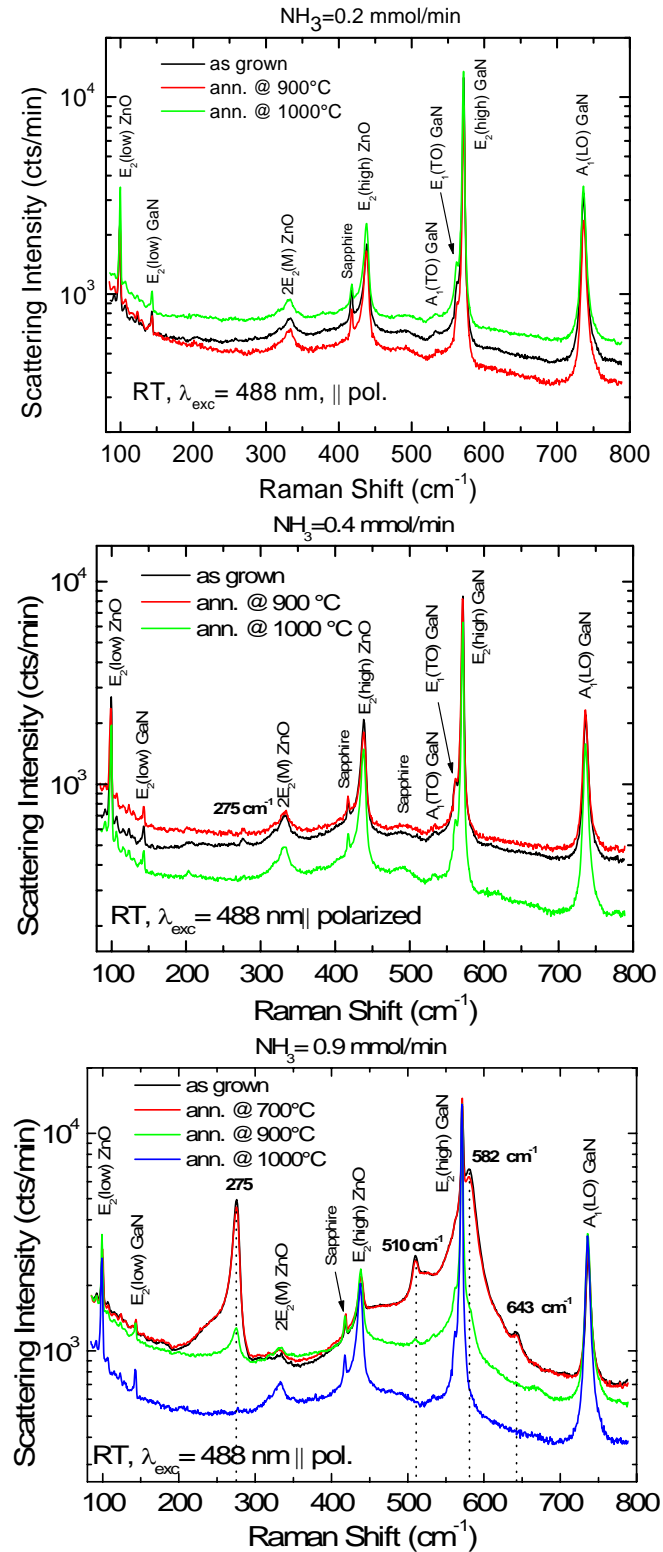


Fig. 6.15. Raman spectra of ammonia-doped ZnO after RTA at different temperatures. $T_{\text{growth}}=800^\circ\text{C}$.

X-ray Diffraction Measurements

In X-ray diffraction measurements it was observed that ammonia-doped ZnO is single-crystalline with (0002) plane parallel to the surface of the substrate. In (0002) θ - 2θ -scans a double-peak reflection from ZnO was observed. The c lattice parameter of the LT layer is larger than that of the HT grown ZnO for the samples grown at 800 °C and doped with 0.2 - 0.9 mmol/min ammonia flows. When the ammonia flow is higher than 0.9 mmol/min, the c lattice parameter of LT ZnO is smaller than that of the HT layer. In $(10\bar{1}0)$ θ - 2θ -scans the peak from the LT ZnO was not observed, except for one sample grown at 850°C doped with 3.2 mmol/min of ammonia. Fig. 6.16 depicts the lattice parameters for some ZnO layers grown at different temperatures and doped with different amounts of ammonia. For the samples grown at 800 °C, an increase of the ammonia flow from 0.7 mmol/min to 0.9 mmol/min leads to an increase of both the a - and c -lattice parameters (Fig. 6.16, a)). The peak-splitting was not observed for undoped two- and three-step grown ZnO layers. From Raman-effect and optical absorption measurements it was concluded that nitrogen is successfully incorporated into ZnO

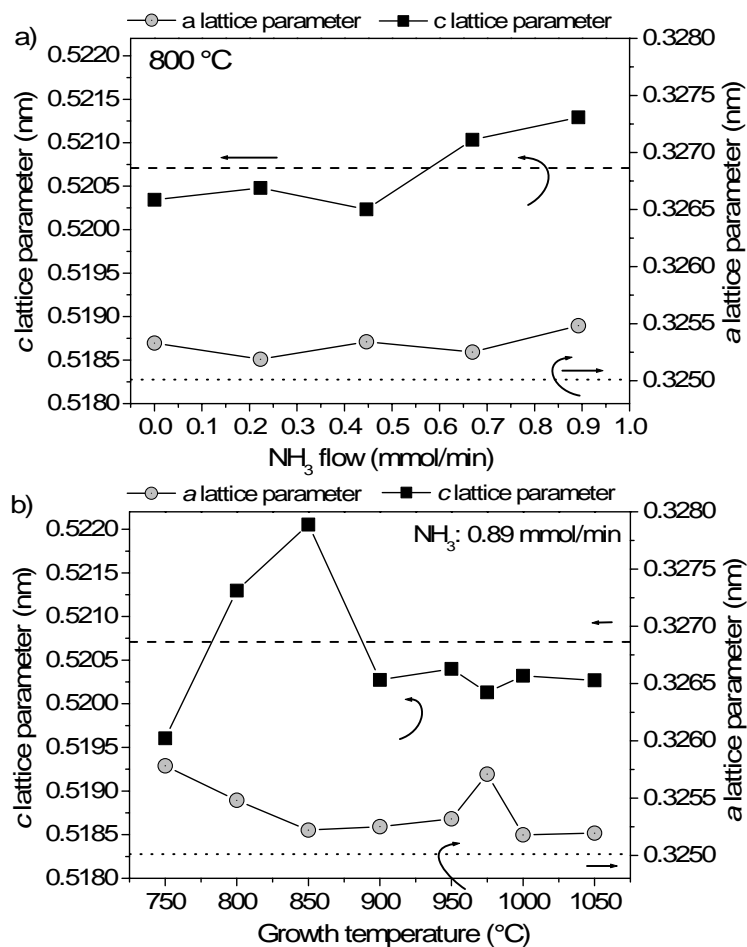


Fig. 6.16. Lattice parameters of ZnO layers grown at different temperatures and doped with different amounts of ammonia. a): growth temperature is 800 °C. b): ammonia flow 0.9 mmol/min.

lattice for some of these samples; however, this can not lead to the ZnO peak splitting due to the low nitrogen concentrations. Probably the main reason for this effect is the ammonia influence on the growth mechanisms on the HT growth step.

Figs. 6.17 – 6.18 depict FWHM values obtained from θ -2 θ and ω -scans measurements performed in different geometries for some samples doped with different amounts of nitrogen. An increase of the ammonia flow for the samples grown at 800 °C leads to a decrease of the crystalline properties of the layers. A variation of the growth temperature from 750 to 1050 °C at constant ammonia flow (0.9 mmol/min) does not lead to a systematical variation of the c and a lattice parameters (Fig. 6.17). When the growth temperature is increased to 900 °C or 950 °C, both lattice parameters are changed in different directions. Further increase of the growth temperature does not lead to a significant variation of the lattice parameters (it is in the order of 10^{-5} nm). An increasing growth temperature leads to an improvement of the crystalline properties (Fig. 6.17).

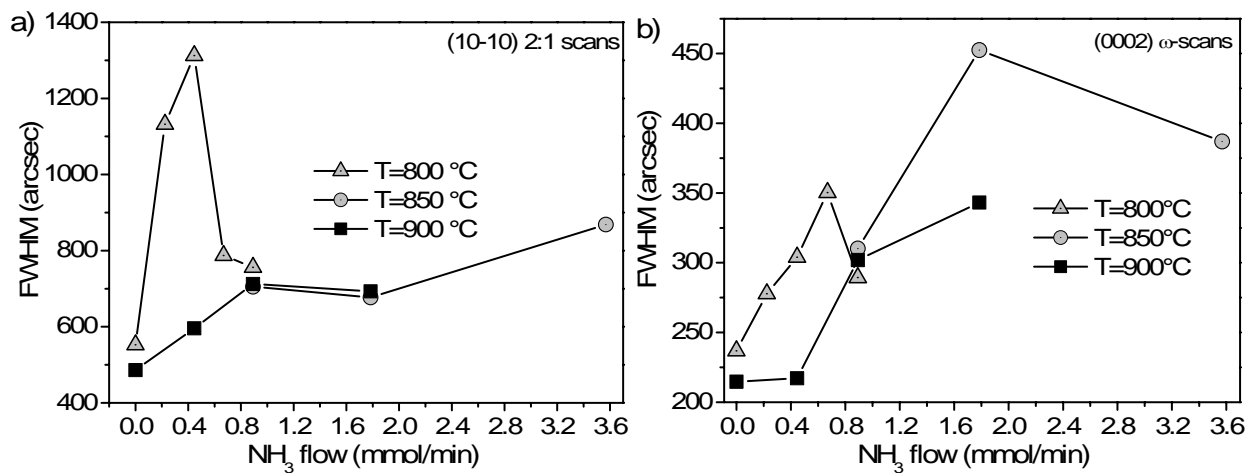


Fig. 6.17. FWHM of a) θ -2 θ -scans of $(10\bar{1}0)$ and b) ω -scans of (0002) ZnO reflections versus ammonia flow.

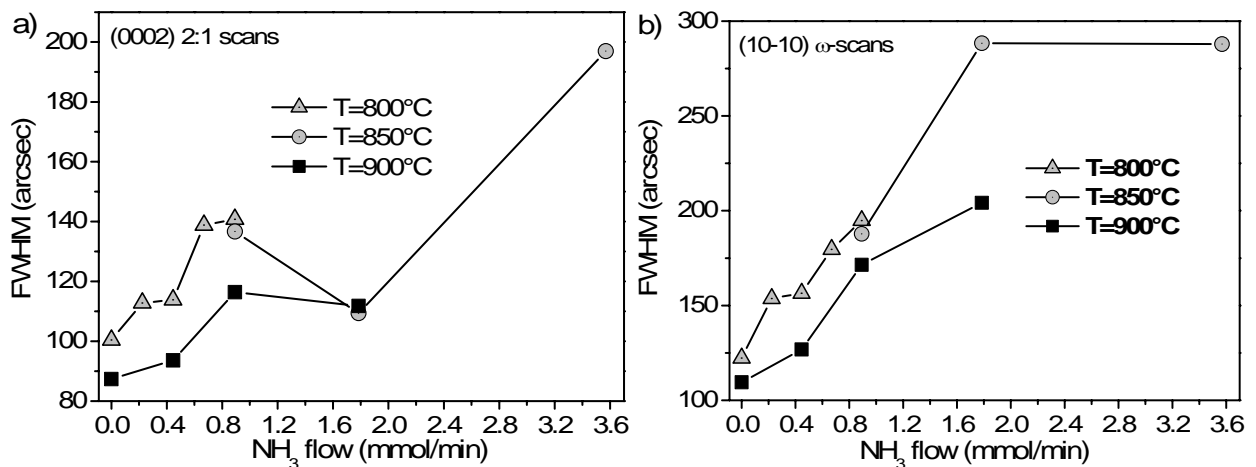


Fig. 6.18. FWHM of a) θ -2 θ -scans of (0002) and b) ω -scans of $(10\bar{1}0)$ ZnO reflections versus ammonia flow.

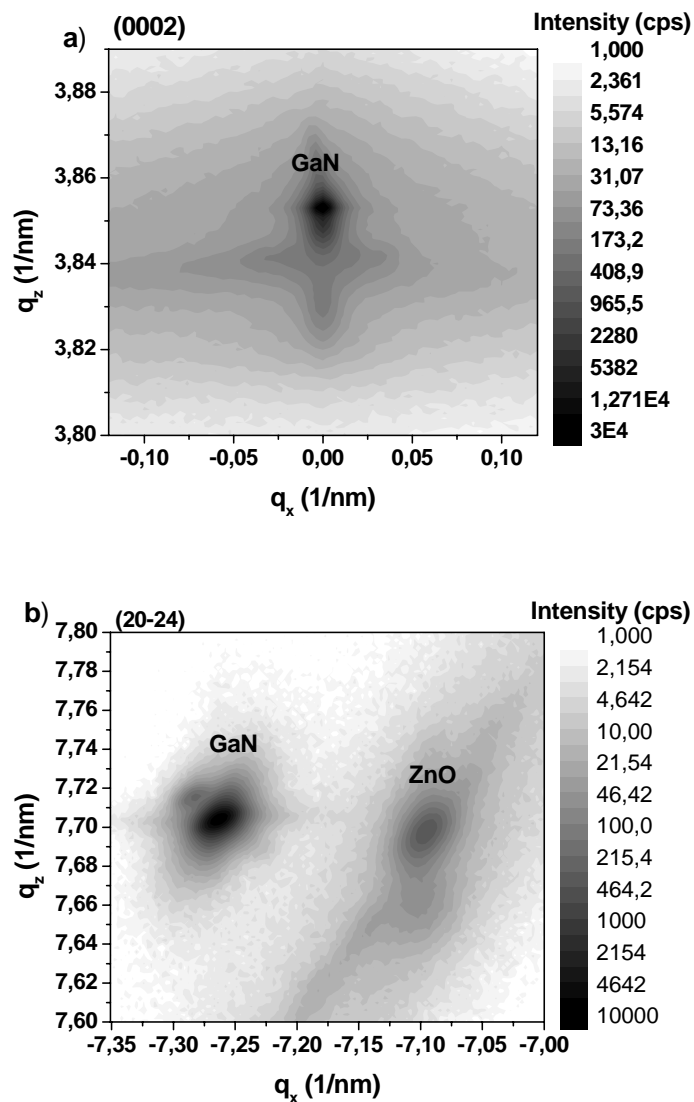


Fig. 6.19. Symmetrical a) and asymmetrical b) X-Ray reciprocal space mapping of the ZnO sample grown at 750 °C with 0.9 mmol/min ammonia flow.

The FWHM values of θ - 2θ and ω -scans are systematically decreasing with increasing growth temperature. Fig. 6.19 depicts the symmetrical (a) and asymmetrical reciprocal space mapping b) for the sample grown at 750°C and doped with 0.9 mmol/min of ammonia. Both maps show an asymmetrical lattice planes in the ZnO crystal which are tilted in one direction to greater extent. An additional broadening of the ZnO peak observable in the asymmetrical mapping (Fig. 6.19, b) originates from cracks in the surface of the layer, which were observed in SEM and Normarski microscopy measurements.

Cathodoluminescence

Non-annealed ZnO

The comparison of the integrated spectra collected from the surface of the non-annealed ZnO grown at 800 °C shows that the overall intensity of ZnO doped with the highest amount of ammonia is lower than that of the undoped sample, Figs. 6.20 and 6.21. The luminescence peak intensity drops by four orders of magnitude when the ammonia flow is increased from 0.2 to 0.9 mmol/min (Fig. 6.21, b)). This correlates to the browning of these samples and to the observed in optical absorption measurements which have shown increased absorbance in this spectral region, Fig. 6.13. The position of the peak energy shows a weak dependence on the amount of ammonia, introduced into the reactor (Fig. 6.21, a)). An increase of the ammonia flow leads to a shift of the peak to the lower energies. An increase of the FWHM

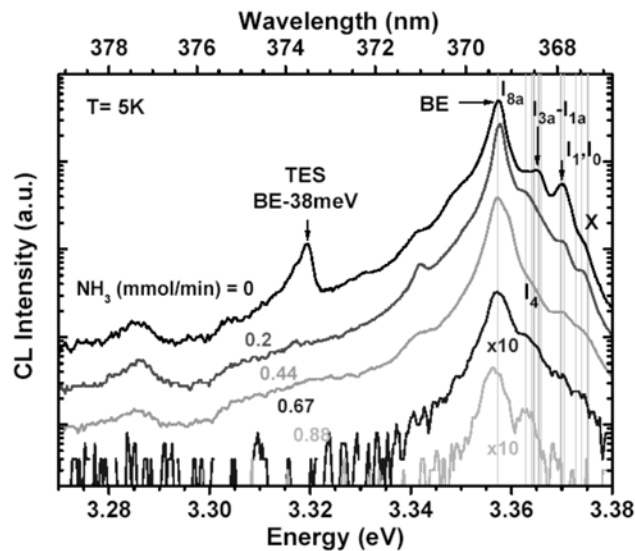


Fig. 6.20. Integrated cathodoluminescence spectra from ZnO surface measured for the not annealed samples doped with different amounts of ammonia. Growth temperature: 800 °C.

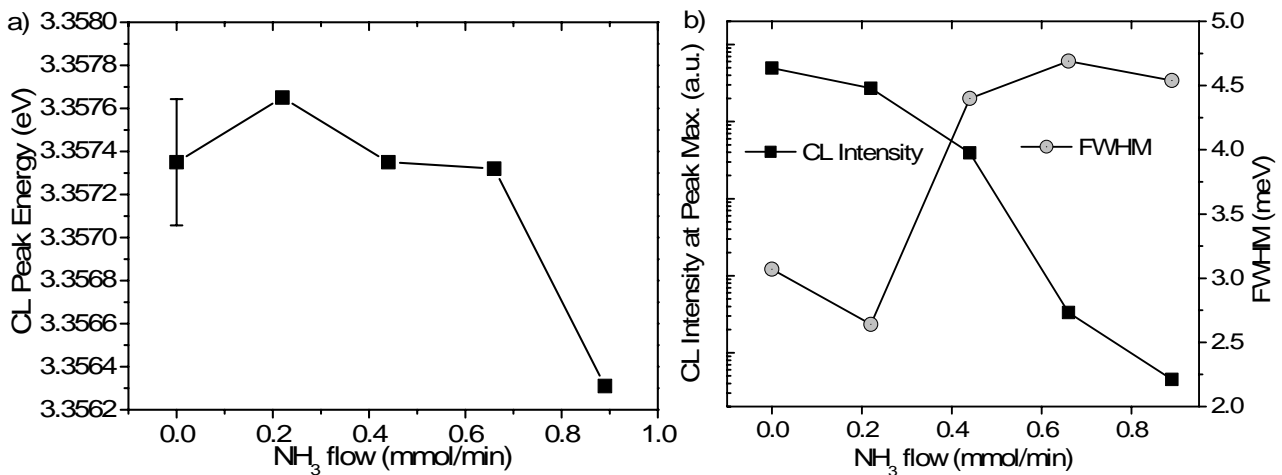


Fig. 6.21. a) CL peak energy, b) FWHM and CL intensity at peak maximum versus ammonia flow.

with an increase of the ammonia flow is mainly caused by the reduction of the luminescence intensity (Fig. 6.21, a) - b)).

In the spectrum corresponding to ZnO doped with 0.7 mmol/min of ammonia, the recombination line I_4 (3.363 nm) appears, which is attributed to the hydrogen donor atom [Mey03]. Spatially resolved CL measurements gave additional information on the origin of luminescence at 3.319 meV emitted from the surface of undoped ZnO (Fig. 6.21). The two-electron satellite (TES) recombination is attributed to the recombination in the holes (Fig. 6.22). In the spectral region from 373.1 to 374.2 nm, the flat regions (domains between the holes) do not show any luminescence (Fig. 6.22, b)).

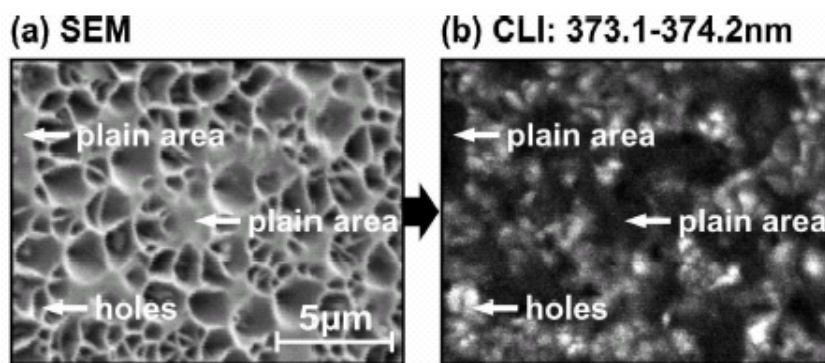


Fig. 6.22. Spatially resolved CL measurements of the as-grown undoped reference sample. $T_{\text{growth}}=800\text{ }^{\circ}\text{C}$

a) SEM picture of the sample. b) CL intensity image at 3.319 eV.

In spatially resolved CL measurements, the surface of the undoped ZnO contains a very low amount of planar regions, in contrast to the samples doped with 0.2 and 0.4 mmol/min of ammonia (Fig. 6.23). In the integrated intensity images bright and dark regions are observable, which correlate with the surface morphology shown in SEM pictures. The dark regions correspond to the part of the surface with a low quantum efficiency, which is caused by defects and dislocations in the ZnO layer. The planar regions show surface morphology defect correlated luminescence. Spatially resolved CL images clearly show that for the undoped ZnO and the sample doped with 0.2 mmol/min ammonia the holes have lower luminescence intensity than the planar regions. An increase of the ammonia flow to 0.4 mmol/min leads to the reversion: the holes show higher luminescence intensity relative to the flat regions of ZnO. This explains the drop of CL quantum efficiency with an increase of the ammonia flow. The surface distribution of the cathodoluminescence wavelength is highly correlated with the surface SEM morphology (Fig. 6.23, g) – i)). In the reference sample the planar regions of the film emit at a higher energy than the regions with holes. The low N-

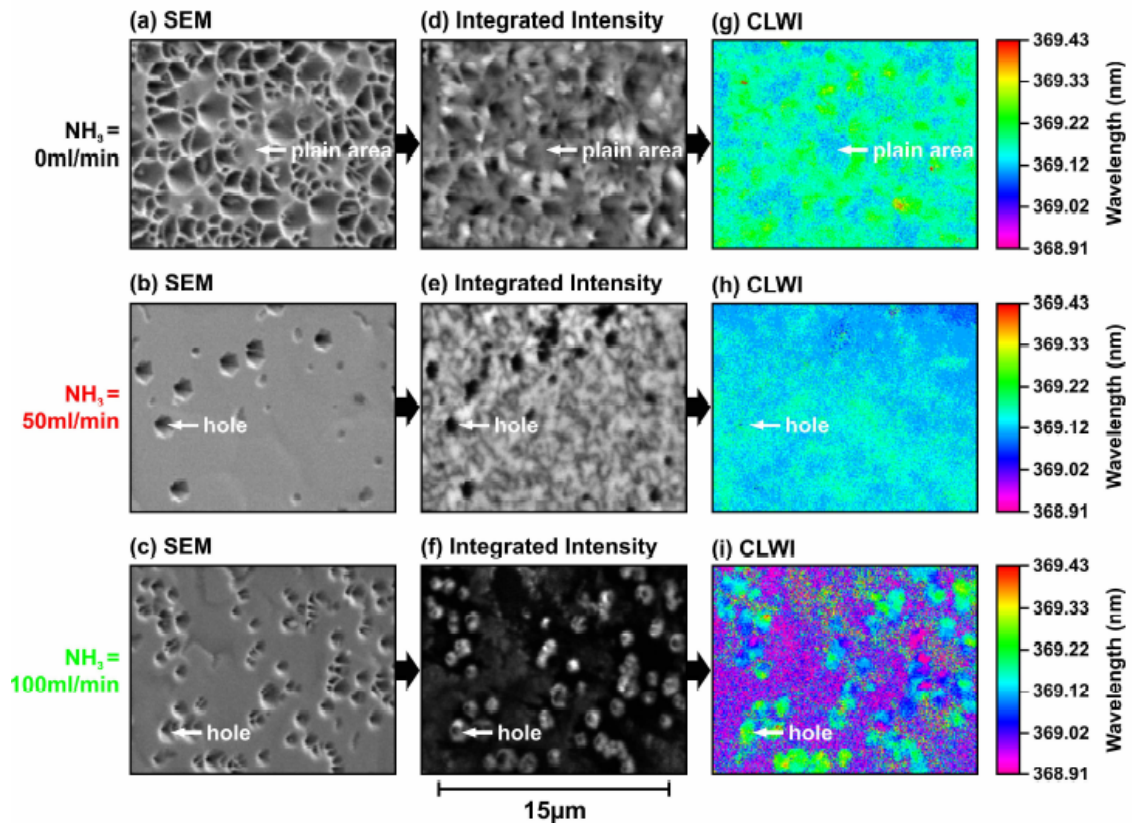


Fig. 6.23. SEM, Integrated intensity and CL wavelength images of three ZnO layers doped with different amounts of ammonia. $T_{\text{growth}}=800\text{ }^{\circ}\text{C}$.

doped ZnO shows a homogeneous distribution of the emission energy. A higher level of doping results in the reversion of the spatial distribution of the luminescence relative to the reference sample: the flat region of ZnO show lower energy emission in comparison to the region of the holes. However, the luminescence emitted from the planar regions of the film has a very low intensity.

Cathodoluminescence

Annealed ZnO

An increase of the RTA temperature for the undoped ZnO leads to a decrease of the overall luminescence intensity, while the defect band (DB) luminescence intensity is increasing (Fig. 6.24, a). In contrast to that, the near-band edge (NBE) luminescence intensity from the doped ZnO is increasing with increasing RTA temperature (Fig. 6.24, b). From the more detailed observation of the NBE luminescence, the position of the recombination peak maxima for the undoped ZnO is not influenced by the RTA temperature (Fig. 6.25). For the undoped ZnO an increase of the annealing temperature results in a disappearance of I_2 , I_{1a} excitonic recombination lines. The sample annealed at $1000\text{ }^{\circ}\text{C}$ shows only I_{8a} - I_9 recombination peaks. The FWHM of the luminescence peaks of undoped ZnO remains nearly

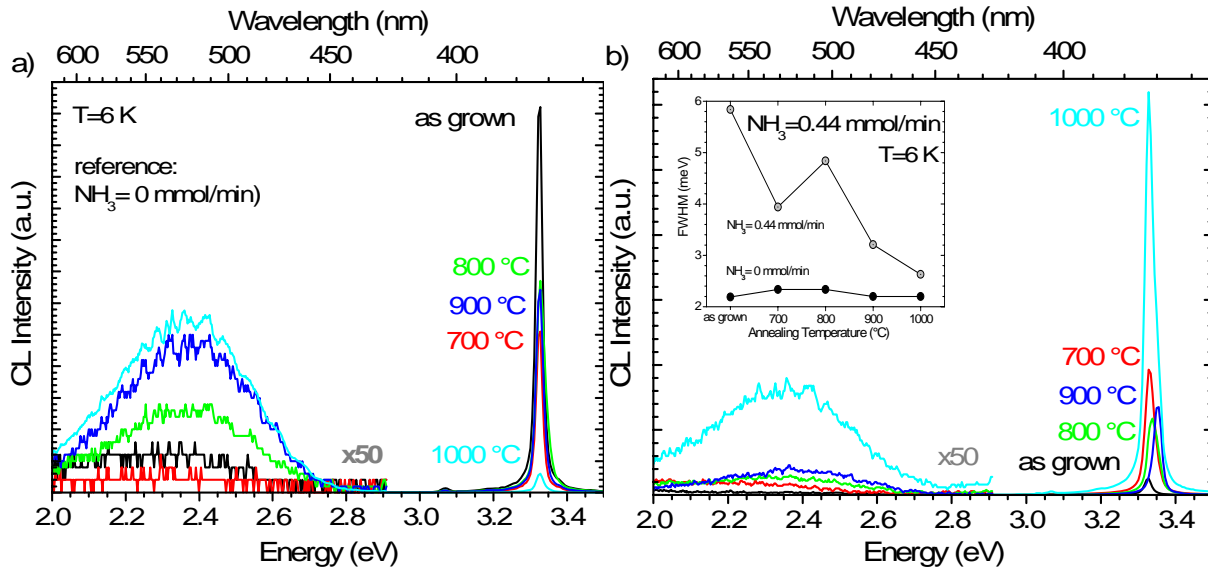


Fig. 6.24. Low temperature integrated spectra of a) undoped and b) doped ZnO annealed at different temperatures.

Inset in b) shows the FWHM of the luminescence peak maxima versus RTA temperature.

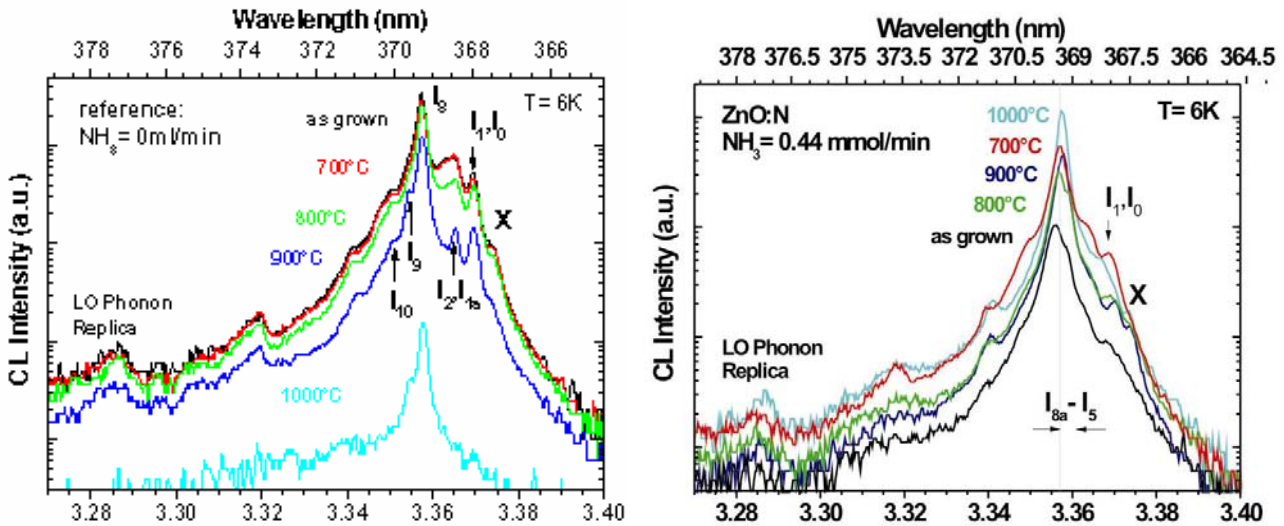


Fig. 6.25. Highly resolved low temperature integrated CL spectra of ZnO. Left: undoped ZnO grown at 800 °C and annealed at different temperatures. Bottom: doped with 0.4 mmol/min ZnO annealed at different temperatures.

constant with an increase of the RTA temperature, while it is decreasing for doped ZnO (Fig. 6.24 b)). For doped ZnO, the overall luminescence intensity is increasing, and the position of the recombination peak maximum shifts towards higher energies (Figs. 6.24 and 6.25).

Capacitance-voltage Measurements

Fig. 6.26 shows the carrier concentration of ZnO films doped and annealed at different temperatures.* The samples have not shown p-type conductivity in capacitance-voltage measurements. The undoped ZnO grown at 800 °C shows nearly the same carrier

* Some samples were damaged after RTA.

concentration after RTA at 700 °C (Fig. 6.26, a)). RTA at 800 and 900 °C results in an increase of the carrier concentration, which can be attributed to the increase of the defects in ZnO layers as a result of RTA. This is supported by the integrated CL spectra measured from the surface of these samples: the intensity of defect band from 2 to 2.6 eV is increased by several orders of magnitude upon annealing, and disappearance of I_2 and I_{1a} recombination lines (Figs. 6.24 and 6.25). ZnO doped with 0.2 and 0.4 mmol/min of ammonia show about the same carrier concentration after RTA at 700 – 900 °C with a small decrease of the carrier concentration (Fig. 6.26, a)). RTA at 1000 °C results in a strong increase of carrier concentration by several orders of magnitude for both doped samples. The as-grown heavily doped (0.9 mmol/min) sample shows very high carrier concentration, probably due to defects induced by doping. An increase of the RTA temperature leads to a monotonic decrease of the carrier concentration by two orders of magnitude. At 900 - 1000 °C the saturation is observed. A decrease of the carrier concentration by about one order of magnitude was observed for the sample grown at 850 °C and doped with ~1.6 mmol/min of ammonia. Annealing at 900 °C of the sample grown at 800 °C results in the lowest carrier concentration which is about 10^{17} cm^{-3} (Fig. 6.26, d). The samples grown at 950 °C and 1000 °C show a lower carrier concentration after annealing at 900 °C and 1000 °C. The behavior of the carrier concentration in all doped samples directly correlates with the bleaching of the brownish color.

In conclusion, an increase of ammonia flow does not influence the growth rate of ZnO, but roughens its surface. The surface defect density is about 10^6 cm^{-2} . RTA has a small impact on the Raman spectra of low N-doped ZnO. Only a highly doped sample (0.9 mmol/min) grown at 800 °C shows a drastic change in the Raman spectra which can be attributed to NH_3 doping. This sample, however, shows higher carrier concentration in initial and RTA-treated films as compared to low N-doped films. Ammonia doping from 0 to 0.4 mmol/min resulted in the reduction of carrier concentration after RTA. XRD measurements have demonstrated that an increase of ammonia flow leads to the increase of FWHM values. In cathodoluminescence measurements it was observed that with an increase of ammonia flow the integrated intensity decreases and FWHM is increasing. A higher level of doping results in the reversion of the spatial distribution of the luminescence relative to the reference sample: the flat region of the film show lower energy emission in comparison to the region of the holes. However, the luminescence emitted from the planar regions of the film has a very low intensity. Thus, high ammonia flow is not practical from the optoelectronic application viewpoint. Taking this into account, further experiments with ammonia doping have been performed, Chapter 6.3.2.

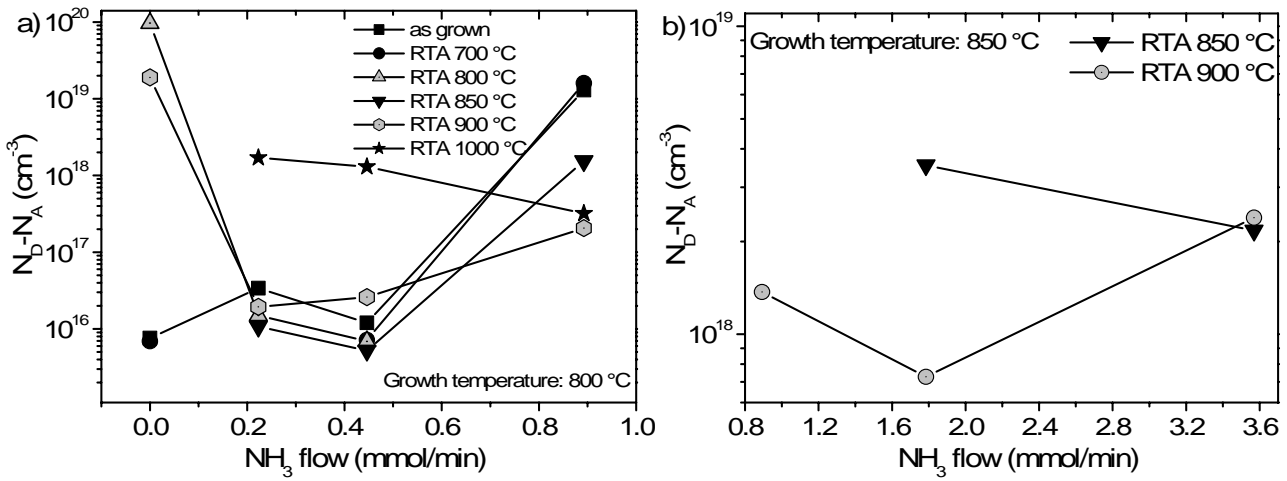


Fig. 6.26. Carrier concentration of the ZnO samples annealed at different temperatures versus the ammonia flow. The growth temperature is a) 800 °C, b) 850 °C.

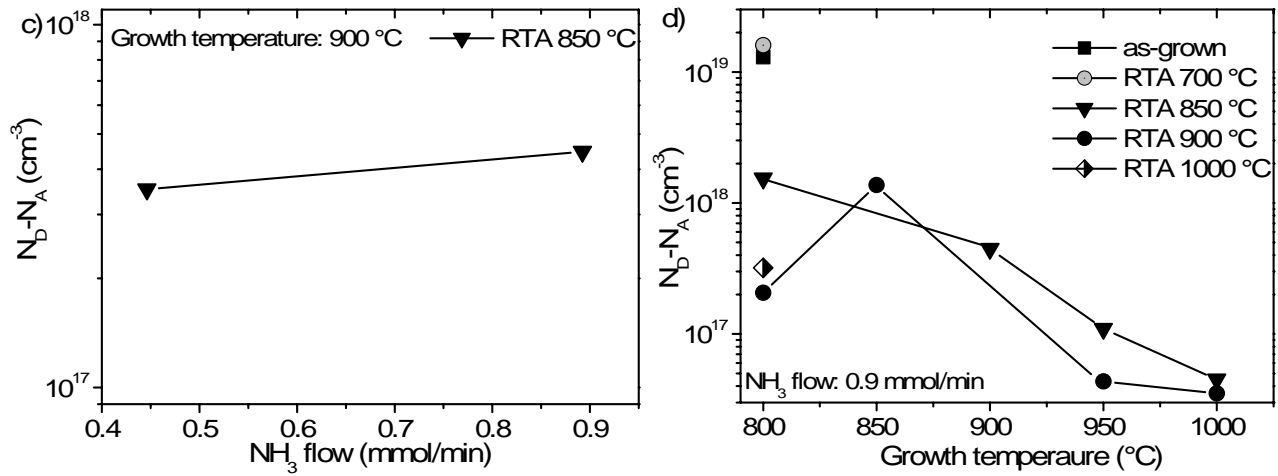


Fig. 6.26. Carrier concentration of the ZnO samples annealed at different temperatures versus c) ammonia flow and d) growth temperature.

6.3.2. Two-step Growth with Reduced DMZn Flow

To study the influence of VI-II ratio on the ammonia doping and improve the quality of nitrogen-doped ZnO, the DMZn flow on the HT step was reduced to ~ 0.55 mmol/min.* Nitrogen incorporation was controlled by ammonia flow, as shown in Tab. 6.3.

| | | | | | | |
|-------------------------------|---|------|-----|-----|-----|-----|
| NH ₃ , mmol/min | 0 | 0.06 | 0.1 | 0.2 | 0.3 | 0.5 |
| T _{growth} , °C | | | | | | |
| 850 | * | * | * | * | * | * |

Tab. 6.3. Doping parameter variation in experiments using two-step growth of ZnO. Iron-doped GaN layers grown on sapphire were used as substrates for ZnO growth (Chapter 3.2).

As expected, ammonia-doped ZnO samples grown with low amount of DMZn have lower hole density than those discussed in the previous chapter. Fig. 6.27 depicts AFM and SEM images of a ZnO layer doped with 0.2 mmol/min of ammonia. Inverted pits and pyramids observable in the SEM picture have a pronounced hexagonal form. Thus, VI-II ratio decreases the defect density in nitrogen-doped ZnO films, while keeping the defect character the same.

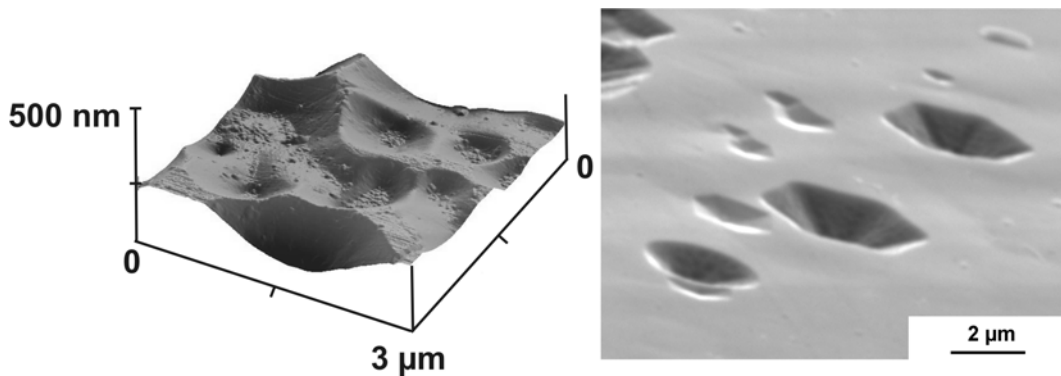


Fig. 6.27. AFM (left) and SEM (right) images of ZnO doped with a low amount of ammonia (~ 0.2 mmol/min).

Similarly to the samples discussed in the Chapter 6.3.1, the structural quality of undoped ZnO layer is better than that of the doped layers, as concluded from θ - 2θ - and ω -scans in $(10\bar{1}0)$ and (0002) geometries (Fig. 6.28). ZnO samples, doped with higher ammonia flow, show about the same variation of FWHM of (0002) ω - and 2:1-scans (Figs. 6.17 - 6.18) in comparison with those of the samples discussed in this chapter (Fig. 6.28). The doped ZnO films grown with reduced DMZn flow show nearly constant FWHM of 2:1 scans performed

* Other growth conditions were as described in Chapter 5.2.3. The growth time is proportionally increased to achieve a layer thickness similar to the layers described in Chapter 6.3.1 (1.5 μm).

in $(10\bar{1}0)$ geometry and varies from $\sim 140''$ to $\sim 170''$. ZnO samples doped with 0.9 – 3.2 mmol/min (Chapter 6.3.1, Fig. 6.17) show FWHM values of 2:1 scans performed in $(10\bar{1}0)$ geometry varying from $\sim 700''$ to $\sim 800''$. ZnO samples grown at 800 °C and 900 °C also show significantly broader XRD peaks (Fig. 6.21, top). Thus, increase of the VI-II ratio does not lead to the improvement of crystalline quality of ammonia-doped ZnO.

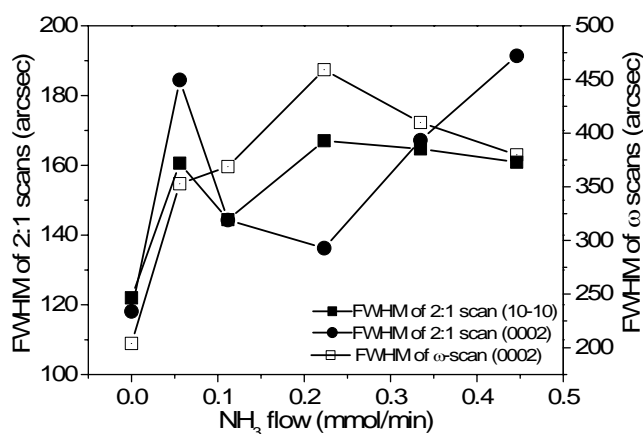


Fig. 6.28. FWHM values obtained from XRD θ - 2θ scans around $(10\bar{1}0)$ and (0002) ZnO layers (left axis) and ω -scans in (0002) geometry (right axis) versus ammonia flow.

No direct correlation between the variation of the ammonia flow and the values of the lattice parameters was observed (Fig. 6.29). On the one side, c - and a -lattice parameters are varying in the relatively small range (10^{-4} nm), similarly to the ZnO samples grown as described in Chapter 6.3.1 (Fig. 6.16). On the other side, the undoped ZnO layers, discussed in the Chapter 5.2.3, show no lattice parameter variation upon decrease the DMZn flow from 1.1 to 0.55 mmol/min too. This indicates that ammonia doping has no influence on the strain state of ZnO films independent on the II-VI ratio. For the samples grown in this series of experiments no cathodoluminescence or photoluminescence measurements were performed.

All samples demonstrate n-type conductivity in capacitance-voltage measurements. The carrier concentration of the non-annealed ZnO increases with an increase of the ammonia flow (Fig. 6.30). This increase of carrier concentration in non-annealed ZnO samples with an increase of ammonia flow was also observed for samples discussed in Chapter 6.3.1 (Fig. 6.26). This can be attributed to the generation of structural defects induced by doping, which is also supported by XRD measurements discussed above. RTA of the undoped sample does not influence the carrier concentration (Fig. 6.30). In contrast to that, RTA results in a decrease of the carrier concentration for some doped samples (Fig. 6.30). This effect is especially pronounced for the sample doped using 0.33 mmol/min of ammonia. This sample

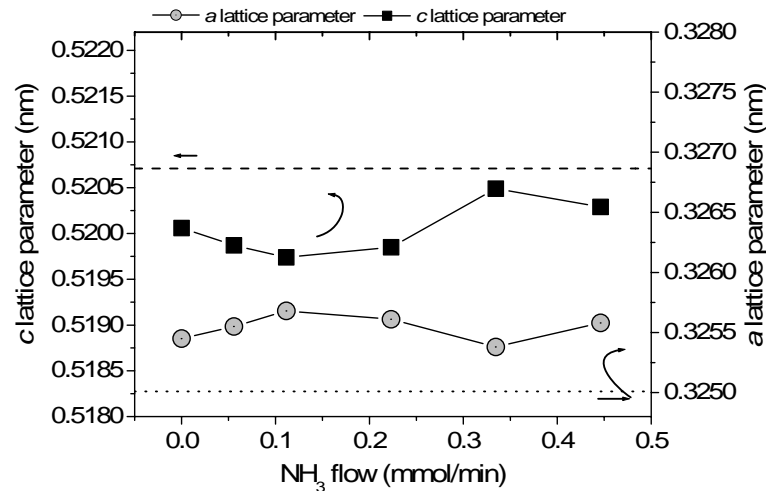


Fig. 6.29. *c*- and *a*- lattice parameters of ZnO films versus the ammonia flow. Dashed and dotted horizontal lines indicate the relaxed values of ZnO lattice parameter [Lan02].

shows a systematical decrease of the carrier concentration with an increase of the RTA temperature. RTA at 1000 °C lead to a severe degradation of the layers, and no electrical measurement was possible. In order to get rid of this effect, the 5×5 mm² samples were put face to face on a ZnO substrate and then annealed during 10 min in oxygen ambient. For the undoped sample this procedure does not significantly change the carrier concentration. Face to face annealing at 1000 °C of the sample doped with 0.11 mmol/min of ammonia results in a carrier concentration comparable with that of the same sample annealed at 800 °C in the usual way. The same annealing of the sample doped with 0.33 mmol/min of ammonia does not significantly change the carrier concentration achieved after RTA in the usual way at 950 °C.

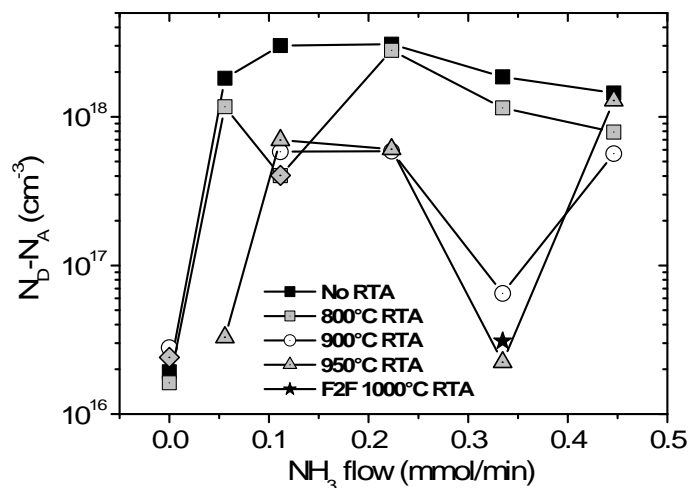


Fig. 6.30. Carrier concentration of the ZnO samples annealed at different temperatures versus the ammonia flow. F2F 1000 °C points to the face-to-face RTA at 1000 °C.

In conclusion, the lowest carrier concentration achieved in this series is around 10¹⁶ cm⁻³ (Fig. 6.30, the sample doped with 0.3 mmol/min of ammonia) is similar to that of two-step grown samples from chapter 6.3.1 (Fig. 6.26, a), the samples grown at 800 °C, doped with 0.2

mmol/min and 0.4 mmol/min of ammonia). Higher ammonia flows or growth temperatures resulted in surface and structural damage of films. Although no p-type conductivity is achieved in these growth series of experiments, further research on ZnO doping using ammonia and implementation of new growth methods can result in better results.

6.4. UDMHy

Unsymmetrical dimethylhydrazine is often used for the growth of nitrides and nitrogen-containing semiconducting compounds in the recent time, and can be an alternative nitrogen precursor to ammonia. The use of UDMHy instead of ammonia is possibly more effective for HT ZnO doping because it fully decomposes at 800 °C, while ammonia decomposes at higher temperatures (Chapters 8.2.1 – 8.2.2). Until now no studies on the ZnO doping with nitrogen using UDMHy were reported. For doping with UDMHy, two- and three-step growth methods were employed in this work.

6.4.1. Two-step Growth

In two-step growth, UDMHy flows were varied on the HT step as shown in Tab. 6.4. The growth rate of the doped ZnO is smaller than the undoped one, probably due to the increase of the total reactor flow. A browning of ZnO was observed when UDMHy flows were

| UDMHy, mmol/min | 0 | 0.03 | 0.05 | 0.06 | 0.09 |
|--------------------------|---|------|------|------|------|
| T_{growth} , °C | | | | | |
| 850 | * | * | * | * | * |

Tab. 6.4. Doping parameter variation in experiments with two-step growth of ZnO.

higher than 0.06 mmol/min. However, the samples were not so dark brown as ammonia-doped ZnO (Fig. 6.12, c)). Similarly to ammonia-doped, the brown UDMHy-doped ZnO bleached out after post-growth RTA.

The surface of UDMHy doped layers consists of pits and inverted hexagonal pyramids, as evaluated from SEM (Fig. 6.31) and AFM (Fig. 6.32) measurements. Compared to undoped ZnO, the surface of doped samples contains more surface defects (Fig 6.32). UDMHy has stronger effect on the surface morphology of ZnO than ammonia, although its flow is one order of magnitude lower (Fig. 6.11).

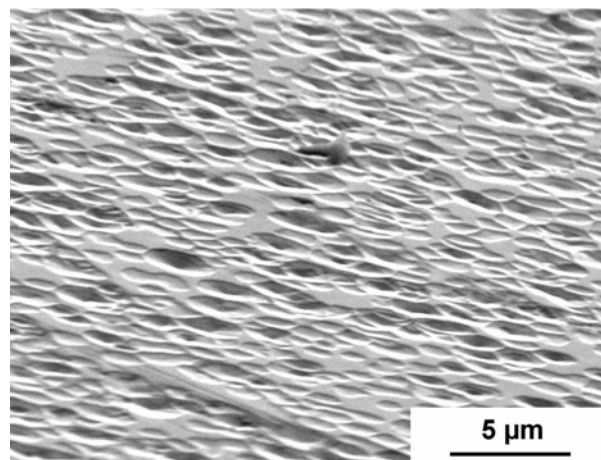


Fig. 6.31. SEM image of ZnO doped with UDMHy.

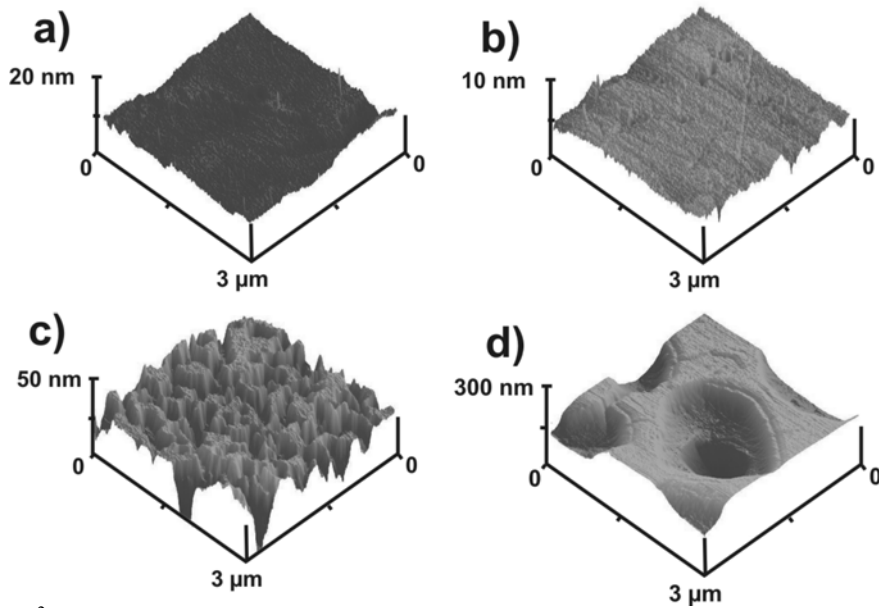


Fig. 6.32. $3 \times 3 \mu\text{m}^2$ AFM images of UDMHy-doped ZnO. a) undoped ZnO, rms roughness: 0.5 nm; b) UDMHy: 0.03 mmol/min, rms roughness: 0.7 nm; c) UDMHy: 0.06 mmol/min, rms roughness: 7.1 nm; d) UDMHy: 0.09 mmol/min, rms roughness: 36 nm.

The FWHM values obtained from XRD 2:1- and ω -scans of not annealed ZnO are increasing with increasing UDMHy flow to 0.06 mmol/min (Fig. 6.34). The sample grown with 0.09 mol/min of UDMHy shows a slightly smaller FWHM values. Thus, UDMHy doping degrades the crystalline quality of ZnO. Similar effect was observed for ZnO layers doped using ammonia (Chapter 6.3). Additionally, FWHMs of ω -scans of (0002) ZnO doped using UDMHy and ammonia are changing from $250''$ to $500''$ and $350''$ to $470''$, respectively (Figs. 6.28 and 6.32)*. FWHM values of the 2:1 XRD scans of (0002) and $(10\bar{1}0)$ of ammonia-doped ZnO are changing from $140''$ to $190''$ and from $140''$ to $170''$, respectively (Fig. 6.28). In the case of UDMHy doping they vary from $120''$ to $250''$ ((0002) scan), and from $120''$ to $300''$ ($(10\bar{1}0)$ scan) (Fig. 6.33, a)). No systematical variation of the lattice parameters with an increase of the UDMHy flow is observed (Fig. 6.33, b)). The variation of the lattice parameters is small ($\sim 10^{-4}$ Å for c -lattice parameters, and $\sim 10^{-5}$ Å for a -lattice parameters). Compared to ZnO films doped using ammonia, a - and c -lattice parameters of ZnO doped using UDMHy are lying in the same range, (Figs. 6.29 and 6.33, b)). Thus, ammonia and UDMHy doping have about the same influence on the crystalline quality of ZnO films.

The intensity of the low temperature (4K) photoluminescence detected from the doped layers is lower compared to that of undoped reference sample (Fig. 6.35). The undoped sam-

* This comparison is performed with the samples from Chapter 6.3.2. Higher ammonia flows resulted in larger FWHM values, Chapter 6.3.1.

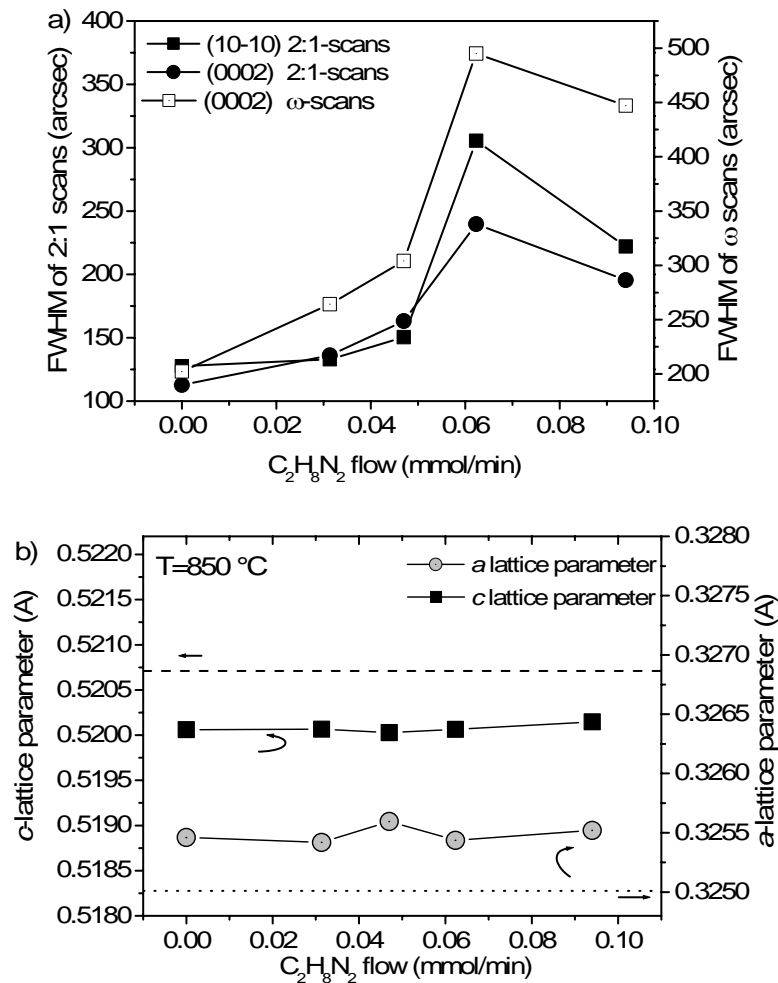


Fig. 6.33. a) FWHM values obtained from XRD θ - 2θ scans in $(10\bar{1}0)$ and (0002) geometries and ω -scans in (0002) geometry versus UDMHy flow. b) c - and a -lattice parameters of ZnO versus UDMHy flow. Dashed and dotted lines represent the relaxed values of ZnO lattice parameters [Lan02].

ple shows a large amount of recombination lines in the NBE spectral region, green luminescence and weak DAP band (Figs 6.34 and 6.35). Even a small amount of UDMHy strongly influences the character of the PL spectrum. The DAP band is strongly pronounced with well resolved LO phonon replicas. When the UDMHy flow is increased, the DAP is still intensive but loses its structure. Fig. 6.35 shows 4K PL spectra of a ZnO layer doped with nitrogen using 0.03 mmol/min UDMHy flow and annealed at 800, 900, 950 and 1000 °C. An increase of the RTA temperature up to 950 °C leads to an increase of the PL intensity (see inset in Fig. 6.35). RTA at 1000 °C lead to a destruction of the layer. Probably due to this damage the luminescence intensity is decreasing. Besides, samples annealed at different temperatures show different spectral features. Fig. 6.39 shows the NBE luminescence of those layers. Free exciton recombinations (X_{af} - X_{al}) in the spectrum shown in Fig. 6.37, are followed by neutral donor bound excitons (I_5 , I_8 , I_9 ; I_5 line is not shown in Fig. 6.36, it lies in between I_{8a} - I_4).

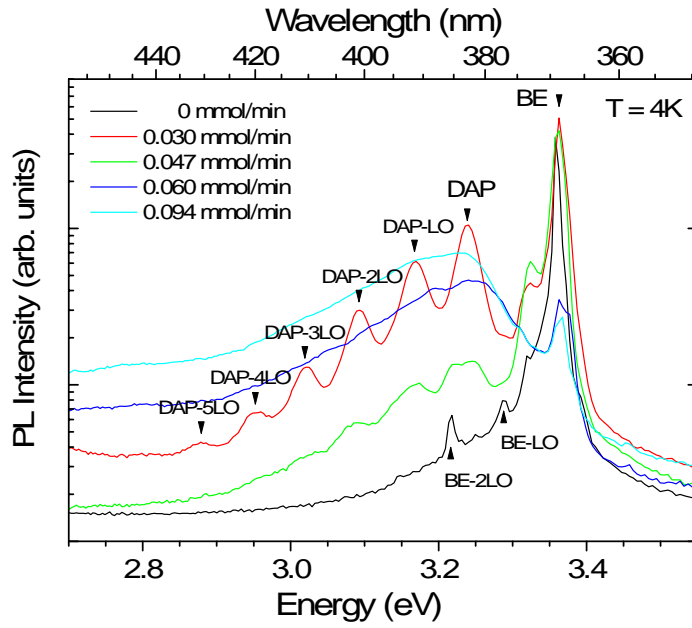


Fig. 6.34. LT PL spectra of as-grown UDMHy-doped ZnO.

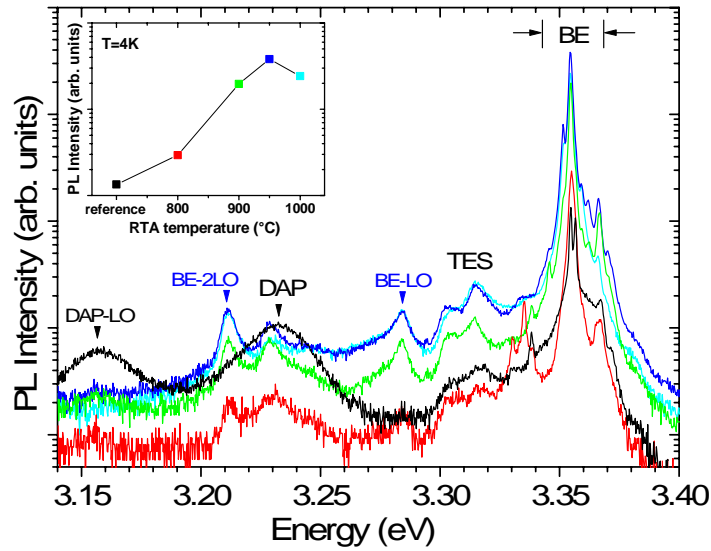


Fig. 6.35. LT PL spectra of annealed UDMHy-doped ZnO. UDMHy flow: 0.03mmol/min.

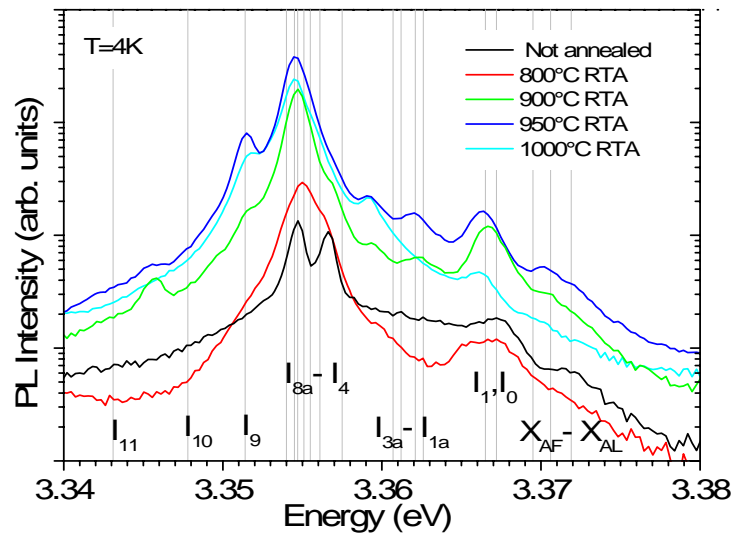


Fig. 6.36. NBE LT PL spectra of annealed ZnO doped with 0.03 mmol/min of UDMHy.

Raman measurements demonstrate the appearance of N-related modes in the spectrum with an increase of UDMHy flow (Fig. 6.37, top). The intensity of the N-related peaks monotonically increases with an increase of the UDMHy flow, which indicates a successful incorporation of nitrogen into the ZnO films. Upon annealing N-related peaks intensity is decreasing (Fig. 6.37, bottom).

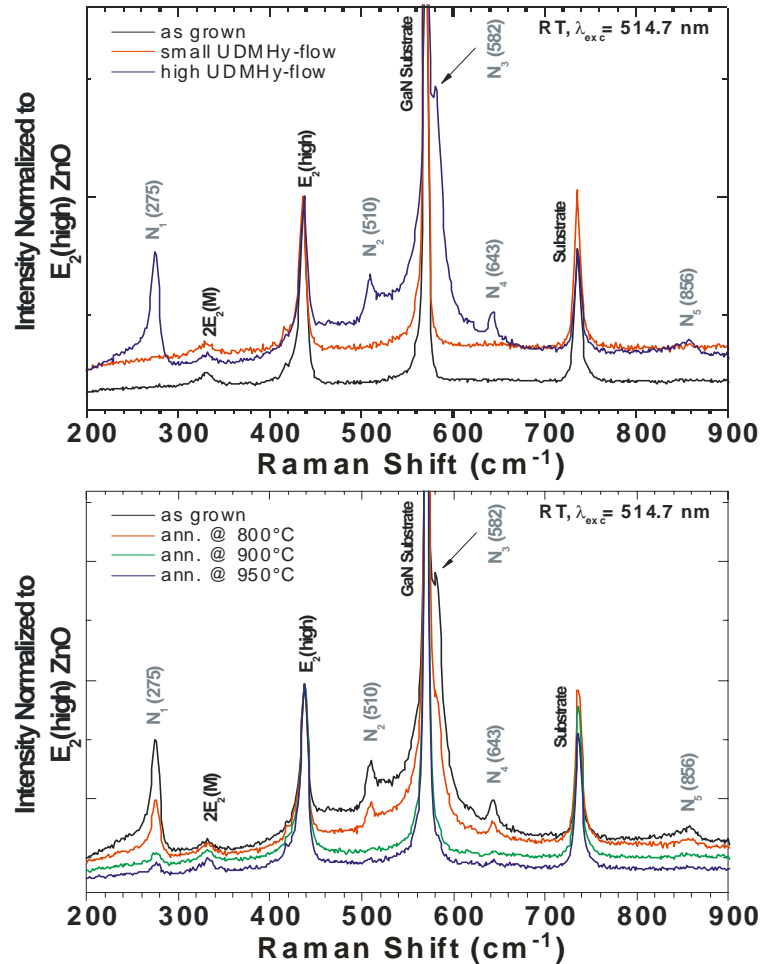


Fig. 6.37. Raman spectra of ZnO samples doped with different amounts of UDMHy. Top: as-grown, and bottom: annealed at different temperatures.

Capacitance-voltage measurements have revealed a strong influence of the doping concentration and the RTA conditions on the electrical properties of the ZnO layers. All samples show n-type conductivity, and no p-type conductivity was observed. Before the samples were annealed, strong increase in the carrier concentration with increasing UDMHy flow was observed (Fig. 6.38). A similar effect was observed for the samples doped with ammonia. Taking into account the results of XRD and Raman measurements, this effect can be attributed to the increase of the structural defect concentration with an increase of UDMHy flow. Besides, hydrogen incorporation from the UDMHy molecule can be also responsible for the increase of

the carrier concentration. A systematical increasing of the RTA temperature up to 950 °C leads to a decrease in the carrier concentration for the doped samples, while the undoped reference sample does not show a significant change of the carrier concentration. Probably, RTA leads to a removal of hydrogen which results in a decrease of the carrier concentration in the annealed films.

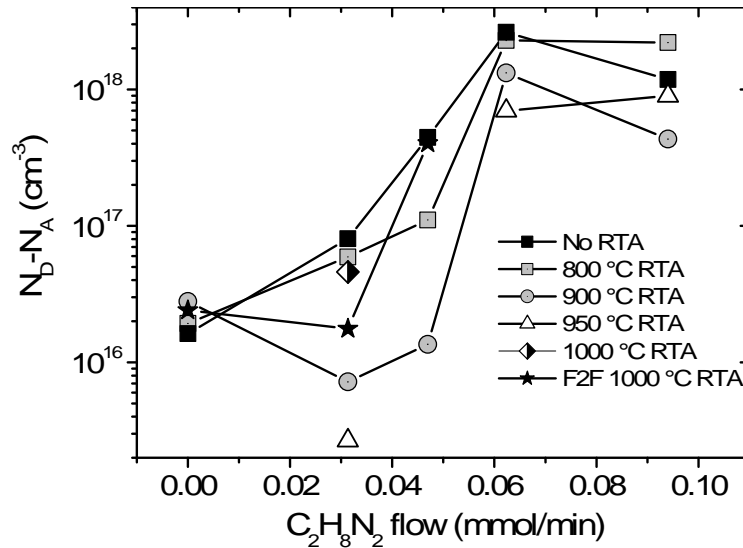


Fig. 6.38. Carrier concentration of ZnO films doped with different amounts of UDMHy and annealed at different temperatures.

In conclusion, compared to ammonia doping (Chapter 6.3.2), UDMHy has similar influence on ZnO surface morphology and crystalline properties while its flow is one order of magnitude lower. A low amount of UDMHy (0.03 mmol/min - 0.05 mmol/min) leads to strongly pronounced DAP band with well resolved LO phonon replicas observed in LT PL measurements. When the UDMHy flow is increased, the DAP is still intensive but loses its structure. The intensity of the N-related peaks in Raman spectra monotonically increases with an increase of the UDMHy flow. These effects were not that pronounced in the case with ammonia doping experiments. Three-step growth method can be applied for the improvement of the ZnO quality in doping experiments using UDMHy. A more detailed study of the samples for UDMHy flows from 0 mmol/min to 0.05 mmol/min is needed, since the samples doped with nitrogen in that UDMHy flow range show decrease of the carrier concentration. Further experiments with UDMHy doping have been performed, Chapter 6.4.2.

6.4.2. Three-step Growth

Nitrogen doping of ZnO films using UDMHy resulted in the drop of N_d-N_a value by nearly two orders of magnitude after RTA processing and strongly pronounced DAP band with well resolved LO phonon replicas in the luminescence spectrum (Chapter 6.4.1). To further study the properties of ZnO, the doping using UDMHy was performed using three-step growth, Tab. 6.5.

| UDMHy, mmol/min $T_{\text{growth}}, ^\circ\text{C}$ | 0 | 0.01 | 0.018 | 0.025 | 0.03 | 0.04 | 0.05 |
|---|---|------|-------|-------|------|------|------|
| 800 | | | | * | | | |
| 850 | * | * | * | * | * | * | * |
| 900 | * | | | * | | | |

Tab. 6.5. Doping parameter variation in experiments with three-step growth of ZnO. No iron doping of underlying GaN layer was performed.

From *in-situ* reflectometry measurements, the growth rate of UDMHy-doped ZnO was the same compared to the reference samples. The AFM rms roughness of undoped ZnO layers was 0.2 nm ($3 \times 3 \mu\text{m}^2$ scanning area), which is smaller compared to the undoped two-step grown ZnO (0.5 nm). UDMHy doping results in a slightly rougher ZnO surface (0.4 nm, Fig. 6.39 b), which is comparable to two-step grown ZnO (0.7 nm, Chapter 6.4.1). The surface de-

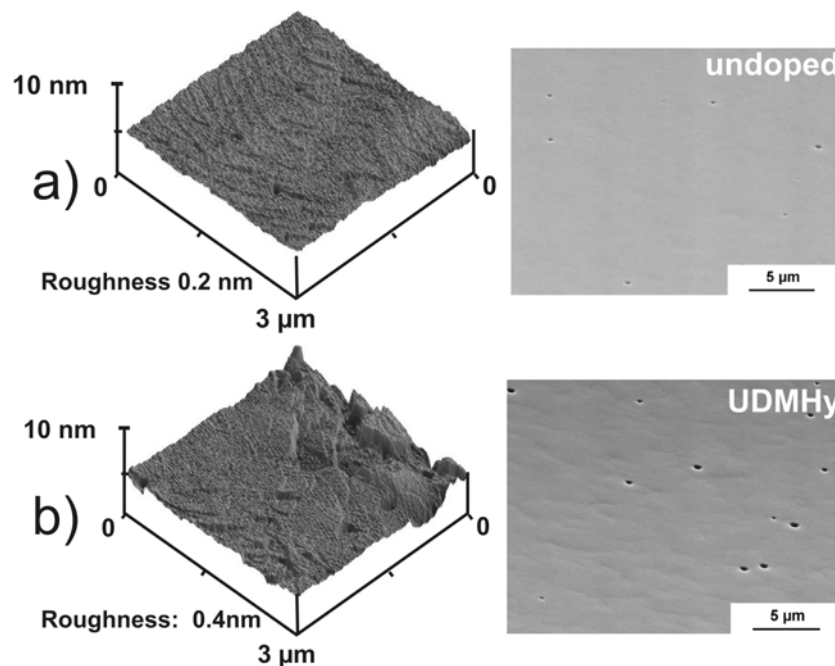


Fig. 6.39. Surface morphology of a) undoped, b) UDMHy doped ZnO layers. The main layer growth temperature is the same for all the layers (850 °C).

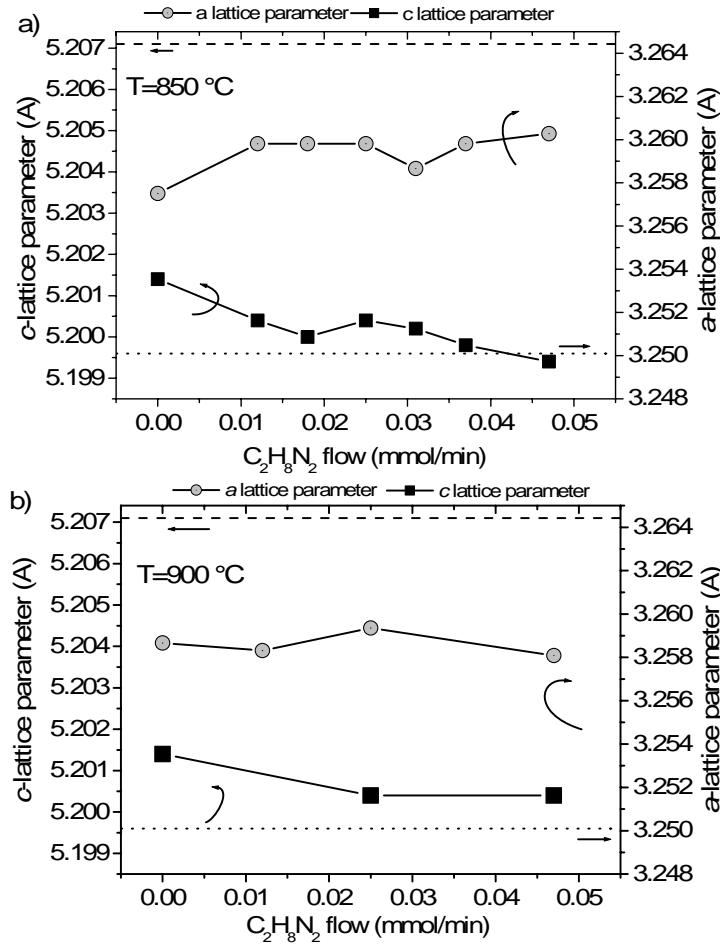


Fig. 6.40. Lattice parameters of UDMHy-doped ZnO. Dashed and dotted lines denote lattice parameters of relaxed ZnO [Lan02].

fect density is slightly higher in the doped than in the undoped ZnO, and lower than in two-step UDMHy-doped ZnO.

The variation of *a*- and *c*-lattice parameters is about 10^{-3} Å (Fig. 6.40). Two-step UDMHy doping resulted in the similar parameters, Fig. 6.33, b). This was also observed for two- and three-step grown undoped ZnO layers (Chapters 5.2.3 and 5.3, respectively). The thickness of the NO-ZnO film is thin (half of the period of reflected intensity in *in-situ* reflectometry measurement, Fig. 5.62) and thus does not influence the lattice parameters of ZnO. The undoped ZnO films grown at 850 °C and 900 °C have the smallest FWHM values (Fig. 6.41). These values are higher when compared to FWHM of XRD measurements performed in the same geometries for two-step grown undoped ZnO, Fig. 6.41, a). Small UDMHy flow increases the FWHM values (0002) 2:1 scans and (0002) ω -scans (Fig. 6.44), while the FWHM value of (10 $\bar{1}$ 0) 2:1 scan stays nearly unaltered. Comparison of FWHM values of XRD measurements of the samples grown at different temperatures reveals no direct correlation.

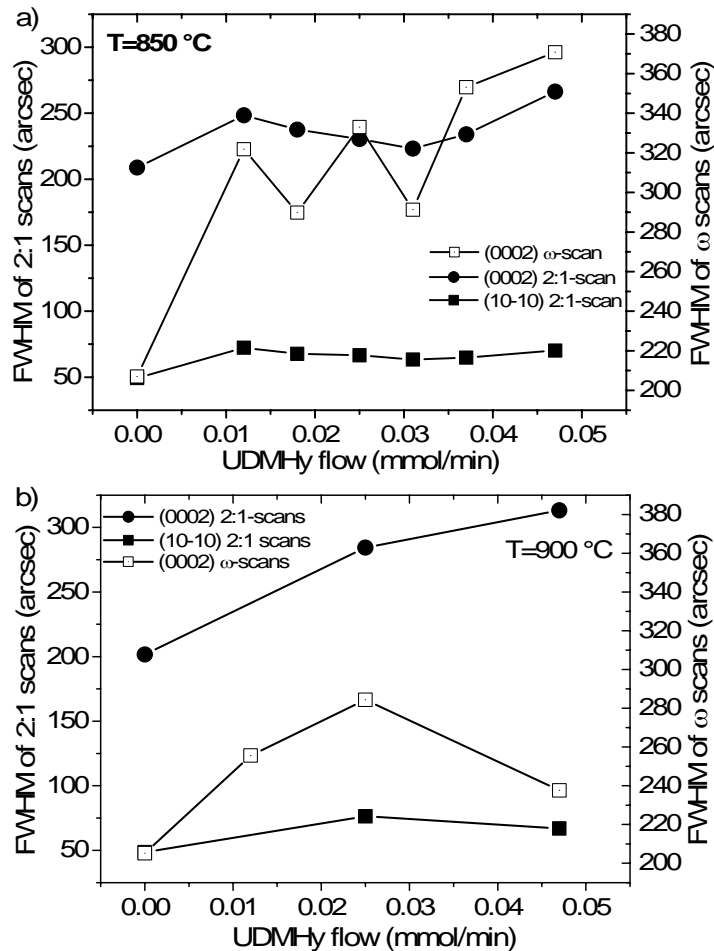


Fig. 6.41. Full width at half maximum obtained from X-ray diffraction measurements of ZnO layers doped with UDMHy. Growth temperatures are 850 °C. a). and 900 °C. b).

No reliable indication of a p-type conductivity was observed in capacitance-voltage measurements. ZnO grown at 850 °C and doped with 0.03 - 0.04 mmol/min of UDMHy were peeled off after RTA at 900 °C. Samples grown at 900 °C could not be measured after RTA at temperatures exceeding 900 °C, Fig. 6.43, b). As it has already been discussed in Chapter 5.3, three-step grown reference samples show reduction of the carrier concentration upon annealing at 850 °C, which was not observed in the case of two-step grown undoped ZnO samples. Carrier concentration of annealed at 850 °C three-step grown undoped ZnO reaches the value of undoped two-step grown ZnO. Considering the influence of RTA on carrier concentration of three-step grown and doped at 850 °C and 900 °C ZnO films, no systematical lowering of this value is observed as compared to the two-step grown film, Figs. 6.42 and 6.43. Still, for low concentrations of UDMHy doping, a reduction in the carrier concentration was observed after annealing at 850 °C in comparison to the non-annealed samples, Fig. 6.42 a).

In conclusion, low level of ZnO doping using UDMHy results in the slight degradation of crystalline and surface morphology properties, and does not influences the strain state of

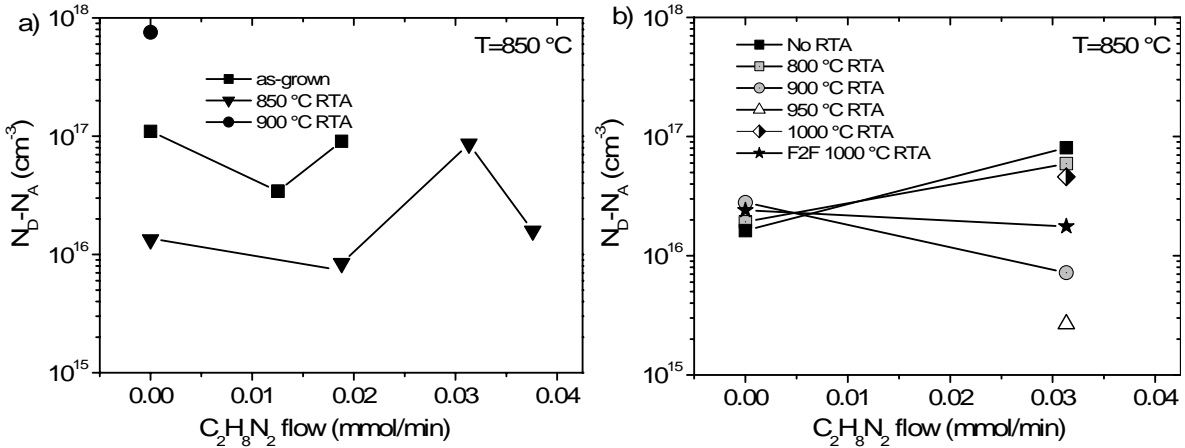


Fig. 6.42. Carrier concentration obtained from capacitance-voltage measurements of ZnO layers doped with UDMHy. Growth temperature: 850 °C. a) three-step grown and doped ZnO; b) Two-step grown and doped ZnO.

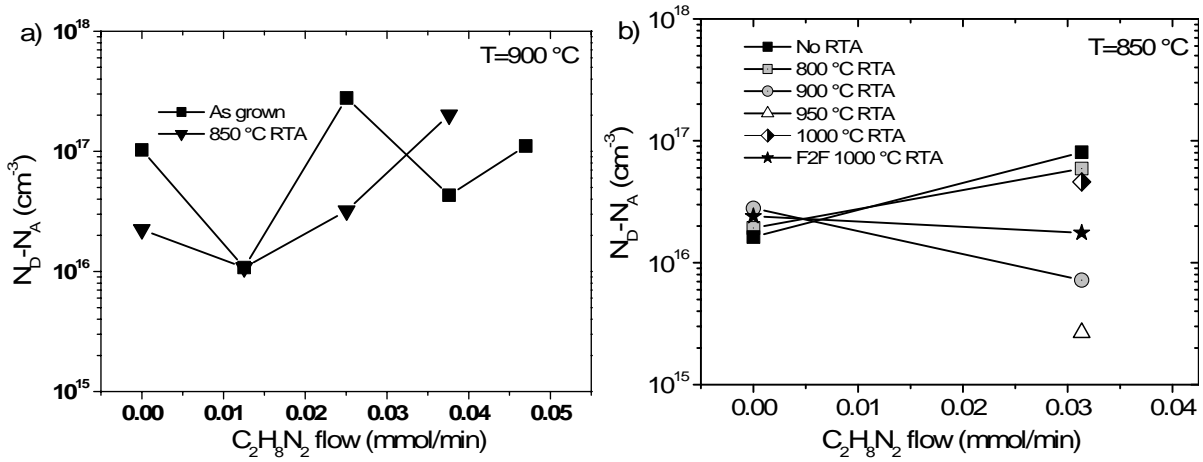


Fig. 6.43. Carrier concentration obtained from capacitance-voltage measurements of ZnO layers doped with UDMHy. a) three-step grown and doped ZnO, growth temperature 900 °C; b) Two-step grown and doped ZnO, growth temperature 850 °C.

the ZnO layers. Three-step growth improves the surface smoothness of ZnO but makes the films instable during RTA processing. Although no p-type conductivity was achieved in two- and three-step grown ZnO, two-step growth is more promising for doping than three-step growth.

7. Summary

In this work new Metalorganic Vapor Phase Epitaxy methods for the growth and doping of ZnO high-quality layers were developed. Acetone, iso-propanol, diethylether, tertiary-butanol, and N₂O precursors were tested under different growth conditions. ZnO growth using iso-propanol provided good surface morphology and intense cathodoluminescence of the films. However, it resulted in the prereactions which narrowed the growth processing of the films. Although this effect was not observed in experiments with acetone and diethyl-ether, a strong carbon contamination took place. Probably due to carbon doping the acetone- and diethyl-ether grown films did not show ZnO correlated luminescence in cathodoluminescence experiments. No ZnO reflection in XRD measurements of ZnO grown using diethyl-ether was found. Thus, the use of iso-propanol, acetone or diethyl-ether is inappropriate for ZnO growth. t-BuOH-grown ZnO films show narrow intensive near-band gap cathodoluminescence emission. The use of tBuOH offers a prereaction-free flexible manipulation of the ZnO properties by variation its growth temperature. Together with an *in-situ* annealing, it results in smooth films with good optical and structural qualities. Compared to iso-propanol, acetone, or diethyl-ether, tertiary butanol is the best O-precursor for the growth of ZnO at low-temperatures. The use of N₂O offered prereaction-free high-temperature growth of ZnO. The optical and crystalline quality of ZnO layers grown with N₂O is superior to those of ZnO grown with tertiary-butanol. However, in contrast to very smooth, homogeneous surface of *in-situ* annealed tBuOH-grown ZnO layers, N₂O-grown layers demonstrated rough spungy surface. The combination of LT ZnO growth using tBuOH with HT ZnO growth using N₂O has improved the surface morphology, crystalline and optical properties of ZnO in comparison to the best single-grown LT or HT ZnO. The best ZnO layers have remarkably higher crystalline quality than the underlying GaN. Very narrow (FWHM is about 160^{''}) high intensity X-ray diffraction peaks are observed in ω -scans around (0002) geometry for ZnO grown at 900 °C on 0.88 μm – thick ZnO buffer layer. The use of different O-precursors, carrier gases and the temperature processing steps in one growth run broadens the space for further improvement of ZnO properties. *In-situ* annealing of LT ZnO layer in two-step grown ZnO did not lead to a drastic changes of the surface morphology and crystalline properties. However, it lowered the luminescence intensity from the ZnO surface. The use of higher VI-II ratio lead to a stable growth of smooth ZnO, and the high-intensity narrow-peak excitonic emission of photoluminescence. High morphological, structural and optical quality of ZnO layers

grown using two- and three-step growth methods has opened prospect for doping experiments.

For nitrogen doping of ZnO, NH_3 , UDMHy, Diisobutylamine, and NO were used. No reproducible and reliable experimental results on the achievement of p-type conductivity with those precursors achieved. From the results of X-ray diffraction, electrical and photoluminescence measurements nitrogen was not incorporated with the use of NO. However, the addition of NO during the high-temperature growth step promotes a smooth surface morphology with a strong drop in growth rate, which is reversely proportional to the NO flow. Nitrogen doping of ZnO using Diisobutylamine leads to the degradation of its surface morphology and its crystalline quality without influence on the strain in ZnO film stack. RTA of diis-doped ZnO films represents an issue because of peeling effects. A reduction in the carrier concentration with increasing annealing temperature was observed for some doped samples. Additionally, low vapour pressure of Diis does not allow the flexible variation of MOVPE growth conditions. Ammonia did not influence the growth rate of ZnO, but surface roughening occurred. The hole density in ammonia-doped ZnO is varying around 10^6 cm^{-2} . A solution was found by use of a lower DMZn flow on the HT growth step. RTA has a small impact on the Raman spectra of low N-doped ZnO. Only a highly doped sample (0.9 mmol/min) grown at $800 \text{ }^\circ\text{C}$ shows a drastic change in the Raman spectra which can be attributed to NH_3 doping. This sample, however, has shown higher carrier concentration in initial and RTA-treated films as compared to low N-doped films. In cathodoluminescence measurements with an increase of ammonia flow decreases the integrated intensity and increases the FWHM of the recombination peaks. A higher level of doping results in the reversion of the spatial distribution of the luminescence relative to the undoped ZnO: the flat region of the film show lower energy emission in comparison to the region of the holes. The lowest carrier concentration achieved in experiments with ammonia is around 10^{16} cm^{-3} . Compared to ammonia doping, UDMHy has similar influence on ZnO surface morphology and crystalline properties while its flow is one order of magnitude lower. A low amount of UDMHy (0.03 mmol/min - 0.05 mmol/min) leads to strongly pronounced DAP band with well resolved LO phonon replicas in luminescence spectrum. When the UDMHy flow is increased, the DAP is still intensive but loses its structure. The intensity of the N-related peaks in Raman spectra monotonically increases with an increase of the UDMHy flow. Nitrogen as an acceptor can be successfully introduced in ZnO using UDMHy, as it is clearly visible from a reduction in the carrier concentration after RTA, and the behavior of the DAP luminescence.

8. Appendix

8.1.1. Dimethylzinc

The DMZn molecule is a non-polar covalently bonded monomeric compound with two collinear zinc-carbon bonds (formally sp hybridized), as was evaluated from a X-ray study [Run63] and the vibrational spectrum [Boy50]. 50 % of DMZn is decomposed at 350°C by Zn-C bond homolysis [Jen92], see Fig. 8.2. The mechanism of homogeneous thermal decomposition was investigated in MOVPE reactor by Fan *et al.* and Dunlop *et al.* [Fan95, Dun70].

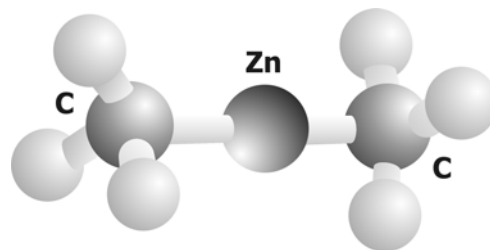


Fig. 8.1. Structural formula of DMZn.

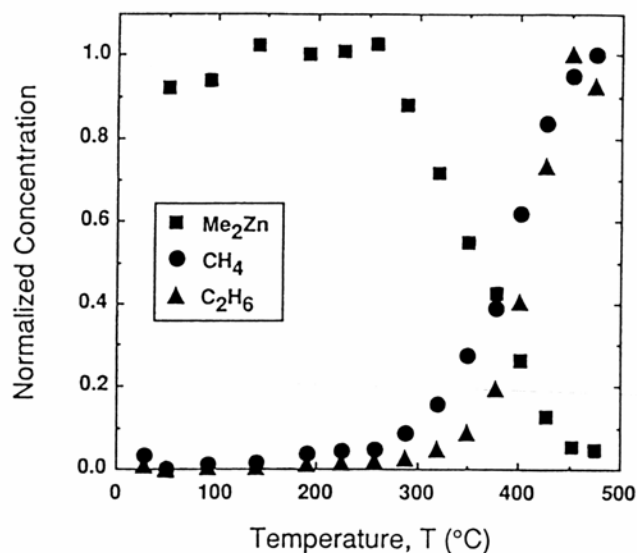


Fig. 8.2. Pyrolysis of DMZn monitored by mass spectroscopy [Jen92].

8.1.2. Iso-propanol

Iso-propanol, $\text{C}_3\text{H}_7\text{OH}$, is an alcohol. Fig. 8.3 shows its structure. The premature reactions observed during ZnO growth using iso-propanol as oxygen precursor* can be attributed to the elimination of alkyl groups from DMZn by acidic hydrogen from iso-propanol.

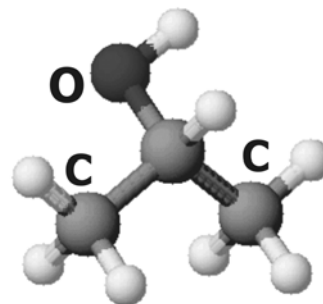


Fig. 8.3. Structural formula of iso-propanol (after Michael Opsölder).

* also called 2-Methyl-2-propanol, Trimethylcarbinol.

8.1.3. Acetone

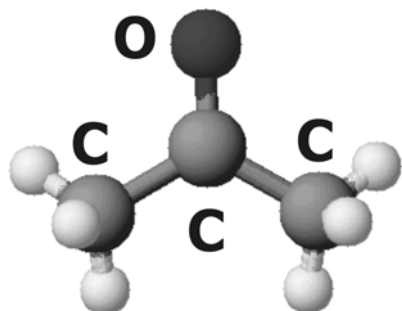


Fig. 8.4. Structural formula of acetone (after Michael Opsölder).

The chemical formula of acetone* is $\text{CH}_3(\text{CO})\text{CH}_3$ and its structure is shown in Fig. 8.4. Acetone was first prepared in 1610 by Jean Béguin by the pyrolysis of lead acetate (Saturn's salt). The name acetone was proposed by Bussy in 1833. The thermal decomposition of acetone is well studied since it has a high octane number and can be used as a fuel for cars [Ric34].

8.1.4. Diethyl-Ether

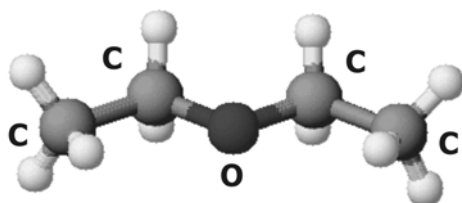


Fig. 8.5. Structural formula of diethyl ether (after Michael Opsölder).

Diethylether**, with the structural formula $\text{CH}_3\text{CH}_2\text{OCH}_2\text{CH}_3$, was discovered by Raymundus Lullius, in 1275. It was first synthesized by Valerius Cordus in 1540. Crawford Williamson Long, M.D., was the first surgeon to use it as an anesthetic agent in 1842. An ether can be generally represented by the

formula $\text{R}_1(\text{O})\text{R}_2$. Fig. 8.5 shows the structure of the Diethylether molecule.

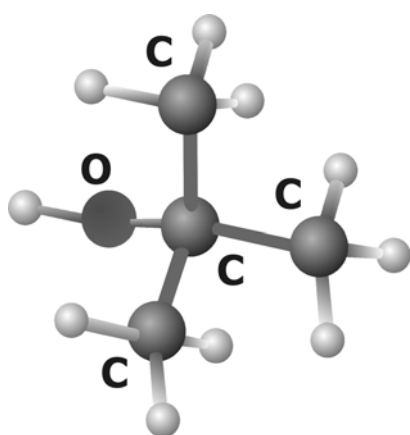


Fig. 8.6. Structural formula of $(\text{CH}_3)_3\text{COH}$, (tBuOH).

8.1.5. Tertiary-butanol

Tertiary-butanol, $(\text{CH}_3)_3\text{COH}$ (tBuOH) is the simplest tertiary alcohol. Spatial arrangement of the atoms in the single tBuOH molecule is shown in Fig. 8.6.

It is known [Coa65] that the addition of excess alcohol ($\text{R}'\text{OH}$) to R_2Zn compounds displaces only one alkyl group to give alkylzinc alcoxides in

* also called dimethyl ketone or 2-propanone and beta-ketopropane.

** also called ethoxyethane.

the form $RZn(OR')$ [Hah98]. This is supported by investigations on the ZnO deposition from preliminary prepared $RZn(OR')$ [Aul94]. Although these compounds are generally tetrameric in the solid state [Coa85], methyl zinc isopropoxide $MeZnOPr^i$, and methyl zinc tertiarybutoxide $MeZnOBu^t$ oligomers have proved sufficiently volatile to be used in the deposition of ZnO in low pressure CVD, in the absence of an added oxygen source [Aul94]. Coates *et al.* and Matsui *et al.* investigated the structural properties of that adduct using X-ray analysis [Mat66].

Stable adducts can be transported intact to the substrate and decomposed at the growing surface [Oda85]. According to Oda *et al.*, tBuOH provided the best adduct properties for CVD process; i. e. an adduct can be formed at low temperatures, is volatile and stable below 250 °C and decomposes at around 300 °C. According to Coates *et al.*, the advantage of tertiary butanol might be due to its form of a three dimensional structure which is effective for protecting zinc atoms from being attacked by foreign molecules during transportation [Coa85].

8.1.6. N_2O

N_2O^* produces laugh, for which reason it is also called "laughing gas". The molecule is linear and asymmetric with two resonance structures (Fig. 8.7). During MOVPE growth of ZnO using N_2O , the N_2O molecule decomposes into N_2 , O_2 , NO, and O and reacts with the products of $Zn(CH_3)_2$ decomposition. The de-

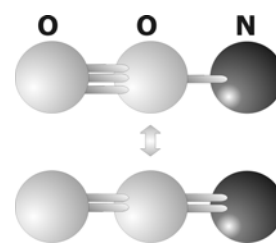


Fig. 8.7. Resonance structures of N_2O .

composition of laughing gas was thoroughly theoretically and experimentally studied e. g. in the investigations of Gusev *et al.* [Gus99]. In contrast to NO, which is a relatively stable molecule, N_2O decomposes rapidly at high temperatures. The reactive oxygen species is generated at the surface of ZnO as an intermediate in catalytic N_2O decomposition over ZnO as established by the studies of Cunningham *et al.* [Cun71]. Much more information is available on the photocatalytic decomposition of N_2O over the ZnO surface but this investigation is not relevant for this study [Kal81].

8.2. N- and P-precursors

8.2.1. NO

* also called dinitrogen oxide; nitrogen monoxide; dinitrogen monoxide; hypo nitrous acid anhydrite; laughing gas; was discovered by Priestley in 1772.

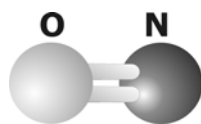


Fig. 8.8. Structural formula of nitric oxide.

Nitric Oxide* is the most stable oxide of nitrogen. It readily loses an electron to form a nitrosyl or nitrosonium ion, NO^+ [Pat03]. Free NO is a stable free radical, because the weak

ON-NO bond hampers dimerization in the gas phase. The decomposition of NO was theoretically and experimentally studied e. g. in the investigations of Ellis *et al.* [Ell99].

8.2.2. Diisobutylamine

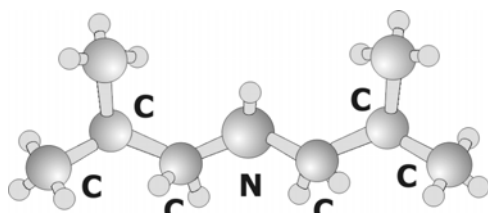


Fig. 8.9. Structural formula of Diisobutylamine.

Diisobutylamine,

$\text{CH}_3\text{CH}(\text{CH}_3)_2\text{CHNHCHCH}(\text{CH}_3)_2\text{CH}_3$, represents a nitrogen atom symmetrically bonded with two $-\text{CHCH}(\text{CH}_3)_2\text{CH}_3$ groups and one hydrogen atom (Fig. 8.9). This compound is liquid at room temperature. During the decomposition of Diisobu-

tylamine in the presence of oxygen nitric oxides are produced. Diisobutylamine has relatively low vapor pressure.

8.2.3. Ammonia

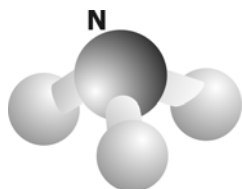


Fig. 8.10. Structural formula of ammonia.

Ammonia** (NH_3) has a tetrahedral geometry (Fig. 8.10). Ammonia is stable at room temperature but begins to decompose at 450°C [Ban75]. In the MOVPE reactor, the decomposition increases with temperature but remains low ($\sim 4\%$ at 950°C)

[Ban75].

8.2.4. Dimethylhydrazine

In contrast to ammonia, asymmetrical dimethyl hydrazine ($(\text{CH}_3)_2\text{NNH}_2$) has two nitrogen atoms, Fig. 8.11. Fig. 8.12 shows the decomposition of dimethylhydrazine as a function of temperature. Dimethylhydrazine starts to decompose at a temperature of 320°C . The evolu-

* also called Nitrogen Monoxide; was discovered by van Helmont in 1620.

** Gaseous ammonia was first isolated by J. Priestley in 1774 and was termed by him "alkaline air." In 1777 Karl Wilhelm Scheele showed that it contained nitrogen, and C. L. Berthollet, in about 1785, ascertained its composition [Shr90].

tion of the reaction products as a function of temperature is given elsewhere [Ast53, Bou00]. From those studies, breaking of the N-N bond by the elimination of the methyl groups at 515°C is the first reaction [Ast53, Bou00]. 50% decomposition is reached at a temperature of 550 °C. The active N radicals recombine with hydrogen above 675 °C. Complete decomposition is achieved at 800 °C.

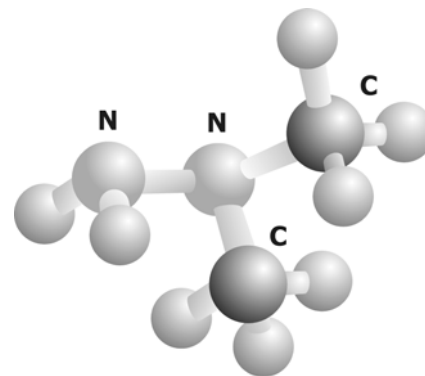


Fig. 8.11. Structural formula of UDMHy.

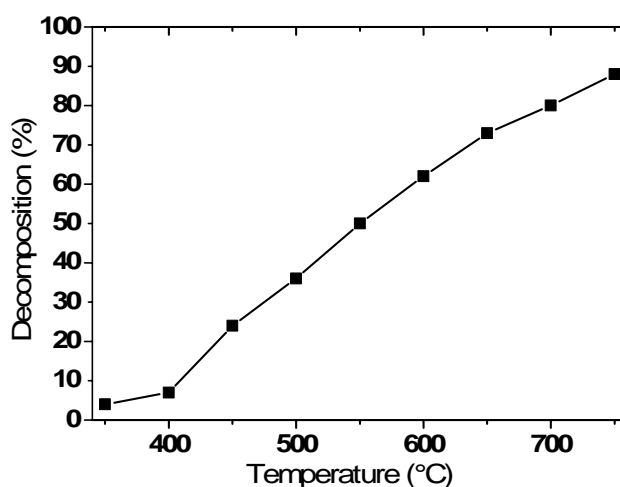


Fig. 8.12. The decomposition of dimethylhydrazine as a function of temperature (after [Bou00], [Ast53]).

8.2.5. Phosphine

Phosphine (PH_3) has a tetrahedral geometry (Fig. 8.13). Phosphine was widely used in semiconductor industry as a dopant source for phosphor. In comparison to a number of theoretical and experimental works on nitrogen doping of ZnO, a number of phosphorus doping studies is significantly smaller, and mostly pulsed laser deposition growth technique is used [Aok00, Ryu00, Ryu02, Mor02, Heo03, Kim03]. Several experiments with phosphine have been performed in this work. The growth conditions of the undoped ZnO layers were similar to those described in Chapter 5.2.2. The Phosphine flow was varied from 0 to 2.23 mmol/min and the growth temperature was 800 °C. In contrast to undoped layers,

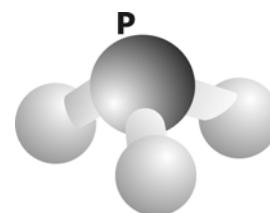


Fig. 8.13. Structural formula of phosphine.

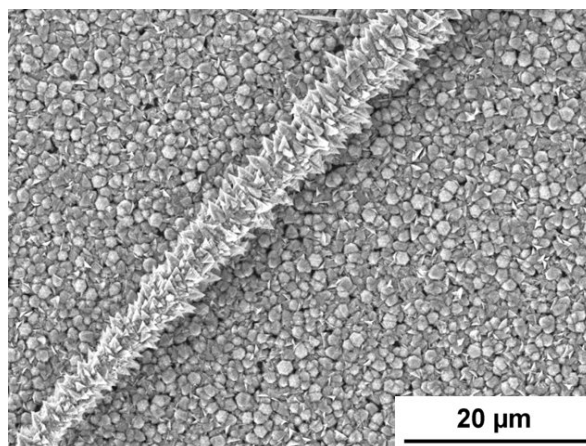


Fig. 8.14. Surface morphology of phosphor doped ZnO layer.

films doped with the flows 0.02 – 0.22 mmol/min of phosphine are polycrystalline with some needle-like depositions ($>100\ \mu\text{m}$ long and $\sim 1\div 5\ \mu\text{m}$ in diameter) on the surface (Fig. 8.14). When the flow of phosphine was increased to 2.23 mmol/min no growth was observed. XRD Θ - 2Θ measurements in different geometries reveal that no ZnO was grown. The carrier concentration and type of conductivity could not be determined due to the rough ZnO surface. Phosphine shows degradation effects on the structural and electrical properties of ZnO. Lower phosphine flow was not possible due to the flow limitation of mass-flow controllers, thus no further experiments with this precursor were performed.

9. References

- [Ale91] H. Alexander, and H. Teichler, *Dislocations*, Materials Science and Technology, **4**, North-Holland Pub. Company, 249 (1991).
- [Aok00] T. Aoki, Y. Hatanaka, and D. C. Look, *Appl. Phys. Lett.* **76**, 3257 (2000).
- [Ash02] M. A. Ashrafi, I. Suemune, H. Kumano, and S. Tanaka, *Jpn. J. Appl. Phys.* **41**, L1281 (2002).
- [Ast53] J. G. Aston, J. L. Wood, and T. P. Zolki, *J. Am. Chem. Soc.* **75**, 6202 (1953).
- [Aul94] J. Auld, D. Houlton, A. C. Jones, R. A. Rushworth, M. A. Malik, P. O'Brien, and G. W. Critchlow, *J. Mater. Chem.* **4**, 1249 (1994).
- [Ave67] M. Aven, *II-VI Semiconducting compounds*, ed. by D. G. Thomas, Benjamin, New York, 1232 (1967).
- [Bag97] D. M. Bagnall, Y. F. Chen, Z. Zhu, T. Yao, S. Koyama, M. Y. Shen, and T. Goto, *Appl. Phys. Lett.* **70**, 2230 (1997).
- [Bag98] D. M. Bagnall, Y. F. Chen, Z. Zhu, T. Yao, M. Y. Shen, and T. Goto, *Appl. Phys. Lett.* **73**, 1038 (1998).
- [Ban75] Ban, J. *Electrochem. Soc.* **122**, 1273 (1975).
- [Bar04] J. Barf, T. Walther, and W. Mader, *Interface Science* **12**, 213 (2004).
- [Bar05] T. M. Barnes, K. Olson, and C. A. Wolden, *Appl. Phys. Lett.* **86**, 112112 (2005).
- [Bet88] S. Bethke, H. Pan, and B. W. Wessels, *Appl. Phys. Lett.* **52**, 2 (1988).
- [Bin86] G. Binnig, C. F. Quate, and Ch. Gerber, *Phys. Rev. Lett.* **56**, 930 (1986); G. Binnig, H. Rohrer, C. Gerber, E. Weibel, *Phys. Rev. Lett.* **49**, 57 (1982).
- [Bou00] E. D. Bourret-Courchesne, K. M. Yu, S. Irvine, A. Stafford, S. A. Rushworth, L. M. Smith, and R. Kanjolia, *ICMOVPE-X*, Sapporo (2000).
- [Bra35] H. Braekken and C. Jore, *Det Norske Videnskabers Skrifter, The Norwegian Science Scripts* **8**, 1 (1935)
- [Bun35] C. W. Bunn, *Proc. Phys. Soc. London* **47**, 835 (1935).
- [But92] T. V. Butkhuzi, A. V. Bureyev, A. N. Georgobiani, N. P. Kekelidze, and Khurlodova, *J. Cryst. Growth* **117**, 366 (1992).
- [Byl78] E. G. Bylander, *J. Appl. Phys.* **49**, 1188 (1978).
- [Car01] W. E. Carlos, E. R. Glaser, and D. C. Look, *Physica B* **308-310**, 976 (2001).
- [Cha75] D. J. Channin, J. M. Hammer, and M. T. Duffy, *Appl. Opt.* **14**, 923 (1975).
- [Che00] Y. Chen, H. J. Ko, S. K. Hong, and T. Yao, *Appl. Phys. Lett.* **76**, 559 (2000).
- [Che01] D. Cherns, and C. G. Jiao, *Phys. Rev. Lett.* **87**, 205504, (2001).

- [Che01] Y. F. Chen, S. K. Hong, H. J. Ko, V. Kirshner, H. Wenisch, T. Yao, K. Inaba, and Y. Segawa, *Appl. Phys. Lett.* **78**, 3352 (2001).
- [Che02] Y. Chen, H. J. Ko, S. K. Hong, T. Yao, and Y. Segawa, *Appl. Phys. Lett.* **80**, (2002).
- [Che05] Z. Q. Chen, A. Kawasuso, Y. Xu, H. Naramoto, X. L. Yuan, T. Sekiguchi, R. Suzuki and T. Ohdaira, *J. Appl. Phys.* **97**, 013528 (2005).
- [Che97] Y. Chen *et al.*, *J. Cryst. Growth* **181**, 165 (1997).
- [Che98] Y. Chen, D. M. Bagnall, H. J. Koh, K. T. Park, K. Hiraga, Z. Q. Zhu, and T. Yao, *J. Appl. Phys.* **84**, 3912 (1998).
- [Chi03] C. H. Chia *et al.*, *Appl. Phys. Lett.* **82**, 1848 (2003).
- [Chr91] J. Christen, M. Grundmann, and D. Bimberg, *J. Vac. Sci. Technol. B*, **9**, 4 (1991).
- [Cim57] A. Cimino, M. Marezio, and A. Santoro, *Naturwiss.* **12**, 348 (1957).
- [Coa65] G. E. Coates and D. Ridley, *J. Chem. Soc.* 1870 (1965).
- [Col62] H. Cole and N. Stemple, *J. Appl. Phys.*, **33**, 2227 (1962).
- [Cun71] J. Cunningham, J. J. Kelly, and Z. L. Penny, *J. Phys. Chem.*, **25**, 118 (1972).
- [Dad99] A. Dadgar, *MOCVD-Wachstum und elektrische Eigenschaften von Eisen und Platinmetallen im Indiumphosphid : Ruthenium, ein thermisch stabiler Kompensator im Indiumphosphid*, Berlin, Mensch-und-Buch-Verl. (1999).
- [Dad00] A. Dadgar, J. Blaesing, A. Diez, A. Alam, M. Heuken and A. Krost, *Jpn. J. Appl. Phys.* **39**, L1183 (2000).
- [Dad03a] A. Dadgar, A. Strittmatter, J. Bläsing, M. Poschenrieder, O. Contreras, P. Veit, T. Riemann, F. Bertram, A. Reiher, A. Krtschil, A. Diez, T. Hempel, T. Finger, A. Kasic, M. Schubert, D. Bimberg, F. A. Ponce, J. Christen, and A. Krost, *Phys. Stat. Sol. C*, **0**, 1583 (2003).
- [Dad03b] A. Dadgar, M. Poschenrieder, A. Reiher, J. Bläsing, J. Christen, A. Krtschil, T. Finger, T. Hempel, A. Diez and A. Krost, *Appl. Phys. Lett.* **82**, 28 (2003).
- [Dat99] L. Date *et al.*, *Surf. Coat. Technol.* **116–119**, 1042 (1999).
- [Dav99] M. W. Davidson and M. Abramowitz, *Optical Microscopy* (1999).
- [Dic94] *Dictionary of organometallic compounds*, CRC Press London-UK (1994).
- [Die00] T. Dietl, H. Ohno, F. Matsukura, J. Cibert, and D. Ferrand, *Science* **287**, 1019 (2000).
- [Du03] G. T. Du *et al.*, *Vacuum* **69**, 473 (2003).
- [Duk77] C. B. Duke, A. R. Lubinsky, S. C. Chang, B. W. Lee, and P. Mark, *Phys. Rev. B* **15**, 4865 (1977).
- [Duk78] C. B. Duke, R. J. Meyer, A. Paton, and P. Mark, *Phys. Rev. B* **18**, 4225 (1978).
- [Dun70] A. N. Dunlop, and S. J. Price, *Can. J. Chem.*, **48**, 3205 (1970).

- [Ege96] H. J. Egelhaaf and D. Oelkrug, *J. Cryst. Growth* **161**, 190 (1996).
- [Ell99] K. A. Ellis and R. A. Buhrman, *IBM J. Res. Develop.* **43**, 3 (1999).
- [Fan01] Z. Q. Fang, D. C. Look, P. Visconti, D. F. Wang, C. Z. Lu, F. Yun, H. Morkoc, S. S. Park, and K. Y. Lee, *Appl. Phys. Lett.* **78**, 2178 (2001).
- [Fan95] G. Fan, N. Maung, T L. Ng, J. O. Williams, and A. C. Wright, *J. Chem. Soc. Faraday Trans.* **91**, 3475 (1995).
- [Flo01] J. A. Floro, E. Chason, in: O. Auciello, A. R. Krauss (Eds.), *In-situ Real-Time Characterization of Thin Films*, Wiley, (2001).
- [Flo02] J. A. Floro, E. Chason, R. C. Cammarata, D. J. Srolovitz, *MRS Bulletin* **27**, 19 (2002).
- [Fon01] P. Fons, *et al.*, *J. Cryst. Growth* **227**, 911 (2001).
- [Fon99] P. Fons, *et al.*, *J. Cryst. Growth* **201–202**, 627 (1999).
- [Gar02] N. Y. Garces, L. Wang, L. Bai, N. C. Giles, L. E. Halliburton, and G. Cantwell, *Appl. Phys. Lett.* **81**, 622 (2002).
- [Gar02] N. Y. Garces, N. C. Giles, L. E. Halliburton, G. Cantwell, D. B. Eason, D. C. Reynolds, and D. C. Look, *Appl. Phys. Lett.* **80**, 1334 (2002).
- [Gar03] N. Y. Garces, L. Wang, N. C. Giles, L. E. Halliburton, G. Cantwell, and D. B. Eason, *J. Appl. Phys.* **94**, 519 (2003).
- [Gar98] J. G. E. Gardeniers, Z. M. Rittersma, and G. J. Burger, *J. Appl. Phys.* **83**, 7844 (1998).
- [Ger86] D. Gerthsen, *Phys. Stat. Sol. (a)* **97**, 527, (1986).
- [Gha80] S. Z. Ghandi, and R.J. Field, *Appl. Phys. Lett.* **37**, 5 (1980).
- [Glo95] S. I. Shah, *Handbook of thin film process technology*, ed. by David A. Glocker, Institute of physics publishing, Bristol and Philadelphia (1995).
- [Gra54] T. J. Gray, *J. Am. Ceram. Soc.* **37**, 534 (1954).
- [Gru02a] Th. Gruber, C. Kirchner, and A. Waag, *Phys. Stat. Sol.* **229**, 2, 841 (2002).
- [Gru02b] Th. Gruber, C. Kirchner, K. Thonke, R. Sauer, and A. Waag, *Phys. Stat. Sol.* **192**, 166 (2002).
- [Gru57] M. Grunze, W. Hirschwald and S. Krebs, *Z. Phys. Chem.*, NF 1021976 (1957).
- [Guo02] X. L. Guo, H. Tabata, and T. Kawai, *Opt. Mater.* **19**, 229 (2002).
- [Gus99] E. P. Gusev *et al.*, *IBM J. Res. Develop.* **43**, 3 (1999).
- [Gut88] J. Gutowski, N. Presser, and I. Broser, *Phys. Rev. B* **38**, 9746 (1988).
- [Hac94] A. Hachigo *et al.*, *Appl. Phys. Lett.* **65**, 2556 (1994).
- [Hag00] K. Haga, *et al.*, *J. Crystal Growth* **77**, 214 (2000).

- [Hah65] D. Hahn and R. Nink, *Physik Cond. Mater.* **3**, 311 (1965).
- [Hah98] B. Hahn, G. Heindel, E. Pschorr-Schoberer and W. Gebhardt, *Semicond. Sci. Technol.* **13**, 788 (1998).
- [Han01] C. S. Han, J. Jun and H. Kim, *Appl. Surf. Sci.* **175/176**, 567 (2001).
- [Har96] H. Hardtdegen, *Use of Nitrogen as the Ambient in the LP-MOVPE of III/V's*, Electrochemical Society Proceedings, **96-2**, 49 (1996).
- [Hel50] R. B. Heller, J. McGannon, and A. H. Weber, *J. Appl. Phys.* **21**, 1283, (1950).
- [Heo03] Y. W. Heo, S. J. Park, K. Ip, S. J. Pearton, and D. P. Norton, *Appl. Phys. Lett.* **83**, 1128 (2003).
- [Heo04] Y. W. Heo, K. Ip, S. J. Park, S. J. Pearton, and D. P. Norton, *Applied Physics A* **78**, 53 (2004).
- [Hey00] B. Heying, R. Averbeck, L. F. Chen, E. Haus, H. Riechert, and J. S. Speck, *J. Appl. Phys.* **88**, 1855 (2000).
- [Hey99] B. Heying, E. J. Tarsa, C. R. Elsass, P. Fini, S. P. DenBaars, and J. S. Speck, *J. Appl. Phys.* **85**, 6470 (1999).
- [Hir98] H. Hiramatsu, K. Imaeda, H. Horio and M. Nawata, *J. Vac. Sci. and Technol. A* **16**, 669 (1998).
- [Hof02] D. M. Hofmann, A. Hofstaetter, F. Leiter, H. Zhou, F. Henecker, B. K. Meyer, S. B. Schmidt and P. G. Baranov, *Phys. Rev. Lett.* **88**, 045504 (2002).
- [Hof76] R. W. Hoffmann, *Thin Solid Films* **34**, 185 (1976).
- [Hon00] Hong, H. J. Ko, Y. Chen, T. Hanada, and T. Yao, *J. Vac. Sci. Technol. B*, **18**, 4, (2000).
- [Hon00] S. K. Hong, C. Hang Ju, T. Yao, *J. Cryst. Growth* **209**, 537, (2000).
- [Hon02] S. K. Hong, H. J. Ko, Y. F. Chen, and T. Yao, *J. Vac. Sci. Technol. B* **20**, 1656 (2002).
- [Hu91] J. Hu and R. G. Gordon, *Solar Cells* **30**, 437 (1991).
- [Hu92] J. Hu, and R.G. Gordon, *J. Appl. Phys.* **71**, 2 (1992).
- [Hua02] J. Y. Huang *et al.*, *Journal of Materials Science Letters* **22**, 249 (2002).
- [Hua03] J. Huang, Z. Ye, H. Chen, B. Zhao, and L. Wang, *J. Mater. Sci. Lett.* **22**, 249 (2003).
- [Huh58] T. L. Huheey, and K.F. Cottrell, *The Strengths of Chemical Bonds*, 2nd ed., Butterworths, London (1958).
- [Hul75] D. Hull, *Introduction to Dislocations*, Pergamon Press, 122 (1975).
- [Hum73] K. Hümmer, *Phys. Stat. Sol. B* **56**, 249 (1973).
- [Hwa03] D. Hwang, K. Bang, M. Jeong, and J. Myoung, *J. Cryst. Growth* **254**, 449 (2003).

- [Ip03] K. Ip, M. E. Overberg, Y. W. Heo, D. P. Norton, S. J. Pearton, C. E. Stutz, B. Luo, F. Ren, D. C. Look, and J. M. Zavada, *Appl. Phys. Lett.* **82**, 385 (2003).
- [Ip05] K. Ip, Y. W. Heo, K. H. Baik, D. P. Norton, and S. J. Pearton, and F. Ren, *J. Vac. Sci. Technol.* **B 22**, 171 (2004).
- [Jen92] K. F. Jensen, ICMOVPE VI, Boston, USA (1992).
- [Jin00] B. J. Jin, S. Im, and S. Y. Lee, *Thin Solid Films* **366**, 107 (2000).
- [Joh92] M. A. L. Johnson, S. Fujita, W. H. Rowland, Jr., W. C. Hughes, J. W. Cook, Jr., and J. F. Schetzina, *J. Electron. Mater.* **21**, 157 (1992).
- [Joh96] M. A. L. Johnson, S. Fujita, W. H. Rowland, Jr., W. C. Hughes, J. W. Cook, and J. F. Schetzina, *J. Electron. Mater.* **25**, 855 (1996).
- [Jos01] M. Joseph, H. Tabata, H. Saeki, K. Ueda, and T. Kawai, *Physica B* **302–303**, 140 (2001).
- [Jos99] M. Joseph, H. Tabata, and T. Kawai, *Jpn. J. Appl. Phys.*, **2 38**, L1205 (1999).
- [Ka91] Y. Kanai, *Jpn. J. Appl. Phys.*, Part 1 **30**, 2021 (1991).
- [Kal81] *Zinc Oxide, Properties and Behaviour of the Bulk, the Solid / Vacuum and Solid/Gas Interface, Current Topics in Materials Science*, ed. by E. Kaldis, North-Holland publishing Company, **7** (1981).
- [Kan91] Y. Kanai, *Jpn. J. Appl. Phys.*, Part 1 **30**, 703 (1991).
- [Kas02] A. Kaschner, *et al.*, *Appl. Phys. Lett.* **80**, 1909 (2002)
- [Kas81] M. Kasuga and M. Mochizuki, *J. Cryst. Growth* **54**, 185 (1981).
- [Kas83] M. Kasuga and S. Ogawa, *Jpn. J. Appl. Phys.*, Part 1 **22**, 794 (1983).
- [Kau88] T. Kaufmann, G. Fuchs, and M. Webert, *Crystal Res. Technol.* **23**, 635 (1988).
- [Kav02] A. Kavokin, M. Zamfirescu, B. Gil, G. Malpuech, *Phys. Stat. Sol. (a)* **192**, 212 (2002)
- [Ker70a] W. Kern and R. C. Heim, *J. Electrochem. Soc.* **117**, 562 (1970).
- [Ker70b] W. Kern, and R.C. Heim, *J. Electrochem. Soc.* **117**, 4 (1970).
- [Kha04] Rohit Khanna, K. Ip, Y. W. Heo, D. P. Norton, F. Ren, and S. J. Pearton, *Appl. Phys. Lett.* **85**, 3648 (2004).
- [Kim03] K. K. Kim *et al.*, *Appl. Phys. Lett.* **83**, 63 (2003).
- [Kim94] Y. J. Kim, and H. J. Kim, *Mat. Lett.* **21**, 351 (1994).
- [Kim97] M. H. Kim, C. Sone, J. H. Yi, and E. Yoon, *Appl. Phys. Lett.* **71**, 1228 (1997).
- [Kio03] K. I. Ogata, K. Maejima, Sz. Fujita, and Sg. Fujita, *J. Cryst. Growth* **248**, 25 (2003).
- [Kir03] C. Kirchner, Th. Gruber, F. Reu, K. Thonke, A. Waag, Ch. Giessen, and M. Heuken, *J. Cryst. Growth* **248**, 20 (2003).

- [Kli78] C. Klingshirn, Phys. Status Solidi B, **41**, 547 (1975); **89**, 431 (1978)
- [Kli82] K. Klier, Adv. Katal. **31**, 243 (1982).
- [Kli95] C.F. Klingshirn, *Semiconductor Optics*, Springer-Verlag (1995).
- [Ko00] H. J. Ko, Y. F. Chen, S. K. Hong, and T. Yao, J. Cryst. Growth 209, **816** (2000).
- [Ko02] H. J. Ko, T. Yao, Y. F. Chen, and S. K. Hong, J. Appl. Phys. **92**, 4354 (2002).
- [Ko03] H. J. Ko, Y. F. Chen, Z. Zhu, T. Hanada, and T. Yao, J. Cryst. Growth **208**, 389 (2000).
- [Kob96] K. Kobayashi, T. Matsubara, S. Matsushima, S. Shirakata, S. Isomura, and G. Okada, J. Mat. Sci. Lett. **15**, 457 (1996).
- [Koh00] A. F. Kohan, G. Geder, D. Morgan, and C. C. van de Walle, Phys. Rev. B, **22**, 15019 (2000).
- [Koh74] D. Kohl, M. Henzler, and G. Heiland, Surf. Sci. **41**, 403 (1974).
- [Kor69] V. F. Korzo, P. S. Kireev, and G. A. Lyashchenko, Neorg. Mater. **5**, 2 (1969).
- [Kro05] A. Krost, A. Dadgar, F. Schulze, J. Blaesing, G. Strassburger, R. Clos, A. Diez, P. Veit, T. Hempel, and J. Christen, J. of Cryst. Growth **275**, 209 (2005).
- [Kro54] F. A. Kroger and H. J. Vink, J. Chem. Phys. **22**, 250 (1954).
- [Kro96] A. Krost, G. Bauer, and J. Woitok, High Resolution X-ray Diffraction, *Optical Characterization of Epitaxial Semiconductor Layers*, ed. by G. Bauer and W. Richter, Springer (1996).
- [Kuc02] S. O. Kucheyev *et al.*, Appl. Phys. Lett. **83**, 3350 (2002).
- [Kuc03] S. O. Kucheyev *et al.*, J. Appl. Phys. **93**, 2972 (2003).
- [Lad80] R. J. Lad, P. D. Funkenbusch, and C. R. Aita, J. Vac. Sci. Technol. **17**, 808 (1980).
- [Lan57] J. J. Lander, J. Phys. Chem. Solids, **3**, 87 (1957).
- [Lan82] *Numerical data and functions in science and technology*, Landolt-Börnstein, Vol. III/17b, Springer-Verlag Berlin (1982).
- [Lan99] *Semimagnetic Compounds*, ed. U. Roessler, Landolt-Börnstein Springer-Verlag Berlin Vols. **III/17**, 22 (1999).
- [Lau80] C. K. Lau, S. K. Tiku, and K. M. Lakin, J. Electrochem. Soc. **127**, 1843 (1980).
- [Law89] D. J. Lawrence, S. T. Lee, T. N. Blanton, J. Appl. Phys, **66** (2), 885 (1989).
- [Lee01] E. C. Lee *et al.*, Phys. Rev. B **64**, 085120 (2001).
- [Lei91] T. Lei, M. Fanciulli, R. J. Molnar, T. D. Moustakas, R. J. Graham, and J. Scanlon, Appl. Phys. Lett. **59**, 944 (1991).

- [Lem01] E.W. Lemmon, and M.O. McLinden, *NIST Standard Reference Database 23: NIST Reference Fluid Thermodynamic and Transport Properties*, Version 7.0 beta, National Institute of Standards and Technology, Standard Reference Data Program, Gaithersburg (2001).
- [Les95] M. Leszczynski *et al.*, J. Phys. D, **28**, A149 (1995).
- [Lim04] S. Limpijumnong, S.B. Zhang, S.H. Wei, and C.H. Park, Phys. Rev. Lett. **92**, 155504 (2004).
- [Lim05] J. H. Lim, K. K. Kim, D. K. Hwang, H. S. Kim, J. Y. Oh, and S. J. Park, J. Electrochem. Soc. **152**, 179 (2005).
- [Li03b] X. Li, Y. Yan, T. A. Gessert, C. De Hart, C. L. Perkins, D. Young, and T. J. Coutts, Electrochem. and Solid-State Lett. **6**, 56 (2003).
- [Li97] Y. Li, G. S. Tompa, S. Liang, C. Gorla, Y. Lu, and J. Doyle, J. Vac. Sci. Technol. **15**, 3 1063 (1997).
- [Lia01] S. Liang, H. Sheng, Y. Liu, Z. Huo, Y. Lu, and H. Shen, J. Cryst. Growth **225**, 110 (2001).
- [Lia98] S. Liang, C. R. Gorla, N. Emanetoglu, Y. Liu, W. E. Mayo, and Y. Lu, J. Electron. Mater. **27**, 11, L72 (1998).
- [Lif61] I. M. Lifshitz, and V. V. Sylozov, J. Phys. Chem. Solids **19**, 35 (1961).
- [Lim01] S. H. Lim, D. Shindo, H. B. Kang, and K. Nakamura, J. Vac. Sci. Technol. B **19**, 506 (2001).
- [Lim05] J. H. Lim, K. K. Kim, D. K. Hwang, H. S. Kim, J. Y. Oh, and S. J. Park, J. Electrochem. Soc. **152**, G179 (2005).
- [Lin04] C. C. Lin, S. Y. Chen, S. Y. Cheng, and H. Y. Lee, Appl. Phys. Lett., **84**, 5040, (2004)
- [Liu00] Y. Liu, C.R. Gorla, S. Liang, N. Emanetoglu, Y. Lu, S. Shen, and M. Wraback, J. Electron. Mater. **29**, 69 (2000).
- [Liu92] M. Liu, A. H. Kitai, and P. Mascher, J. Lumin. **54**, 35 (1992).
- [Loo01] D. C. Look, Materials Science and Engineering B **80**, 383 (2001).
- [Li03a] B. S. Li, Y. C. Liu, D. Z. Shen, J. Y. Zhang, Y. M. Lu, and X. W. Fan, J. Cryst. Growth **248**, 179 (2003).
- [Loo01] D. C. Look, Mater. Sci. Eng., B **80**, 383 (2001).
- [Loo02] D. C. Look, D. C. Reynolds, C. W. Litton, R. L. Jones, D. B. Eason, and G. Cantwell, Appl. Phys. Lett. **81**, 1830 (2002).
- [Loo04a] D. C. Look, B. Claflin, Y. I. Alivov, and S. J. Park, Phys. Stat. Sol. (b) **241**, 624 (2004).

- [Loo04b] D. C. Look, G. M. Renlund, R. H. Burgener, and J. R. Sizelove, *Appl. Phys. Lett.* **85**, 5269 (2004).
- [Loo05] D. C. Look, *Semicond. Sci. Technol.* **20**, S55 (2005).
- [Loo76] P. Loose, M. Rosenzweig, and M. Wölecke, *Phys. Stat. Sol. B* **75**, 137 (1976).
- [Loo98] D. C. Look, D. C. Reynolds, J. R. Sizelove, R. L. Jones, C. W. Litton, G. Cantwell, and W. C. Harsch, *Solid State Commun.* **105**, 399 (1998).
- [Loo99] D. C. Look, D. C. Reynolds, J. W. Hemsley, R. L. Jones, and J. R. Sizelove, *Appl. Phys. Lett.* **75**, 811 (1999).
- [Lor00] K. Lorenz, M. Gonsalves, W. Kim, V. Narayanan, and S. Mahajan, *Appl. Phys. Lett.* **77**, 3391 (2000).
- [Los05] M. Losurdo and M. M. Giangregorio, *Appl. Phys. Lett.* **86**, 091901 (2005).
- [Lu03] J. Lu, Y. Zhang, Z. Ye, L. Wang, B. Zhao, and J. Huang, *Mater. Lett.* **57**, 3311 (2003).
- [Mad91] R. Madelung, *Semiconductors Group IV and III-V compounds* Springer, Berlin (1991).
- [Mak01] T. Makino *et al.*, *Appl. Phys. Lett.* **78**, 1237 (2001).
- [Man64] G. Mandel, *Phys. Rev.* **134**, A1073 (1964).
- [Man69] H. M. Manasevit and W. I. Simpson, *J. Electrochem. Soc.* **116**, 1725 (1969).
- [Mar62] A. N. Mariano, R. E. Hannemann, *J. Appl. Phys.*, **34**, 384 (1962).
- [Mar69] H. P. Maruska and J. J. Tietjen, *Appl. Phys. Lett.* **15**, 327 (1969).
- [Mar89] T. Maruyama, and A. Nakai, *Jpn. J. Appl. Phys.* **28**, 3 (1989).
- [Mat03] H. Matsui *et al.*, *Japanese Journal of Applied Physics* **42**, 5494 (2003).
- [Mat66] Y. Matsui, K. Kamiya and M. Nishikawa, *J. Chem. Soc. Japan*, **39**, 1828 (1966).
- [Mat90] K. Matsumoto and K. Noda, *J. Cryst. Growth* **102**, 137 (1990).
- [Mey03] B. Meyer and D. Marx, *J. Phys. Condens. Matter* **15**, L89 (2003).
- [Mey04] B. K. Meyer, H. Alves, D. M. Hoffmann, W. Kriegseis, D. Forster, F. Bertram, J. Christen, A. Hoffmann, M. Strassburg, M. Dworzak, U. Haboeck, and A. V. Rodina, *Phys. Stat. Sol. B* **241**, No. 2, 231 (2004).
- [Mey05] B. K. Meyer, J. Sann, D. M. Hofmann, C. Neumann and A. Zeuner, *Semicond. Sci. Technol.* **20**, S62 (2005).
- [Min85] T. Minami, H. Sato, H. Nanto and S. Takata, *Jpn. J. Appl. Phys.* **24**, L781 (1985).
- [Min94] T. Minami *et al.*, *Thin Solid Films* **253**, 14 (1994).
- [Min97] K. Minegishi, Y. Koiwai, Y. Kikuchi, K. Yano, M. Kasuga, and A. Shimizu, *Jpn. J. Appl. Phys.*, **36**, L1453 (1997).

- [Mok80] W. Mokva, D. Kohl, and G. Heiland, *Surf. Sci.* **99**, 202 (1980).
- [Mol54] E. Mollwo, *Z. Physik* **138**, 478 (1954).
- [Mor02] C. Morhain *et al.*, *Phys. Status Solidi B* **229**, 881 (2002).
- [Mor02] H. Morkoc, J. Jasinki, Z. Liliental-Weber, and C. W. Litton, *J. Vac. Sci. Technol. B* **20**, 2256 (2002).
- [Mue05] E. Mueller, D. Livinov, D. Gerthsen, C. Kirchner, A. Waag, N. Oleynik, A. Dadgar, and A. Krost, *NATO Science Series, II: Mathematics, Physics and Chemistry*, 194 (Zinc Oxide), **99**, 111 (2005), Springer.
- [Mut01] S. Muthukumar, N. W. Emanetoglu, G. Patounakis, C. R. Gorla, S. Liang, and Y. Lua, *IEEE*, **2**, 1 (2003).
- [Mut03] S. Muthukumar, H. Sheng, J. Zhong, Zh. Zhang, N. W. Emanetoglu, and Y. Lu, *J. Vac. Sci. Technol. A* **19** (2001).
- [Nah01] A. Nahhas, H. K. Kim, and J. Blachere, *Appl. Phys. Lett.* **75**, 1511 (2001).
- [Nak01] K. Nakahara, H. Takasu, P. Fons, A. Yamada, K. Iwata, K. Matsubara, R. Hunger, and S. Niki, *Appl. Phys. Lett.* **79**, 4139 (2001).
- [Nak96] S. Nakamura, M. Senoh, S. Nagahama, N. Isawa, T. Yamada, T. Matsushita, H. Kiyoku, and Y. Sugimoto, *Jpn. J. Appl. Phys.* **35**, L74 (1996).
- [Nak98] B. Kang, K. Nakamura, S. H. Lim, and D. Shindo, *Jpn. J. Appl. Phys., Part 1* **37**, 781 (1998).
- [Nar98] J. Narayan, K. Dovidenko, A. K. Sharma, and S. Oktyabrsky, *J. Appl. Phys.* **84**, 2597 (1998).
- [Nar02] J. Narayan, and B. C. Larson, *J. Appl. Phys.* **93**, 278 (2002).
- [Nau99] J. Nause, *III-Vs Review* **12**, 28 (1999).
- [Neu95] J. Neugebauer, and C. C. van der Walle, *Phys. Rev. Lett.* **75**, 4452 (1995).
- [Nin97] Z. Y. Ning *et al.*, *Thin Solid Films* **307**, 50 (1997).
- [Nte99] J. M. Ntep *et al.*, *J. Cryst. Growth* **207**, 30 (1999).
- [Oba01] F. Oba *et al.*, *J. Appl. Phys.* **90**, 824 (2001).
- [Oda85] S. Oda, H. Tokunaga, N. Kitajima, J. Hanna, I. Shimizu, and H. Kokado, *Jpn. J. Appl. Phys.* **24**, 1607 (1985).
- [Oga01] K. I. Ogata, T. Kawanishi, K. Maejima, K. Sakurai, S. Fujita, and S. Fujita, *Jpn. J. Appl. Phys.* **40**, L657 (2001) .
- [Oga02a] K. Ogata, S. W. Kim, Sz. Fujita, and Sg. Fujita, *J. Cryst. Growth* **240**, 112 (2002).
- [Oga02b] K. I. Ogata, T. Kawanishi, K. Maejima, K. Sakurai, Sz. Fujita, and Sg. Fujita, *J. Crystal Growth* **237-239**, 553 (2002).

- [Oga90] M. F. Ogawa, Y. Natsume, T. Hirayama, and H. Sakata, *J. Mat. Sci. Lett.* **9**, 1351 (1990).
- [Oha02] N. Ohashi, T. Ishigaki, N. Okada, T. Sekiguchi, and H. Haneda, *Appl. Phys. Lett.* **80**, 2869 (2002).
- [Oht98] A. Ohtomo *et al.*, *Appl. Phys. Lett.* **72**, 2466 (1998).
- [Oht99] A. Ohtomo, K. Tamura, K. Saikusa, K. Takahashi, T. Makino, Y. Segawa, H. Koinuma, and M. Kawasaki, *Appl. Phys. Lett.* **75**, 2635 (1999).
- [Ost00] W. Ostwald, *Z. Phys. Chem.* **34**, 495 (1900).
- [Pan71] J. I. Pankove, E. A. Miller, and J. E. Berkeyheiser, *RCA review* **32**, 383 (1971).
- [Par02] C. H. Park, S. B. Zhang, and S. H. Wei, *Phys. Rev. B* **66**, 073 202 (2002).
- [Pat03] P. Patnaik, *Handbook of inorganic chemicals*, The McGraw Hill Companies (2003).
- [Per05] C. L. Perkins, S. H. Lee, X. Li, S. E. Asher, and T. J. Coutts, *J. Appl. Phys.* **97**, 034907 (2005).
- [Pol03] A. Y. Polyakov *et al.*, *J. Appl. Phys.* **94**, 400 (2003).
- [Pre88] N. Presser, Diplomarbeit, *Spektroskopie exzitonischer Komplexe in ZnO bei hohen Magnetfeldern und Anregungsintensitäten*, Technische Universität Berlin (1988).
- [Pro95] I. Y. Prosanov and A. A. Politov, *Inorg. Mater.* **31**, 663 (1995).
- [Rac93] G. A. Racine *et al.*, *MEMS Proceedings*, 128, see also www.samlab.unine.ch (1993).
- [Rei98] L. Reimer, *Scanning Electron Microscopy – Physics of Image Formation and Micro analysis*, Springer-Verlag Berlin (1998).
- [Rey65] D. C. Reynolds, C. W. Litton, and T.C. Collins, *Phys. Rev.* **140**, A1726 (1965).
- [Ric34] F. O. Rice and K. F. Herzfeld, *J. Amer. Chem. Soc.*, **56**, 284 (1934).
- [Rie01] T. Riemann, Dissertation, Otto-von-Guericke Universität Magdeburg, 2001.
- [Rie02] T. Riemann, J. Christen, G. Kaczmarczyk, A. Kaschner, A. Hoffmann, A. Zeuner, D. Hofmann, and B. K. Meyer, *Phys. Stat. Sol. b* **229**, 891 (2002).
- [Rie41] N. Riehl, *Physik und Technische Anwendungen der Lumineszenz*, Julius-Springer-Verlag, Berlin (1941).
- [Rie52] N. Riehl and O. Ortman, *Z. Elektrochem.* **60**, 149 (1952).
- [Rom03] J. F. Rommeluere, L. Svob, F. Jomard, J. Mimila Arroyo, A. Lusson, V. Sallet, and Y. Marfaing, *Appl. Phys. Lett.* **83**, 287 (2003).

- [Ron04] C. Ronning, P. X. Gao, Y. Ding, Z. L. Wang, and D. Schwen, *Appl. Phys. Lett.* **84**, 783 (2004).
- [Rot81] A.P. Roth, and D.F. Williams, *J. Appl. Phys.* **52**, 11 (1981).
- [Rou99] J. L. Rouvière, J. Simon, N. Pelekanos, B. Daudin, and G. Feuillet, *Appl. Phys. Lett.* **75**, 2632 (1999).
- [Rya68] L. A. Ryabova, Y. S. Savitskaya, and R. N. Sheftal, *Izv. Akad. Nauk SSSR Neorg. Mater.* **4**, 602 (1968).
- [Rym52] T. B. Rymer and G. D. Archard, *Research London* **5**, 292 (1952).
- [Ryu00] Y. R. Ryu, S. Zhu, D. C. Look, J. M. Wrobel, H. M. Jeong, and H. W. White, *J. Cryst. Growth* **216**, 330 (2000).
- [Ryu02] M. K. Ryu, S. H. Lee, and M. S. Jang, *J. Appl. Phys.* **92**, 158 (2002).
- [Ryu03] Y. R. Ryu, T. S. Lee, J. H. Leem, H. W. White, *Appl. Phys. Lett.* **83**, 4032 (2003).
- [Sak00] K. Sakurai, M. Kanehiro, K. Nakahara, T. Tanabe, S. Fujita, and S. Fujita, *J. Cryst. Growth* **209**, 522 (2000).
- [Sak01] T. Sakagami *et al.*, *J. Cryst. Growth* **229**, 98 (2001).
- [San98a] B. Sang, A. Yamada, and M. Konagai, *Jpn. J. Appl. Phys.* **37**, L1125 (1998).
- [San98b] B. Sang, A. Yamada, and M. Konagai, *Jpn. J. Appl. Phys.* **37**, L206 (1998).
- [Sat94] H. Sato *et al.*, *Thin Solid Films* **246**, 65 (1994).
- [Sav64] Y. S. Savitskaya and L. A. Ryabova, *Zh. Prikl. Khim.* **37**, 796 (1964).
- [Sch68] O. F. Schirmer, *J. Phys. Chem. Solids* **29**, 1407 (1968).
- [Sch70] O. F. Schirmer and D. Zwingel, *Solid State Commun.* **8**, 1559 (1970).
- [Sch85] M. Schilling, R. Helbig and G. Pensl, *J. Lumin.* **33**, 201 (1985).
- [Sch38] W. Schottky, *Naturwissenschaften*, **26**, 843 (1938).
- [Sek00] T. Sekiguchi, K. Haga, and K. Inaba, *J. Cryst. Growth* **214/215**, 68 (2000).
- [Sek00] T. Sekiguchi, S. Miyashita, K. Obara, T. Shishido, and N. Sakagami, *J. Cryst. Growth* **214/215**, 72 (2000).
- [Set04] A. Setiawan *et al.*, *J. Appl. Phys.*, **96**, 3793 (2004).
- [She00] X. Q. Shen, T. Ide, S. H. Cho, M. Shimizu, S. Hara, and H. Okumura, *Appl. Phys. Lett.* **77**, 4013 (2000).
- [She03] H. Sheng, N.W. Emanetoglu, S. Muthukumar, B.V. Yakshinskiy, S. Feng, and Y. Lu, *Journal of Electronic Materials* **32**, 935 (2003).
- [Shi02] S. Shirakata, K. Saeki, and T. Terasako, *J. Cryst. Growth* **237-239**, 528 (2002).
- [Shi71] M. Shiloh and J. Gutman, *J. Cryst. Growth* **11**, 105 (1971).

- [Shi78] T. Shiosaki, S. Ohnishi, Y. Hirokwa, and A. Kawabata, *Appl. Phys. Lett.*, **35**, 406 (1978).
- [Shi81] T. Shiozaki et al., *Appl. Phys. Lett.* **39**, 5 (1981).
- [Shi88] M. Shimuzu, H. Kamei, M. Tanizawa, T. Shiosaki, and A. Kawabata, *J. Cryst. Growth* **89** (1988).
- [Shi90] M. Shimuzu, T. Takayama, Y. Tanaka, T. Shiosaki, and A. Kawabata, *J. Cryst. Growth* **101**, 171 (1990).
- [Shi94] W. Shih and M. Wu, *J. Cryst. Growth* **137**, 319 (1994).
- [Shi99] W. J. Li, E. W. Shi, W. Z. Zhong, and Z. W. Yin, *J. Cryst. Growth* **203**, 186 (1999).
- [Shr90] D. F. Shriver, P. W. Atkins, and C. H. Langford, *Anorganische chemie*, Oxford University Press (1990).
- [Sin03] A. V. Singh, R. M. Mehra, A. Wakahara, and A. Yoshida, *J. Appl. Phys.* **93**, 396 (2003).
- [Sla72] G. A. Slack, *Phys. Rev.* **6**, 3791 (1972).
- [Smi83] F. T. J. Smith, *Appl. Phys. Lett.* **43**, 12 (1983).
- [Sol83] R. Solanki, and G.J. Collins, *Appl. Phys. Lett.* **42**, 8 (1983).
- [Son03] J. O. Song, K. K. Kim, S. J. Park, and T. Y. Seong, *Appl. Phys. Lett.* **83**, 479 (2003).
- [Sou88] P. Souletie and B. W. Wessels, *Journal of Mat. Res.*, **3**, 740 (1989).
- [Sri95] V. Srikant, V. Sergo, and D. R. Clarke, *Appl. Phys. Lett.* **16**, 439 (1995).
- [Ste97] S. Stepanov, 3th Autumn School on X-ray Scattering from Surfaces and Thin Layers, Slovakia (1997).
- [Str03] A. Strecker, U. Salzgeber, and J. Mayer, *Prakt. Metallographie* **30**, 482 (1993).
- [Str03] Y. M. Strzhemechny, J. Nemergut, P. E. Smith, J. Bae, D. C. Look, and L. J. Brillson, *J. Appl. Phys.* **94**, 4256 (2003).
- [Suk82] M. H. Sukkar, and H. L. Tuller, *Advances in Ceramics*, edited by M. F. Yan and A. H. Heuer, American Ceramic Society, Columbus, **7**, 71 (1982).
- [Sun00] H. D. Sun *et al.*, *Appl. Phys. Lett.* **77**, 4250 (2000).
- [Sus99] M. Suscavage *et al.*, *MRS Internet J. Nitride Semicond. Res.* **4S1**, G3.40 (1999).
- [Sze91] S. M. Sze, *Physics of Semiconductor Devices*, 2nd edition (1991).
- [Tab02] X. L. Guo, H. Tabata, and T. Kawai, *J. Cryst. Growth* **223**, 135 (2001).
- [Tab95] T. V. Tabenskaya, V. P. Ovsyannikov, and E. A. Mazurenko, *J. Phys.* **IV**, C5-711 (1995).
- [Tak03] T. Takagi, H. Tanaka, and S. Fujita, *Jpn. J. Appl. Phys.* **42**, L401 (2003).

- [Tak99] N. Takahashi, K. Kaiya, T. Nakamura, Y. Momose, and H. Yamamoto, *Jpn. J. Appl. Phys.*, **38**, L454 (1999).
- [Tar97] E. J. Tarsa, B. Heying, X. H. Wu, P. Fini, S. P. DenBaars, and J. S. Speck, *J. Appl. Phys.* **82**, 5472 (1997).
- [The02] B. Theys *et al.* *J. Appl. Phys.* **91**, 3922 (2002).
- [The03] B. Theys, V. Sallet, F. Jomard, A. Lusson, J. F. Rommeluere, and Z. Teukam, *J. Appl. Phys.* **91**, 3922 (2002).
- [Tho56] D. G. Thomas and J. J. Lander, *the Journal of Chemical Physics*, **25**, 1136 (1956).
- [Tho59] D. G. Thomas, *J. Phys. Chem. Solids* **9**, 31 (1959).
- [Tik80] S. K. Tiku, C. K. Lau, and K. M. Lakin, *Appl. Phys. Lett.* **36**, 318 (1980).
- [Tom76] E. Tomzig and H. Helbig, *J. Lumin.* **14**, 403 (1976).
- [Tuz01] S. Tuzemen, G. Xiong, J. Wilkinson, B. Mischuck, K.B. Ucer, R.T. Williams, *Physica B* **308**, 1197 (2001).
- [Vai05] V. Vaithianathan, B. T. Lee, and S. S. Kim, *Appl. Phys. Lett.* **86**, 062101 (2005).
- [Val91] A. Valentini, F. Quaranta, M. Rossi, and G. Battaglin, *J. Vac. Sci. Technol. A* **9**, 286 (1991).
- [Veh67] W. H. Vehse, V. A. Sibley, F. J. Kell, and Y. Chen, *Phys. Rev.* **167** (1967).
- [Vel90] Vellekoop *et al.*, "Compatibility of Zinc Oxide with Silicon IC Processing", *Sensors and Actuators A*, **21-23**, 1027, (1990).
- [Vig01] F. V. Vigué, P. Vézian, S. Laügt, and J. P. Aurie, *Appl. Phys. Lett.* **79**, 194, (2001).
- [Vis98] R. D. Vispute *et al.*, *Appl. Phys. Lett.* **73**, 348 (1998).
- [Wal00] C. C. van der Walle, *Phys. Rev. Lett.* **85**, 1012 (2000).
- [Wal01] C. C. van de Walle, *Physica B*, **308-310**, 899 (2001).
- [Wal02] C. C. van de Walle, *Phys. Stat. Solidi B*, **229**, 221 (2002).
- [Wal04] T. Walther, N. Daneu and A. Rechnik, *Interface Science* **12**, 267 (2004).
- [Wan01] X. Wang *et al.*, *J. Cryst. Growth* **226**, 123 (2001).
- [Wan02a] X. Wang, S. Yang, J. Wang, X. Jiang, G. Du, X. Liu, and R.P.H. Chang, *Optic. Quant. Electron.* **34**, 883 (2002).
- [Wan02b] J. Z. Wang *et al.*, *Chin. Phys. Lett.* **19**, 581 (2002).
- [Wan03a] L. G. Wang and A. Zunger, *Phys Rev Lett* **90**, 256401 (2003).
- [Wan03b] C. Wang, Z. Ji, K. Liu, Y. Xiang, and Z. Ye, *J. Cryst. Growth* **259**, 279 (2003).
- [Wan03c] J. Wang, G. Du, B. Zhao, X. Yang, Y. Zhang, Y. Ma, D. Liu, Y. Chang, H. Wang, H. Yang, and S. Yang, *J. Cryst. Growth* **255**, 293 (2003).
- [Wan05] X. Wang, Y. Tomita, O. H. Roh, M. Ohsugi, S. B. Che, Y. Ishitani, and

- A. Yoshikawa, Appl. Phys. Lett. **86**, 1192 (2005).
- [Wen03] H. von Wenckstern, E. M. Kaidashev, M. Lorenz, H. Hochmuth, G. Biehne, J. Lenzner, V. Gottschalch, R. Pickenhain, and M. Grundmann, Appl. Phys. Lett. **84**, 79 (2001).
- [Wen91] W. W. Wenas, A. Yamada, M. Konagai, and K. Takahashi, Jpn. J. Appl. Phys. **30**, L 441 (1991).
- [Wil96] D. B. Williams, C. B. Carter, Plenum Publishing Corporation, *Transmission Electron Microscopy*, (1996).
- [Wra99] M. Wraback *et al.*, Appl. Phys. Lett. **76**, 507 (1999).
- [Wri84] P. J. Wright, R. J. M. Griffiths, and B. Cokayne, J. Cryst. Growth **66** (1984).
- [Xli05] X. Li, B. Keyes, S. Asher, S. B. Zhang, S. H. Wei, T. J. Coutts, S. Limpijumnong, C. G. Van de Walle, Appl. Phys. Lett. **86**, 122107 (2005).
- [Xu04] W. Z. Xu *et al.* J. Cryst. Growth **265**, 133 (2004).
- [Yam00] T. Yamamoto and H. Katayama-Yoshida, J. Cryst. Growth **214**, 552 (2000).
- [Yam02] T. Yamamoto, Thin Solid Films **420–421**, 100 (2002).
- [Yam99] T. Yamamoto and H. Katayama-Yoshida, Jpn. J. Appl. Phys., **38**, L166 (1999).
- [Yan01] Y. Yan, S. B. Zhang, and S. T. Pantelides, Phys. Rev. Lett., **86**, 5723 (2001).
- [Yan03] X. Li, Y. Yan, T. A. Gessert, C. L. Perkins, D. Young, C. Dehart, M. Young, and T. J. Coutts, J. Vac. Sci. Technol. A **21**, 1342 (2003).
- [Ye03] Z. Z. Ye *et al.*, J. Cryst. Growth **253**, 258 (2003).
- [Ye04] Z. Z. Ye, F. Zhu-Ge, J. Cryst. Growth **265**, 127 (2004).
- [Ye05] Z. Z. Ye, *et al.*, J. Cryst. Growth **274**, 178 (2005).
- [Yos02] A. Yoshikawa and K. Xu, Thin Solid Films **412**, 38 (2002).
- [Yos93] M. Yoshino *et al.*, Jpn. J. Appl. Phys. **32**, 726 (1993).
- [Yu97] P. Yu *et al.*, Solid State Commun. **103**, 459 (1997).
- [Yua05] G. D. Yuan, Z. Z. Ye, Q. Qian, U. P. Zhu, J. Y. Huang, and B. H. Zhao, J. Cryst. Growth **273**, 451(2005).
- [Zam02] M. Zamfirescu, A. Kavokin, B. Gil, G. Malpuech, and M. Kaliteevski, Phys. Rev. B **65**, 161205 (2002).
- [Zaw94] C. L. Zaws, *Handbook of vapor pressure*, Gulf publishing company, **1**, 164 (1994).
- [Zha01] S. B. Zhang, S. H. Wei, and A. Zunger, Phys. Rev. B, **63**, 075205 (2001).
- [Zhu04] J. Zhu, N.W. Emanetoglu, Y. Chen, B. V. Yakshinskiy, Y. Lu, J. El. Mat., **33**, 556 (2004).
- [Zun03] A. Zunger, Appl. Phys. Lett. **83**, 57 (2003).

Acknowledgements

I would like to thank:

Prof. Dr. Alois Krost, for the opportunity to work in his group, the interesting research topic, and excellent work conditions,

Dr. Armin Dadgar, for the great support, helpful discussions, constructive critics, corrections, and optimism,

The research teams from the department of solid state physics: Prof. Dr. J. Christen, Dr. F. Bertram, Dr. J. Bläsing, Dr. A. Krtschil, Dr. H. Witte, Dr. T. Hempel, Dr. T. Riemann, Dr. P. Veit, A. Diez, F. Schulze, S. Deiter, M. Adam, A. Reiher, D. Forster, S. Petzold, M. Hinz, H. Witek for the great team spirit, measurements, friendly support, constructive critics, and helpful discussions,

German Ministry of Research and Education (BMBF) for their financial support of the project,

Ute Haboeck, for Raman measurements and helpful discussions,

Prof. Gerthsen and E. Mueller from University of Karlsruhe for TEM measurements,

Prof. Dr. B. Meyer and his team from the University of Giessen for the fruitful cooperation,

Prof. Dr. A. Hoffmann and his team from the Technical University of Berlin for the fruitful cooperation,

Prof. Dr. M. Grundmann and his team in the University of Leipzig for the fruitful cooperation,

Prof. Dr. A. Waag and his team in the University of Baunschweig for the fruitful cooperation,

Dr. Peter Kohlert for the helpful discussions, and sense of humor,

Dr. Matthias Schroeter for discussions and corrections of this thesis,

V. Mazovetskaya,

Моя глубочайшая признательность Родителям и Бабуле за их моральную поддержку и понимание (my Father, Mother, and my Grandma for their moral support and understanding).

Erklaerung

Hiermit erkläre ich, dass ich die von mir eingereichte Dissertation zum dem Thema „MOVPE Growth and Characterisation of ZnO Properties for Optoelectronic Applications“ selbstständig erfasst, nicht schon als Dissertation verwendet habe und bei benutzten Hilfsmittel und Quellen vollständig angegeben wurden.

Weiterhin erkläre ich, dass ich werde dieser noch eine andere Arbeit zur Erlangung des akademischen Grades doctor reum naturalium (Dr. rer. nat.) an anderen Einrichtungen eingereicht habe.

Dresden,

Dipl. Phys. Nikolay Oleynik

.....

Lebenslauf

Persönliches

Familienname Oleynik
Vorname Nikolay
Fruehere Namen Oleynik
Geburtsdatum 25.04.1979
Geburtsort Siedlung Kirovskij, Gebiet Taldy-Kurgan, Kasachstan
Geschlecht M
Wohnzitz und
Korrespondenzanschrift Fichtenstrasse 6, 01097 Dresden
Staatsangehoerigkeit Russland
Familienstand Ledig

Schulbildung

09.1986 –05.1994 Schule №4, Semipalatinsk, Kasachstan
09.1994 –05.1996 Specialized Educational Scientific Center for Physics,
Mathematics, Chemistry and Biology Education of Novosibirsk
State University, Novosibirsk, Russland

Studium

09.1996 –06.1998 Beginn der Physikstudiums an der Staatlichen Universität
Novosibirsk, Novosibirsk, Russland
09.1998 –06.2001 Physikstudium mit der Spezialisierung Mikroelektronik an der
Weissrussischen Staatlichen Universität, Minsk, Weissrussland
09.2000 - 06.2001 Diplomarbeit: „*Untersuchung Elektrophysikalischer
Eigenschaften on Polykristallinen Siliziumschichten und
Entwicklung einer Wirkwiderstandsmatrix auf deren Grundlage*“
06.2001 Diplom in Physik

Promotion

09.2001 – 03.2007 Promotionsstudium an der Otto-von-Guericke Universität
Magdeburg, im Fachbereich Halbleiterepitaxie.
Promotionsarbeit: „*MOVPE Growth and Characterisation of
ZnO Properties for Optoelectronic Applications*“

Jetztige Beschäftigung

Seit 10.2004 Fertigungsingenier bei AMD Fab36 LLC&Co, Dresden
Dresden, 03.04.2007

Nikolay Oleynik

Biography

Personal

Family name Oleynik
Fist name Nikolay
Earlier names Oleynik
Date of birth 25.04.1979
Place of birth Settement Kirovskij, Taldy-Kurgan, Kasachstan
Sex M
Correspondence Adress Fichtenstrasse 6, 01097 Dresden
Nationality Russia
Family status Single

School Education

09.1986 –05.1994 School №4, Semipalatinsk, Kasachstan
09.1994 –05.1996 Specialized Educational Scientific Center for Physics,
Mathematics, Chemistry and Biology Education of Novosibirsk
State University, Novosibirsk, Russia

High School Education

09.1996 –06.1998 Begin of the physics study in the Novosibirsk State University,
Novosibirsk, Russia
09.1998 –06.2001 Physics study with the specialisation in microelectronics.
Belarus State University, Minsk, Belarus
09.2000 - 06.2001 Diplom: „*Study of the electro-physical properties of the
polycrystalline silicon films and the development of the resistor
matrix on their basis*“
06.2001 Diplom in Physics

Promotion

09.2001 – 03.2007 PhD study in Otto-von-Guericke University Magdeburg, with a
specialisation in semiconductor epitaxy.
Dissertation: „*MOVPE Growth and Characterisation of ZnO
Properties for Optoelectronic Applications*“

Current Activity

Since 10.2004 Manufacturing Engineer at AMD Fab36 LLC&Co, Dresden
Dresden, 03.04.2007

Nikolay Oleynik

